Laser Assisted Synthesis of Precious Metal Electrocatalysts

A thesis submitted to

The University of Manchester

for the degree of

Doctor of Philosophy (PhD)

in the Faculty of Science and Engineering

2020

Yudong Peng

Department of Materials, School of Natural Sciences

List of Contents

List of Figures

List of Tables

List of Abbreviations

2D	Two Dimensional
3D	Three Dimensional
Ar	Argon
CV	Cyclic Voltammetry
CW	Continuous Wave
DP	Diffraction Pattern
ECSA	Electrochemically active Surface Area
EDS	Energy Dispersive X-ray Spectroscopy
EGO	Electrochemical Graphene Oxide
EIS	Electrochemical Impedance Spectroscopy
FC	Fuel Cell
FE	Finite Element
FEG	Field Emission Gun
FWHM	Full Width Half Maximum
GO	Graphene Oxide
rEGO	reduced Electrochemical Graphene Oxide
rGO	reduced Graphene Oxide
HAADF	High Angle Annular Dark Field
HER	Hydrogen Evolution Reaction
ICP-OES	Inductively Coupled Plasma - Optical Emission Spectroscopy
IR	Infrared
LSV	Linear Sweep Voltammogram
Mn	Manganese
NP	Nanoparticle
OER	Oxygen Evolution Reaction
ORR	Oxygen Reduction Reaction
PEMFC	Proton Exchange Membrane Fuel Cell
PLAL	Pulsed Laser Ablation in Liquid
Pd	Palladium
Pt	Platinum
RHE	Reversible Hydrogen Electrode
Ru	Ruthenium
SAC	Single Atom Catalyst
SADP	Selected Area Diffraction Pattern
SEs	Secondary Electrons
SEM	Scanning Electron Microscopy
STEM	Scanning Transmission Electron Microscopy
TEM	Transmission Electron Microscopy
TOF	Turn Over Frequency
UV	Ultraviolet
UV-Vis	Ultraviolet - Visible
XPS	X-ray Photoelectron Spectroscopy
XRD	X-ray Diffraction
YAG	Yttrium Aluminium Garnet

Laser Assisted Synthesis of Precious Metal Electrocatalysts

A thesis submitted to The University of Manchester for the degree of Doctor of Philosophy (PhD) in the Faculty of Science and Engineering

2020

Yudong Peng

Department of Materials, School of Natural Sciences

Abstract

Precious metal (e.g. Pt, Ru, Pd) as a promising class of metal electrocatalysts are widely used in various energy conversion and storage scenarios, e.g. oxygen reduction reaction (ORR), oxygen evolution reaction (OER) and hydrogen evolution reaction (HER) etc. However, the conventional synthesis routes through wet chemistry generally led to several issues: using harsh chemicals and stabilizer, which requires post-process purification and the ligand may cover the catalyst's surface and hinder further application; a relatively long processing time; and lack of universality. The laser-assisted fabrication stands out as a promising approach for electrocatalysts synthesis, for its free of ligands coverage, which guarantees nanoparticles (NPs) with bare surface exposure and avoids extensive post-synthesis purification and cleaning. Additionally, the laser-assisted approaches are not materials specific, *i.e.* the methods are not designed for specific elements/materials, which can be easily extended to a wide variety of nanomaterials fabrication. In this thesis, the laser fabrication technique as a fast, facile and versatile tool for the synthesis of precious metal electrocatalysts was studied. Moreover, the thesis dedicates to explore the potential of laser fabrication methods for effective size reduction of nanomaterials, as the catalysts dimension has a significant impact on the active site exposure and precious metal utilization.

In this work, benefiting by the monochromaticity, high brightness and wide range of wavelengths, various laser-assisted synthesis routes are developed to fabricate platinum group metal catalysts. The main contributions include: **(i)** Laser ablation of a Pt target in liquid and further size refinement using an ultraviolet (UV) Excimer laser. Monodispersed Pt nanoparticles (NPs) with an average size of 4.7 nm were successfully synthesized, and the laser refined Pt NPs possesses enhanced ORR performance. The Pt NPs size tailoring through the exposure of 248 nm laser irradiation was simulated by considering the size-dependent

absorption of the incident beam, heat accumulation and dissipation, and phase changes. The mechanism of Pt NPs size refinement through selective surface vaporization was proposed. **(ii)** A laser-assisted facile, continuous, solution route for simultaneously reducing graphene oxide and metal precursors was developed. Benefit by the semiconductor characteristic of graphene oxide, and high photon energy together with a high laser fluence of the 248 nm Excimer laser, the obtained RuO_2 and Pt nanoparticles with average sizes of 2.8 and 2.0 nm, respectively, were rapidly deposited on the reduced graphene oxide (GO) flakes. Further electro-catalytical tests demonstrated the promising performance of RuO_2 and Pt functionalized graphene composites in OER, HER, ORR and supercapacitor applications. Based on the experimental findings, the photo-deposition mechanism was deduced to be the photo-induced electron-hole pairs on the GO flakes under UV irradiation. **(iii)** Graphene-based Pt single-atom catalysts (SACs) fabrication through fast photothermal reduction of both GO and Pt precursor using 1064 nm picosecond laser was demonstrated for the first time. Several key aspects were addressed to successfully fabrication Pt SACs through the solid-phase laser synthesis strategy, including the laser wavelength, pulse overlaps, selection of metal precursors *etc*. To understand the effect of laser process parameters on the single-atom synthesis, a numerical model was built to study the temporal evolution of heat. In the later electrochemical tests, the graphene-based Pt SACs exhibits comparable HER activity to the commercial catalyst but with ultrahigh precious metal utilization. Owing to the rapid scanning process, the productivity in current lab-scale can reach ~ 2 mg/s (i.e. ~ 7.2 g/h). The non-contact and fast SACs synthesis process is deemed compatible with roll-to-roll fabrication, thereby demonstrating its flexible and robust production capability.

Declaration

I hereby declare that no portion of this work referred to in the thesis has been submitted in support of an application for another degree or qualification of this or any other university or other institute of learning.

Copyright Statement

Acknowledgements

Firstly, I would like to offer my sincerely gratitude to my supervisors, Dr. Zhu Liu and Prof. Lin Li, for all of their help, guidance and support throughout my postgraduate studies. Not only I have been inspired by their comprehensive knowledge and key suggestion, but also their rigorous criteria and genuine interest in research taught me how to become a qualified researcher. Their enthusiasm and professionalism to work will be remembered and followed in my future career life.

I am grateful to my parents for their unconditional love and continuing support throughout my studies.

I would like to convey my appreciativeness towards those who I have had pleasure to collaborate with these years of studies. I especially thank Dr. Jianyun Cao, Mr. Jie Yang and Ms. Wenji Yang for sharing their knowledge, idea and experience. My sincere thanks also go to Prof. Dirk Engelberg who reviewed and examined my annual report and gave me useful advice on my projects.

I am indebted to my colleges for establishing a well-being working environment, and I sincerely thanks to their everlasting patience and generosity at all time. Particularly, I appreciate Dr. Claudius Dichtl, Dr. Qian Chen, Dr. Chao Zhang and Dr. Zaheen Shah for their precious support in dealing with all of life's problems. And I am thankful to Mr. Matthew Smith and Dr. John E Warren, for sharing their expertise in TEM and XRD without reservation and bearing my mistakes.

I also sincerely thank the committee members for their valuable time for reading, reviewing and discussion of my thesis.

Publications and Conferences

Publications

Peng, Y., Cao, J., Yang, J., Yang, W., Zhang, C., Li, X., Dryfe, R. A. W., Li, L., Kinloch, I. A., Liu, Z., **Laser Assisted Solution Synthesis of High Performance Graphene Supported Electrocatalysts**. *Adv. Funct. Mater.* 2020, doi:10.1002/adfm.202001756. (Included as Chapter 5)

Peng, Y., Cao, J., Sha, Y., Yang, W., Li, L., Liu, Z., **Laser Solid-Phase Synthesis of Single Atom Catalysts**, *Light Science & Applications* (Submitted). (Included as Chapter 6)

Conferences

Peng, Y, Li, L., Liu, Z., *A top-down strategy of synthesizing FePt, Fe_3Pt and Pt nanoparticles with controllable phase, structure and size for oxygen reduction reaction*, ILAS 2019, 6th UK industrial laser symposium, March 2019. (Oral presentation)

Peng, Y., Cao, J., Yang, J., Yang, W., Zhang, C., Li, X., Dryfe, R. A. W., Li, L., Kinloch, I. A., Liu, Z., *Laser Assisted Solution Synthesis of High Performance Graphene Supported Electrocatalysts*, NanoteC20 Virtual meeting, August 2020. (e-Poster presentation)

Chapter 1. General Introduction

1.1 Background

Nanomaterials are defined as materials with a size down to 100 nanometers, which exhibit different and novel properties from their bulk counterparts. Despite concerns about the hazards of nanoscale materials, it cannot be denied that these unique properties offered by nanomaterials lead to manifold applications. Nanocatalysts as a typical example are critical to the renewable energy, chemical process and environmental industries. To date, using hydrogen as a fuel is a promising pathway to the decarbonisation of both the transportation and power generation sectors. Additionally, hydrogen acts as an essential raw material for a wide variety of chemical synthesis that are used on a daily basis. The effective production of hydrogen and the efficient conversion of hydrogen to electrical power rely on electrocatalytic technologies. In electrocatalysis, the chemical reaction in solid, gas and liquid phases can be boosted by introducing a large amount of active sites for reactants adsorption, reaction and desorption. In order to optimize the catalyst performance, the dimension of catalytic particles should be decreased for increasing the numbers of active sites and expand the surface area. Nowadays, researchers still dedicate to develop novel nanocatalysts fabrication methods to optimize the intrinsic catalytic activities through size, shape and materials design.

Developing a versatile and cost-effective nanocatalysts synthesis technique is one of the key challenges in applying novel nanomaterials in various catalysis applications. Laser fabrication represents an alternative technique for the synthesis of nanomaterials by means of photothermal and photochemical manners, which potentially provides a rapid and flexible fabrication route for a wide variety of nanomaterials production. This emerging approach attracts lots of attention for its simplicity in production setups and processing steps, versatility in materials composition and morphology design. Moreover, the most valuable feature of the laser fabricated nanomaterials is the absence of ligand coverage. Benefiting by the purity and bare surface exposure, the laser assisted synthesized nanocatalysts allow efficient adsorption of adsorbates and prevents the shielding and pH effect by the attached ligands[1]. From an economic perspective, in an industrial scale production the laser-based synthesis routes can significantly reduce its operation cost for the few processing steps, low raw material costs and flexibility in a wide variety of nanomaterials production[2].

With the development of laser technologies, the availability of a wide range adjustable wavelengths lasers with high power and high beam quality, together with delicate modulated

pulsed laser systems with high speed and high precision galvanometer mirror scanners, which have opened up new opportunities to achieve laser nanofabrication through different approaches with high product quality control and high productivity.

So far, the catalysis study of the emerging laser assisted methods on electrocatalysts synthesis is still limited. And some scientific challenges in laser nanofabrication of electrocatalysts have not yet been resolved from the previous pioneering studies and techniques. The major issues and challenges are listed as follows:

1) One of the challenges of the laser synthesised nanomaterials in catalysis applications is the effective size reduction and precise size distribution control. As the catalyst performance of nanomaterials is sensitive to the numbers of active sites, and accessible surface area. Thus, effective size reduction and precise size control of nanomaterials are critical to the catalysis applications. Previous studies have demonstrated the capability for synthesising nanomaterials ranging from several nanometres to micron scale. The size map still contains some uncovered ranges, such as monodisperse ultrafine nanoparticles (< 5 nm) and isolated dispersion of single atoms.
2) Another challenge is the clarification of the laser assisted nanofabrication mechanisms. Although, the laser assisted method is facile and simple, in terms of the processing steps, involved “reactants”. However, the mechanisms of laser fabrication through either photothermal and/or photochemical require a better understanding through experimental and theoretical investigations.
3) The laser fabricated nanomaterial in electrocatalysis applications is still limited. To date, the majority of studies focus on the applications in biology, chemical sensing and optical devices *etc*. Admittedly, the commonly investigated Au nanoparticles synthesized via laser fabrication exhibit great potential in bio-conjugation and spectroscopy studies for the ligands-free surface and unique optical properties. However, characteristics, such as nanomaterials with bare surface exposure and tuneable size *etc.*, are also beneficial in catalytic applications. Systematic studies of laser fabricated nano catalysts meet the urgent need for sustainable and clean energy storage and conversion techniques.
4) The feasibility of laser fabrication methods for a wide range of nanomaterials production is also challenging. As the surface chemistry, size, and crystal structure of synthesized nanomaterials via the same synthesis route might be varied, for the different properties of individual elements and compounds. The knowledge transfer to a wide

variety of materials based on the laser assisted synthesis methods would benefit to the versatility of this technique and extend its manifold applications.

Considering the above-mentioned issues and challenges, development of new laser nanofabrication techniques, detailed studies of the processing parameters for nanomaterials synthesis, investigate the nanomaterials formation mechanisms, and explore the catalytical performance of the laser-produced nano catalysts, are essential to achieve high-quality production of novel catalysts.

1.2 Research Objectives

The aim of this project is to explore the feasibility and characteristics of laser nanofabrication via various laser processing systems, processing parameters and techniques, and potential improvement of laser synthesised electrocatalysts performance. In this study, Pt is chosen as a representative candidate for its excellent catalytic properties, which can act as reference material to reveal the difference between laser fabrication methods and other existing approaches. The specific objectives of this project are listed as follows:

1) To develop suitable laser fabrication methods for flexible and reliable synthesis Pt electrocatalysts with controlled size and size distribution.
2) To explore the potential of laser fabrication in size reduction of nanomaterials.
3) To evaluate the processing parameters effect on the formation of nanocatalysts, for example: the laser wavelength, laser fluence and precursor/target materials. And to optimize the processing conditions for high-quality nanomaterials production.
4) To investigate the nanomaterials formation mechanisms during various laser processing approaches by experiments and numerical simulation techniques.
5) To evaluate the catalytic performance of laser synthesised precious metal catalysts in various energy storage and conversion applications, such as fuel cell, electrolyzer *etc*.
6) Furthermore, to improve the catalytic performance by optimizing the processing conditions.

1.3 Thesis Structure

The aim of this thesis dedicates to develop the methodology for precious metal nano-electrocatalysts synthesis with the assistance of laser technology. Three approaches for synthesizing Pt (and Pt group metals) nano-electrocatalysts that size from sub-5 nm monodisperse nanoparticles to ~ 2 nm clusters and finally down to atomic level has been

developed. The manuscripts and data in this thesis consist of one paper published in a peer-reviewed journal, and two manuscripts not yet published but have been reviewed by collaborators. Thus, chapters of these manuscripts have self-contained figures, tables and citations. The results of the work mainly contributed by the thesis author with the assistance of collaborators. The contributions are clarified at the start of each chapter.

The thesis comprises six main chapters listed as follows:

Chapter 1. Introduction. The chapter starts with a brief introduction of nanomaterials and the application in energy storage and conversion, followed by research objectives and the thesis structure.

Chapter 2. Literature Review. An overview of nanoparticles, the commonly used synthesis methods for nanomaterials synthesis, and an introduction of energy storage and conversion techniques which focuses on fuel cells and electrolyzers. The laser fundamentals, typical laser-assisted synthesis methods, outcome materials and their applications are reviewed and discussed in detail.

Chapter 3. UV Laser Assisted Pt Nanoparticles Size Refinement for Enhanced Oxygen Reduction Reaction. In this chapter, a UV laser-assisted size tailoring method for tuning the particle size of PLAL generated Pt NPs with a broad size distribution was presented. The outcome monodisperse Pt NPs with an average size of 4.7 nm were successfully synthesized. The morphologies evolution of Pt NPs with varying laser parameters and processing duration were investigated. The Pt nanoparticles size tailoring through the 248 nm laser irradiation was simulated by considering the size-dependent absorption of the incident beam, heat accumulation and dissipation, and phase changes. Based on the experiments and modelling, a size refinement mechanism was proposed. Finally, the ORR performance of laser refined Pt NPs was examined, which shows an enhanced catalytic activity and long-term durability and outperforms the commercially available Pt/C catalyst.

Chapter 4. Laser-Assisted Solution Synthesis of High-Performance Graphene Supported Electrocatalysts. A laser-induced, continuous, photodeposition route for NPs functionalized graphene composites synthesis has been addressed. Benefiting by the semiconducting nature of graphene oxide (GO), photon-induced electrons in the GO flakes simultaneously reduced GO and metal ions, and photo-excited holes were consumed by the sacrificial electron donors. By using a pulsed 248 nm Excimer laser, RuO_2 and Pt nanoparticles with average sizes of 2.8 and 2.0 nm, respectively, were rapidly deposited on the reduced graphene oxide (rGO) flakes.

Further electro-catalytical tests demonstrated the promising performance of RuO_2 and Pt functionalized graphene composites in OER, HER, ORR and supercapacitor applications. Based on the experimental findings, the photo-deposition mechanism was deduced to be the photo-induced electron-hole pairs on the GO flakes under UV irradiation.

Chapter 5. Laser Enabled Synthesis of Single Atom Catalysts. Graphene-based Pt single-atom catalysts (SACs) fabrication through fast photothermal reduction of both GO and Pt precursor using 1064 nm picosecond laser was developed for the first time. Several key aspects were addressed to successfully fabricate Pt SACs through the solid-phase laser synthesis strategy, including the laser wavelength, pulse overlaps, selection of metal precursors etc. To understand the effect of laser process parameters on the single-atom synthesis, a numerical model was built to study the temporal evolution of heat. In the later electrochemical tests, the graphene-based Pt SACs exhibits comparable HER activity to the commercial catalyst but with ultrahigh precious metal utilization. The present work opens up a fast, versatile avenue for precious metal catalysts fabrication that can be applied in various catalytical scenarios.

Chapter 6. Conclusions and Perspectives. The final chapter consists of the Summary of the work, followed by future recommendations and considerations.

Chapter 2. Literature Review

2.1 Introduction to Nanoparticles

2.1.1 Introduction

Since the 1980s, particularly after the invention of the scanning tunnelling microscope which allows researchers to observe and manipulate individual atoms, there has been a rapid increase of scientific and technological interest in the nanotechnology for its commercial importance [3-4]. Achievements in nanotechnology lead to many applications in various fields, such as medicine, automobile, sports goods, food industry and electronics (**Figure 2-1**). Based on Lux Research report[5], the global revenue from the nanotechnology-enabled product has increased gradually from $339 billion in 2010 to $731 billion in 2012, and it is estimated the global value of the nano-enabled product with reach $4.4 trillion by 2018.

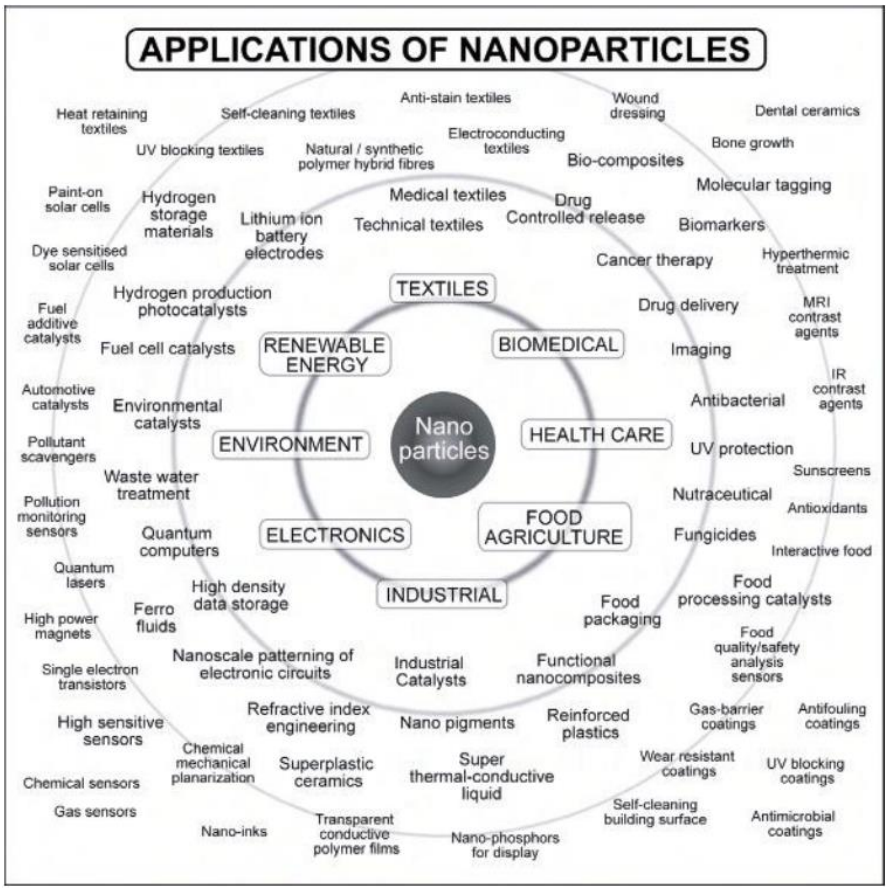

Figure 2-1 Major application of nanoparticles[3].

2.1.2 Classification of Nanomaterials

By size

By definition, nanomaterials are materials that have at least one dimension within the nanoscale, i.e. 1 - 100 nm[6]. The 100 nm boundary, as discussed by Kreyling *et al.* [6], is likely used to give a simple clear-cut distinction to differentiate the materials in nanoscale from their counterparts in micro or macro scale, for the 100 nm does not draw a clear line based on a change in material properties. Although, the definition based on the size boundary is under debate for its scientific basis[6-7], but for general materials classification, it is widely accepted in many standard documents globally[8].

By dimensionality

Nanomaterials can also be classified by the dimensionality based on their size in a three-dimensional (3D) coordinate system[9]. Based on the distinction in dimensionality, nanomaterials can thus be categorized into four kinds: 1) For a zero-dimensional (0D) nanomaterial, the size in all x, y and z dimensions are in the nano region, and this kind of material usually appears as a dot through direct observation. From small to large scale, nanomaterials like, single atoms, quantum dots, clusters and NPs can be grouped in this type. 2) A one-dimensional (1D) nanomaterial is an object that elongates in one direction, and the others remain in nanoscale, typical nanomaterials in this type are: nanorods, nanotubes, nanowires etc. 3) A two-dimensional (2D) material expands its size in two directions, *e.g.* x and y in a coordinate system, and the size along the z-axis is in nanoscale. This type of materials appears as flakes, films, and disks *etc.* with a thickness in nanometers. New emerging materials, such as graphene, MoS_2 and Mxene *etc.* are typical examples of this type of nanomaterial. 4) A three-dimensional (3D) nanomaterial grows in all three directions, but its size confined in nanoscale. The degree of freedom in 3D offers plentiful geometries of the nanomaterials. Furthermore, typical examples are nanocubes, nanofoams and nanoarrays *etc*.[10]

By morphology

In many applications, the nanomaterial aspect ratio (also known as the surface area to volume ratio), plays an important role, as their functionalities depend on the exposure of the surface and specific facets. The morphology, thus, is taken into account for it is a key character effect on the aspect ratio. For example, a porous nanosphere usually possesses high aspect ratio than that of NPs with a similar size[11]. Nanomaterials morphologies can be classified by their aspect ratio. High aspect ratio nanomaterials contain, nanowires, nanotubes and nanoribbons etc. In

contrast, low aspect ratio morphologies usually include, nanospheres, nano-size prisms and nanocubes *etc*.[12].

2.1.3 Size-Dependent Unique Properties of Nanomaterials

Materials with all three external dimensions in the nanoscale, more precisely, with a size range approximately from 1nm to 100nm[8], normally exhibit enhanced and novel properties different from their bulk counterpart. Apart from the size, properties of NPs are also strongly influenced by the geometry of individual NPs. Therefore, unique properties include mechanical, electrical, optical, chemical and thermal behaviour becomes dependent on the size and shape of particles[13]. This section is devoted to discussing the size-dependent unique properties of NPs.

High surface area

Due to the small dimension of NPs, materials in nanoscale have a larger fraction of atoms sited at the surface compared with their bulk counterpart. This could be demonstrated by the specific surface area, which is defined by the surface area of particles per unit mass, as expressed in Eq. 1-1 (in this case, the shape of NPs is assumed to be a sphere):

$$S = \frac{A}{V\rho} = \frac{3}{\rho r_{NPs}} \tag{1-1}$$

Where S is the specific surface area (m^2/kg), r_{NPs} is the radius of NPs and ρ is the density of the materials. It is evident that the specific surface area increases with the decrease in radius of the sphere, which means there will be a large portion of atoms exposed on the NPs surface if the particle size is reduced. Taking silver as an example, 1 g of Ag NPs with a radius of 1nm could have a surface area of a.u. 285 m^2. Particles with a high surface area could make materials extremely prone to interact with the surrounding environment, which could be widely used, for instance, as chemical catalyzers or pharmaceutical solutes with high solubility.

Size-dependent melting temperature

The melting temperature of materials is related to cohesive energy which indicates the energy required to separate solid materials into isolated free atoms. Generally, the higher the cohesive energy, the higher the melting temperature of materials. According to experimental and theoretical results from previous researches [14-16], melting temperature of NPs with the relatively free surface is lower than that of the bulk condition. This size-dependent phenomenon associated with cohesive energy can be understood by applying Liquid-drop model (LDM). The modified model provided by Qi and coworkers[15] gives a more intuitive explanation of both

size and shape-dependent melting temperature of crystals (expressed by Eq. (2-2)), while the original Liquid-drop model is only applicable for spherical particles.

$$T_m = T_{mb}(1 - 3\alpha \frac{r_a}{r_{NPs}}) \quad (2\text{-}2)$$

T_m and T_{mb} are the melting temperatures of particles and bulk materials respectively, and the r_a and r_{NPs} denote the radius of atoms and NPs, α is the shape factor of NPs. Clearly, the melting temperature of NPs decreases with the decrease in particle size, while the temperature remains unchanged if the particle is big enough, which makes the last term negligible. **Figure 2-2** demonstrates the example of melting temperature depression in gold NPs[16].

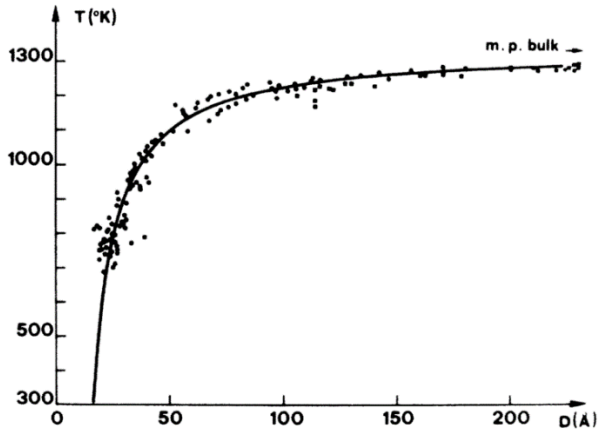

Figure 2-2 Experimental data of the melting temperature of gold NPs as a function of particle size[16]

Thermodynamically metastable crystal structure

Naturally, the crystal structure of particles has the same crystal symmetry as the bulk solid of the same materials in the same ambient atmosphere, if the particle size is considered larger than the critical size. However, polymorphs could exhibit different crystal structure from that of the bulk material with the same chemical compound, when the particle diameter is below a specific value. From the thermodynamic point of view, the surface energy, ΔG, is proportional to the surface area, A, of the particles:

$$\Delta G = \gamma \cdot A \quad (1\text{-}3)$$

Where, γ, is the free surface energy per unit surface area. Owing to the relatively large surface area that nanoscale particles have, the surface energy of NPs is considerably higher than that of the bulk material. As a result, the crystal structure, which is determined in order to minimize the systematic energy, could be altered by the large surface energy[17].

For instance, by cooling from around 1000℃ to the room temperature, the crystal structure of bulk zirconia will undergo a martensitic transformation from cubic to tetragonal and finally monoclinic phase [17-19]. In the bulk form, the monoclinic phase in thermodynamically more stable than the tetragonal phase. However, when the diameter of zirconia particles is reduced to the nanoscale, in order to reduce the total energy of the system, the metastable tetragonal phase could be more favourable instead of the monoclinic phase, for the lower surface energy of tetragonal zirconia, 0.77 J/m^2, compared to the monoclinic zirconia, 1.13 J/m^2 [18]. For zirconia, the critical size of NPs, which permits the tetragonal phase is around 10-40 nm has been reported by several researchers [20-23]. The value range of the critical size could be caused by different preparation methods used by researchers, for the critical particle diameter can be affected by the intrinsic and/or the extrinsic factors, such as the constituent compounds, ambient atmosphere and the preparation method, etc.[17]. **Table 2-1** shows the critical size and preferential phases of other materials in nanoscale.

Table 2-1 Critical size and metastable crystal phase of materials in nanoscale.

Materials	NPs diameter	Crystal structure in NPs	Stable phase in the bulk materials	Ref.
ZrO_2	10-40 nm	Tetragonal	Monoclinic	[20-23]
TiO_2	5-14 nm	Anatase	Rutile	[24-25]
Al_2O_3	30 nm	Cubic	Hexagonal	[26]
Fe_2O_3	<39 nm	Cubic	Hexagonal	[27]
$BaTiO_3$	20-200 nm	Cubic	Tetragonal	[28-29]
$PbTiO_3$	7-11 nm	Cubic	Tetragonal	[30-31]

Optical properties

NPs can show variation in colour with the size of the particles. For example, the colour of spherical gold NPs could appear purple or red, which is very different from their bulk colours. This fact leads to various useful applications, for instance, photothermal ablation of cancer cells[32]. The optical phenomenon of NPs is driven by the surface plasma resonance and the quantum size effect.

As the diameter of metallic NPs reduces, the electronic properties of materials change drastically, which leads to restriction of electron motion. Consequently, metallic NPs absorb and scatter light more substantial than bulk materials[3]. Based on the theory presented by Mie[33], when spherical particles size is far smaller than the wavelength of the incident light, the electron cloud of NPs could interact with the incident light for its electromagnetic nature. A schematic of plasmon oscillation provided by Kelly et al.[34] is shown in **Figure 2-3 a**. When

the incident light matches the frequency of the localized surface plasmon resonance (LSPR, i.e. a collective oscillation of conduction band electrons in metallic nanoparticles excited by the electromagnetic wave) frequency of materials, the light is absorbed by metallic NPs and then re-emitted by the particles[3].

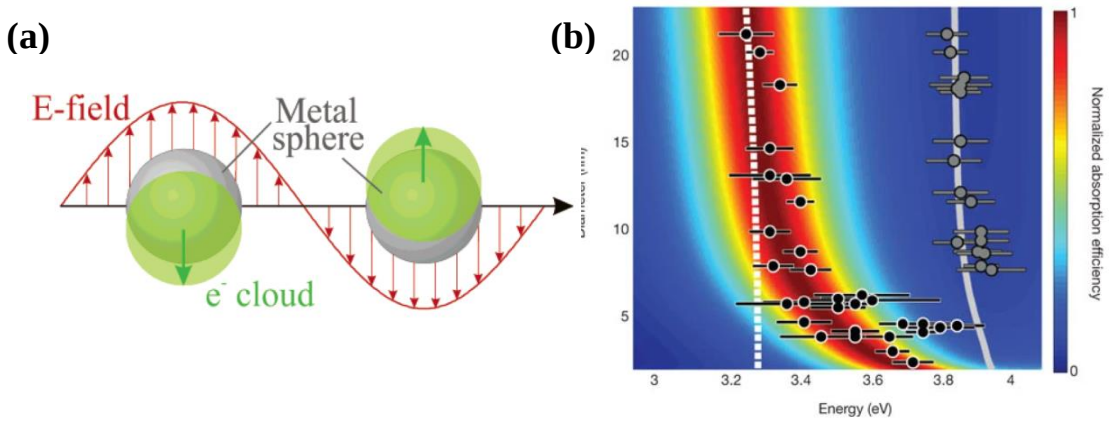

Figure 2-3 (**a**) The interaction of electron cloud with the incident light, showing a displacement of the conduction-free electron cloud to the nuclei[34]. (**b**) The colour map represents the calculated absorption efficiency of Au NPs, and black dots and grey dots are the experimental results and prediction based on classical Mie theory model, respectively[32].

When the diameter of a metal nanosphere is in the quantum size regime, the quantum size effect takes place and leads to a discretized conduction band. Owing to the energy levels of metallic materials in this regime are not continuous as in bulk. The overlapping of the valance and conduction bands disappears. By absorbing light with a certain frequency, the excited electrons could then overcome the bandgap, which leaves positively charged holes in the valance band when electrons move back to the hole, a photon is emitted. This phenomenon is known as luminescence. With the further decrease of the particle size, the bandgap energy increases. Results provided by Scholl et al.[32] show a substantial blueshift occurs as the Au particle size decreases to several nanometres, indicating the increase of the bandgap energy (**Figure 2-3 b**).

2.1.4 Synthesis Routes of Nanomaterials

With the increase of interest in nanomaterials development and contributions by global researchers, the synthesis methods become more diverse and mature. According to the synthesis strategy, the fabrication of nanomaterials can be categorized into the top-down approach and the bottom-up approach. A top-down route represents the nanomaterial is produced by breaking down its bulk counterpart into nanoscale dimension[35]. Typical top-down methods include, chemical exfoliation[36-37], ball milling[38], laser ablation[1], and so on. The bottom-up strategy, on the other hand, describes the nanomaterial is assembled from its basic units into a nanoscale structure. Common nanofabrication methods via the bottom-up strategy include,

hydrothermal/solvothermal synthesis[39], chemical reduction[40] and photodeposition[41] *etc.* Based on the strategies mentioned above, a wide variety of synthesis routes are developed for generating NPs. Basically, these techniques can be divided into two types: physical and chemical methods. This section presents a short review of typical synthesis techniques of metal NPs in both bottom-up and top-down manners.

2.1.4.1 Bottom-Up Approach

The bottom-up approach can be described as a temporal sequence of nucleation and growth. However, the mechanisms behind this phenomenon could be complex and different between the methods applied. Industrial production of NPs with chemical routes, such as precipitation and flame synthesis, is mostly benefit from their high yield rates, great flexibility in reaction routes and better particles size control, *etc.* [3]. However, owing to the complexity of chemical synthesis routes, since they mostly require various reactants and demanding reaction conditions [42], dealing with, by-products, chemical waste and high energy consumption, *etc.* is also necessary for further application and scale-up production. A brief description of conventional chemical synthesis approaches for NPs production is presented below.

Chemical reduction

1857 Michael Faraday prepared Au colloids by reducing gold chloride with phosphorus in water, which believed is the first recorded chemical reduction example for NPs production[43]. In this early nanofabrication experiment, Au precursor ($NaAuCl_4$) was used by phosphorus and formed Au colloid. Generally, NPs produced through chemical reduction are formed by chemical reduction of metal salts with the help of reducing agents. These reducing agents reduce metal ion and lead to nucleation and growth of metallic particles. Different from the conventional reduction reaction in other industry, like silver mirror reaction, stabilizers are required for preventing NPs aggregation. Citrate is widely used in nanofabrication of precious metal NPs, e.g. Au[44], Ag[45] and Pt[46] *et al.*, as it not only serves as a reducing agent, but also acts as a stabilizer that weakly interacts with the noble metal surface. Lee and Meisel gave a typical example in 1980[45], who reduced $AgNO_3$ in boiled aqueous citrate solution and synthesized stable Ag NPs with particle size range from 30 to 150 nm. As explained in the latter mechanism study conducted by Pillai and Kamat[47], citrate reduces Ag^+ ion into Ag^0, meanwhile complexes with the surface Ag and forms a repelling layer that prevents further aggregation of formed NPs. For the simplicity of the process and reactants, this technique was then followed by many research groups for improving the reaction conditions and for tuning the particle size and shape.

To modify the NPs size in a controllable fashion, lots of effort have been made to tune the reaction kinetics by varying the metal precursors, reducing agents, reaction conditions and by adding nucleation seeds *etc.*[39-40]. As a typical bottom-up strategy, NPs formation through chemical reduction usually experiences the following sequence: (1) the reactants reach a critical supersaturated condition, (2) followed by nucleation, and (3) finally small particles tend to grow and aggregate to form thermodynamically stable large particles. Thus, controlling the reaction kinetics is key for synthesizing NPs with tunable size and narrow distribution. For example, Puntes *et al.* [48] used mixed reducing agents, i.e. sodium citrate and tannic acid, to precisely control the reduction kinetics in Ag NPs production. In their study, tannic acid shows a lower tendency in forming Ag complex and reduce Ag^+ faster compare with citrate. Thus, by varying the tannic acid to sodium citrate ratio, monodispersed Ag NPs with tuneable size from 10 to ~50 nm (as shown in **Figure 2-4 a**). Another typical approach for NPs size control is to use stabilizers with different affinity to the NPs surface. Sun and Murray et al. used carboxylic acid, and trialkyl phosphine to tune FePt NPs size[49]. Among the two capping agents, carboxylic acid interacts strongly with the FePt NPs, while trialkyl phosphine shows weaker affinity to the FePt surface. Thus, changing the ratio of two capping agents can control the nucleation and growth rate, and thus tune the NPs size (**Figure 2-4 b**).

Additionally, by choosing capping agents which preferentially bind on specific facets of materials, a wide range shape of NPs can thus be produced. For spherical NPs synthesis, the growth rate of each facet of metal is similar. However, preferential attachment of capping agents can inhibit the growth of the attached facets, and hence, control the structure of outcome nanomaterials. Sun *et al.* [50] successfully synthesized Ag nanowires by adding poly(vinyl pyrrolidone) (PVP), as shown in **Figure 2-4 c**. PVP as a stabilizer preferentially attaches on the Ag (100) facets and passivates their growth, while the (111) facets grow in a relatively high rate thus lead to a side extension. Liao *et al.*[51] observed the nucleation and growth of Pt nanocrystals through in-situ TEM with the assistance of oleyl amine. As shown in **Figure 2-4 d**, with increasing reaction time, the preferential growth along the (111) facets lead to a cubic structure. In this case, oleyl amine favorably attaches on the Pt (100) facets, and blocks the growth along these facets, and promotes the evolution of Pt (111) facets.

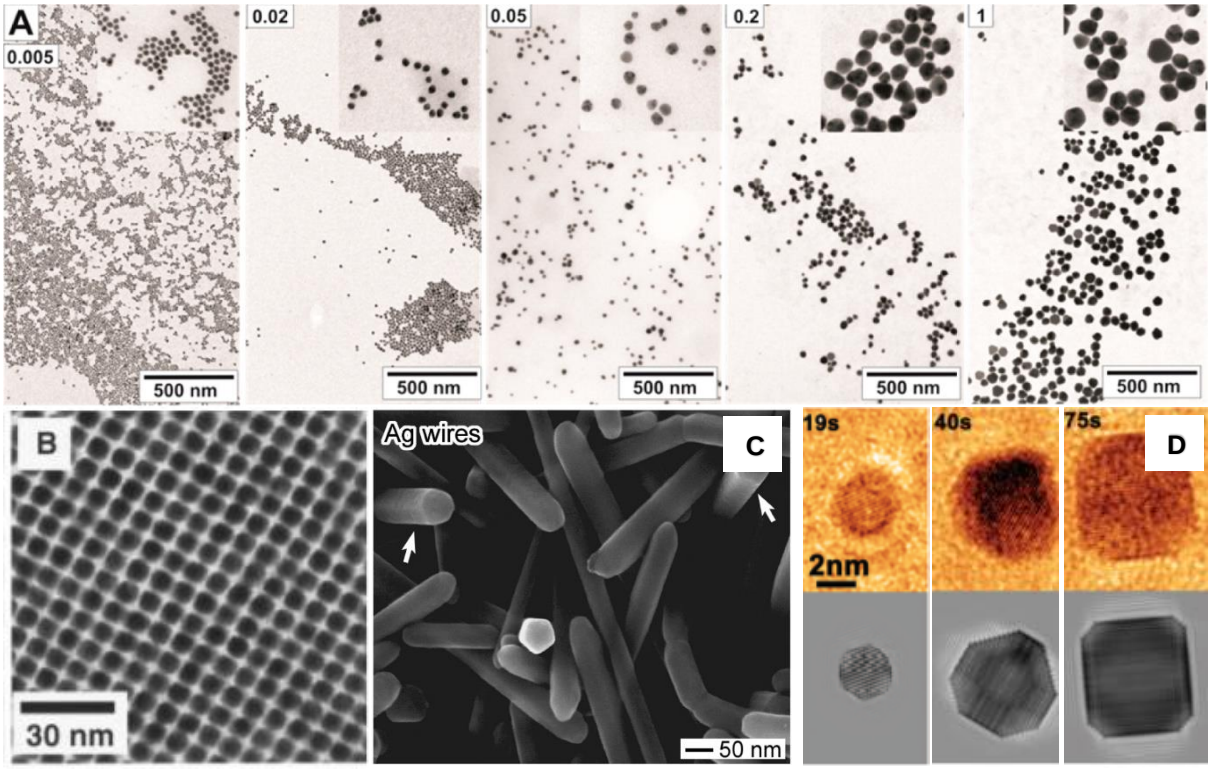

Figure 2-4 (**a**) TEM images of Ag NPs obtained by using different sodium citrate to tannic acid ratio. The average Ag NPs size increased from 10.1 ± 0.9 nm, to 14.8 ± 1.4 nm, 23.4 ± 5.0 nm, 36.9 ± 6.2 nm, and 46.1 ± 8.3 nm as the concentration of tannic acid increased from 0.025 mM to 5 mM[48]. (b) TEM image of a 3D assembly of 6 nm FePt NPs[49]. (c) SEM images of silver nanowires[50]. (d) Sequential TEM images show the growth of a Pt nanocubes with the oleyl amine molecule attachment[51].

Benefiting by the versatility and high degree of freedom in NPs size and shape control, chemical reduction methods are well-developed and widely used in industrial-scale production. However, drawbacks of the chemical reduction process are also apparent, for instance, capping agents, such as PVP, at the surface inhibit the further functionalities of the as-prepared NPs[52-53]. Moreover, the extensive purification process is also inevitable for a wide range of chemicals, ince products and intermediates are involved in the process[1].

Electrochemical method

Compared with the chemical reduction methods, precipitation of nanoparticles requires external current applying on a cathode or an anode where reduction or oxidation reactions take place. Typical three-electrodes electrolytic cells for both cathodic and anodic electrochemical deposition are shown in **Figure 2-5 a and b** and consist of the following components: a working electrode (WE) provides a reaction site for nanoparticles precipitation through either cathodic or anodic reaction, a counter electrode (CE) is used to close the current circuit of an electrochemical cell, a reference electrode (RE) is used to set a reference point and allow one to measure the potential of the WE, a power supply and an ionic conducting electrolyte. Rodríguez-Sánchez *et al*.[54] synthesized Ag NPs using an Ag anode in H_2SO_4 electrolyte, the dissolved Ag ions were then electrochemically reduced on a polished platinum cathode. To

avoid aggregation, a tetrabutylammonium salt was added as a stabilizer. By changing the applied current density, the size of Ag NPs can be between 2 and 7 nm.

Apart from the surfactant control of NPs shape, the electrochemical method provides another way to tune the NPs structure, *i.e.* by changing the applied potential. Tian *et al.*[55] used sweep square-wave potential between -0.1 to 1.2 V to generate tetra-hexahedral Pt NPs. During the anodic scan, the surface Pt atoms were either dissolved into the electrolyte or invaded by oxygen and formed Pt-O. While, during the cathodic scan, Pt ions redeposited back onto the original Pt NPs surface in a random manner. Due to the high-index planes, such as (730) plane, preferentially adsorb oxygen molecule, these planes can be preserved during the Pt oxidation. Finally, by repetitive potential sweep, tetra-hexahedral Pt NPs with high-index planes is formed (**Figure 2-5 c**).

Furthermore, the electrode not only provides a reaction site during the electrodeposition but can also act as confinement that inhibits atoms migration, which effectively reduces the size of synthesized nanomaterials. Zhang *et al.*[56] electrochemically deposited a wide variety of elements on an amorphous $Co(OH)_2$ substrate. By tuning the precursor concentration, the metal ions were reduced and anchored on the supporting materials, and formed isolated atomic dispersion (**Figure 2-5 d**).

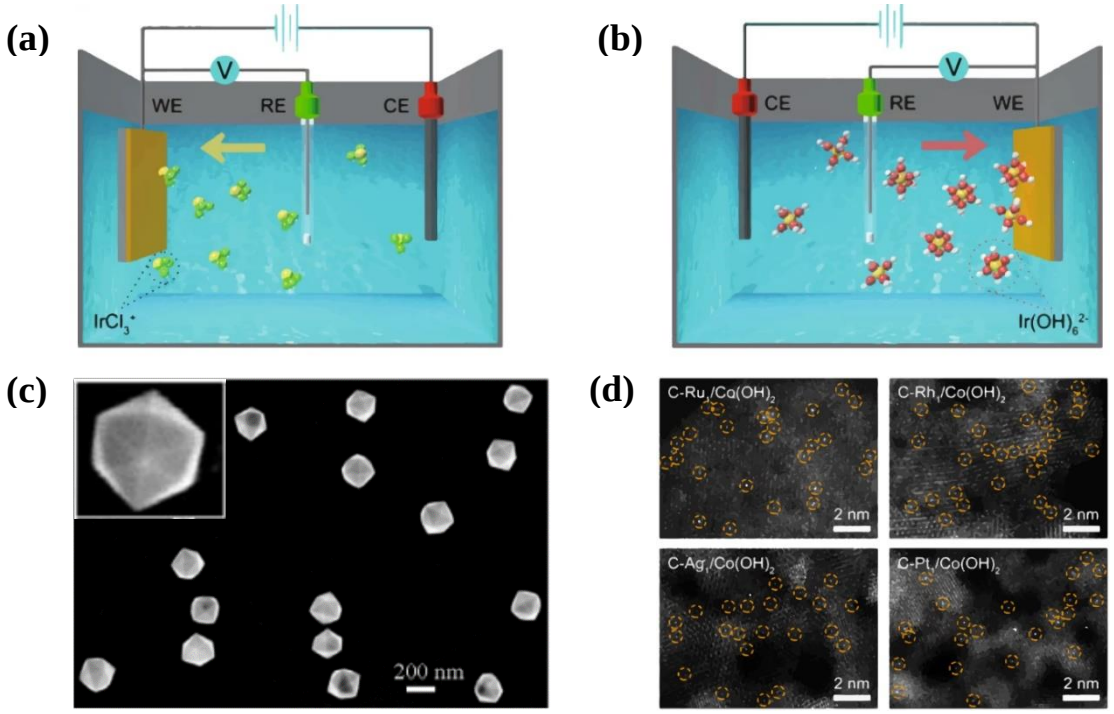

Figure 2-5 Schematic of typical experimental setups for cathodic (**a**) and anodic (**b**) electrochemical deposition for NPs synthesis[56]. (**c**) SEM images of tetra-hexahedral Pt NPs with high-index facets synthesized via the electrochemical method[55]. (**d**) STEM images of single atom Ru, Rh, Ag and Pt deposited on a $Co(OH)_2$ substrate[56].

Photodeposition

Photodeposition for NPs synthesis is achieved by light-induced electrochemical reactions. Semiconducting medium or substrates with a discrete bandgap are commonly required. When the photon energy of the incident irradiation exceeds the bandgap of substrates, electron-hole pairs are generated and can participate in redox reactions[41]. Similar to the electrochemical methods, targeting species can either be reductively or oxidatively deposited on semiconducting support (**Figure 2-6 a and b**). **Figure 2-6 c** shows the band positions of several representative semiconductors. TiO_2 is a popular semiconducting substrate for its wide availability and wide range of redox potentials. Lee and Choi[57] used TiO_2 as the semiconducting substrate, the photon excited electron reduced the Pt precursor and deposited Pt NPs on the surface of TiO_2 (**Figure 2-6 d**). The photon generated holes in their experiment were consumed by electron donors, *i.e.* methanol.

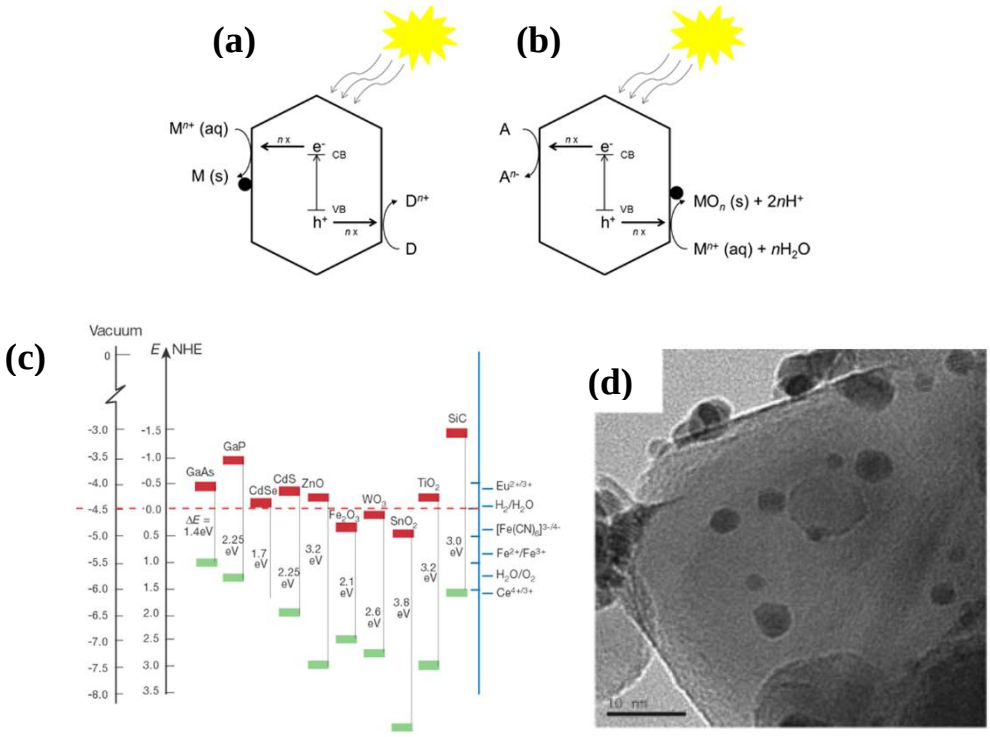

Figure 2-6 Schematic of reductive (**a**) and oxidative (**b**) photodeposition of NPs[41]. (**c**) Overview of band positions of representative semiconducting materials in energy scale and in voltage (vs. normal hydrogen electrode) scale, the blue label shows reduction potentials of some species[41]. (d) TEM image of Pt NPs deposited on TiO_2 substrate via photodeposition[57].

2.1.4.2 Top-Down Approach

Most of the physical methods for NPs generation are categorized into the top-down approach, which suggests nano-scale particles are obtained from macroscopic materials by thoroughly controlling the processing route[35]. NPs preparation through the top-down approach is usually produced by melting or evaporating bulk materials, or generated through mechnial cleavage of the bulk counterparts. In the first case, the melted or vaporized materials form particles in nano-

scale through subsequent condensation in a liquid or gaseous environment. NPs produced by those methods commonly possess high quality and are free of ligands attachment. In spite of some drawbacks of these routes, such as low yield rate and high cost[58], those techniques are still highly demanded in commercial-scale production, for composition and quality of products mightily influence the selection of industrial fabricating methods. Examples of the top-down methods are listed below.

Electro-explosion of wire

This process can be defined as a condensation of the explosive fragment caused by very high pulsed current applied to a thin conducting wire[59]. Preparation of metal, metal oxides, metal fluorides and metal nitrides NPs through this method has been reported by several researchers [58, 60-62]. The further chemical reaction of outcome vapour can carry on by altering the inert or reactive ambient gas. For instance, by applying pulsed current to Ti wire in different ambient gas (oxygen or nitrogen), TiO_2 and TiN can be obtained respectively. This technique is most suitable for generating metallic NPs with sufficient production rate (180 g/h) [61]. However, high electricity consumption is required for commercial-scale production.

Ion sputtering

Ion sputtering is a "top-down" approach for NPs production. In this method, atoms from the target materials surface are removed due to energetic particle bombardment. In a macroscopic point of view, this technique is analogous to sandblasting, while the sand particles are altered to high energy gas ions/plasma. Sputtering yield is mainly affected by three factors: ion flux, ion energy and the incident angle of the ion beam[63]. Typical sputtering rate for Pt/C catalyst layer can reach 7.5 mg/min with a bias voltage of 600 V[64].

Mechanic methods

Mechanical methods in NPs production are mainly grinding and milling, which use mechanical energy on micro-scale particles to crush and refine powders. In some cases, solid-state chemical reactions could be involved during the process, for the high thermal energy generated by the collision of particles and milling media[65]. The intensive collision of particles during high energy milling can produce alloy NPs via cold welding, which offers this technique a capability to produce a wide range of nanomaterials. In contrary to other synthesis methods, NPs production in a mechanical way has several advantages[3]:

1. It's simplicity.
2. It is suitable to produce a wide range of NPs.
3. It is possible to produce large quantities.
4. The equipment is commercially available.

However, the milling process has difficulty in controlling particles size uniformly. Additionally, contamination of NPs products could be involved, owing to the fierce collision of the milling media[66].

2.2 Applications of Noble Metal NPs in Energy Storage and Conversion

2.2.1 Introduction

Accelerating the electrification of the automotive and aviation industries reflects the urgent need of coping climate and global energy challenges[67-68], and speeds up the development of renewable energy conversion, storage and utilization. Among the practical technologies, using hydrogen as a fuel demonstrates its importance in the increasing energy demands. Because, on the one hand, it shows as an alternative complement to the conventional fossil fuels with reducing carbon dioxide emissions[69]. On the other hand, hydrogen acts as an essential raw material for a wide variety of chemicals synthesis that used on a daily basis[70]. In detail, the pathway of generating hydrogen and oxygen through electrochemical water splitting involves several key reactions: hydrogen evolution reaction (HER) and oxygen evolution reaction (OER). Moreover, within a fuel cell unit, where chemical energy converts to electric energy, the oxygen reduction reaction (ORR) and hydrogen oxidation reaction (HOR) play essential roles. However, owing to the sluggish reaction kinetics these energy conversion reactions, catalysts, primarily precious metal catalysts, are required to minimize the overpotential and maximize the energy conversion efficiency.

The following sections dedicate to give a brief introduction of NPs applications in fuel cell and electrolysis. Typical reaction mechanisms, characteristics of precious metal catalysts and examples of catalysts design are also included.

2.2.2 Fuel Cell

With the development of fuel cell technologies, several types of fuel cell systems are invented. Based on the applied electrolyte, the fuel cell devices can be categorized as the following types[71]: alkaline fuel cell (AFC) – use alkaline an electrolyte, *e.g.* KOH; Solid oxide fuel cell (SOFC) – use solid-state oxides as an electrolyte, *e.g.* zirconia; Phosphoric acid fuel cell (PAFC) – use phosphoric acid as an electrolyte; Molten carbonate fuel cell (MCFC) – use molten carbonate salt as an electrolyte, *e.g.* lithium carbonate; Proton exchange membrane fuel cell (PEMFC) – use fluoropolymer film as an electrolyte, *e.g.* sulfonated tetrafluoroethylene.

Among the wide variety of fuel cell design, PEMFC has been widely studied and demonstrated its commercial viability in automobile, auxiliary power unit and portable devices *etc*.[72-74] for its mild working temperature and high-power density.

2.2.2.1 Working Principle

Figure 2-7 demonstrates the main components of a PEMFC unit within a fuel cell stack. A PEMFC uses a proton exchange membrane (PEM) as an electrolyte.

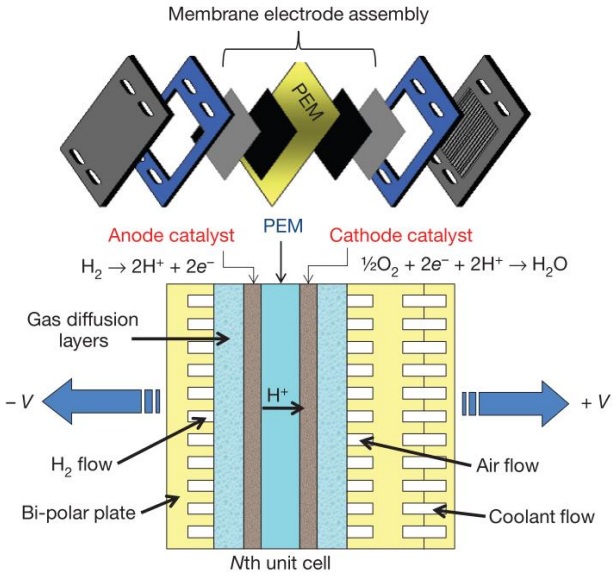

Figure 2-7 Schematic of a PEMFC unit cell in a fuel cell stack, showing the main components of bi-polar plates, gas diffusion layers, catalysts layers and a proton exchange film[75].

The PEM film is an ionic conductor but an electron insulator, where protons can be transferred from the cathode to the anode, while electrons and other reactants and products (O_2, H_2 and intermediates) are separated and blocked by the PEM film. A catalyst layer consists of catalyst particles loaded on electroconductive support (e.g. carbon black), where HOR and ORR take place. The catalyst layer is the key component in a fuel cell unit, as it is responsible for the chemical reactions and electron transfer. To maximize the reaction efficiency, the catalyst layer is supposed to have a high surface area to increase the contact area with the PEM film interface, thus to enhance the exposure to reactants. And meanwhile, the catalyst layer should be kept as a thin film, in order to reduce the intrinsic resistance and precious metal usage. A gas diffusion layer is responsible for supporting the catalyst layer, conducting electrons and transporting the reactants and products. Carbon papers are widely used as the gas diffusion layer to provide good electrical conductivity between the catalyst layer and the bi-polar plate, and to avoid the leakage of the catalyst layer during long-term operation. Furthermore, as water is the main product generates on the anode side, an efficient water-repellent property of the gas diffusion

layer is preferential to avoid immersion of the catalysts layer that retards the reaction. The bi-polar plate is commonly made of graphite with microchannels engraved on the site that directly contacts to the gas diffusion layer. The bi-polar plate, on the one hand, transfers the collected electrons to the circuit, on the other hand, responsible for reactants (H_2 and O_2) transportation[71].

Different to a conventional combustion engine, where fuel is ignited and releases its chemical energy into heat, and then the energy harvested mechanically, a fuel cell converts the chemical energy from the fuel directly to electricity via electrochemical reactions. The direct energy converting manner provides a fuel cell with a better energy conversion efficiency. For a PEMFC, the electrochemical reactions are:

Anodic reaction, HOR:

$$H_2 \rightarrow 2H^+ + 2e^-$$

Cathodic reaction, ORR:

$$\frac{1}{2}O_2 + 2H^+ + 2e^- \rightarrow H_2O$$

Among the two electrochemical reactions, the reaction kinetics of ORR is several orders of magnitude lower than that of HOR, thus retards the overall energy conversion efficiency and becomes a short plank in PEMFC development[71]. ORR is a multi-electron reaction process, which consists of several primitive steps, and the reaction rate is determined by the minimum rate step. According to the ORR mechanisms, there are two reaction pathways, *i.e.* the "direct" four-electron pathway and the "indirect" two-electron pathway[76]:

Four-electron pathway:

$$O_2 + 4H^+ + 4e^- \rightarrow 4H_2O$$

Two-electron pathway:

$$O_2 + 2H^+ + 2e^- \rightarrow H_2O_2$$

$$H_2O_2 + 2H^+ + 2e^- \rightarrow 2H_2O$$

Based on in-situ experiment observation and density function theory (DFT) calculation, the ORR mechanism highly depends on the adsorption and desorption of oxygen molecules and intermediates[77-78]. Dong *et al.*[78] carried out in-situ Raman spectroscopy analysis of ORR at a single crystal Pt electrode surface in an acidic electrolyte and found out that: the ORR starts

when an O_2 molecule adsorbs on the Pt surface; and O_2^- forms HO_2* by reacting with a proton through an electron transfer (* denotes a surface site, and *A denotes the adsorbed intermediate of A); and the HO_2* rapidly dissociates and splits into OH^* and O^* on the neighboring Pt atom; finally, the OH* species further react with protons and generate H_2O. The reaction pathway differs between various catalytic materials, for instance, two-electron pathway reduction is commonly found in Au and Ag, and "direct" four-electron transfer occurs on Pt surface[77].

2.2.2.2 Characteristics of Precious metal Nanocatalysts

The catalytic activity of catalysts relies on the binding energy of reactants and reactive intermediates. For a weak interaction with oxygen, the activation of reactants on the catalysts surface and the splitting of O_2 molecules are inhibited. In contrast, for strong binding energy between O_2 and the catalysts surface, the rapid desorption of the reactants and reactive intermediates become difficult. And in the worst case, the catalyst's surface can be occupied by such oxygen-containing species and then be poisoned. Thus, moderate binding energy as a compromise between above-mentioned two extreme cases is preferred. The electronic structure of the metal surface has a considerable impact on the binding energy of the catalyst surface to the absorbates. **Figure 2-8** shows the volcano plot of oxygen reduction activity against oxygen adsorption energy calculated by Nørskov et al.[79] Pt possesses the best ORR activity among other single element catalysts, e.g. Pd, Ag, Au, Ir, Cu *etc*., and becomes the most widely used catalytical elements in commercial applications[80].

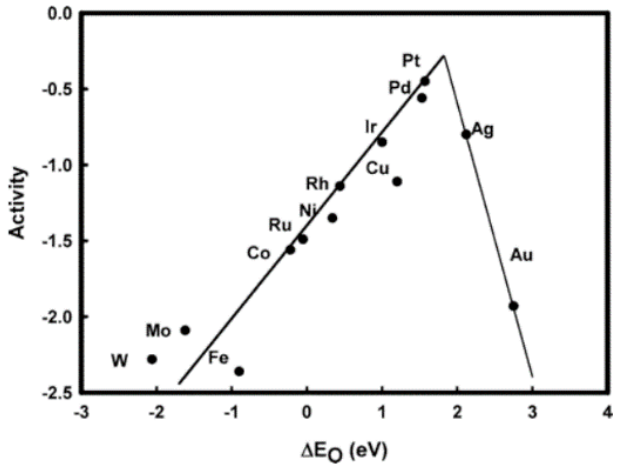

Figure 2-8 The volcano plot of oxygen reduction activity as a function of oxygen binding energy for various materials[79].

Effect of size

Size of catalysts NPs is important to the ORR catalytic activity, for small NPs show a large surface area, and provide more active sites where reactive absorbates can attach on.

Additionally, the high specific surface area of small NPs offers a better precious metal utilization, thus reduce the cost for their commercial applications. However, when the NPs size reduces to a certain level, the catalytical performance might be retarded. Perez-Alonso *et al.*[81] used gas aggregation technique to deposit Pt NPs with various size (2 to 11 nm) onto a glassy carbon electrode. As shown in **Figure 2-9 a and b**, the specific current density decreases smoothly with reducing Pt particle size, for the reduce of Pt NPs loading, while a steep drop in the kinetic current was also found with a Pt particles size of 2 nm. In addition, the mass activity is enhanced significantly with decreasing particles size, especially, the particles with ~ 3 nm show two-fold increment in mass activity in contrast to that of the 7 nm Pt NPs. The limited ORR activity of Pt NPs size down to ~ 2 nm was later studied by Garlyyev *et al.*[82] In their theoretical study, the active Pt atoms with coordination number between 7.5 and 8.3 at the NPs surface are expected to be more active. However, the surface-active site's configuration is sensitive to the particles size. The Pt NPs with a size of 1.5 nm show low active sites exposure, thus obstacles the overall catalytic activity.

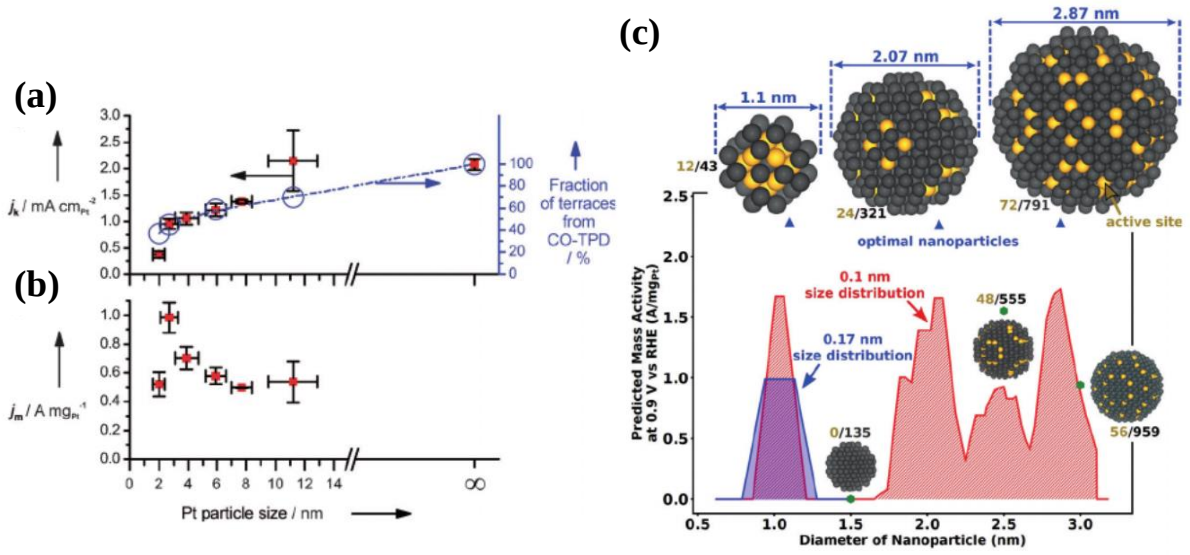

Figure 2-9 (**a**) ORR kinetic current densities and (**b**) mass activities at 0.9 V (vs. RHE) of Pt NPs with different particles size[81]. (c) Predicted ORR mass activities of Pt NPs with different size[82].

Effect of structure

As mentioned above, for Pt NPs, the structure and hence the surface configuration of Pt atoms also alter the catalytic activity. For low index Pt surface, the ORR activity in an acidic electrolyte follows the order of Pt (100) < Pt (111) ~ Pt (110)[83]. Additionally, for high index planes, the presence of terraces and steps promote the catalytic performance, may attribute to the change in the surface coverage of oxygen-containing species and the adsorption energy of the different reactive intermediates[84].

Effect of alloying elements

Adding alloying elements, can tune the Pt-Pt bond distance, modify the electron configuration of Pt, and reduce the loading of precious metals. Transient elements, such as Ni, Fe, Co *etc*. are widely studied and exhibit promising enhancement in ORR activity and long-term durability[83]. Huang *et al*.[85] demonstrated that Pt octahedra NPs alloyed with Ni exhibited 73-fold enhancement in the mass activity compares with the commercially available Pt/C catalyst. Based on their calculation, by adding Ni, the oxygen-binding energy on the Pt_3Ni (111) surface decreased ~ 0.2 eV compares with Pt (111) may be responsible for the high reaction kinetics. Additionally, with additional Mo doping, the catalytical durability can be further enhanced, for the formation of strong Pt-Mo and Ni-Mo bonds, which prevents the dissolution of Ni in acidic environment.

2.2.3 Electrolysis

Within the "hydrogen society", hydrogen not only acts as a link connects the power grids to other energy sectors, but it is also an essential raw material for a wide variety of chemicals synthesis that used on a daily basis[70]. To date, hydrogen as a fuel and a chemical raw material is mainly produced via steam reforming natural gas and other fossil fuels[86]. However, water splitting via an electrochemical manner provides a green pathway for generating high-quality hydrogen and also oxygen, which becomes a promising technique fits the green energy transition as proposed by many countries[87-88]. For electrochemical water splitting, three types of electrolysis techniques are commonly used: Alkaline water electrolysis – use a liquid alkaline electrolyte, *e.g.* KOH; solid oxide electrolysis (SOEC) is similar to SOFC – use a solid oxide electrolyte, *e.g.* zirconia; PEM electrolysis which is analogous to PEMFC – use a PEM film as an electrolyte. Among these electrolyzers, the alkaline water electrolysis is a well-matured technology that has been commercialized worldwide. However, the drawbacks of the alkaline water electrolysis, such as low current density, a crossover of generated gases and low operating pressure *etc*., limit its applications in new coming infrastructures like, hydrogen refueling station and compact bi-functional fuel cell[86]. The PEM electrolyzer, on the other hand, shows a high current density and voltage efficiency, high gas purity and rapid system response *etc*. and attracts increasing attention. The following sections give a short review of PEM electrolyzer working function, and characteristics of commonly used precious metal catalysts in PEM electrolysis.

2.2.3.1 Working Principle

The design of a PEM electrolyzer is similar to a typical PEMFC, and hence, in some cases, the cell can be designed for both water splitting and power generating. Like a PEMFC, a PEM electrolyzer cell also consists of bi-polar plates, gas diffusion layers, catalysts layers and a PEM film (**Figure 2-10**). However, due to the reactions take place in an acidic environment, and the high anodic potential applied on the anode side, corrosion resistance of the bi-polar plates and the gas diffusion layers need to be considered. Under this corrosive working condition, carbon black is suspected to be oxidized, thus porous titanium is widely used as the gas diffusion layer to support the catalysts layers and to transfer electrons[89].

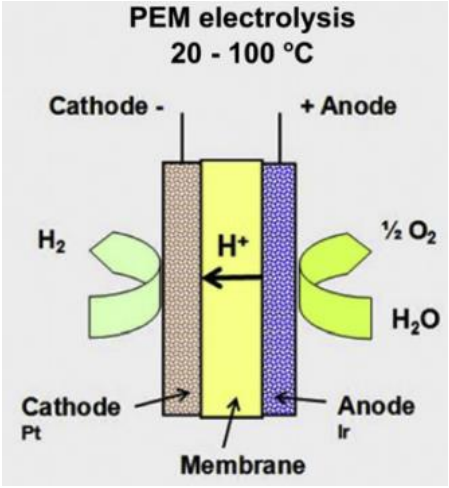

Figure 2-10 Schematic of a PEM water electrolysis unit cell, showing the main components of a cathode, an anode and a PEM film[86].

Different to the PEMFC, the electrochemical reactions of the PEM electrolyser include:

Anodic reaction, OER:

$$H_2O \rightarrow 2H^+ + \frac{1}{2}O_2 + 2e^-$$

Cathodic reaction, HER:

$$2H^+ + 2e^- \rightarrow H_2$$

For OER, the reaction is a reverse reaction of ORR, the H_2O molecule is oxidized to O_2. Similarly, various intermediates generate during water oxidation[90]. In an acid electrolyte, the water molecule discharges on the electrode surface and forms an adsorbed hydroxy species (OH*) at the active sites via an electron transfer. The second step occurs either by further oxidation of OH* into O*, or by a combination of two neighbouring M-OH and forms a H_2O

molecule and an O*. Finally, an O_2 molecule is generated via the O* combination from two active sites.

In the HER, the reaction is more straightforward. The reaction begins with the adsorption of a proton on the electrode surface and forms an absorbate (H*) by receiving an electron. The hydrogen gas evolution is achieved either by the combination of the H* from two active sites, or by further reduction of the H* with one proton from the electrolyte[84].

2.2.3.2 Characteristics of Precious Metal Nanocatalysts

Analogous to ORR, the adsorption and desorption of reactants, intermediates and products are important to OER and HER reaction rate. As shown in **Figure 2-11 a**, the ascending branch of oxides activities increases with increasing adsorption energy, while on the descending branch, the oxygen binding energy is too high that inhibits the OER performance. Precious metal oxides, such as RuO_2, IrO_2 and RhO_2 *etc.*, exhibit excellent OER activity and only require minimum overpotential to drive the reaction. The RuO_2 shows the highest OER activity in both acidic and alkaline electrolyte, however, at high anodic potential RuO_2 is dissolvable which limits its long-term stability. Thus, IrO_2 with good OER activity and excellent stability becomes a good alternative to RuO_2[84].

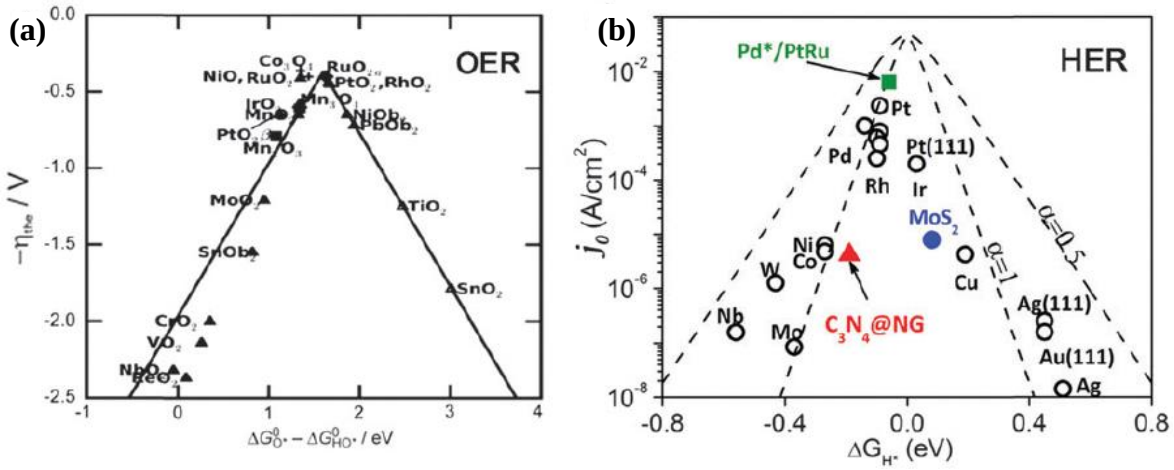

Figure 2-11 Volcano plots of (**a**) OER overpotential as a function of the relative adsorption energy between O* and OH* for various oxides[91], and (**b**) HER exchange current density against the H* binding energy on various materials[92].

As shown in **Figure 2-11 b**, Pt group precious metals, such as Pd, Pt and Rh *etc.*, locate at the summit of the volcano plots, indicating their excellent HER activity. Similar to Pt catalysts for ORR, the adsorption of protons is sensitive to the Pt surface. The HER activity of Pt follows the order of (111) < (100) < (110) planes in both alkaline and acidic electrolytes[84]. Adding alloying elements also shows its importance in enhancing HER activity and reducing the cost

of precious metals. Additionally, the development of single atom catalysts (SACs) provides a promising solution to balance the HER activities and the precious metals utilization. Yin *et al*.[93] synthesised single atom Pt decorated graphene catalysts as shown in **Figure 2-12 a**. As characterized by the Fourier transferred extended X-ray absorption fine structure spectra (FT-EXAFS) spectroscopy (**Figure 2-12 b**), the coordination number of the SACs show a significantly downshift in contrast to that of the bulk Pt counterpart. The results hint toward a possible modification of electron configuration of the graphene anchored Pt atoms, which provides an opportunity to tune the Pt HER activities via controlling metal substrate interactions. The HER mass activity of Pt SACs exhibits 26.9 times increment compare with that of the commercial Pt/C catalyst (**Figure 2-12 c**), demonstrating its superb HER activity and Pt atom utilization.

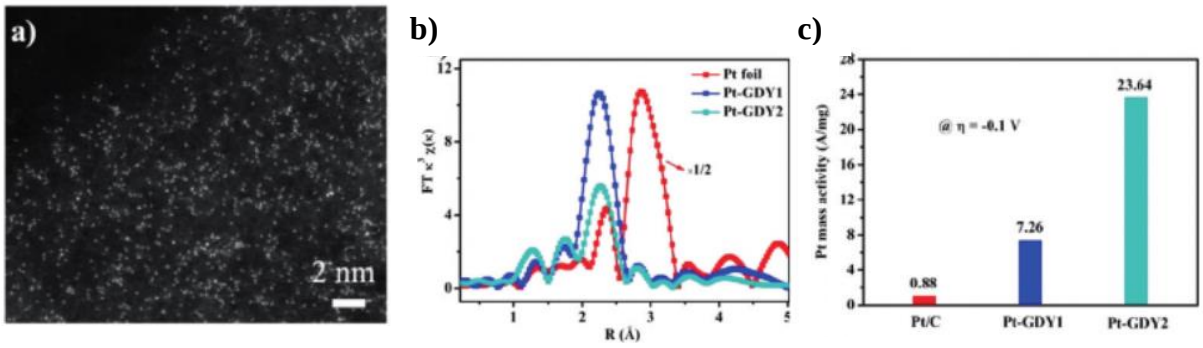

Figure 2-12 (**a**) High resolution STEM image of single atom Pt decorated graphene catalyst, (**b**) L_3-edge FT-EXAFS spectra of Pt SACs and Pt foil, (**c**) the HER mass activity for Pt SACs and commercial Pt/C catalysts at an overpotential of – 0.1 V in 0.5 M H_2SO_4 electrolyte[93].

2.3 Characteristics of Laser

2.3.1 Introduction

This section dedicates to describe the laser fundamentals, characteristics of a laser beam.

2.3.2 Laser Fundamentals

According to ISO 11145:2016 [94], the word laser is an acronym for the term "Light Amplification by Stimulated Emission of Radiation," which refers to the most significant feature of laser operation. After the first ruby laser, based on the light emission theory discovered by Albert Einstein, was invented by T. H. Maiman in 1960, laser techniques have been providing increasingly attractive options for materials manufacturing, telecommunication and medical applications, *etc*.

Based on the laser principle, three essential components are required:

1. A pumping source, which is a means to excite atoms of amplifying medium to higher energy levels.
2. An amplifier, which serves as a means to absorb increment energy from the pump and create population inversion, finally, lead to stimulated emission.
3. A resonate cavity, which provides optical feedback of the light generated by the amplifying medium.

Within the laser amplifier, atoms or molecules of the active medium interact with the electromagnetic field of the pump, normally as a form of light lamp or laser. Take the atomic system as an example: atoms of the active medium undergo quantum jumps between ground-state level and higher energy levels repeatedly. During the process, atoms jump to a higher energy state as a result of accepting energy from the input and convert the energy to photons as they jump to a lower energy state. The energy conversion can be demonstrated clearly by a two energy levels diagram (As shown in **Figure 2-13**).

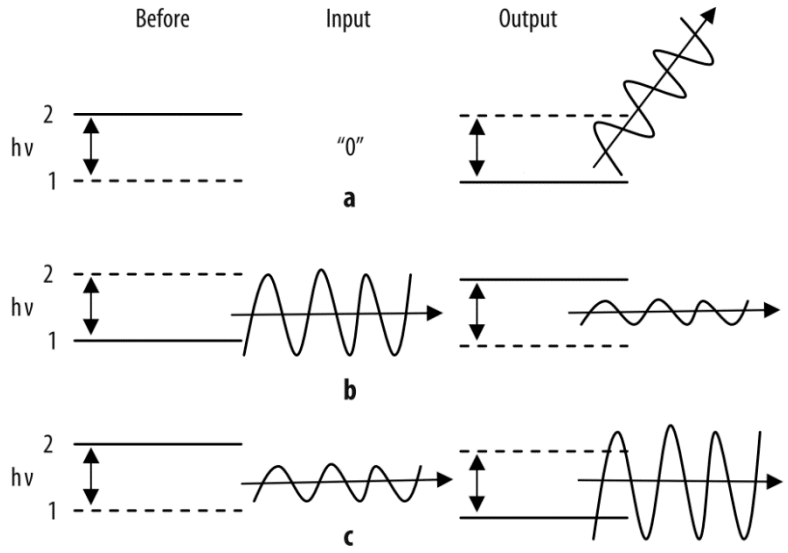

Figure 2-13 Energy conversion of a two-level system, (**a**) spontaneous emission of a photon energy $\Delta E=\Delta E_2-\Delta E_1$, (**b**) absorption of energy ΔE, (**c**) stimulated emission of a photon with energy ΔE [95].

Three energy conversion processes in **Figure 2-13** are interpreted as follows:

(a) Spontaneous emission of a photon as the atom decays from the higher energy level 2 to the ground energy level 1. The photon energy could be expressed as:

$$h\nu = \frac{hc}{\lambda} = E_2 - E_1 \qquad (2\text{-}1)$$

Where, h is the Planck's constant (6.625×10^{-34}J s), v is the frequency of light, c is the speed of light, λ is the wavelength of light, E_2-E_1 is the energy difference between the two energy levels. This process occurs spontaneously without any other external interaction.

(b) Absorption of an energy increment $\Delta E=\Delta E_2-\Delta E_1$ from an incident light with a certain frequency, the atom in the ground state is excited to the higher energy level 2. Consequently, the incident light losses its energy. The resonant frequency of light when absorption occurs could also be calculated by the equation (2-1).

(c) Stimulated emission: as the light passes by, the excited atom jumps down from level 2 to ground level 1 results in an emission of a photon with energy $\Delta E=\Delta E_2-\Delta E_1$. Different from the spontaneous process, the emitted photon is a replica of the incident light, which means it has the same frequency and direction as the passing photon. As a result, the incident light is amplified. And the resonant frequency is again defined by the energy difference between the two energy levels.

In order to achieve amplification, the number of atoms in the higher energy level (N_2) needs to be greater than the number of atoms in the lower level (N_1). Otherwise, there will be more absorption than stimulated emission, and amplification could not occur. The term "population inversion" ($N_2>N_1$) distinguishes the amplifying medium and absorbing medium, and it is shown in **Figure 2-14**.

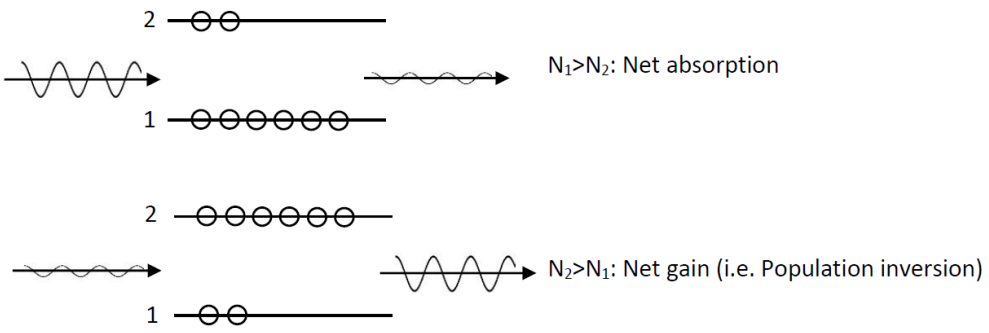

Figure 2-14 Schematic of population inversion of an absorbing medium and an amplifying medium.

In real laser operation, the two-level laser scheme is barely seen. Because, the incident radiation could induce both stimulated emission and absorption, which results in a balance of atoms number between level 1 and 2. In this case, population inversion could not occur. In order to achieve population inversion, the rate of excitation of ground-level atoms to a higher level must

greatly exceed the rate of the decay rate, which reduces the population at a higher level. One solution to overcome this difficulty is to use a lasing medium with more than one excited state.

2.3.3 Continuous-Wave (CW) Laser and Pulsed Laser

Output laser radiation can be divided into two categories in terms of the time period of the emitted radiation, they are CW laser and pulsed laser. According to the British standards [94], a laser that emits radiation continuously over a time period greater than 0.25 s is CW laser, while laser emits radiation in a single pulse which duration less than 0.25 s is called pulsed laser.

For obtaining short and powerful pulses of laser radiation, two methods are applied: Q-switch and mode lock. The concept of Q-switching technique will be explained in detail.

Q refers to a quality factor which is defined as the ratio of stored energy to the energy dissipated per each oscillating cycle. A high Q value of a laser system commonly means an optical resonator has a relatively low loss, while a low Q indicates the resonators has a large loss during operation. Thus, the term Q-switching refers to an abrupt change of resonator's loss. **Figure 2-15** demonstrates the behavior of laser parameters during a Q-switched pulse generation. Initially, the resonator Q value is kept at a low level, which indicates the laser cavity is very lossy. In this stage, the gain is smaller than the loss, laser oscillation could not occur. Furthermore, the energy fed by the flash lamp accumulates in the gain medium, resulting in an increase of population inversion until saturation energy is reached. Then, the Q value suddenly increases to a high level, resulting in a rapidly stimulated emission and considerable output energy, as the high population inversion which has been built up during the previous step is much higher than current saturation state. Once the population inversion drops to the saturation state (gain equals to loss), a peak power of this pulse is reached. The pulse power then starts decay, for the depletion of the stored energy.

Four types of Q-switches are used in laser, they are dye Q-switch, mechanical, electro-optical and acoustic-optical switches[96]. This technique is usually used for generating high energy laser with nanosecond scale pulse width.

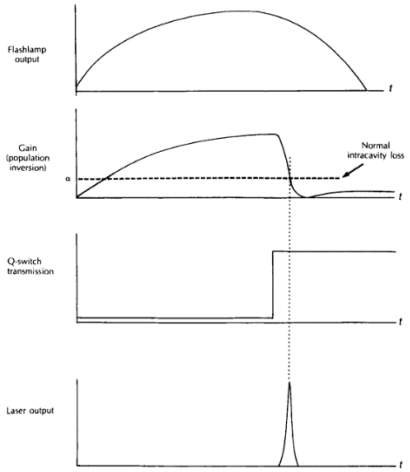

Figure 2-15 Demonstration of a flash-pump Q-switched laser. The total time (t) is about one-half ms[97].

2.3.4 Characteristics of Laser Beam

This section provides a brief overview of the characteristics of the laser beam.

Monochromaticity

Unlike broadband light, such as the sunlight that covers a broad range of wavelengths (spectral width of sunlight is more than 10^{14} Hz in frequency), the laser could produce light with a very narrow band of wavelength (bandwidth of practice lasers could be less than 100Hz).

High temporal and spatial coherence

Temporal coherence is defined as the time beyond which the correlation of the field decays. In other words, radiation emitted by the laser, within the coherent time span, can exhibit a phase relationship whenever the radiation follows a particular point. The coherence time can be expressed by equation 2-2.

$$\tau_c = \frac{1}{2\pi\delta\nu} \tag{2-2}$$

Where τ_c denotes the coherent time, $\delta\nu$ is the radiation bandwidth. In agreement with experiments[96], light with an extremely narrow bandwidth has a very high temporal coherence.

Spatial coherence means a strong correlation between the fields at any spatial positions across the beam profile.

Directionality

For sustained laser oscillation within a cavity, the light propagation direction of a laser is mostly orthogonal to mirrors of a cavity, which gives laser beam a minimal divergence angle. The divergence angle, θ, of the laser is proportional to its wavelength, λ, of the laser beam, and

inversely proportional to the beam diameter (*D*), which is different to ordinary lamps. The relation is shown in the following equation 2-3.

$$\theta \sim \frac{\lambda}{D} \tag{2-3}$$

High brightness

In many cases, power and intensity, which could be changed by a focusing lens, are not proper measures of brightness, for the brightness of a light source is an invariant quantity. The brightness of a light source is defined as the emitted power per unit area per unit solid angle[96]. Expression of brightness is shown in equation 2-4.

$$\mathrm{B} = \frac{I_{max}}{\Omega} = \frac{2Pwr}{\lambda^2} \tag{2-4}$$

Where I_{max} is the peak intensity, Ω is the solid angle, and *Pwr* denotes the total transported by the beam. Brightness as to conventional lights is lower than the laser beam because of the lack of directionality.

2.3.5 Types of Laser

As mentioned previously, the wavelength of the laser is decided by the excited species of the amplifying medium. It can be any state: gas, solid or liquid, *etc*. Commonly, the types of laser are designated by the lasing materials. A brief description of different types of laser is listed as follow.

Gas laser. Commonly, amplifying materials of the gas laser are excited by applying a high voltage so as to achieve electron discharge. Amplifying species are thus excited by undergoing collisional interaction between atom/molecule and electron. Atoms or molecules in the excited state then releases the excess energy through stimulated emission or spontaneous emission. Typical examples of the gas laser are CO_2, He-Ne and excimer lasers.

Solid-state laser. The laser amplifier of solid-state lasers usually is active species (Nd^{3+}, Ti^{3+}) doped in an insulating crystal or amorphous glass ($Y_3Al_5O_{12}$, Al_2O_3). The active medium needs to be excited by the optical pump, such as a light lamp, diode or another laser. Laser action of solid-state lasers is accomplished by undergoing excited atoms (or ions) decay between discrete energy levels. Common solid-state lasers are neodymium-doped yttrium aluminium garnet (Nd:YAG) laser, neodymium-doped yttrium orthovanadate ($Nd:YVO_4$) laser and titanium-doped sapphire(Ti:sapphire) laser.

Dye laser. Active media of dye lasers are normally solvents, such as alcohol or water, contains large organic molecules. Excitation of the liquid amplifying media is achieved by the optical pump. The most useful characteristic of dye lasers is that they are able to emit radiation over a broad wavelength by tuning the cavity, changing the concentration of the solution and altering the pressure[96].

2.3.6 Key Laser Parameters in the Laser-Assisted Nanofabrication

During laser ablation in a liquid medium, which will be discussed in detail in the next section, there are three main constituents. These are laser, liquid media and bulk solid materials. So, it is worthy of listing key laser parameters contribute to the laser ablation process.

Wavelength

The wavelength of light defines the shortest distance between two successive points with the same phase along the light propagation direction. The expression of wavelength λ is shown in equation (2-1). The wavelength of a laser system highly depends on the stimulated emission of common lasing materials lasers and their dominant operating wavelengths are shown in **Table 2-2**.

Table 2-2 Common lasers and the major wavelengths associated with them[98].

Lasing medium	Laser Type	Wavelength (nm)
ArF	Gas-Ion	193
KrF	Gas-Ion	248
XeCl	Gas-Ion	308 and 459
Ar_2	Gas-Ion	457-528
Frequency-doubled Nd: YAG	Solid State	532
He-Ne	Gas	543, 594, 612 and 633
Ruby	Solid State	694.3
Ti: sapphire	Solid State	690-950
Nd: YAG	Solid State	1064
CO_2	Gas	10600

Among above listed lasing medium, CO_2, Excimer and Nd: YAG have been widely employed in micro/macro-machining, welding as well as in surgery applications[95-96]. CO_2 lasers use gas molecules, including carbon dioxide, nitrogen, helium, etc. as lasing medium. With AC or DC electrical discharge, CO_2 molecules are excited and then emit radiation during relaxation. The CO_2 laser emits radiation with a wavelength of 10.6 μm. CO_2 laser have been widely used in industrial applications, which contributed to over 40% of industrial lasers[95]. Excimer lasers are also categorized as gas lasers, which commonly use gas mixture of Kr, F_2, Ne and He as

gain medium. With electric discharge, an excited dimmer $Kr^{+}F^{-}$ can be formed, with a lifetime of 5 – 15 ns, which then undergoes the stimulated emission process. It generates ultraviolet photons (248 nm) in a short pulse for each discharge of the condenser bank into the gas mixture[95]. Nd: YAH lasers use 1-2% dopants (Neodymium, Nd^{3+}) embedded in Yttrium-Aluminum-Garnet (YAG) crystalline matrix (with the chemical composition $Y_3Al_5O_{12}$) as the lasing medium. Pump sources are krypton or xenon flash lamps. The wavelength of an Nd: YAG laser is 1064 nm in the near-infrared spectrum.

Pulse width

The pulse width of the laser, τ_L, is the duration of the optical pulses. The definition of the pulse width is based on the full width at half-maximum (FWHM) of laser power versus time[96] (illustrated in **Figure 2-16**). For a pulsed laser, a pulse width could be in a range of millisecond (ms, 10^{-3} s), microsecond (μs, 10^{-6} s), nanosecond (ns, 10^{-9} s), picosecond (ps, 10^{-12} s) or femtosecond (fs, 10^{-15} s).

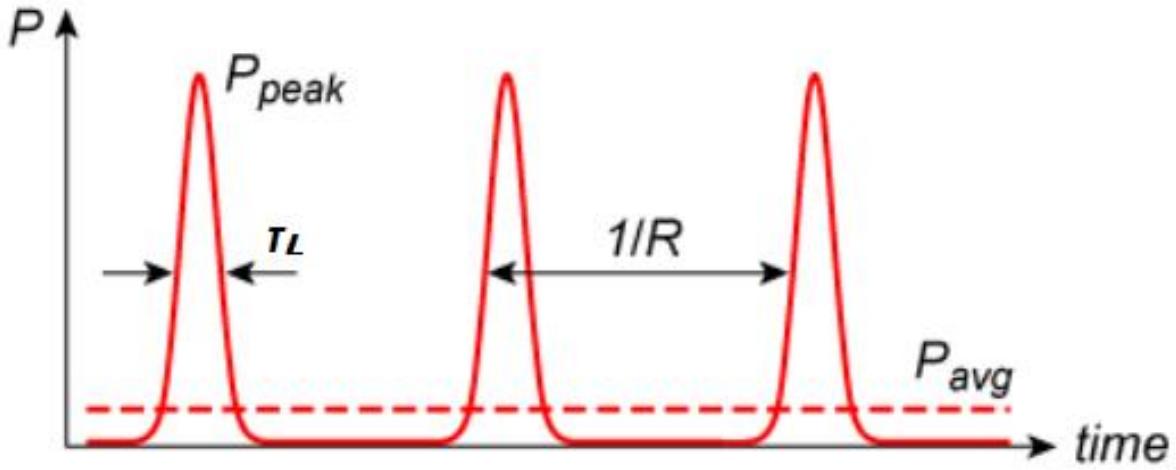

Figure 2-16 Illustration of laser peak and average power, repetition rate and pulse width.

Pulse energy & pulse power

The pulse energy, E_p, of a pulsed laser is the total optical energy of a single pulse. The laser power, P, could be indicated by the peak power, P_{peak}, which is the maximum optical power in every pulse, and the average power, P_{avg}, defined as the rate of energy flow averaged over one repetition period, $1/R$ (illustrated in **Figure 2-16**). Expressions of those parameters are shown as follows:

$$P_{peak} = {E_p}/{\tau_L}$$
$$P_{avg} = E_p \times R \quad (2\text{-}7)$$

Laser fluence and intensity

Laser fluence, *F*, is defined as the optical energy of a laser pulse delivered per unit area (J/cm^2). The expression is shown below:

$$F = {E_p}/{A} \tag{2-8}$$

Where *A* is the area of the laser spot.

Laser intensity, *I*, is the average power of the laser beam per unit area (W/cm^2).

$$I = {P}/{A} \tag{2-9}$$

Beam radius

The radius of a laser beam, ω, could be defined in several ways, the most used method is derived from the laser beam with a Gaussian profile. Beam radius determined in this way is the distance at which the beam intensity falls to 1/e (≈ 37%) of the beam axis intensity[99].

Beam quality

Laser beam quality could be defined in several ways, the most understood is that beam quality is a measure of the ability to focus a laser beam under a certain condition. Three ways are usually used to define the beam quality: the beam parameter product (BPP), the M^2 factor and the inverse M^2 factor[95].

Take the M^2 concept of beam quality as an example. The expression of M^2 beam quality is shown below:

$$M^2 = \frac{D_0 \theta_\infty \pi}{4\lambda} \tag{2-10}$$

Where, D_0, is the beam diameter of an unmodified laser beam, θ_∞, indicates the far-field divergence angle. A diffraction-limited Gaussian beam has an M^2 of 1, and a M^2 value below 1 is physically impossible. The M^2 value could be understood as to how close to "diffraction-limited Gaussian profile" an actual laser beam is.

Depth of focus

The depth of focus is described as the distance along the lasing axis in which the focused beam with the same intensity[95]. In practice, it is commonly defined as the distance over which the focal spot size changes ±5%.

2.4 Laser Assisted Method for Nanoparticles Generation

2.4.1 Introduction

Laser ablation is an attractive and a widely used laser-assisted fabrication method for nanomaterials synthesis which gives access to the production of a library of NPs for versatile applications, such as bio-conjugated medicine, catalysts and various energy-related applications *etc*., for its simple nature of the experimental setup (shown in **Figure 2-17 a**) and just one-step for NPs fabrication could be achieved by this approach[100-101]. Nevertheless, the ablation of solid materials by laser irradiation, especially in a liquid environment, is also a very complex chemical and physical processes, which involves melting, vaporization and fragmentation induced by photon-matter interaction, generation and expansion of plasma and chemical reaction between products and a liquid medium, etc.[102-106] The constituents of PLAL and possible combinatorial interactions are shown in **Figure 2-17 b**. As mentioned in Section 1.3, NPs generation methods are categorized into "top-down" and "bottom-up" approaches. Interestingly, NPs generated through PLAL are considered to be a hybrid route which embodies both physical top-down and chemical bottom-up characteristics. In top-down physical perspective, the target material is fragmented down to nano-scale particles by intense photon-matter interaction. While from the bottom-up chemical point of view, nucleation and growth of laser-ablated species frequently take place in the liquid confinement.

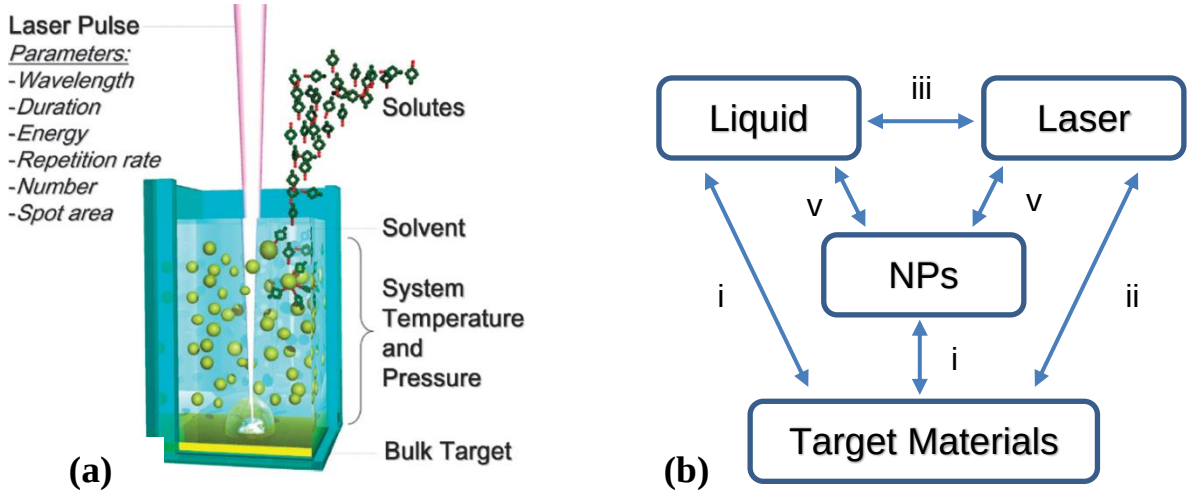

Figure 2-17 (**a**) schematic of a typical PLAL laboratory setup [107], (**b**) possible interactions during PLAL: i) target-liquid interaction, ii) laser-matter interaction, iii) laser-liquid interaction, iv) Ablation of target and re-deposit of NPs, v) liquid-NPs interaction, vi) laser-NPs interaction.

According to the definition of BSI standards[8], laser ablation is a physical process, which leads to ejection of the macroscopic amount of particles from the surface of a target material where

photo-matter interaction takes place. The process is typically induced by laser with a short pulse width (ns to fs scale), and high intensity (~10^6-10^{14}W/cm^2) interacts optically and thermally with materials surface. In principle, the interaction could take place in a vacuum, gas phase or liquid medium, which has only limited attenuation to laser energy. Researchers in this field have been researching laser ablation in vacuum and gas ambient since 1965[108]. Laser ablation in vacuum or gas environment has been successfully applied to deposit a thin film on a substrate for various applications, which is known as pulsed laser deposition (PLD).

However, for the purpose of NPs generation, laser ablation in liquid confinement is seen as a more promising approach, for the absence of post-preparation filtering and NPs are stored in liquid as a colloidal solution after processing which could be used directly for relating applications[100-101, 109]. Additionally, the local thermodynamic and kinetic conditions are seen to be more extreme in a liquid medium, which leads to a higher temperature, higher pressure and higher cooling rate situations, for ejected species, plasma plume is confined more strongly in solution than in vacuum or gas atmosphere[110-112]. Consequently, ejected species, and even a a noble element such as gold, could react with the solute molecule.

Early investigation of PLAL was done by Patil and Ogale's groups in 1987 [113-114], who explored iron NPs generation in liquid through PLAL. Their pioneering work proved the possibility of NPs fabrication through PLAL, attracted a significant research interest and inspired numerous research groups to work on this topic. During the early of the 90s, more researchers[115] reported the synthesis of colloidal solution through PLAL of various metallic targets in water and different organic solvent. Since then, PLAL has been developed into a straightforward and reliable route to produce NPs with bare surface exposure. Until now, intensive research has been focused on NPs in modified size and shape producing by PLAL with various targets, laser parameters and liquid media, *etc*. Those pioneering investigations demonstrated this unique physical-chemical approach possesses several advantages:

- PLAL offers a wide variety of outcome materials in versatile of the liquid medium. Besides, by carefully controlling laser parameters and liquid confinement, adequate controlled size, size distribution, and aggregation state could be achieved[107-108, 111].
- NPs synthesized by PLAL could be contaminated free, for there is not necessarily required of chemical compounds such as precursors, stabilizers and reduction agents, *etc*. Owing to this characteristic, PLAL allows to reduce costs of expensive chemicals and minimize residual toxicity in medical applications.

- In many cases, functionalized NPs with bio-conjugation could be produced in one step, by using in-situ or ex-situ devices[100-101, 116]. The efficiency of production, hence, could be primarily enhanced.

The following sections introduce the widely used PLAL method for nanomaterials fabrication, and to build up a basic understanding of temporal evolution during the PLAL process, possible mechanisms and the combinational interactions of constituents involved. In the first part, a systematical description of laser-matter interaction, PLAL procedures and possible mechanisms will be provided. Then, the influence of the liquid medium, so as the outcome NPs will be summarized.

2.4.2 Laser Beam-Matter Interaction

Laser-matter interactions are usually non-thermal at a first moment when a solid material starts to absorb an incident laser beam. For metallic materials, conduction band electrons are excited by absorbing photon energy, and intraband electronic transition takes place. At this stage, the absorbed energy is not directly converted into heat. Generation of heat takes place by collisions between the excited electrons, with a time scale, τ_e, from 10fs to 1ps, until a thermal equilibrium of electrons is reached. Then, energy transfers from the hot electrons to metal lattice through the electron-phonon coupling, also known as relaxation. The relaxation time, $\tau_{e\text{-}ph}$, is much longer (normally $\tau_{e\text{-}ph}$ is of the order of 1-100ps), for the huge size difference between electron and lattice atom. Finally, heat diffusion within lattice occurs through the phonon-phonon coupling. According to the temperature achieved, materials, then, could be melted, vaporized or transferred into a plasma state.

Throughout the literature[117-119], laser ablation is generally caused by thermal and/or non-thermal microscopic mechanisms. The dominant ablation mechanism highly relies on the pulse width of the laser and the target material's properties. Additionally, modified laser fluence and wavelength are also necessary to achieve ablation at the desired scale.

Under this section, influential parameters, pulse width dependent thermal descriptions are discussed.

2.4.2.1 Thermal and Optical Penetration

When an incident laser beam meets a target material's surface, a portion of the light will be reflected at the interface between light propagation medium and the target material, and the partial laser beam will penetrate the bulk material and be absorbed. Reflectivity causes energy

loss and often limits the overall ablation efficiency. Throughout the literature[95, 117], reflectivity is strongly affected by temperature and surface condition of target materials and the incident angle of the laser beam. For the purpose of modifying the ablation rate during PLAL, it is wise to choose an optimized irradiation condition. If the ablation rate is defined as the thickness of the ablated layer by a laser strike, a simple equation could be applied[117]:

$$\Delta h = \max(l_T, l_\alpha)$$
$$l_T = \sqrt{D\tau_L} \qquad (2\text{-}5)$$
$$l_\alpha = {}^{1}/_{\alpha}$$

Where Δh is the ablation depth affected by thermal (l_T) and optical penetration length (l_α, also be named as light absorption depth), D, α and τ_L represent the thermal diffusivity of material, absorption coefficient and pulse width, respectively. The optical penetration is defined by the absorption coefficient, which highly depends on the properties of target materials and wavelength of the laser beam, which is being absorbed. The expression of the (linear) absorption coefficient is shown as follow [117]:

$$\alpha = \frac{4\pi k}{\lambda} \qquad (2\text{-}6)$$

Where λ is the wavelength of the laser beam, k is the extinction coefficient of the target materials. As a result, for a given material, the optical absorption depth mainly depends on the laser wavelength. **Figure 2-18** shows the optical absorption depth of different metals and semiconductors as a function of laser wavelength. Usually, laser wavelength at the UV regime could be absorbed efficiently by the interband transitions of metallic materials, which gives a relatively large absorption coefficient at the short wavelength regime. Compared to metallic materials, the optical absorption depth of semiconductors, such as Si and Ge shown in **Figure 2-18**, typically exhibits a sharp edge when the laser wavelength reaches a certain value. This phenomenon results by the separated bandgap between the conduction band and the valence band, since the electron could not be excited when the photon energy is below the bandgap.

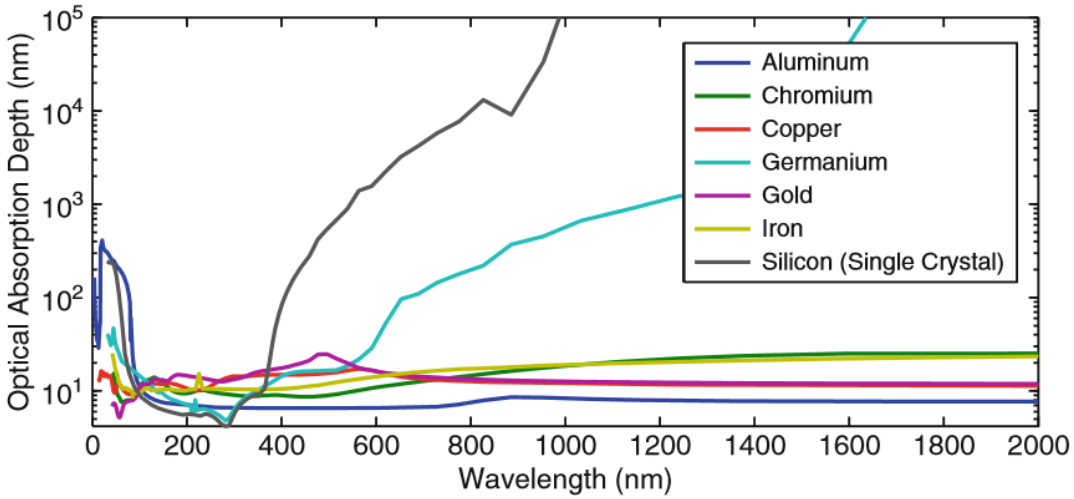

Figure 2-18 Optical absorption depths of several metallic materials and semiconductors[117].

Moreover, the interaction of the laser beam with as-formed NPs in the liquid medium should also be considered. Due to the generated NPs could act as a shield, which scatters and absorbs the incoming laser beam at a specific wavelength. This phenomenon not only results in an attenuation of laser energy, but could also lead to further modification of NPs shape and size [112, 116, 120].

2.4.2.2 The Threshold Fluence

The laser fluence not only effects the ablation rate during PLAL, but also dominants the ablation mechanism[107, 111, 121]. Obvious ablation could be observed when the laser fluence is above a certain value. This specific fluence, which causes significant ablation, then, be denoted as the threshold fluence, F_{th}. The threshold fluence varies mainly according to the properties of the particular target material and to laser parameters, in particular, the wavelength and laser pulse width. For most metallic materials, the average threshold fluence is found in a range between 1-10J/cm^2 [118].

From laser parameters point of view, on the one hand, the threshold fluence decreases with an increase of the absorption coefficient, which under the assumption that only finite laser energy is absorbed. As mentioned in the previous section, the absorption coefficient highly depends on the laser wavelength. On the other hand, the threshold fluence decreases with a decreasing of the laser pulse width. With an ultra-short pulse, the excitation energy only dissipates within a restricted spatial volume, thus, the threshold fluence could be reduced. An intuitive relation between threshold fluence and pulse width could be found in Stuart's group research[122], which is shown in **Figure 2-19**.

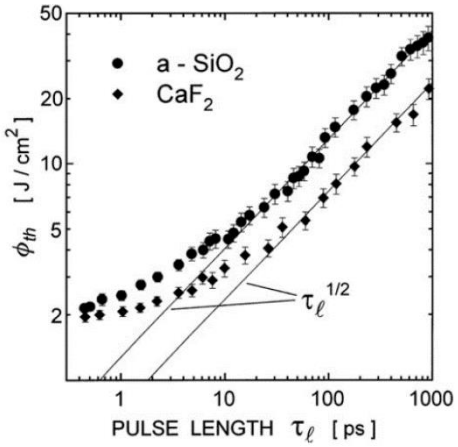

Figure 2-19 Threshold fluence of α-SiO_2 and CaF_2 ablated by incoming Ti: sapphire laser at the wavelength of 1053nm[122].

The ablation threshold of particular target material irradiated by a laser system could be measured by observing the surface damage. The test set up and the testing procedures could be found in the currently valid ISO standard[123]. The principle of this approach is erected on the extrapolation of the observed damage dimensions as a function of threshold fluence[121, 124-126]. The dimension of laser-induced damage could be measured by the crater's diameter. The threshold fluence causes material surface damage in a diameter *D* scales could be expressed in Equation 2-7. Assuming the laser beam has a Gaussian profile, heat diffusion within materials could be neglected, and ablation occurs when the laser fluence exceeds the threshold value[124].

$$D^2 = 2\omega_0^2 \ln(\frac{F_{peak}}{F_{th}}) \tag{2-7}$$

Where, ω_o, is the Gaussian beam radius, F_{peak} and F_{th} are the peak fluence of a pulsed laser and the threshold fluence, respectively. However, in practice, the threshold value developed from this approach exhibiting relatively high discrepancies of the values derived by other methods. This discrepancy is mainly caused by thermal effects, for the measured damage diameter is usually larger than the laser-irradiated regime[126-127]. Therefore, it is an adaptive approach for ultra-short pulse laser, where heat effects only play a limited role during ablation, instead of the laser with a longer pulse width range.

2.4.2.3 Pulse Width Dependent Thermal Descriptions

As the laser fluence reaches the ablation threshold, the laser ablation process then occurs. For laser pulse duration in a relatively more extended range (ns-μs regime), which makes the electronic excitation rate far lower than the electron relaxation rate, laser ablation could, thus, be considered as a mere thermal process. Because, in this case, absorbed laser energy is

transferred directly into heat, which results in heat dissipation, melting, evaporating and plasma formation of the target material (the schematic of this photothermal ablation is shown in **Figure 2-20 a**). Ablation rate, under this condition, is primarily contributed by liquid-phase expulsion, ejection of liquid droplets and evaporation. Temperature dissipation of this long pulse width beam-matter interaction within bulk materials could be described by the heat equation[117]. The heat equation, in general, describes the change of temperature as a function of time and spatial coordinates. Leitz *et al.* [119] give a simplified way to calculate the ablation rate based on the heat equation by assuming 100% photon energy absorption by the material, heat diffusion and overheating during the process is negligible:

$$m = \frac{N \cdot E}{c_p(T_V - T_0) + \Delta H_m + \Delta H_v} \tag{2-8}$$

Where, m, is the ablated mass, N is the duty cycle of a pulsed laser, E is the pulse energy, c_p is the heat capacity, T_v and T_0 are the evaporation temperature of the target materials and the ambient temperature respectively, ΔH_m and ΔH_v are the enthalpies of melting and evaporation.

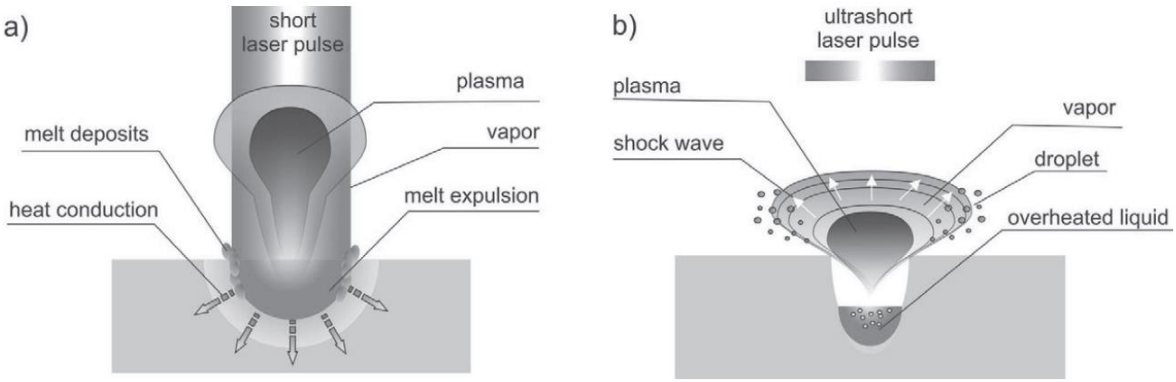

Figure 2-20 Schematic of pulsed laser ablation mechanisms: (**a**) photothermal ablation mechanism; (**b**) ablation mechanism of an ultra-short laser pulse[119].

However, when the laser-induced electronic excitation rate is high enough, the electron-phonon coupling is not a thermal equilibrium process and, thus, the excitation energy could not be dissipated into the lattice, which causes a non-thermal ablation phenomenon (schematic of the beam-matter interaction with ultra-short pulses is shown in **Figure 2-20 b**). For this ultra-short laser beam- matter interaction, the heat equation, which is used to describe the thermal equilibrium process, loses validity. Hence, a new thermal description aims to describe the temporal and spatial evolution of the non-equilibrium state between the excited electrons and the material lattice, is derived from the Boltzmann-Bloch-Peierls kinetic equation[128] and extended to metallic materials exposed to ultrashort laser pulses by Anisimov *et al.* [129]. This

new thermal description is known as the two-temperature model (TTM). Briefly, the TTM is under the assumption that: relaxation time is much slower than electron-electron and phonon-phonon coupling, so the electron temperature and lattice temperature maintain their local equilibrium. In the TTM, the excited electrons temperature, T_e, and the lattice temperature, T, are described by two coupled nonlinear differential equations:

$$C_e(T_e)\frac{\partial T_e}{\partial t} = \nabla[k_e(T_e,T)\nabla T_e] - \Gamma_{e-ph}(T_e)[T_e - T] + Q(x_\alpha, t) \quad (2\text{-}9)$$

$$C(T)\frac{\partial T}{\partial t} = \nabla[k(T)\nabla T] + \Gamma_{e-ph}(T_e)[T_e - T] \quad (2\text{-}10)$$

Where C_e and C are the heat capacities of electron and lattice respectively, the thermal conductivities of electrons and lattice are denoted by k_e and k respectively, $\Gamma_{e\text{-}ph}$ is the strength of electron-phonon coupling, and Q is the source function associated with laser irradiation.

In femtosecond regime, the pulse width is assumed much shorter than the time needed for electron-electron Coulomb interaction ($\tau_e \gg \tau_L$), thus the non-equilibrium electronic energy redistribution occurs, and the electron-phonon coupling could be ignored. In this case, the lattice temperature could be seen unchanged, and the irradiated area undergoes a direct and rapid solid-vapour (or solid-plasma) transition (shown in **Figure 2-21 c**). The crater, in this case, generally with a dimension precisely defined by laser beam spatial profile. As the electron-phonon coupling and the heat conductivity are ignored, the ablation depth, then, could be solved from equation 2-9 and 2-10 [118]:

$$\Delta h = \alpha^{-1}\ln(F_{act}/F_{th}) \quad (2\text{-}11)$$

Where, F_{act}, is the effect laser fluence. The logarithmic laser fluence dependence of the ablation depth of metallic targets ablated by the fs pulsed laser has been widely observed in the literature by many researchers [118, 130].

In the picosecond regime, where $\tau_{e\text{-}ph} > \tau_L > \tau_e$, heat conduction of electrons could not be ignored. Additionally, since the relaxation time is longer than the pulse width, the temperature of the lattice is much lower than that of the electron. In this regime, the expression for ablation depth derived from the TTM remains approximately the same as fs laser pulses (equation 2-11). The crater morphology induced by ps pulsed laser is shown in **Figure 2-21 b**, which exhibits a morphology similar to crater induced by fs pulsed laser. However, a conspicuous molten area

could be observed from the SEM image, which may attribute to the coexistence of direct ionization and photothermal process.

In the nanosecond regime, where $\tau_L > \tau_{e\text{-}ph}$, the electron-phonon coupling is fulfilled, thus, there is no differential temperature between the electrons and lattice. As the thermal wave could propagate into the lattice during laser energy deposition, a relatively large heat-affected zone (HAZ) and the molten area could be observed (shown in **Figure 2-21 a**). In this case, the target is ablated through both evaporation and liquid droplets ejection, which is similar to the photothermal mechanisms caused by long laser pulses. As the lattice temperature equals to the electron temperature, $T=T_e$, the governing equation is the classical heat equation but with an optical source term[118]. The ablation depth could then be solved from the heat equation as:

$$\Delta h \approx l_T = \sqrt{D\tau_L} \tag{2-12}$$

Hereby, the ablation depth is defined by the thermal penetration depth, as shown in 2.3.1.1.

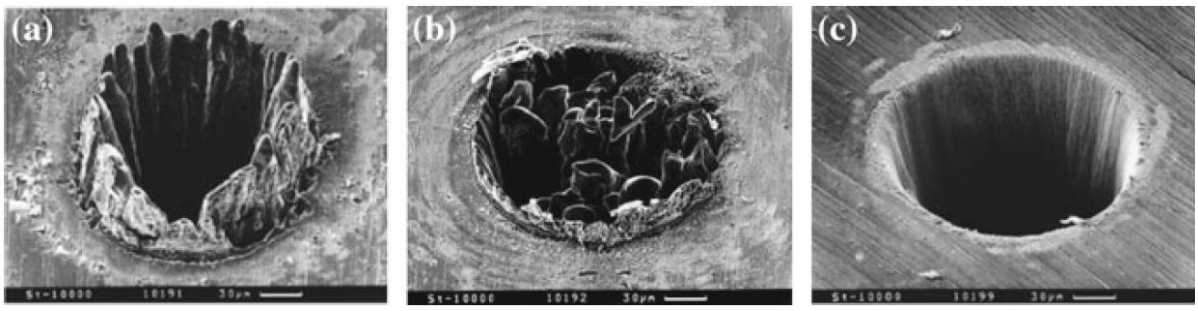

Figure 2-21 SEM micrographs show laser induced craters with diameter around 100 μm in steel, Ti-sapphire laser with (**a**) 3.3 ns (4.2 J/cm^2), (**b**) 80 ps (3.7 J/cm^2) and (**c**) 200 fs (0.5 J/cm^2)[131].

2.4.2.4 The Temporal Sequence of PLAL Process

The temporal sequence of PLAL process could be summarized as follow: the incoming laser penetrates through the liquid medium, and laser beam-matter interaction takes place once the target material irradiated by the incoming laser beam, followed by the first shockwave emission, then a cavitation bubble which contains plasma of ablated materials is formed. The plasma plume within the cavitation bubble expands for its high temperature and high pressure, and cools down by releasing energy to the liquid medium. And once the cavitation bubble collapses, ablated species are released into the liquid medium. The temporal evolution of these unique phenomena has been studied by many research groups[110, 132-134] through the in-situ time-resolved shadowgraph camera. **Figure 2-22** shows the time-resolved shadowgraph images of PLAL process of an Ag target irradiated by a 1064nm Nd: YAG laser, which shows the temporal evolution of PLAL process.

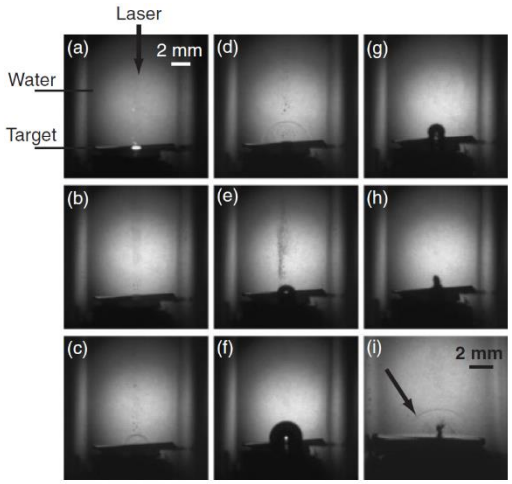

Figure 2-22 Time-resolved shadowgraph images of a silver target irradiated by a 1064nm Nd:YAG laser in water. The delay times in each image are: (**a**) 0 ns, (**b**) 60 ns, (**c**) 570 ns, (**d**) 1.3 μs, (**e**) 9 μs, (**f**) 169 μs, (**g**) 260 μs, (**h**) 290 μs, and (**i**) 300 μs[134].

In the following, the temporal evolution of physical-chemical phenomena in PLAL, with an assumption that laser fluence is slightly above the threshold, is discussed.

Laser beam penetration through the liquid

For the standard PLAL experimental setup, the laser beam must penetrate the liquid phase before irradiating on the target surface. During the penetration, the liquid solution could change the laser focusing length and attenuate laser energy.

The laser focusing length could be shifted as a result of refraction change or even self-focusing. The changing of laser focusing length, Δf, could be calculated by the following equation[135]:

$$\Delta f = l\left(1 - \frac{f}{\sqrt{n^2 f^2 + (n^2 - 1)\omega^2}}\right) \tag{2-13}$$

Where, f, is the laser focusing length in air, l is the distance between the air-liquid interface to the target surface, and n is the refractive index of the liquid solution. For optimum PLAL efficiency, the change of laser focusing length by the liquid solution must be taken into account.

The liquid medium could also affect the laser energy by absorption and scattering of the solution. This energy attenuation is caused by the laser interaction with matter within the liquid, such as solute molecules, ions and ablated particles *etc.* Therefore, the interaction between laser and liquid should be minimized. And, in particular, high fluence laser-induced optical breakdown of the liquid phase causes a severe interaction between laser beam and the liquid medium, which has to be minimized for avoiding attenuation of local beam intensity at the target surface.

Decreasing of laser intensity when laser travels through the liquid medium could be simplified and expressed by the Lambert-Beer law:

$$I = I_0 e^{-\alpha l} \quad (2\text{-}14)$$

Where, *l*, is the depth of the solution, I_0 and I are the initial and the attenuated laser intensities, respectively.

Mahdieh and Fattahi[136] studied the effect of water depth on NPs size and ablation rate of both aluminium and titanium targets irradiated by a 1064 nm Nd:YAG laser. Their study shows the ablation rate decrease with the increase of liquid height above target materials, which refers to the attenuation of laser energy. Nevertheless, with the increase of water depth, the NPs average size of both targets dropped first and then increased after a specific liquid depth. This phenomenon explained in their study is associated with two competitive effects between shockwave emission and energy attenuation.

Target absorbs laser energy and shock wave emission

After penetrating the liquid medium, the focused laser beam then reaches the surface of the target material, and the laser-matter interaction occurs. Before the ablation takes place, a shock wave emission and propagation could be observed (**Figure 2-22 c** and **d**). A shock wave is defined as the formation of discontinuities in flow variables (such as density)[135]. Two high-pressure waves are generated from the laser-irradiated region and propagate into both liquid medium and solid target[137]. In the solid phase, the target material is compressed and heated up after propagation of the shock wave. In the liquid phase, the shock wave dissipates energy by heating up the liquid medium.

Tsuji's group estimated the velocity of pressure reduction of shockwave front through a microsecond-resolution system[134]. The velocity of the shockwave front dropped from around 2600 m/s to 1600 m/s within 200 ns. The estimated pressure of the shockwave reduced from around 1200MPa to 80MPa in 200 ns.

Ablation of the target materials

After the deposition of photon energy through laser-matter interaction, mass removal occurs. Laser ablation mechanisms are varied according to the pulse duration, laser fluence and physical properties of the target materials. In practice, the ablation process is not caused by a single and specific mechanism, it is usually contributed by multiple fragmentation processes. The precise identification of the ablation mechanism is difficult for the difference of laser intensity along

the laser spot radius. In general, ablation mechanisms can be divided into two categories: thermal processes and non-thermal processes.

As mentioned in Section 2.4.2.3, thermalization results in transferring thermal energy from hot electrons to the lattice, which occurs if the pulse width is longer than the time required for the electron-phonon coupling. In this case, thermal processes are dominant. Determining by thermodynamic and kinetic limits, there are, mainly, three kinds of thermal processes:

- **Vaporization**. Vaporization refers to the simple physical process that the phase transition of vaporized target materials from the laser-irradiated region into particles through condensation.
- **Normal boiling**. This thermal process consists of the heterogeneous nucleation of the laser-induced vapor bubble. Nucleation of nanoparticles takes place at the interface between superheated liquid of the target material and other phases, such as gas impurities, solutes or the target surface.
- **Explosive boiling**. When the target is heated up to the critical boiling temperature, the superheated liquid transfers to vapor or liquid droplet through homogeneous nucleation, which refers to explosive boiling.

For ultra-short pulsed laser ablation, the dominant ablation mechanisms are commonly non-thermal. Three major types of non-thermal processes are found in the literature[111-112, 135]:

- **Spallation**. During laser irradiation, defects within the target surface caused by mechanical stress in the target lattice lead to fragmentation of the surface region. The accumulation of stress is considered as a result of the shockwave propagation within the target[53]. The shockwave generated through PLA contains 10-50% of the deposited laser energy[107]. When the shockwave travels through the target, the energy of shockwave releases by heating up the liquid and the solid, and inducing stress within the solid phase, which promotes the fragmentation of the target material.
- **Fragmentation**. Fragmentation refers to decomposition of the solid target caused by the rapid volume expansion of the superheated area. NPs are formed by these ejected fragments, and aggregation of fragments could also occur.
- **Coulomb explosion**. When the laser fluence is high enough, drastic electrons emission from the target surface could occur, leaving the surface positively charged. Repulsion caused by the surface charges leads to fragmentation of the target surface.

Laser-induced cavitation bubble

Following the shockwave emission, the formation, expansion and collapse of laser-induced cavitation bubble could be observed (shown in **Figure 2-23**). The energy released from the plasma plume to the surrounding liquid medium is widely accepted as a pathway of the cavitation bubble generation[107, 133, 135]. The cavitation bubble rises on a timescale of 0.1-1 μs, and expands on a timespan of the order of 10^{-4} s[132-134, 138]. During the expansion, the bubble front could travel at supersonic speed (~10^3 m/s) under common PLAL experimental condition[107]. The bubble reaches the maximum radius when the equilibrium state is attained between the inside gas and the surrounding liquid, meaning the bubble's temperature and pressure are approximate to that of the liquid medium, and, then, the cavitation bubble compressed, collapses and emits the second shockwave. The lifespan of cavitation bubble largely depends on the fluid properties of the surrounding liquid, such as viscosity[135] and compressibility[139], and the laser properties, such as laser fluence[133] and pulse width[140]. The lifetime increases with the increase of viscosity, for the viscosity affects the expansion and collapse of the cavitation bubble[135]. The maximum bubble's radius and the lifetime as a function of laser fluence are reported by Giacomo's group[133], showing good agreement with the empirical equation given by Chen *et al.* [141]. Moreover, Sasaki's group[142] report that the cavitation bubble dynamics could be manipulated by changing the external pressure to the liquid medium. The cavitation bubble radius decreases 75% with an external pressure at 10^6 Pa as compared to the PLA in the water at ambient atmosphere.

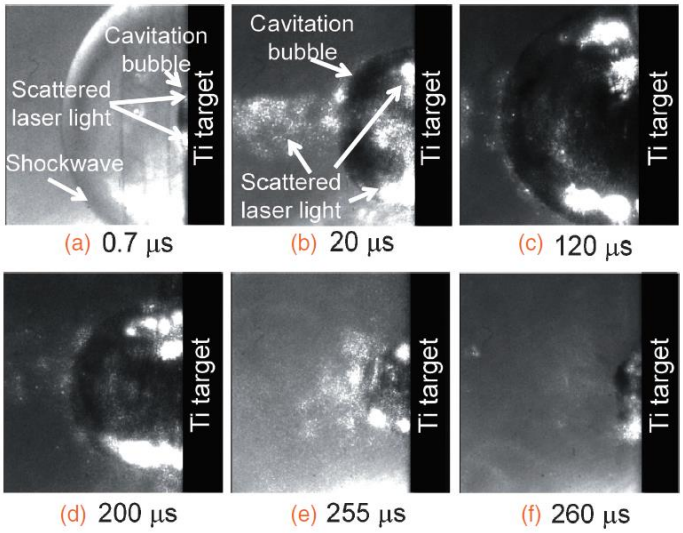

Figure 2-23 Superimposed images of laser-induced cavitation bubble and laser beam scattered by the bubble[138].

From **Figure 2-23**, a scattering of the incoming laser beam both inside and outside of the gas bubble could be clearly seen. Numerous small bubbles observed on the periphery of the

cavitation bubble are considered as the reason which causes the scattering outside of the cavitation bubble[138]. As reported in the literature[138, 143], the distribution of scattered laser beam within the cavitation bubble corresponding to the spatial dispersing of NPs. Because of the high local concentration of NPs and the bubble wall reflecting the incident laser beam[133, 138], the cavitation bubble could prevent following laser pulses from reaching the target, which directly affects the energy deposited on the material and, thus, the ablation rate. For the purpose of attaining higher productivity, interference of the cavitation bubble should be avoided by spatial or temporal separation of the successive laser pulses. The NPs productivity as a function of laser scanning speed is demonstrated by Barcikowski's group[143] and shown in **Figure 2-24**. In this case, the productivity of NPs continuously increases at a scan speed of 50-500 mm/s, and suddenly drops when the scan speed exceeded a critical value. This phenomenon, concluded by them, caused by two competitive effects: on the one hand, the attenuation of laser energy caused by bubble shielding decreases with increasing of laser scanning speed; on the other hand, the laser scanning speed could also affect heat accumulation in the lattice, which effects on NPs productivity.

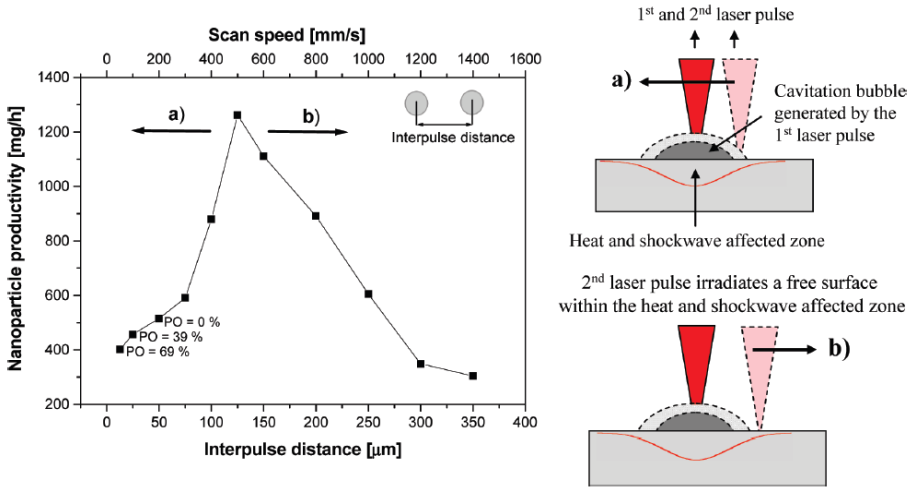

Figure 2-24 The productivity of Al_2O_3 NPs as a function of interpulse distance and the laser scanning speed using a 1047nm Nd:YLF laser with a fixed pulse energy of 4.6 mJ at 4 kHz repetition rate. PO indicates the calculated laser pulse overlaps in percentage. (**a**) and (**b**) are schemes of ablation, cavitation bubble, and the heat and shockwave affected zone[143].

Admittedly, the precise timing of generation and spatial distribution of NPs are not clear[107, 132-133]. The lack of comprehensive understanding of the transient process is due to the difficulty of observing and analyzing experimentally in this extremely short timescale (10^{-9}-10^{-3}s). However, it is widely accepted by researchers[111, 134-135, 138] that the majority of NPs are generated inside of the cavitation bubble during the bubble expansion. Thus, the changes in the cavitation bubble dynamics could influence the nucleation and the growth of generated NPs significantly.

Nucleation and growth of NPs during PLAL could be addressed by classical thermodynamic approach[102, 118]. Thermodynamically, the driving force for the phase transition is the negative change of free energy, which increases with undercooling. As nucleation and particle growth are competitive processes (for limited mass in the cavitation bubble), tailoring particles size is thermodynamically possible by controlling the pressure and temperature of the vapour. Besides, owing to the low thermal conductivity of the gas phase compared with the liquid, nucleation likely tends to occur at the bubble-liquid interface, for the high-temperature gradient could be achieved at the interface[107].

2.4.3 Non-Reactive and Reactive Liquid Media

The liquid media in PLAL process not only act as confinement for the laser-induced plasma and a carrier for ablated species, but they could also get involved in the process as reactants which can influence the composition of the product. The liquid media can be categorized into two kinds- non-reactive and reactive liquid medium- depending on whether the solution can react with the ablated species and contribute to the composition of products.

2.4.3.1 Non-Reactive Liquid Media

The liquid medium used in the PLAL process do not react with the ablated species, hence, the composition of generated NPs corresponds to the target material. The influence of non-reactive liquid on PLA generated NPs has been extensively investigated.

As mentioned in the previous section, the liquid solution used in PLAL process could be modified so as to control the fluid properties, such as viscosity and compressibility, and, hence, affect the confinement of the plasma plume. Tsuji's group analyzed the influence of PVP concentration on the size of silver NPs generated by PLAL process[144]. Improved confinement is observed with the increase in density and viscosity of PVP solvent. However, the size of as-ablated NPs is less affected by the PVP concentration. While the NPs after the second laser irradiation show a remarkable size reduction with an increase of the PVP concentration, which suggested the improved confinement may enhance the ablation efficiency. Additionally, more significant bubble volume caused by a liquid with high compressibility could depress the particle growth, resulting in a less collision possibility within the bubble and, thus, finer NPs[139].

Mafune's group [145-146] investigated separately the influence of sodium dodecyl sulfate (SDS) concentration on the size and the size distribution of silver and gold NPs generated by a 532 nm Nd:YAG irradiation on pure Ag and Au plates in an aqueous environment. From their studies, the average size of both Ag and Au NPs decreases with the increase of SDS

concentration. A dynamic formation mechanism proposed by them shows two competition effects occur during NPs formation: on the one hand, both embryonic Ag and Au NPs grow by the thermodynamic driving force; on the other hand, SDS acts as ligands and covers over the NPs surface, and, thus, terminates the growth of NPs by limiting their absorption of free atoms. As a result, the size of the NPs could be manipulated by changing the concentration of SDS. Similar effects have been reported by other groups by using cyclodextrin (CD)[147], PVP[144], polyethene glycol (PEG)[148] *etc.*

Besides the influence on the size, the non-reactive liquid medium also provides an attractive PLA processing environment for fabricating NPs in complex and unique structures. Chrisey's group[149] synthesized Pt NPs with a hollow structure through pulsed KrF excimer laser ablation of a Pt plate in water. TEM images of Pt hollow NPs produced by them are shown in **Figure 2-25**. The NPs with the hollow structure are considered to form the laser-induced bubbles (illustration is shown in **Figure 2-25 c**). After the collapse of the cavitation bubble, released nanocrystals and droplets preferentially attach the surface of laser-produced bubbles so as to minimize their interfacial energy. Therefore, in this hollow structure formation scenario, both thermodynamic and kinetic requirements should be satisfied, for instance, by choosing a suitable liquid solution and elongating bubbles' lifetime. Hollow micro-/nano scale particles formed by this mechanism are also found in PLA of bulk Mg[150], Al[151], Ag[152], Zn[153] and Fe-Ni alloy[154] in an aqueous environment.

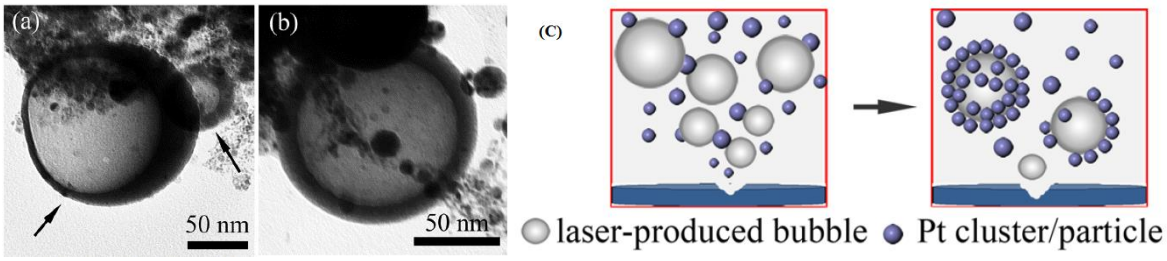

Figure 2-25 (**a**) and (**b**), TEM images of Pt hollow NPs fabricated by 248nm KrF laser ablation with a laser fluence of 3.6 J/cm^2, (**c**) schematic illustration of formation processes of hollow Pt NPs[92].

2.4.3.2 Reactive Liquid Media

In contrast with PLA in non-reactive liquid as discussed in the previous section, the reactive liquid medium (or byproducts of solvent molecules degraded under laser-induced extreme conditions) could react with the ablated species, resulting in a different composition of generated NPs from the target materials. Generally, a large variety of product composition, such as metal oxide, nitride, carbide and sulfide, *etc.* could be smartly designed by selecting targets and reactive liquid medium.

Numerous metal oxides have been investigated by ablating metal targets, including noble materials[155-157], in the different liquid medium. By laser ablating a pure zinc plate in pure water or in SDS with various concentration, Zeng's group[158] generated ZnO NPs and Zn@ZnO core-shell NPs separately. The NPs morphology, according to their study, changes from fully oxidized ZnO to Zn@ZnO core-shell structure, with an increase of SDS concentration. Furthermore, the thickness of the ZnO shell reduced by increasing SDS concentration. In pure water, Zn clusters quenched from plasma plume form ZnO in water via the following reactions:

$$Zn_{(clusters)} + H_2O = Zn(OH)_2 + H_2 \quad (1)$$

$$Zn(OH)_2 \xrightarrow{decomposition} ZnO + H_2O \quad (2)$$

While partially oxidized NPs could also be found in pure water, which caused by the incomplete oxidation of big particles formed in the cavitation bubble. When the SDS concentration is higher than its critical micelle concentration (CMC), the oxidation rate starts to be depressed, which leads to a Zn@ZnO metal-semiconductor morphology. Finally, when the SDS concentration is up to 10 times of CMC, owing to the high surface coverage by SDS, a nanostructure of a zinc core covered by a very thin $Zn(OH)_2$ could be observed. Sylvestre's group[159] ablated gold plate in water via an 800 nm Ti:sapphire fs pulsed laser. Through zeta-potential measurement and XPS analysis, they found that the surface of generated Au NPs is negatively charged, suggesting that Au particle was partly oxidized. A similar result also found by Muto's group[157] who ablated pure Au plate in water by a 1064 nm Nd:YAG pulsed laser irradiation.

Takada's group[160] separately ablated Ti and Si targets in liquid nitrogen by a 1064 nm Nd:YAG pulsed laser and prepared TiN and Si NPs respectively. The ablation was carried out in a stainless-steel chamber where the influences of other gas elements and water were eliminated. Through XRD and TEM analysis, polycrystalline TiN and pure Si particles with average diameters of hundreds nm were observed, respectively. Although the synthesis mechanism of ablation in this extreme environment is not yet understood, it still gives a possible route of synthesizing metal nitride via PLAL process. Other titanium compounds, such as TiC and TiH, were reported by Golightly and Castleman[161] who ablated Ti targets in liquid 2-propanol and n-hexane respectively.

Additionally, laser ablation in metal salt precursors solution also significantly expands the variety of generated NPs. In this case, two kinds of mechanisms, including photochemical reactions and high temperature pyrolysis of metal precursors, are proposed to generate NPs.

Photochemical reactions

As-ablated metals or semiconductors are usually surface charged, which provides a favorable site for metal ions be absorbed on the NPs surface through a reduction reaction. The deposition of metal ions on the as-ablated NPs gives an ideal pathway of generation metal/semiconductor @ metal core-shell NPs. Take semiconductors as an example, TiO_2 could act as an ideal substrate and shows a high efficient photocatalytic decomposition of noble metal precursors, such as Au, Ag and Pt salts, on its surface, which could be used in semiconductor @ metal core-shell NPs generation, for instance, TiO_2@Au[162], TiO_2@Cu and TiO_2@Ag[163]. Similarly, SnO_2[162] and ZnO[164] semiconductor@metal core-shell NPs also be synthesized through this approach. Sheykhifard's group[165] and Mottaghi's group[166] synthesized Au@Pd and Ag@Pd NPs via PLA in $PdCl_2$ solution, respectively. Owing to the negatively charged surface of as-ablated Au/Ag NPs, Pd^{2+} ions are attracted and deposited on the NPs surface, which forms NPs with core-shell structure.

Pyrolysis of metal precursors

Due to the intense optical field generated by the laser system and high-temperature high pressure induced by the photon-matter interactions, metal ions in the precursors tend to reduce or decomposed into zero-valence metal atoms by photochemical reactions or high-temperature decomposition. Photochemical reactions of metal salt precursors are mainly contributed by the free electrons generated via multiphoton absorption of the liquid. As the metal ions react with the free electrons, metal atoms and clusters are formed[167-169]. An example of photochemical reactions of $AuCl_4^-$ are shown in (3) and (4) [168]. Decomposition of precursors attributed to the high pressure and high temperature-induced during the ablation process. As the hot plasma and the cavitation bubble expand in supersonic speed, energy will be suddenly released and transferred to the surrounding liquid. Under this circumstance, atoms will be produced from the metal salt precursors and then form NPs (as shown in (5) and (6)[168]).

$$H_2O + nhv \rightarrow e^- + Q \quad (3)$$

$$AuCl_4^- + 3e^- \rightarrow Au^0 + 4Cl^- \quad (4)$$

$$AuCl_4^- + Q \rightarrow Au^0 + 3Cl + Cl^- \quad (5)$$

$$mAu^0 \rightarrow (Au^0)_m \quad (6)$$

Where, *Q*, is the caloric given by the hot plasma.

Jimenez *et al*.[170] proposed a smartly designed reaction, they ablated a silicon target in precursor solutions ($AgNO_3$, $HAuCl_4$ or a mixture of both salts) and successfully generated Ag@SiO_2, Au@SiO_2 and AuAg@SiO_2 NPs respectively. The NPs formation mechanisms explained by them is mainly contributed by a redox reaction between as-ablated Si and metal ions. Take $AgNO_3$ as an example, the formation of Ag@SiO_2 NPs is contributed by following redox reaction[170]:

$$Si(NP) + 4AgNO_3 + 2H_2O \rightarrow SiO_2(NP) + 4Ag(NP) + 4H^+ + 4NO_3^- \quad (7)$$

Similar results obtained by them via PLA of Ge and W targets in metal salt precursors[170] and also found in a recent study reported by Castillo's group who ablated a pure silicon target in $AgNO_3$ solution and synthesized Ag@SiO_2 NPs. However, a study reported by Liu's group[171] recently shows an adverse result, they synthesized Si@metal (Au, Ag, Pd and Pt) NPs by laser ablating a bulk Si target in different metal salt precursors. Liu's result shows that the formation of Si@metal NPs depends significantly on the photochemical reduction and high temperature-induced decomposition instead of redox reactions between Si NPs and metal ions. Furthermore, Zhang's group[172] ablated a Ge target in $AuCl_3$ and $AgNO_3$ solution respectively, and synthesized Ge-Ag alloy NPs and Ge-Au@Au NPs. Although, the NPs generation mechanism, in this case, is not completely understood, for the complex physical-chemical nature of PLAL process, but the process proposed by Jimenez's group[170] still gives an applicable pathway of synthesizing NPs with various compositions in a single step.

2.4.4 Nanoparticles Fabricated via Laser Techniques

This review primarily focuses on the widely reported laser fabrication techniques for metallic NPs fabrication. A wide variety of target materials/precursors has been used and investigated for NPs synthesis via this technique. Typical studies provided by pioneers have summarized in **Table 2-3**, including target materials, liquid media, laser operating parameters (and experimental procedures) and generated nanostructures:

Table 2-3 Synthesis of alloy and metallic core-shell NPs via PLAL.

Targets	Liquid media	Laser parameters, and processing procedures	Synthesized products (size, structure and note)
Ag	$HAuCl_4$+anhydrous alcohol	Nd-YAG, 1064nm, 6ns, 10Hz, 24J/cm^2, 50min	Ag@Au NPs, size from 32.5 nm to 1.8 nm (change with the increasing concentration of $HAuCl_4$)[173]
$Au_{75}Ag_{25}$	Water	Nd-YAG, 532nm, 8ns, 10Hz, 40mJ/pulse(1.27J/cm^2), 2-20 min	$Au_{75}Ag_{25}$ alloy NPs, with mean diameter from 6.7nm-8.3nm (size increases with operating time)[174]
Au & Ag	PVP	Nd-YAG, 1064nm, 9ns, 10Hz, 10^3 J/cm^2, 10min for Au+ PLA time for Ag	Au@Ag, size~25nm Au-Ag nano-alloy formed with further ablation of Ag plate[175]
	Water	Nd-YAG, 1064nm, 6-9ns, 5Hz, 300mJ, 30min of ablating Ag firstly and then target replaced by Au ablated for 30-150min	Ag@Au NPs[176]
Au	Water	Ytterbium fibre laser, 1064nm, 70ns, 20kHz, 13J/cm^2, N/A. Post-preparation size reduction by Nd:YAG, 532nm, 50kHz, 0.5J/cm^2, 5-45min	Au NPs, size from 20-150nm (size decreases with the increasing of post-preparation irradiation time)[177]
Al & Ag & Au	Water	Nd:YAG, 532nm, 5ns, 10Hz, 4.5J/cm^2 (for Al target); 17.6J/cm^2(for Ag or Au targets), Al target be ablated for 20-40min, then ablate Ag target in Al colloidal solution, finally replace Ag to Au and ablate in Al+Ag colloidal solution	Al@Al_2O_3@Ag@Au, and Al@Al_2O_3@AgAu trimetallic NPs were observed[178]
Ag-Cu alloy	PVP	Nd-YAG, 1064nm, 8ns, 10Hz, 50mJ/pulse, N/A	Ag-Cu bimetal, 5-20nm, NPs morphology changes from alloy to core-shell with the increasing of Cu concentration[179]
Cu	Colloidal Ag	Nd:YAG, 1064nm, 12ns, 1Hz, 6.8J/cm^2, 60min	Ag@Cu core-shell NPs (with additional pure Cu NPs within the solution, with a diameter of 4-8nm), with size of 90-180nm[180]
Ag & Al	Water+PVP	Nd-YAG, 532nm, 5ns, 10Hz, 14.3J/cm^2(Ag); 4.5J/cm^2(Al), 40min for fragmentation of individual metal plate; post-ablation cots 90min	Rattle-type Ag@Al_2O_3, with a mean size of 25nm[181]
Ag & Zn	Water	KrF, 248nm, 20ns, 10Hz, 400mJ, 30min (Ag); 5-30min within the Ag colloid (Zn)	Ag@ZnO NPs, 50-60nm[182]
Ag	SBA-15/ MCM-41 Si nano-porous colloidal solutions	Ti: Sapphire, 800nm, 120fs, 1kHz, 9J/cm^2, 30-1200s	Ag NPs generated and located within silica mesoporous, decomposition of Si mesoporous colloid leads to the generation of Ag@Si NPs, with a size distribution of

			22.5±2.6nm(MCM-31) and 15.4±5.7nm(SBA-15)[183]
Au	Tetrathyl orthosilicate(TEOS) + ammonia + 2-propanol	N/A, 1030nm, 10ns, 20kHz, 10J/cm^2, N/A	Au@Si NPs[184]
Au & Cu	Acetone	Nd-YAG, 1064nm, 10ns, 10Hz, 5J/cm^2, N/A (stage1: generate Au and Cu NPs separately) 0.3 J/cm^2 (stage2: mix NP colloids from stage1)	Au@Cu alloy NPs, Au and Cu NPs are found, the size of Au and Cu NPs are 1-7 and 5-12nm; Au@Cu with size around 20nm[185]
Au-Ge alloy	Water	N_2, 337nm, 10ns, N/A, 50J/cm^2, N/A	AuGe nanowire has higher Ge content than thermodynamically stable α-AuGe phase[186]
Au@Pd	$PdCl_2$ solution	Nd-YAG, 1064nm, 5ns, 10Hz, 360mJ, N/A	Au@Pd NPs, NPs size increases with the increasing of $PdCl_2$ concentration[165]
Ag	Water & $PdCl_2$ solution	Nd:YAG, 1064nm, 5ns, 10Hz, 10J/cm^2, 40min, laser ablation carries out in water, then, $PdCl_2$ solution added in the as-prepared Ag colloid	Pd^{2+} ions are reduced and partial Ag particles are oxidized, leading to the generation of Ag@Pd NPs[166]
Ag	Water	Nd-YAG, 1064nm, 7ns, 15Hz, 300 mJ with a spot size of 2 mm	Ag NPs, mean size of 24 nm[187]
$Au_{56}Fe_{44}$	Water/acetone/methyl methacrylate(MMA)	Nd:YAG, 1064nm, 10ps, 100kHz, 160μJ, 10min; Nd:YAG, 1064nm, 8ns, 15kHz, 0.8mJ, 10min	Majority of Fe@Au NPs were formed in acetone and MMA, with average diameters of 68nm and 87nm respectively; Au@Fe_3O_4 formed in water, with an average diameter of 70nm ($Fe_{44}Au_{56}$ alloy NPs were found in all solvents)[188]
$Au_{73}Fe_{27}$	Ethanol	Nd:YAG, 1064nm, 9ns, 10Hz, 30J/cm^2, N/A	$Au_{89}Fe_{11}$ NPs, with a diameter of 30-60nm[189]
$Fe_{50}Pt_{50}$	Water/hexane	Nd:YAG, 532nm, N/A, 10Hz, 100mJ, 30min	$Fe_{23}Pt_{77}$ and $Fe_{38}Pt_{62}$ NPs were found in hexane, $Fe_{26}Pt_{74}$ was obtained in water[190]
Ti-Al bimetal plate	Isopropanol (saturated with H_2)	Nd-YAG, 1064nm, 10ps, 200kHz, 10J/cm^2, 30min (laser beam scanned across the interface of bimetal)	Al@Ti NPs (Ti_2O, Ti and Al NPs also generated, no sign of Al-Ti alloy), 40nm[191]
$Ni_{75}Pd_{25}$	water	Nd-YAG, 532nm, 8ns, 10Hz, 40mJ/pulse(1.27J/cm^2), 2-16 min	Pd-Ni alloy NPs, size <5nm[174]
NiFe alloy	Cyclopentanone	Ti/sapphire, 800nm,120fs, 5kHz, 300μJ, 10-80min	Ni-Fe alloy NPs (element composition accordance with the target alloy), size is 60±6nm[192]
NiFe alloy	water+SDS	KrF, 248nm, 30ns, 20Hz, 7J/cm^2,20min-9h	Ni-Fe NPs (partially oxidized), hollow aggregates depending on ablating time[154]
NiTi alloy	Water	N/A, 1030nm, 300fs, 20kHz, 8.5μJ, 1min	NiTi NPs with composition corresponding with bulk materials, wide size distribution[193]
NiTi alloy	Water	Nd:YGA, 1064/532/355nm, 5-8ns, 10Hz, 40;30;20J/cm^2, 45min	NiTi alloy NPs, NPs size from 10-140nm (size changes with wavelength)[194]
CIGS ($CuLnGaSe_2$)	Water + acetone + ethanol	Nd-YAG, 1064nm; 532nm, 10ns, 10Hz, 9-30J/cm^2 for 1064nm; 6-	CIGS NPs, morphologies and size vary with fluence and wavelength[195]

		27.6J/cm^2 for 532nm (change by the focal point), 5min	
InSb	Water/ ethanol	Nd-YAG, 1064nm, 20ns, 1kHz, 50J/cm^2, 15-35min. / 800nm, 90fs, 1kHz, 11J/cm^2, 15-35min	InSb NPs in zincblende crystal structure with fcc lattice (also generate Sb and In oxides)[196]
Amorphous SiSn thin film	Water	KrF, 245nm, 10ns, 20Hz, 23.5mJ/cm^2, 10min	SiSn alloy NPs, mean size 17nm[197]
PtPb	Methanol/ethanol	N/A, 1041nm, 550fs, 100kHz, 0.73J/cm^2, N/A	Intermetallic PtPb NPs, with size 29±20nm[198]
Sm_2Co_{17}	Cyclopentanone	Ti/sapphire, 800nm,120fs, 5kHz, 300μJ, 10-80min	SmCo alloy NPs (with distortion composition compare to the target material, may cause by the different evaporation temperature of Sm and Co), 30±6nm[199]

As shown in **Figure 2-26**, multiple bimetallic alloys and metallic based composite NPs have been synthesized via ablating various targets in different liquid media. As-prepared metallic NPs have attracted much interest owing to their unique properties which are widely implemented in bioengineering, medical technology and chemical field, *etc*.[109] For instance, Au NPs surface can conjugate electron donors, such as thiol or amino groups, directly without the need for chemical additives[100]. By embedding functional core materials, such as magnetic iron oxide, utilities of these core-shell NPs could be significantly expanded. Although, extensive reports provided by pioneers give information on the relevant processing parameters and the characteristics of generated NPs, but the formation mechanisms of NPs, particularly alloy NPs and NPs with core-shell structure, are still not clear. This section by no means aims at providing a comprehensive understanding of NPs formation, for the comparison of literature results given by different experimental parameters and various physical and chemical environments are not straightforward. It, instead, focuses on finding and describing analogies of the structure and composition of ablated NPs from previous studies, particularly when target materials with similar physical and chemical properties are ablated by analogical methodologies. Generally, the synthesis methodologies for bulk targets could be illustrated by the schematic provided by Navas and Soni[200], as shown in **Figure 2-26 a**.

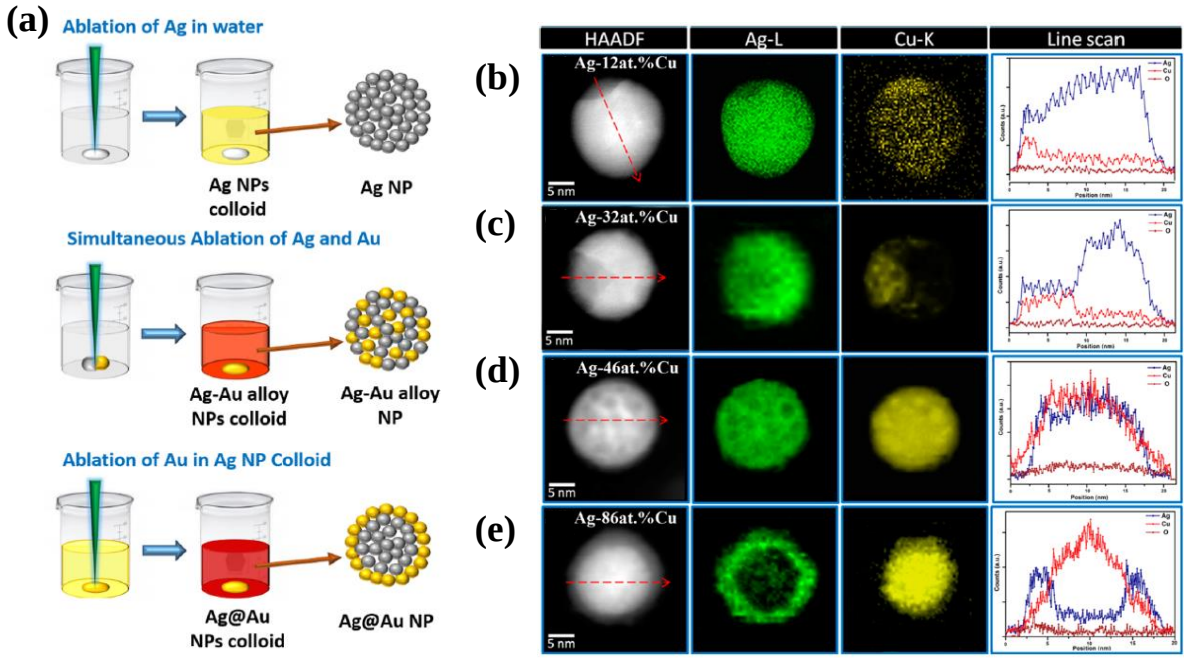

Figure 2-26 (a) Schematic of NPs formation via PLAL and the estimated structures[200], (**b-e**) compositional variation in NPs corresponding to target composition Ag-X atom Cu (X=20, 40, 60, 80), respectively[179].

Alloy NPs, especially noble metal alloys, are synthesized via PLAL of bulk alloy targets with compositional elements have similar lattice constants[201]. In most of the cases, the composition of as-prepared NPs is accordance with that of the target materials. For instance, laser ablation of noble metal alloys, such as Au-Ag[174, 200-201], Pt-Au[202-203] and PtIr[204], provides NPs with stoichiometry very similar to their bulk counterparts. In some cases, depending on the solution used, active alloy NPs, for instance, Ni-Fe[192], Ni-Ti[193] and Fe-Au[188] alloys, could also preserve the composition from disproportionality. The mechanism of whether the generated NPs preserve the composition of its target is not very clear. Based on the literature, there are mainly two possible reasons. For instance, Sm-Co alloy NPs synthesized by Jakobi's group[192] are found 54.5% more in Sm and 26.2% less in Co compared with the composition of the target. This phenomenon may attribute to the difference evaporation heats between Sm and Co (ΔH=56%). Conversely, Amendola's group[205-206] found that the generated AuFe alloy NPs through PLA in water exhibit "iron-poor" feature. In this case, the evaporation heats of Au (324 kJ/mol) and Fe (340 kJ/mol) are similar. The loss of iron may attribute to that iron reacts with water and forms hydroxides or dissolvable contents. And the FePt alloy NPs generated through PLA in hexane and water also support this hypothesis, as the evaporation heat of Pt (490 kJ/mol) is much higher than that of Fe (340 kJ/mol) but the synthesized NPs possess high Pt concentration[190]. Furthermore, since noble bimetallic materials such as Pt-Au and Pt-Ir also have different elemental evaporation heats but the synthesized NPs possess the stoichiometry

of their bulk counter-parts , the hypothesis of the different reactivity of the elements with solution molecules might be more probable[107].

Despite using reducing agents as mentioned in the previous section, NPs with core-shell structures are normally formed via ablation the "shell" target in the "core" colloidal solution. The colloidal solution provides a preferential heterogeneous nucleation site for ablated elements. Metal core-shell NPs, such as Ag@Au[176, 200], and metal@semiconductor NPs, like Ag@ZnO[182], could be formed by ablating targets in colloidal solution. Interestingly, Singh and Soni[178] generated trimetallic core-shell NPs, Al@Al_2O_3@Ag@Au and Al@Al_2O_3@AuAg, through two-step ablation method.

Core-shell structure NPs are also reported that could be synthesized by alloy targets. Malviya and Chattopadhyay[179] ablated Ag-Cu alloy targets with different compositions in liquid. The generated nanostructures transfer from biphasic to a core-shell structure with an increase in Cu concentration. The change of NPs morphology with the target's composition is shown in **Figure 2-26 b-e**. This composition-dependent morphology is defined by the incorporation of the size and composition-dependent surface energy. Another example is reported by Serkov's group[191], who synthesized Ti@Al alloy NPs via ablation of a Ti-Al alloy target in liquid isopropanol saturated with molecular hydrogen. As the different evaporation heats between Ti and Al, Ti is likely solidifies first during the condensation, while Al still remains liquidus. Then, the liquid Al could wet the surface of solidified Ti particles and form Ti@Al NPs. Mahfouz's group[174] find the surface of the prepared Ni-Pd NPs enriches Ni with increasing irradiation time, which may be attributed to the preferential oxidation and superficial migration of Ni.

2.4.5 Electrocatalysis Applications of Laser Fabricated NPs

Contemporary synthesis methods, such as chemical reduction[207-208] and solvothermal synthesis[209-210], use caping agents selectively adsorbed on Pt surface to modify the NPs shape and size. However, the capping agents[211] and CO containing precursors[212] can potentially block the NPs surface and, hence, inhibits the exposure of the active site. As a result, extensive purification and cleaning required for removing the surface attached ligands prior to the catalytic applications. The laser-assisted fabrication stands out as a promising approach for electrocatalysts synthesis, for its free of ligands coverage, which guarantees NPs with bare surface exposure and avoids extensive post-synthesis purification and cleaning[1]. Owing to the high temperature and high pressure generated locally during laser irradiation, which induces defects and disordered structures in nanomaterials (*e.g.* stacking disorder[187, 213], oxygen

vacancies[214]) and provides a pathway to finely tune the electron configuration and, hence, the intrinsic catalytic activities of nano catalysts. Furthermore, the laser-assisted approach is feasible for a wide range of nanomaterials synthesis, heterogenous elements doping and alloying can be achieved by using reactive media or by applying alloy targets. Although, the catalysis study of the emerging laser assisted methods on electrocatalysts synthesis is limited, but the pioneer works conducted recent years demonstrate its promising potential in energy storage and conversion applications.

Kohsakowski *et al*.[215] designed a flow-through configuration for laser ablation of Pt target in pure water (**Figure 2-27 a**). The condensed Pt NPs in the flowing water are transferred directly to the collection tank and mixed with carbon black, which avoids subsequent scattering of the laser beam. Although, the Pt NPs exhibits a large average size and a broad size distribution. However, gram-scale production (~ 4g/h) demonstrates the potential to meet an application-relevant scale. Moreover, the synthesised Pt NPs shows a comparable mass activity to the commercial Pt/C catalyst in a self-made fuel cell unit. In the case of alloy NPs synthesis, Hu *et al*.[216] ablated a cobalt target in a reactive medium consists of $PtCl_4^{2-}$ ions (**Figure 2-27 b**). PtCo alloy NPs was successfully synthesised with a size range from 3 to 18 nm, and the Pt to Co ratio can be precisely tuned by varying the Pt precursor concentration. The obtained $PtCo_2$ NPs shows a 3 and 6-fold increase in ORR mass and specific activities than that of the commercially available Pt catalyst.

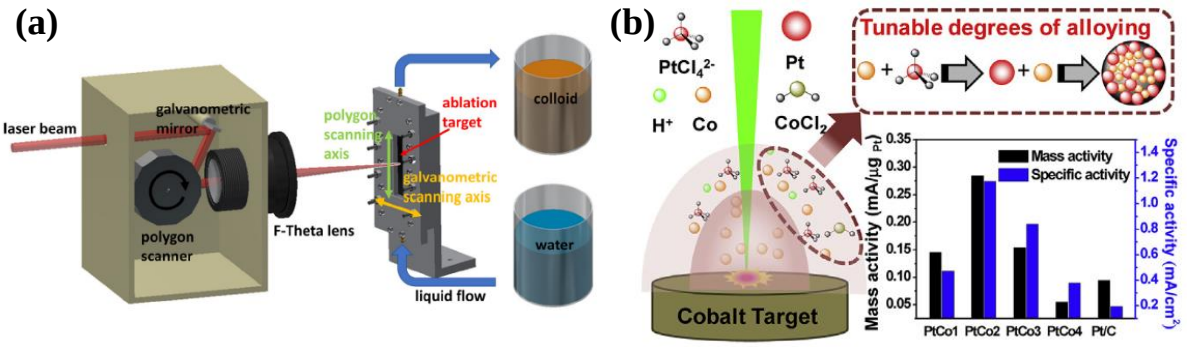

Figure 2-27 (**a**) Schematic of the up-scaled Pt NPs generation in a flow-through chamber[215]. (**b**) Schematic diagram of the formation of PtCo NPs via laser ablating a cobalt target in a reactive medium consists $PtCl_4^{2-}$ ions, and the ORR mass activity and specific activity of PtCo alloy NPs with various composition and the commercial Pt/C catalysts[216].

Defect engineering of electrocatalysts is an important strategy to modify catalysts surface atoms configuration and tune the atom electron configuration. Li *et al*.[187] utilized laser ablation for Ag NPs (denote as L-Ag) synthesis in water. Interestingly, the as-synthesized L-Ag NPs display abundant stacking faults (**Figure 2-28 a**), owing to the rapid heating and cooling in the liquid

medium. The internal strain caused by the stacking disorder leads to plentiful atomic steps formation at the L-Ag NPs surface (**Figure 2-28 b**). For comparison, they prepared monocrystal (S-Ag) and twin crystal (T-Ag) NPs chemically, and applied FT-EXAFS analysis to reveal the coordination number of surface Ag atoms from all samples. As shown in **Figure 2-28 c**, the chemically synthesised S-Ag and T-Ag NPs show a slight decrease in coordination number compared to the reference Ag foil, for their small particles size. However, a drastic decrease in coordination number of L-Ag was found (~8.37), for the abundant surface steps. The significant change in the surface Ag atom arrangement adjusts the hydrogen adsorption energy on the Ag surface (~ 0.3 eV less than Ag (111) plane). Based on previous studies, Ag is not seemed as a HER catalyst for its high binding energy with hydrogen, as shown in section 2.2.3.2. However, the defect-rich structure contributes to an extraordinary enhancement of Ag HER activity (**Figure 2-28 d**), with a Tafel slope of 31 mV/dec outperforms that of the commercial Pt/C catalyst (35 mV/dec). A similar finding was reported by them in the later RhO_2 fabrication via PLAL[213]. The laser-generated RuO_2 shows a shorter Ru-O bond length (1.59 Å) than that of the reference Rh_2O_3/RhO_2 (1.65/1.68 Å). Benefit by the defect construction, the laser synthesized RhO_2 NPs show a superior HER activity that only requires 14 mV overpotential to drive 10 mA/cm^2 in 1 M KOH electrolyte.

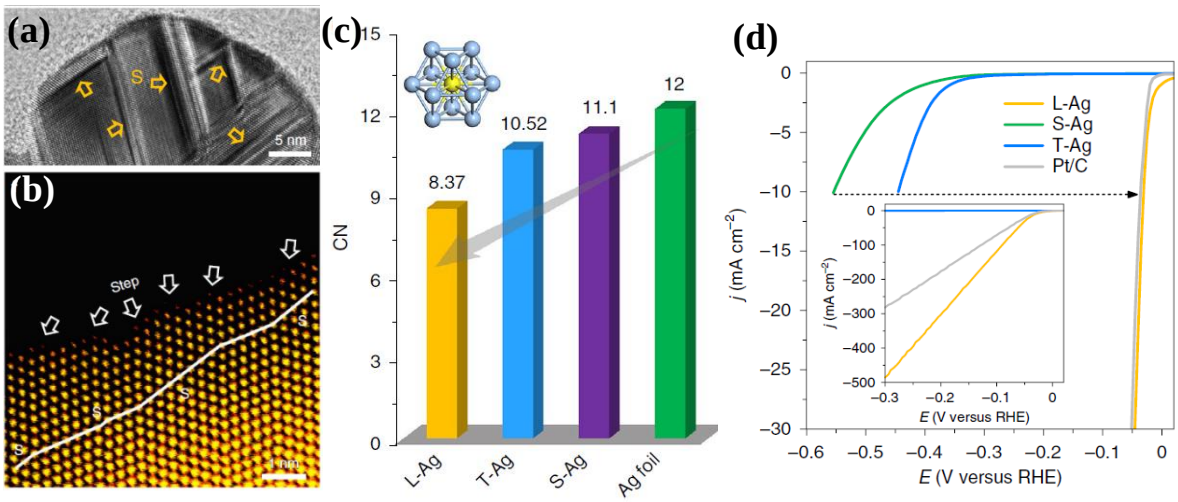

Figure 2-28 (**a**) the HRTEM image of L-Ag NPs consist of stacking faults, and (**b**) an aberration-corrected HAADF-STEM image of L-Ag NPs showing stacking disorder-induced atomic steps at the particle surface. (**c**) the average coordination number of L-Ag, S-Ag, T-Ag and the standard Ag foil reference, the coordination number was calculated based on FT-EXAFS spectra. (**d**) The polarization curves of L-Ag NPs catalysts and other reference materials[187].

Direct synthesis of heterogeneous catalysts via laser technique offers an opportunity to combine a wide range of functional materials with various substrates, and thus to modify the composite functionalities. Ren *et al.*[217] synthesized Co_3O_4 decorated laser-induced graphene (LIG)

composite through laser-induced pyrolysis of $Co(NO_3)_2$ precursor treated LIG substrate (**Figure 2-29 a**). After laser irradiation, ultrafine Co_3O_4 NPs was deposited on the porous LIG flakes, with an average size of 5 – 10 nm. The synthesised Co_3O_4/LIG composite display comparable ORR and OER activities to that of the commercial catalysts. More importantly, this method is not limited to the poly(amic acid) soluble metal precursor, which can extend easily to other elements decoration of the LIG substrate.

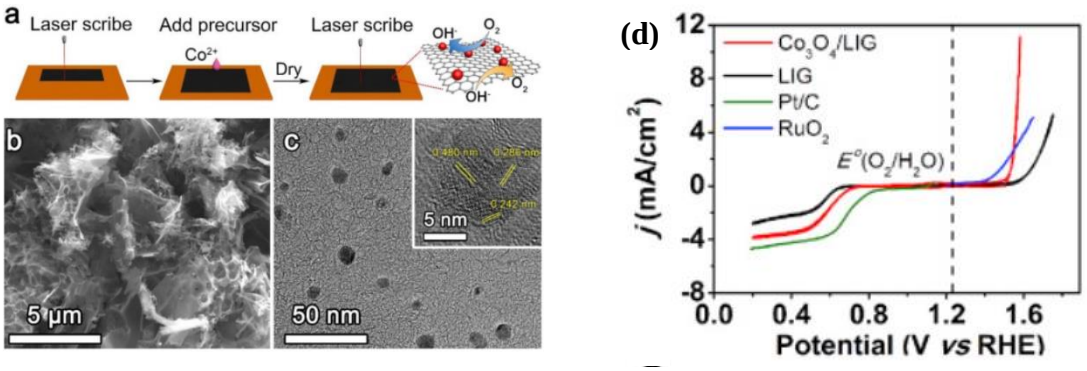

Figure 2-29 (**a**) Schematic of Co_3O_4/LIG composite fabrication through laser scribing, and (**b**) the SEM image and (**c**) the representative TEM image of the Co_3O_4/LIG composite. (**d**) Cyclic voltammetry curves of Co_3O_4/LIG composite and other reference materials in 0.1 M KOH electrolyte[217].

2.5 Summary

In this chapter, a review has been made to cover the characteristics of nanomaterials, applications of nanomaterials as electrocatalysts, the laser properties and the laser techniques for engineering nanoparticles (especially through PLAL method). Outstanding characteristics of laser nano-fabrications have been addressed, such as free surface exposure, versatility in manufacturing nanomaterials with various shape and compositions, feasibility in defect engineering etc. The laser nanofabrication is considered as a rapid, robust, and flexible process for nano-catalysts synthesis.

In order to expand the applications of laser fabricated nanomaterials in catalysis, the laser synthesis methods have to meet the high requirement of precise particle size control for enhancing the catalytical activity, active site utilization and performance reliability. However, some challenges in laser nanofabrication (especially the commonly used PLAL method) have not been resolved by the previous studies and techniques. Such as:

1) The mixture of a broad size distribution of PLAL generated particles. Owing to the high temperature and high pressure of laser induced cavitation bubble that contains plasma

and molten droplets, the PLAL generated NPs have large mean particle size and broad size distribution (as listed in **Table 2-3**). The broad size distribution limits its catalytical applications, for: 1. only a small fraction of products can serve as catalytic active species; 2. High metal consumption along with the ablation process; 3. Relatively low active sites utilization efficiency and pore selectivity.

2) Previous studies have demonstrated the capability for synthesising nanomaterials ranging from several nanometres to micron scale. The size map still contains some uncovered ranges, such as monodisperse ultrafine nanoparticles (< 5 nm) and isolated dispersion of single atoms. As the catalyst performance of nanomaterials is sensitive to the numbers of active sites, and accessible surface area. Thus, effective size reduction and precise size control of nanomaterials are critical to the catalysis applications.
3) The PLAL generated nanoparticles are dispersed in liquid medium as colloidal solution. For heterogeneous catalysts synthesis, a second step mixture of catalytical active species with supporting materials is required, and aggregation may occur during the following process. By inducing the supporting materials in the laser fabrication can not only reduce the processing procedures, but can also provide a platform for altering the activity and stability of heterogeneous catalyst by tuning the metal-support interactions.
4) To date, the mechanisms of laser nanofabrication techniques have not been revealed completely due to the complicated multi-physical phenomena occurring during laser ablation of metal targets (PLAL), photothermal (laser pyrolysis) or photochemical reduction of precursors. Therefore, it is difficult to control the fabrication process for high quality catalysts production.

Considering the above-mentioned challenges in laser fabricated nanomaterials, it is essential to further expand the processing method that able to produce ultrafine nanoparticles (< 5 nm), and study the effects of processing parameters on nanomaterials size and structure, and investigate the unrevealed mechanisms, and finally explore the potential of new fabrication techniques for engineering high-performance catalysts.

Chapter 3. Experimental methods

This chapter lists all materials used, and aims to provide details of the experimental procedures for synthesizing catalysts the characterization techniques. The brief background of the analytic methods, and the sample preparation methods and the instrumentation will be described.

3.1 Materials

Table 3-1 shows the list of chemicals used for synthesizing catalysts and materials testing.

Table 3-1 Lists of used materials and chemicals used in the experiments.

Materials/Chemicals	Supplier
Target Material	
Platinum plate (99.99%, ϕ: 2.54 cm, thk: 1 mm)	Good fellow
Chemicals	
Isopropanol alcohol (99.5%, anhydrous)	Sigma Aldrich
Ethanol (99.0%, anhydrous)	Sigma Aldrich
Acetone (99.5%)	Sigma Aldrich
Potassium hydroxide solution (1/0.1 M)	VWR
Sulfuric acid (95.5 - 98.0%)	Sigma Aldrich
Nitric acid (70%)	Sigma Aldrich
Hydrochloric acid (37%)	Sigma Aldrich
Nafion (5 wt.% in lower alphatic alcohols and water)	Sigma Aldrich
Chloroplatinic acid hydrate (99.995%)	Sigma Aldrich
Ruthenium(III) chloride hydrate (99.98%)	Sigma Aldrich
Sodium tetrachloroplalladate(II) (99.99%)	Sigma Aldrich
Manganese(II) chloride tetrahydrate (99.0%)	Sigma Aldrich
Platinum(IV) chloride (99.99%)	Sigma Aldrich
Reference Materials	
Pt/C (20 wt.%, Hispec 3000)	Alfa Aesar
RuO_2 anhydrous (99.95%, Ru 75.2% min, Premion)	Alfa Aesar
Platinum stock solution (1000 µg/ml)	SPEC CertiPrep
Ruthenium stock solution (1000 µg/ml)	SPEC CertiPrep
Miscellaneous	
Nitrogen gas (99.8%)	BOC
Oxygen gas (99.5 %)	BOC
Argon gas (99.99 %)	BOC
Carbon Black (Vulcan 72)	Cabot Corporation
De-ionized water (15 MΩ cm)	ELGA VEOLIA
Syringe filter (0.2 µm, Whatman)	Fisher Scientific
PTFE filtration membrane (0.2 µm)	Millipore

3.2 Experimental setups

3.2.1 Pt NPs synthesized through PLAL and UV laser post-irradiation

Before PLAL process, the target material (pure platinum, 99.99%, with 2.54 cm diameter and 1 mm thickness) was polished and ultrasonically cleaned in ethanol for 15 min to remove contamination and then dried in ambient condition. For PLAL process the target material was placed at the bottom of a glass vessel and immersed in de-ionized water (with liquid height of 5 mm from the target's upper surface) (**Figure 3-1 a**). A Q-switched nanosecond Nd:YVO_4 solid-state laser (Violino Green, LNA Laser Technology) operating at the second harmonic mode, with a central wavelength of 532 nm (7 ns) was used to ablate the Pt target. The incoming laser beam was focused on the surface of the Pt plate with a beam size of ~ 55 µm. To ablate the Pt target, the laser beam was scanned in a spiral manner at 1000 mm/s, at pulse energy up to 400 µJ (~16.8 J/cm^2), a repetition rate of 25 kHz, a processing time of 10 min. The colloidal solution (denoted as LPt) was collected for further treatment and analysis.

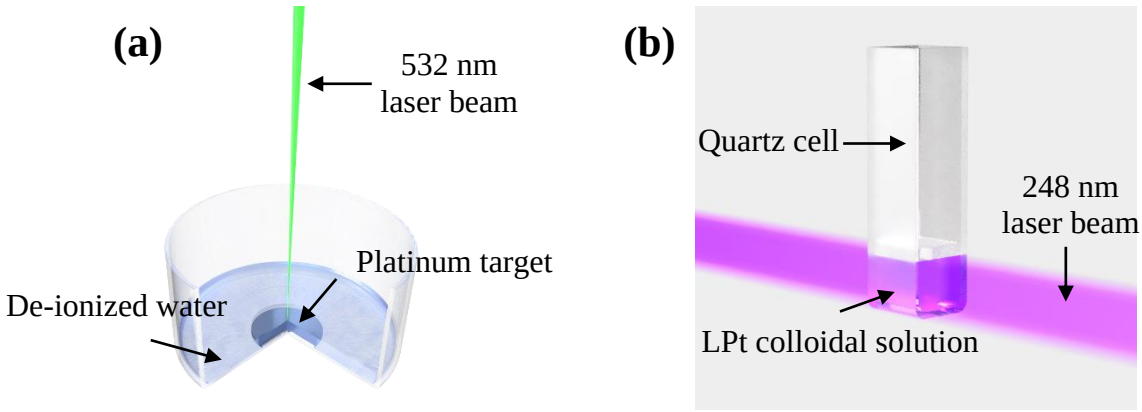

Figure 3-1 (a) Schematic illustration of the PLAL setup for LPt NPs production, (**b**) post UV laser irradiation.

The post-irradiation of LPt colloidal solution was carried out using a KrF pulsed excimer laser (Lumonics IPEX-848, LightMachinery) with a central wavelength of 248 nm (10 ns). 1 ml as-prepared LPt colloidal solution (within 1 hour after laser ablation) was transferred into a quartz cuvette (QS100 – Macrocells, Hellma) with a light path of 10 mm and wavelength range from 200 to 2500 nm. The laser beam irradiated on the quartz cell horizontally with a beam size of 1.1 × 0.4 cm^2, at a repetition rate of 10 Hz, and laser fluences of 0.5, 0.8 and 1.1 J/cm^2 (**Figure 3-1b**). To reveal the NPs size evolution at a give laser fluence, the processing time was set to 0.5, 1, 2, 5, 10 and 20 min. The refined LPt NPs were denoted as : LPt-500, LPt-800 and LPt-1100, respectively, correlate to the processing laser fluences. The resulting Pt colloidal was then collected for further analysis (within 1 hour).

3.2.2 Laser assisted solution synthesis of high performance graphene supported elecrocatalysts

The electrochemical graphene oxide (EGO) was prepared using the method reported elsewhere[218]. The EGO solution was diluted with de-ionized water (15 MΩ cm) to a concentration of 0.1 mg/ml, and mixed with metal salt (i.e. H2PtCl6, RuCl3, Na2PdCl4, MnCl2, 50 $\mu g_{metal\ ion}$/ml). Small amounts of isopropanol and acetone were added into the solution ($m_{isoporpanol}$: $m_{acetone}$: m_{water} = 2:1:100). The mixed solution was purged with Ar gas, stirred vigorously and pumped into a home-mode flow cell (with a light path of 1 cm) through a peristaltic tubing pump (FH15, Fisher Scientific) with a volumetric flow rate of 100 ml/min (As shown in **Figure 3-2**). A Krf pulsed excimer laser (Lumonics IPEX-848, LightMachinery) with a wavelength of 248 nm (10 ns) irradiated at the flowing solution with a beam size of 1.1 × 0.4 cm^2, at a repetition rate of 100 Hz. The laser energy was set to 100, 150, 200, 250 and 300 mJ, which corresponds to laser fluences of 227, 340, 454, 568 and 681 mJ/cm^2. The 100 ml solution flowed through the quartz cell with 30 min processing time to ensure the solution was evenly processed. The as-prepared solution was then collected, washed (with water, 3times) and vacuum filtered (0.2 μm, PTFE membrane, millipore), and freeze-dried (Labconco FreeZone 2.5 L -50°C 230V model, Fisher Scientific) to obtain the graphene nanoparticle composites.

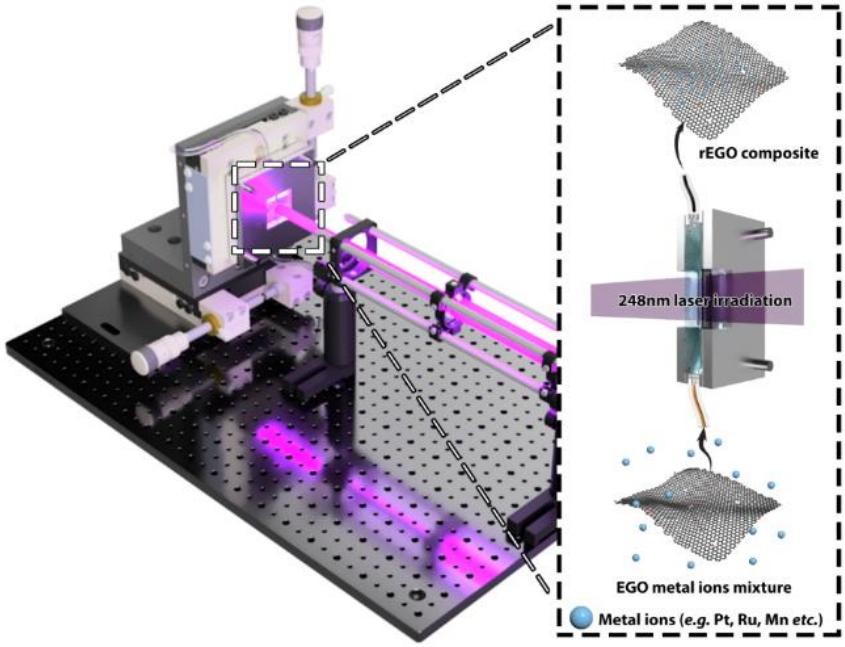

Figure 3-2 Schematic illustration of the home-mode flow cell, and experimental setup of laser assisted solution phase synthesis of graphene composites.

3.2.3 Laser solid phase synthesis of single-atom catalysts

The EGO was prepared using the method reported elsewhere[218]. To prepare the EGO film, 4 ml of 1 mg/ml EGO water dispersion was vacuum filter through a PTFE filtration membrane (0.2 μm pore size, Millipore), the dimension of the EGO film was 3.2 cm in diameter and 1.5 ± 0.2 μm in thickness. In the case of Pt-EGO film, 1 mL metal precursor solution (H_2PtCl_6 / $PtCl_4$, 0.1 – 10 mmol L^{-1}) was vacuum filtered through the EGO membrane. The EGO or Pt-EGO films were then immersed in liquid nitrogen and freeze dried (Labconco FreeZone 2.5 L -50°C 230V model, Fisher Scientific) to reduce localized precipitation of metal salts. The dried GO and Pt-EGO films were subjected to direct laser beam patterning in constant Ar flow (**Figure 3-3**).

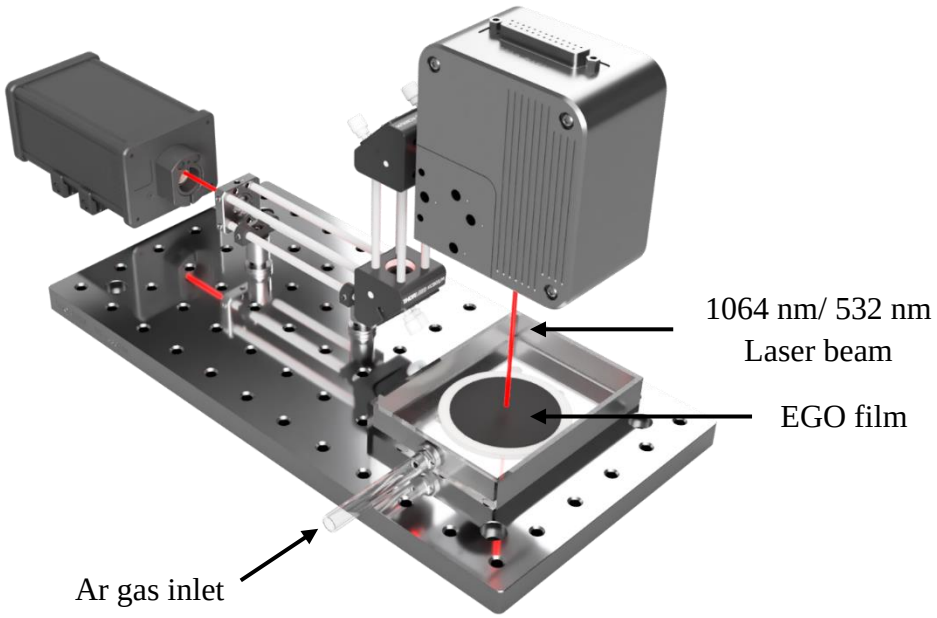

Figure 3-3 Schematic illustration of the fabrication of graphene supported single atom Pt composites.

Two laser sources were used to study the temperature dependent SAC synthesis and the electrolysis stability:

an infrared laser system of 1064 nm central wavelength (IPG Photonics, USA), 5 ns pulse width, 30 kHz repetition rate and average power 3-10 W was focused into the EGO film with a spot size of ~ 1 mm. an ultraviolet laser system (355 nm, 10 ps pulse duration, EdgeWave GmbH, Germany) with a pulse energy up to 54.4 μJ, a repetition rate of 404 kHz, a spot size of ~ 1 mm. A raster scanner with a line spacing of 0.5 mm, which equal to the radius of the laser spot, was scanned across the Pt-EGO film in a zigzag manner with a pattern dimension of 1 cm × 1 cm. The galvo head scanning speed of both lasers was set to 1000 mm/s.

The Pt-LrEGO were peeled off from the filtration membrane, the collected film samples were then sonicated in water, repeatedly washed (in deionized water, 3 times) and finally freeze-dried to obtain the catalyst powder for further electrochemical experiments.

3.3 Characterisation techniques

In the following sections, the mainly used characterization techniques, sample preparation methods and the instrumentation will be briefly described, including: scanning electron microscopy (SEM), transmission electron microscopy (TEM), X-ray diffraction (XRD), X-ray photoelectron spectroscopy (XPS), inductively coupled plasma optical emission spectroscopy (ICP-OES), Raman spectroscopy, ultraviolet-visible (UV-Vis) spectroscopy, electrochemical characterization methods.

3.3.1 Scanning electron microscopy (SEM)

SEM uses a focused electron beam with high energy to generate a variety of signals from the sample, which could provide surface topography, chemical composition and orientation of materials be analyzed. SEM is a powerful technique in terms of morphology observation for its high resolution and depth of field. High-resolution images are commonly contributed by secondary electrons (SEs) signal which generated from the inelastic electron-matter interactions. Furthermore, with the help of in-lens detector which located rotationally around the optical axis, low voltage and small working distances operation are possible. Owing to this feature, SEM in-lens detector could receive a direct SE1 signal from the sample with less background indirect SE signal and more surface details.

The sample morphologies were analyzed by using a high-resolution scanning electron microscope (Zeiss Sigma VP) equipped with a field emission gun (FEG), with acceleration voltage between 1-20 kV. The samples were drop-casted on a polished silicon wafer (thickness: ~ 500 µm, roughness: 2 nm, Agar Scientific) with a dimension of 5 × 5 mm, and dried under ambient condition. The silicon wafer was then sticked on a aluminum SEM stab using a carbon sticker. To reveal the surface morphologies, especially garphene based materials, the FEG-SEM was operated at 3 kV to decrease the interaction volume of samples. The topographic information was then obtained from the SE signal in in-lens mode.

3.3.2 Transmission electron microscopy (TEM)

TEM is a powerful technique which utilizes high energy electrons pass through the sample and form images and signals which contain morphology, crystallographic and chemical information

etc. of the sample. For conventional TEM, there are several features which allow this technique be widely used in NPs characterization[219]:

1. **High resolution**. In terms of resolution, a TEM image shares a similar concept with the visible light microscopy, which the Rayleigh criterion is adaptable:

$$\delta = 0.61\lambda/\mu sin\beta \quad (3\text{-}1)$$

   Where, δ, is the Rayleigh diffraction limit which indicates the smallest distance two resolvable points, λ, is the wavelength of radiation, μ, is the refractive index, and, β, is the semi-angle subtended at the object. Based on the Rayleigh criterion, the Rayleigh diffraction limit is proportional to the radiation wavelength. Furthermore, based on the Louis de Brogie's equation, the wavelength of an electron beam is inversely proportional to its energy. When a conventional TEM operates at 200 kV, which is 20 times higher than normal SEM operating condition, the resolution could reach 0.2 nm. Thus, nanomaterials' morphology could easily be observed through a TEM. Additionally, due to the interference of transmitted and scattered electrons, the information about materials crystallographic planes, shown as lattice fringes, could be observed in a high-resolution TEM (HRTEM) images. In a more advanced TEM system, lattice structural images could be resolved.
2. **Electron diffraction**. Electron diffraction patterns (DPs) provided by a TEM system give researchers crystallographic information of specimen. As the wavelength in a TEM system is much smaller then the lattice planes spacing, constructive interference of scattered electron beam occurs for the condition of the Bragg's law is fulfilled:

$$n\lambda = 2dsin\theta \quad (3\text{-}2)$$

   Where, n is an integer, λ, is the wavelength of electrons, d, is the lattice planes spacing, and θ is the beam incident angle. Admittedly, the Bragg's law gives only the mathematical description of electrons scattering in matters. But this useful equation establishes a relation between specimen crystallography and electron diffraction, which makes crystallographic analysis applicable in a TEM.
3. **Interaction of electrons with matter**. The interaction of electrons with matter within a TEM system is similar to the SEM where electrons interact elastically and inelastically with the matter and generate a variety of signals. Analytical techniques such as X-ray

energy-dispersive spectrometry (EDS) and electron energy-loss spectrometry (EELS) could be integrated into a TEM system, which enables chemical analysis in the TEM.

In present work, a LaB_6 crystal thermionic emission TEM, FEI Tecnai 20, was used for nanoparticles morphology and crystallography investigation. In practice, the synthesized colloidal/solution sample was ultrasonically dispersed in pure ethanol for 15min. After the ultrasonic dispersion, few drops of solution were placed on a holey carbon film covered 300 mesh copper grid (Agar Scientific). The sample deposited copper grid was dried in air ambient for 30min. TEM images were taken by FEI Tecnai 20 operated at 200 kV. Selective area diffraction patterns (SADPs) and fast Fourier transform (FFT) images were analyzed by using Digital micrograph (Gatan), and the results were compared with Powder Diffraction (PDF) database.

The HRTEM images, and EDS were carried out on a FEG S/TEM (FEI Talos F200X) operating at 200 kV equipped with a high-efficiency Super-X EDS detector system. Single atom samples were characterized through a spherical abberration corrected FEG S/TEM (FEI Titan G2 80-200) operating at 200 keV.

3.3.3 X-ray diffraction (XRD)

XRD is also a useful technique used to identify the crystal structure of the materials in a rapid and non-destructive manner. The crystal structure identification through XRD also obey the Bragg's law, as the wavelength of X-ray is minuscule (e.g. 1.78 Å, for Co anode). However, the scattering mechanisms are less complex than in TEM. When X-rays incident on the matter, the rays interact with the extranuclear electrons of matters and then be scattered.

In present work, the XRD analysis was carried out by using a Proto AXRD benchtop powder X-ray diffractometer with a Cu anode (λ = 1.5406 Å). For XRD analysis, several drops of solution was drop-casted on a zero background single-crystal silicon substrate, and dried in air ambient. The samples were scanned through a range of 2θ angle (5° to 90°) with a scan rate of 1 degree/min. The obtained diffraction patterns were then processed in Highscore analysis software for baseline subtraction and curve fitting, and finally compared with standard reference patterns given by the International Center for Diffraction Data (ICDD).

3.3.4 X-ray photoelectron spectroscopy (XPS)

XPS is a surface sensitive technique to characterise the elemental composition and reveal the chemical environment where the analyzed elements exist[220]. When the samples are irradiated

by X-ray with sufficient energy, electrons emit from the atom/ion of the sample via X-ray. The photoelectron emission process can be primarily categorized into two types: fluorescence process and Auger process (**Figure 3-4**). For fluorescence process, the electrons are excited and emitted directly from the inner orbitals of atoms. While the Auger electrons are generated in a three steps process. The inner shall electron is excited by the incident X-ray. Emission of the excited electron leaves a hole at its original orbit, and the hole is filled by an outer shell electron through relaxation. Energy releases during the relaxation process may convert into X-ray and subsequently excite other outer shell electron. The kinetic energy remains on the emitted electron (through fluorescence process) can be measured, which contains information of the element and the electron binding energy.

The binding energy of elements can be calculated according to the following equation:

$$E_{bin} = h\upsilon - E_{kin} - \Phi \tag{3-3}$$

Where, E_{bin}, is the binding energy of elements of interest, h, is the Planck's constant, υ, is the wavelength of the incident X-ray, E_{kin} is the kinetic energy of the emitted photoelectron, and, Φ, is the work function of the instrument.

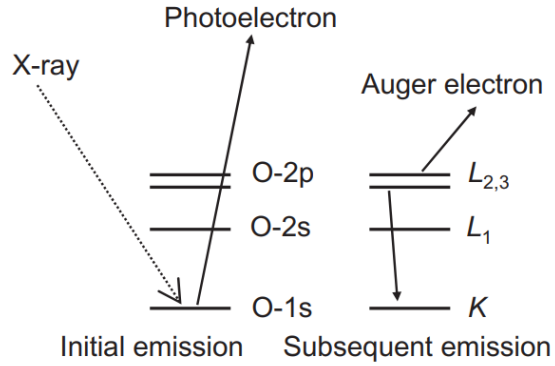

Figure 3-4 Schematic illustration of the photoelectron process (left) and Auger process (right)[220].

XPS was performed with a SPECS NAP-XPS system equiped with a monochromatic Al Kα X-ray source (1486.6 eV, 10 mA emission, 15 kV) and a charge neutraliser to remove the effects of differential charging. The samples were drop-casted on a clean silicon wafer (thickness: ~ 500 µm, roughness: 2 nm, Agar Scientific) with a dimension of 10 × 10 mm, followed by vacuum drying at room temperature. After sample preparation, the samples were stored in vacuum starge container (Labtech) (~ 15 mbar), and transferred to the instrument. The XPS spectra curve fittings were accomplished by CasaXPS software.

3.3.5 Inductively coupled plasma optical emission spectroscopy (ICP-OES)

ICP-OES is widely used in analysis the composition of elements in samples. This technique is suitable for solution samples. The solution to be analysed is pump through a nebulizer into a spray chamber. The sample aerosol is then mixed with argon gas and transferred into an argon plasma. Atoms within the aerosol are ionized and turned into plasma by a torch coil. And when the excited atoms return to ground state, specific rays irradiate and the photon wavelength corresponds to their respective elements. The plasma induced rays are then dispersed via combining prism and diffraction grating, and collected by a charge-coupled device (CCD) detector. Owing to the linear relationship between the elemental emission intensity and solution concentration, quantification of elements concentration can be accomplished using calibrated intensity – concentration plots. Solution with known concentrations that contain elements of interest is measured firstly to depict the calibration plot. The emission intensity of the analyte is then captured, and checked against the element's calibration plot to determine its concentration corresponding to the intensity[221].

To prepare the solution sample for ICP-OES characterization, nano-catalysts samples contain Pt and Ru with known total weight were digested in aqua regia (V_{HNO3} : V_{HCl} = 1:3, 1 ml) for 48 hours. The solution was then diluted to 10 ml and filtered through a syringe filter (PTFE, 0.2 μm) to separate the solution and solid residues (carbon based supporting materials, e.g. carbon black and graphene). To prepare standard solution, platinum stock solution (1000 μg/ml, SPEC CertiPrep) and ruthenium stock solution (1000 μg/ml, SPEC CertiPrep) were diluted to 5, 10, 20, 50, 100, 200 and 500 μg/ml. All samples were then analysed by using an Analytikjena PlasmaQuant 9000 Elite system.

3.3.6 Raman spectroscopy

Raman spectroscopy is a well-established technique for carbon materials characterization, which can probe the defects in carbon materials and their degree of graphitization in a rapid and non-destructive manner. Raman spectroscopy uses inelastic scattering of incident monochromatic photons by phonons (e.g. laser beam with wavelengths of 532 and 633 nm) which is sensitive to the structural and electronic properties of materials[222]. It can provide different kinds of information upon carbon materials such as doping, strain, defects, disorder and chemical functionalities etc.[222-224]

Raman spectroscopy was conducted using a Renishaw InVia Raman spectrometer equipped a 633 nm HeNe laser with 50x objective lens (spot size of 2 μm). Calibration was undertaken for the spectrometer using a silicon standard with a Raman band at 520 cm^{-1}. Raman spectra of samples were measured at Extended mode (1000 – 2000 cm^{-1}), acquisition time of 20 s, and a laser power of 10% (< 1 mW). The obtained Raman spectra were then analysed using Wire 4.2 software, with Lorentzian function fitting after baseline subtraction. The peak intensity ratio of Raman D band to G band (I_D/I_G) was obtained from the fitted peak intensities. And the full width at half-maximum (FWHM) of D and G bands was directly obtained from the curve fitting results.

3.3.7 Ultraviolet-Visible (UV-Vis) spectroscopy

Owing to the simplicity and efficiency, UV-Visible spectroscopy is a common technique be used in nanomaterials characterization. This technique is based on the interactions between radiation and matter, in the forms of absorbance, transmittance and scattering. In terms of absorption, it has been found that the concentration of the analyte directly relates to the amount of incoming radiation be absorbed, which is described by the Beer-Lambert's law:

$$Abs = \log_{10}(I_0/I_T) = \varepsilon lC \quad (3\text{-}4)$$

Where Abs is the absorbance, ε ($M^{-1}cm^{-1}$ or L/mol cm), is the coefficient of molar extinction, l, is the length of the light path in the solution, and, C (mol/L), is the concentration of the analyte. In many cases, the precise concentration value of an analyte is rather difficult to be measured through UV-Vis spectroscopy, as the molar extinction coefficient is unknown, and this law is not adaptable at high concentration. However, the change in concentration could be seen by comparing the intensity difference between several absorbance results. Furthermore, the stability of colloid can also be measured, as the decrease of absorbance of an analyte after a period reflects the decrease in stability.

For nanoparticles with well-defined absorption bands, such as Au, Ag and Pt which show SPR at a certain wavelength, the UV-Vis spectroscopy could give the absolute certainty of their presence. In addition, the specific SPR wavelength could shift slightly with particles size, which gives a macroscopic view of particle size variation. For dielectric particles, there's no distinct SPR peak could be observed in the absence of free electron electrons on the particle surface.

In present work, the UV-Vis spectra analysis was measured by using Specord® 250 from Analytikjena. The optical properties of colloidal samples were studied within the wavelength range from 200 to 800nm with a precision of 2nm. The solution was placed in a quartz cuvette

(QS100, Helma) with a light path length of 10mm. The UV-Vis spectra analysis was carried out immediately after PLAL process (within 10 min after sample preparation). Concentration-related results were further confirmed by observing the weight change of target materials before and after ablation, which measured by BL 210S analytical balance produced by Sartorius with the readability of 0.1mg.

3.3.8 Electrochemical characterization

This section describes the electrochemical measurements, the experimental setup used for catalysts testing is given, followed by electrochemical measurement techniques carried out in the studies.

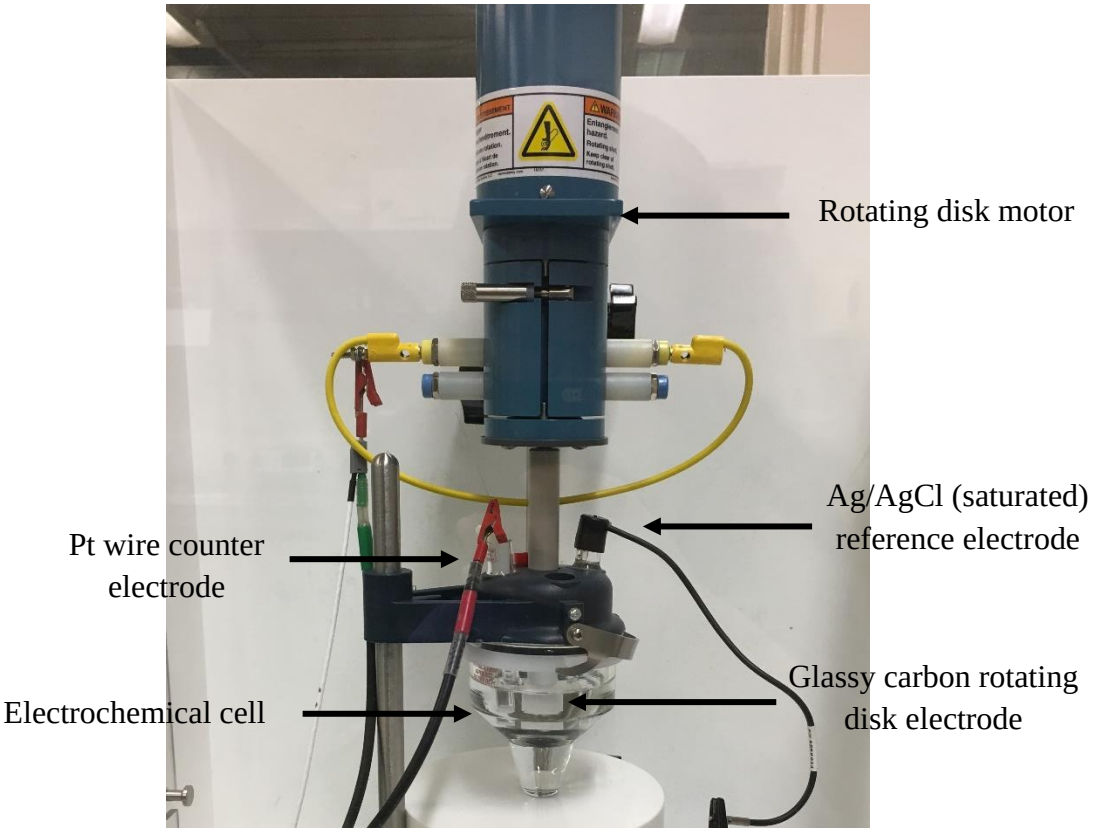

Figure 3-5 Photo of a three electrodes electrochemical cell with different components.

All experiments were conducted using a three-electrode cell (**Figure 3-5**) at room temperature. An Ag/AgCl (saturated KCl filling solution) was used as the reference electrode, a platinum wire was used as the counter electrode, and a glassy carbon rotating disk electrode (RDE, Pine research) with a diameter of 5 mm (0.196 cm^2) was used as the working electrode. The measured potential corresponding to the Ag/AgCl reference electrode was converted and versus the reverse hydrogen electrode (RHE) by using Nernst equation:

$$E_{RHE} = E_{Ag/AgCl} + 0.059\,pH + E^0_{Ag/AgCl} \quad (3\text{-}5)$$

Where E_{RHE} is the potential in RHE scale, $E_{Ag/AgCl}$ is the measured potential against the Ag/AgCl reference electrode, $E^0_{Ag/AgCl}$ = 0.197 at 25 °C.

Before electrochemical measurement, the glassy carbon electrode was polished with 0.05 µm alumina polishing liquid (BlueScientific) using a polishing cloth. The polished electrode was then ultrasonic cleaned in isopropanol and de-ionized water. All catalysts, if not specific noted, were weighted (5 mg) and mixed with 450 µl deionized water, 500 µl isopropanol, and 50 µl Nafion solution to a final catalyst concentration of 5 mg/ml. The as prepared catalysts ink was then ultrasonicated in an ice bath for 1 hour. After ultrasonication, 10 µl of well-mixed ink was drop-casted on the glassy carbon electrode, resulting in a total catalyst loading of 50 µg (255.1 µg/cm^2).

3.3.8.1 Cyclic voltammetry

Cyclic voltammetry (CV) is a potentiodynamic electrochemical measurement technique which can be used to probe the intermediates in a redox rection, the reversibility of a reaction, determine the electrochemical active surface area (ECSA) of catalysts and the capacity of both double layer capacitance and pseudocapacitance[225-226].

The Columbic charge of a surface redox reaction can be used to determine the ECSA of a platinum electrode/ Pt based catalyst via CV. A representative cyclic voltammogram of commercial Pt/C catalyst in 0.1 M $HClO_4$ is shown in **Figure 3-6**. The cyclic voltammogram can be categorized into three regions: the region of hydrogen adsorption/desorption (~0.05 – 0.4 V), the region of double layer capacitance (~0.4 – 0.6 V), and the region of oxygen adsorption/desorption (>0.6 V).

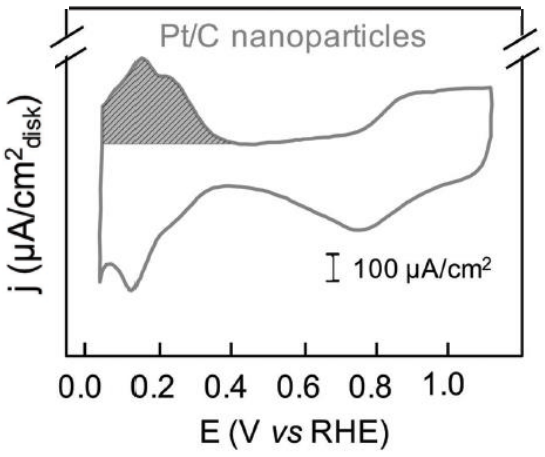

Figure 3-6 The cyclic voltammogram of hydrogen underpotential deposition region of a commercial Pt/C catalysts (46 wt.%, TKK) measured at 50 mV/s in N_2-saturated 0.1 M $HClO_4$ at room temperature[227].

The shaded area in **Figure 3-6** represents the desorption of submonolayer amounts of hydrogen atoms at the Pt based catalyst surface, which can be used to estimate the ECSA of the catalyst[227]. The ECSA can be estimated using the following equation:

$$ECSA\left(\frac{m_{Pt}^2}{g_{Pt}}\right) = \frac{Q}{\Gamma_{Pt} m_{Pt}} \tag{3-6}$$

Where Q is the charge necessary for releasing the adsorbed hydrogen atom at the catalyst surface, Γ_{Pt}, represents charge requires to oxidize a monolayer of H_2 on Pt surface (210 μC/cm^2), and m_{Pt} is Pt loading.

The ECSA in the following studies was quantified by integrating the coulombic charge of the hydrogen desorption region from a CV scan (-0.9 to 0.2 vs. Ag/AgCl) at a scan speed of 50 mV/s in N_2-saturated 0.1 M KOH electrolyte.

3.3.8.2 Rotating disk electrode

A rotating disk electrode spins at a controllable rate. When the electrode rotates, the bulk electrolyte is dragged to the spinning electrode surface, and then be flushed outward from the electrode center in a radial direction by centrifugal force. This electrode gives precise control of the diffusion layer at the electrode surface, and thus can provide a steady state mass-transport current[228].

For determining the Oxygen reduction reaction (ORR) activity, cathodic scan (-9 to 0.2 V vs Ag/AgCl) at a scan rate of 10 mV/s was carried out at varying rotating speed (400 to 2025 rpm) in the O_2-saturated KOH electrolyte. The number of electrons transferred (n) and the kinetic current density (J_k) were extracted by using the Koutechy-Levich (K-L) equation:

$$\frac{1}{J} = \frac{1}{B\omega^{1/2}} + \frac{1}{J_k} \tag{3-7}$$

$$B = 0.62nFC_0(D_0)^{2/3}\nu^{-1/6} \tag{3-8}$$

where J is the measured current density, ω is the angular velocity of the RDE, F is the Faraday constant (F = 96485 C mol^{-1}), C_0 is the bulk concentration of O_2 in 0.1 M KOH aqueous solution (C_0 = 1.2 × 10^{-6} mol cm^{-3}),[229] D_0 is the diffusion coefficient of O_2 in KOH solution (1.9 × 10^{-5} cm^2 s^{-1}),[230] ν is the kinematic viscosity of KOH (0.01 m^2 s^{-1}).[230] The number of electrons transferred (n) is found from the slope of the linear fit lines of the K-L equation, and the kinetic current density (J_k) is the current density-intercept of the fitted lines. The mass

activities of ORR were calculated by normalizing the measured current at given overpotential to the Pt mass loading.

3.3.8.3 Durability test

The durability of catalytic materials in certain electrochemical reactions can be evaluated through either chronopotentiometry or chronoamperometry. For chronopotentiometry, the transient current of the working electrode is recorded at a certain potential. And for chronoamperometry, the potential of the working electrode is set, and the resulting current is monitored as a function of time.

The durability of catalyst for ORR was evaluated by chronoamperometry in the following studies, and tested in O_2-saturated 0.1 M KOH electrolyte at 0.55 V vs RHE with a rotation speed of 1600 rpm to achieve the diffusion-limit current density. The durability performance was estimated by chronoamperometric test for 20000 s (~5.5 hours). For gas evolution reactions, e.g. hydrogen evolution reaction (HER) and oxygen evolution reaction (OER), chronopotentiometry was performed in N_2/O_2-saturated electrolyte at an absolute current density of 10 mA/cm^2 at a rotating speed of 2000 rpm to avoid bubble accumulation.

Chapter 4. UV Laser Assisted Pt Nanoparticles Size Refinement for Enhanced Oxygen Reduction Reaction

4.1 Chapter Introduction

The PLAL method demonstrates its feasibility in production of ligand-free NPs, versatility in a and wide range of materials synthesis. But the broad size distribution and relatively large particles size inhibit its functionalities. Especially, in catalysis applications, like ORR, a monodisperse ultrafine particles size is desired to maximize precious metal utilization, to enhance the catalytic activity and to guarantee the reproducible performance. Hence, this chapter is concerned with developing a second step UV laser refinement for PLAL synthesized Pt NPs and exploring the size tailoring mechanism, as well as the effect of size tailored Pt NPs ORR performance.

The as-prepared Pt NPs via PLAL were irradiated by a UV Excimer laser with varying laser fluence (0.5 to 1.1 J cm^{-2}) and processing time (0 to 20 min). It was found that effective particle refinement with an average size of 4.7 ± 0.3 nm can be achieved by 0.8 J cm^{-2} irradiation with a processing time of 10 min. The LPt NPs size tailoring through the 248 nm laser irradiation was simulated via Mie theory by considering the size-dependent absorption of the incident beam, heat accumulation and dissipation, and phase changes. The threshold fluence of Pt vaporization derived from the calculation is applicable to estimate the required laser energy for a target particles size. The size refinement of LPt NPs by the UV laser is attributed to selective surface vaporization. For the pristine LPt NPs with an average size of 24 ± 8.2 nm, the high absorption efficiency of UV radiation and relatively slow heat dissipation leads to a low vaporization threshold fluence, thus, its size can be effectively refined. While for the low energy absorption efficiency and fast heat loss of small Pt NPs, further size reduction of Pt NPs well below sub-5 nm will come at the cost of exponentially growing laser fluence. For catalytical application in ORR, the LPt NPs processed via 0.8 J cm^{-2} irradiation outperforms the commercially available Pt/C, which have a superior performance that is ~ 6 times and ~ 4.7 times higher in mass activity at 0.9 V and 0.85 V, respectively. The straightforward approach can potentially extend to a wide variety of NPs synthesis, and offer the nanomaterials with tuneable size and functionalities.

In this work, the thesis author conceived this study under the supervision of Dr. Zhu Liu, and the thesis author carried out materials fabrication (i.e. pristine Pt NPs, and laser refined Pt NPs),

TEM/XRD/ICP-OES/UV-Vis spectroscopy and zeta potential characterization and data analysis, Mie theory simulation, electrochemical measurements and wrote the paper. All authors contributed to the review of the manuscript. The original manuscript is presented in the following sections.

Paper: UV Laser Assisted Pt Nanoparticles Size Refinement for Enhanced Oxygen Reduction Reaction

Yudong Peng[1], Lin Li[2], Zhu Liu[1]

[1]: Department of Materials, School of Natural Sciences, University of Manchester, Oxford Road, Manchester, M13 9PL, UK

[2]: Laser Processing Research Centre, Department of Mechanical, Aerospace and Civil Engineering, Faculty of Science and Engineering, University of Manchester, Oxford Road, Manchester, M13 9PL, U.K.

KEYWORDS: Lasers, Monodisperse nanoparticles, Electrocatalysts, Fragmentation.

4.2 Abstract

Synthesis of ultrafine and uniformly dispersed Pt nanoparticles (NPs) are crucial and desired for achieving high catalytical activity and stable performance in various catalytic applications. Laser synthesis of nanomaterials demonstrates its advantages in catalytical applications for its versatility, simplicity and free of ligands coverage. However, the laser-based production of NPs suffers from broad size distribution, which inhibits its performance in catalysis. We demonstrate an effective size refinement strategy for the formation of monodispersed Pt NPs by selective vaporization of Pt particles using UV laser irradiation. Sub-5 nm Pt NPs with narrow size distribution was formed by fragmenting the pristine Pt colloids with an average size of 24 nm. Experimental data and theoretical simulation indicate that the selective vaporization mechanism relies on the applied laser fluence and Pt NPs size-dependent optical property and heat dissipation. When employed as an oxygen reduction reaction (ORR) catalyst, the refined Pt NPs exhibits excellent catalytic performance with an onset potential of 0.97 V and a mass activity of 0.83 $mA/\mu g_{Pt}$ at 0.85 V, which outperforms the commercial Pt/C catalysts. This work demonstrates an effective method for monodispersed Pt NPs fabrication. Additionally, the facile synthesis route can potentially apply to a wide variety of nanomaterials with tuneable size and functionalities.

4.3 Introduction

Accelerating the electrification of the automotive and aviation industries reflects the urgent need of coping climate and global energy challenges[67-68], and speeds up the development of renewable energy conversion, storage and utilization. Among the practical technologies, using hydrogen as a fuel demonstrates its importance in the increasing energy demands. Because, on the one hand, it shows as an alternative complement to the conventional fossil fuels with reducing carbon dioxide emissions[69]. On the other hand, hydrogen acts as an essential raw material for a wide variety of chemicals synthesis that used on a daily basis[70]. Within the hydrogen society, the proton exchange membrane fuel cell (PEMFC) plays a promising power source for various applications, e.g. vehicles, chargers and electronic devices, for its moderate working condition, high power density and efficient energy conversion[75, 231]. However, the cathode, where oxygen reduction reaction (ORR) takes place, becomes a short plank in PEMFC development for its sluggish reaction kinetics[75, 83]. To overcome the ORR barrier, noble metal catalysts, e.g. Pt, Pd and Ir *etc.*, are widely used for the unique electron configuration[83-84]. Yet, commercialization of precious metal catalysts still facing high cost and limited reserve[232]. Thus, an urgent pursue of precious metal catalysts with a high mass activity, and low fabrication cost promotes enormous interest in the field of catalysts development.

To increase the utilization Pt, several attempts were made by adding alloy elements[233-234], shape control (e.g. core-shell[235-236], facet engineering[237-238]) and reducing the Pt nanoparticle (NP) size[239]. Contemporary synthesis methods, e.g. chemical reduction[207-208] and solvothermal synthesis[209-210], use caping agents selectively adsorbed on Pt surface to modify the NPs shape and size. However, the capping agents[21] and CO containing precursors[212] can potentially block the Pt NPs surface and, hence, inhibits the exposure of the active site. As a result, extensive purification and cleaning required for removing the surface attached ligands prior to the catalytic applications. Recently, pulsed laser ablation in liquid (PLAL) for NPs production stands out as a promising physical approach for electrocatalysts synthesis. Briefly, the metal targets in a liquid environment (commonly use pure water) are ablated by focused laser beam, and the ejected species condense and dispersed in the liquid solvent. Owing to the chemical-free configuration, the synthesized NPs with bare surface exposure can be subsequently used as catalysts. Due to the high temperature and pressure triggered by the fierce laser-matter interaction, followed by a rapid cooling, defects (stacking faults[187], oxygen vacancies[214]) are preferentially found in the generated NPs. Remarkably boost in activity was found in the PLAL induced Ag NPs due to the modification of surface Ag coordination number

by stacking faults and internal strain created in the high temperature and pressure process[187]. Additionally, scaling up of NPs in PLAL was found to be straightforward, by varying the laser parameters, and using flow-through strategy, the optimized production of NPs can reach up to 4 g/h[215]. Therefore, the laser ablation method is desirable for catalysts production, and can potentially reach large scale production. To date, the synthesis of fuel cell catalysts via PLAL is still limited[215-216, 240]. Kohsakowski et al., successfully synthesized Pt NPs via PLAL and used as ORR catalysts, and demonstrated the mass production capability of the method in catalysts production. However, the electrochemical active surface area (ECSA) was found to be 50.8 m^2/g_{Pt}, which is lower than that of the commercial Pt/C catalysts. The drop in active site exposure may attribute to the large average Pt NPs size, and diverse size distribution. The morphology of broadened size distribution is commonly found in the direct ablated NPs in PLAL[216], which may attribute to the beam energy distribution that leads to several ablation mechanisms, including thermal vaporization, molten metal ejection[1]. Thus, there is plenty of room for improving the catalytical activity and performance stability through refining the particles size and size distribution.

Herein, we utilized an additional pulsed laser fragmentation (PLF) step to refine the Pt NPs size produced via PLAL. The PLF method has demonstrated its effectiveness in controlling Ag and Au NPs size by using a laser with a wavelength in the visible region[241-242]. Pt, on the other hand, with high melting and vaporization temperature and weak localized surface plasmonic resonance (LSPR) property is barely studied. Hence, the Pt NPs fragmentation was achieved by using a 248 nm (pulse width of 10 ns) Excimer laser (Lumonics IPEX-848, LightMachinery) with a spot size of 1.1 × 0.4 cm^2. Sub-5nm monodispersed Pt NPs was produced through PLF of the pristine PLAL synthesized Pt NPs with an average size of 24 nm and wide size distribution. To evaluate the ORR performance, the produced Pt NPs were deposited on carbon black, and then compared with the commercial reference. It was found out the refined Pt NPs exhibits boosted catalytic performance in ORR comparing with the original Pt NPs and the commercially available Pt/C catalyst.

4.4 Experiment Details

Preparation of the pristine LPt NPs

A Q-switched nanosecond Nd:YVO_4 solid-state laser (Violino Green, LNA Laser Technology) operating at the second harmonic mode, with a central wavelength of 532 nm (7 ns) was used to ablate a Pt target with 2.54 cm diameter and 1 mm thickness (99.99%, Good fellow). The polished target disk was placed at the bottom of an open vessel and immersed in de-ionized

water with a liquid height of 5 mm. To ablate the Pt target, the laser beam was focused on the target surface with a beam size of ~ 55 μm, and scanned in a spiral manner at 1000 mm/s, at pulse energy up to 400 μJ (~ 16.8 J/cm^2), a repetition rate of 25 kHz, a processing time of 10 min. The colloidal solution was collected for further analysis.

Particle size refinement via UV laser irradiation

To refine the size of poly-dispersed LPt NPs, a KrF pulsed excimer laser (Lumonics IPEX-848, LightMachinery) with a central wavelength of 248 nm (10 ns) was used. Briefly, 1 ml fresh as-prepared LPt colloidal solution (10 min after synthesis) was transferred into a quartz cuvette (100 – Macrocells, Hellma) with a light path of 10 mm and wavelength range from 200 to 2500 nm. The laser beam irradiating on the quartz cuvette horizontally has a beam size of 1.1 × 0.4 cm^2, a repetition rate of 10 Hz, and laser fluences of 0.5, 0.8 and 1.1 J/cm^2. To reveal the NPs size evolution at a given laser fluence, the processing time was set to 0.5, 1, 2, 5, 10 and 20 min. The refined Pt NPs were denoted as: LPt-500, LPt-800 and LPt-1100, respectively, correlate to the processing laser fluences. The resulting Pt colloid was collected for further analysis.

Characterization

The S/TEM images were captured on a FEI Talos F200X operating at 200 kV. For high-resolution HAADF-STEM imaging, a C_s-corrected FEI Titan G2 80-200 operating at 200 kV was used. The UV-Vis spectroscopy was performed by using a Specord 250 spectrophotometer (Analytikjena) within the wavelength range from 200 to 800 nm. The Pt colloid concentration was determined by Inductively Coupled Plasma Optical Emission Spectroscopy (ICP-OES) using a PlasmaQuant 9000 Elite system (Analytikjena). Zeta potential of the LPt NPs was carried out using Zetasizer 3000 HAS (Malvern) equipped with a 10 mW He-Ne laser (633 nm) operating at room temperature.

Electrochemical measurements

Catalysts were prepared by mixing 20 wt% of freshly made LPt/refined LPt NPs and 80 wt% carbon black (Vulcan 72, Cabot) in de-ionized water and isopropyl alcohol (v:v = 1:1) (99%, Aldrich), followed by ultrasonication in an ice bath for 1 hour and stirring overnight at room temperature. The loading of Pt content was confirmed by ICP-OES. The mixed solution was filtered and wash by de-ionized water 3 times through vacuum filtration, and then vacuum freeze-dried to obtain catalyst powder. The catalyst ink of both self-made catalysts and commercial 20 wt$_{Pt}$% Pt/C (HISPEC 3000, Alfa Aesar) was conducted by mixing the catalyst powder with de-ionized water, isopropyl alcohol and Nafion (5%, Aldrich) with a volume ratio

of 9:10:1, respectively, to a final concentration of 5 mg/ml. After ultrasonication in an ice bath for 1 hour, 2 µl homogeneous ink was deposited on the polished 5 mm glassy carbon rotation disk electrode (RDE) (Pine research) and dried in ambient.

The electrochemical measurements were conducted in N_2 and O_2 saturated 0.1 M KOH electrolyte in a typical three electrodes cell using a 636A electrode rotator (AMETEK) and a VersaSTAT4 potentiostat (AMETEK). A coiled Pt wire was used as the counter electrode, and an Ag/AgCl (saturated KCl solution) electrode was used as the reference. All potential was converted to the RHE by using the following equation: $E_{RHE} = E_{Ag/AgCl} + 0.197 + 0.059$ pH. The Ohmic losses within the system were compensated by applying *IR*-correction. ECSA was determined by integrating the coulombic charge of the hydrogen underpotential deposition region from cyclic voltammetry (CV) scans (-0.9 V to 0.2 V vs Ag/AgCl) at a scan speed of 50 mV/s in N_2 saturated electrolyte. The ORR activity was evaluated through linear sweep voltammetry (LSV) scan (from 0.2 V to -0.9 V vs Ag/AgCl) at 10 mV/s with a rotating speed from 400 to 2025 rpm.

4.5 Results and Discussion

4.5.1 Characterization of Laser Synthesized and Refined Pt NPs

We first prepared the laser-generated Pt (LPt) NPs through laser ablation of Pt target immersed in de-ionized water. The processing strategy of the pristine LPt NPs is illustrated in **Figure 4-1**. The laser beam at 532 nm (25 kHz and 7 ns) of an Nd:YVO_4 laser system (Lumonics IPEX-848, LightMachinery) were focused on a Pt target, and the laser fluence was set to ~ 16.8 J/cm^2 to maximize the production efficiency. The incident laser pulses immediately heat the Pt target immersed in water, and followed by a generated cavitation bubble on the surface contains ablated species. Owing to the Gaussian energy distribution of the incident laser beam, the ejected species contain ion/plasma and molten droplets depending on the spatial energy distribution[243]. Finally, the ablated matter quenched and condensed in the liquid forming nanoparticles after the cavitation bubble collapses[1, 102]. The transmission electron microscopy (TEM) image (**Figure 4-2 a**) of the consequent LPt NPs shows their spherical morphology and an average diameter of 24 nm with a relatively broad distribution of $\sigma = 8.2$.

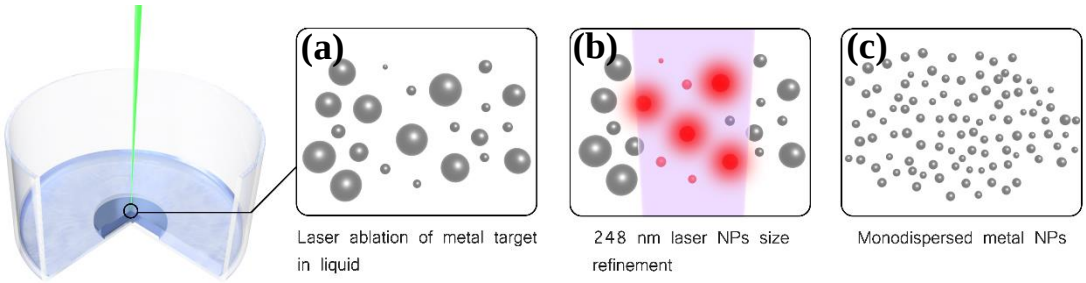

Figure 4-1. Schematic illustration of laser synthesizing route for monodispersed LPt NPs in liquid. (**a)** laser ablation of Pt target plate using 532 nm focused beam patterning in de-ionized water. (**b)** The prepared LPt NPs colloid was contained in a quartz cell and irradiated by a 248 nm laser beam (beam size: 1.1 × 0.4 cm^2) to refine the particle size. (**c)** Monodispersed LPt NPs dispersed in water, for further applications.

To tailor the size and to reduce the size dispersion of pristine LPt NPs, an excimer laser (248 nm, 10 ns) was chosen to reduce the particle size further. 1 ml pristine LPt colloidal solution with a concentration of ~ 152 µg/ml (quantified by ICP-OES) was transferred into a quartz cuvette (1 cm light path), and the UV laser was focused at the liquid centre horizontally with a spot size of 1.1 × 0.4 cm^2. Various laser fluences (0.5, 0.8, 1.1 J/cm^2) and processing time (0 to 20 min) were chosen to investigate the energy and time dependence of the process, respectively. As shown in **Figure 4-2 b**, compare with the pristine LPt NPs, the particles size of LPt-800 reduced dramatically and exhibited high size uniformity after 10 min irradiation. Despite the minor variation in particles size and size dispersion, the LPt-500, LPt-800, and LPt-1100 samples after 10 min irradiation (**Figure 4-2 c-e**) all reflect high monodispersity. Further structure details of the LPt-800 NPs were provided by selective area electron diffraction pattern (SADP) and high-resolution high-angle annular dark-field scanning transmission electron microscopy (HADDF-STEM) analysis. Distinctive diffraction rings observed through SADP analysis (**Figure 4-2 f**) confirms the high crystallinity of LPt-800 NPs, and the patterns attribute to the Pt (200), (111), (220) and (311) crystal planes of metallic Pt (ICDD No. 00-004-0802). A high-resolution HADDF-STEM image of LPt-800 (**Figure 4-2 g**) displays lattice spacings of 0.229 nm and 0.197 nm, which are indexed to the (111) and (200) planes of cubic Pt. The fast Fourier transform (FFT) image indicates the corresponding (111) and (200) planes with the viewing direction of [022] zone axis (**Figure 4-2 h**). Interestingly, the refined Pt NPs displayed a clear twin structure with a (111) twin interface. As the small particles that exhibit high order facets have higher internal energy and chemical potential, a coalescence of such small particles and clusters is preferential[244].

To investigate the transformation of mono-dispersed fine particles from the pristine LPt with relatively huge variation in size, we counted the size distribution analysis of the UV laser refined LPt at various laser fluences irradiation (0.5, 0.8 and 1.1 J/cm^2) for a range of processing

time (0 to 20 min). Statistics analysis of the particles size were conducted by TEM imaging of each sample by counting 1000 particles in random areas. The resulting histograms were then fitted with a log-normal function. As shown in **Figure 4-3 a and b**, the particle size distribution and the average size rapidly narrowed and decreased with increasing irradiation time, especially in the first 5 min. As the irradiation time prolongs, the variation in the size distribution of all samples was minimized, and the particles average diameter reaches a steady size of 9.3 nm (σ = 1.3), 4.7 nm (σ = 0.3) and 5.2 nm (σ = 1.3), corresponding to the 10 min laser irradiation with fluences of 0.5, 0.8 and 1.1 J/cm^2, respectively, which are significantly reduced compared with the pristine counterpart (24 nm, σ = 8.2). Interestingly, despite the efficient size reduction at 1.1 J/cm^2, the steady mean particle size hardly reduces further after irradiation at such high beam intensity, and the size dispersion expands slightly instead.

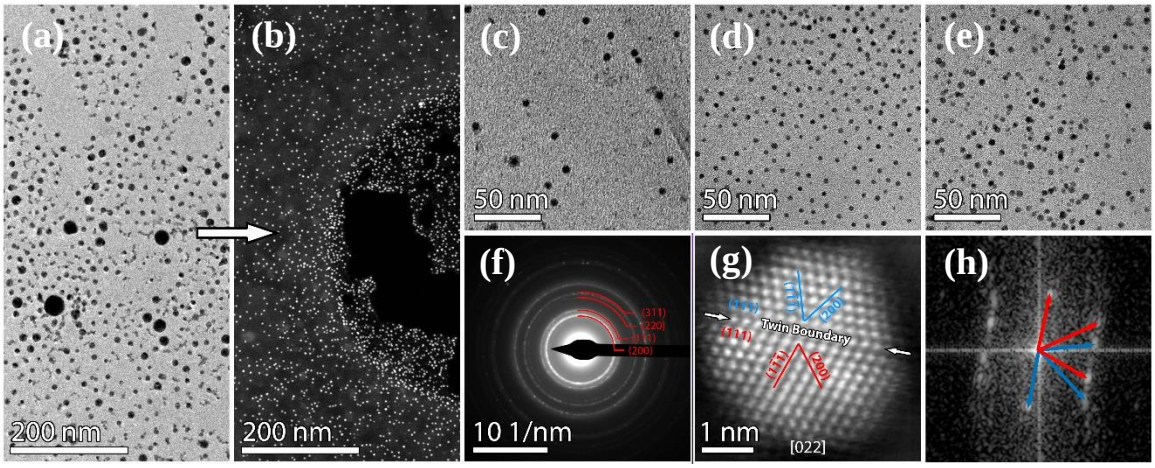

Figure 4-2. (**a**) TEM image of polydisperse pristine LPt prepared through laser ablation in de-ionized water and (**b**) the STEM image of the monodispersed LPt-800 refined by 248 nm laser irradiation at 0.8 J/cm^2 for 10 min. Representative TEM images of (**c**) LPt-500 NPs, (**d**) LPt-800 NPs and (**e**) LPt-1100 NPs. (**f**) SADP of LPt-800 NPs, and (**g**) representative HR-STEM image of LPt-800 particles viewed along [022] direction and (**h**) the FFT image.

After UV laser refinement, the colour of the colloidal solution changed from dark grey (pristine LPt) to a brownish colour. As the optical properties of particles with a given shape are size-dependent[34, 245], we carried out UV-Vis spectroscopy to sense the size variation before and after laser refinement. The UV-Vis extinction spectrum of the pristine LPt (**Figure 4-3 c**) shows a broad optical extinction peak and an extinction maximum located at a wavelength of 238 nm, which is assigned to the LSPR peak of Pt NPs that typically found from Pt colloid with an average size greater than 10 nm[246-247]. The evolution of the LSPR bands of the refined LPt NPs at various fluences after 10 min irradiation with the size changes is evidently shown in the optical extinction spectrum. In contrast to the pristine LPt NPs, the refined samples exhibit a blue shift of the extinction maximum, but no distinct LSPR peak was found in the range of 200

to 800 nm which shows the same trends in the previous optical studies of ultrafine Pt NPs dispersion[248-249]. Although the clear LSPR peak was not able to be identified, the outcome colloidal solution after fluences at 0.8 and 1.1 J/cm^2 shows similar magnitude absorbance in the wavelength range of 200 to 800 nm which is clearly lower than that of the LPt-500 and the pristine counterpart. The decrease in optical absorbance hints towards the reduction of extinction cross-section of the ultrafine Pt particles, which implies a smaller particles size was produced with enhanced laser fluence.

In order to verify the change of optical of LPt NPs against particles size, we calculated the extinction efficiency of LPt NPs via Lorenz-Mie theory[250]. **Figure 4-3 d** shows the calculated extinction efficiency of Pt NPs with various particles size. As shown in the figure, the LSPR peak gradually blue shifts from 244.2 to 231.1 nm with respect to the particles size due to the reduction in the electrons mean free path, which agrees with the trend in the extinction spectra. The broadened LSPR peak of the pristine LPt NPs in the UV-Vis spectrum is in part attributed to the polydispersity in size distribution, while the particle with a specific geometry was considered in the calculation. Additionally, the extinction efficiency declines with reducing particle size, which is in consonance with the experimental findings. It should be noted that the distinct LSPR band of Pt NPs was also predicted by Creighton *et al.* [249] and Henglein *et al.* [251] that near 200 nm. To date, however, experimental observation of ultrafine (< 10 nm) Pt LSPR band is rather rare[251-253]. Owing to the large imaginary part of the complex dielectric constant of Pt in the visible light wavelength, which significantly suppresses the LSPR in this range through the damping process[254]. Thus, unlike other noble metals possess strong absorption band in the visible range, *e.g.* silver and gold, the weak absorption band of Pt was predicted in the ultraviolet region. The featureless extinction spectrum of Pt NPs is considered as a consequence of the surface absorbates, such as citrate and poly (N-vinyl-2-pyrrolidone, PVP), which potentially alters the dielectric properties of Pt NPs[251, 253]. Despite the capping agent free environment for LPt synthesis, the surface oxidation of noble metal NPs through PLAL was widely reported[246, 255]. The oxidized layer of Pt has been proved to significantly effect on the dielectric constant[256], and hence may deviate the experimental value from the prediction.

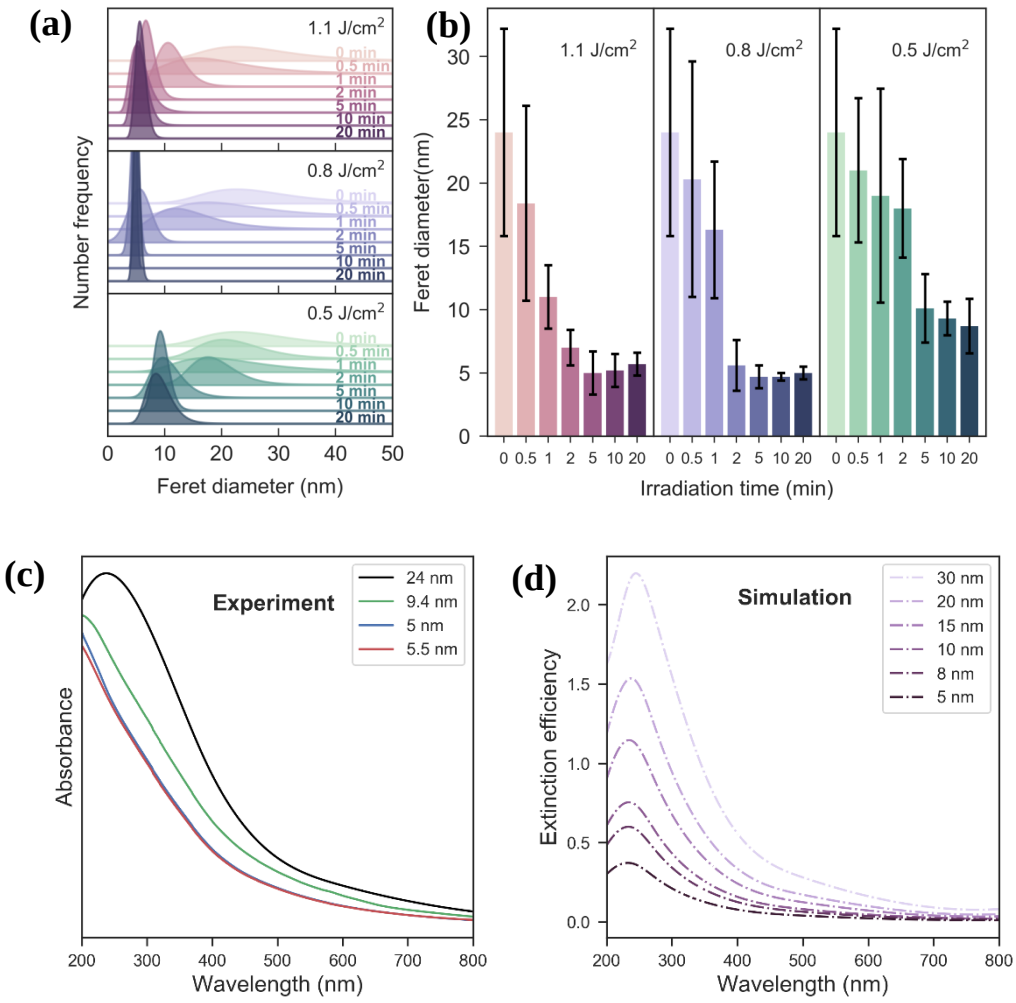

Figure 4-3. (**a**) Size distribution evolution of Pt NPs irradiated by 248 nm laser at fluences of 0.5 J/cm^2, 0.8 J/cm^2 and 1.1 J/cm^2, respectively, up to 20 min. (**b**) Variation of the Pt NPs the average Feret diameter and the size deviation as a function of laser irradiation time and laser fluences: 0.5, 0.8 and 1.1 J/cm^2. (**c**) UV-Vis extinction spectra of the pristine LPt NPs, and refined LPt after 10 min irradiation: LPt-500, LPt-800 and LPt-1100, respectively. (**d**) Calculated Pt NPs extinction efficiency in dependence of wavelength and particle diameter 5, 8, 10, 15, 20 and 30 nm.

4.5.2 Size Refinement Mechanism

The size refinement of the metallic NPs under laser irradiation is generally categorized by two dominating mechanisms depending on the laser pulse duration, i.e. photothermal vaporization and Coulomb explosion[1]. In the first scenario analogue to conventional metal heating, the metallic particles experience heating, melting and vaporization when the laser fluence exceeds a certain threshold. The later mechanism, ionization of metallic particles via charge repulsion fragments the original particles when the laser pulse width (in fs region) is much shorter than the electron-phonon coupling time. In our study, the refinement process should be dominated by photothermal phase changes, as the pulse width of the Excimer laser is 10 ns.

Heating of the LPt NPs ascribes to the proportion of received photon energy from the incident radiation. The energy that individual particle absorbed depends on the laser fluence (F), the wavelength (λ) and the absorption cross-section of the particles (C_{abs}). For spherical particles, the absorption cross-section at a given wavelength can be calculated by the following equation:

$$C_{abs} = \frac{\pi D^2 Q_{abs}}{4} \quad (4\text{-}1)$$

Where D is the particle diameter, and Q_{abs} if the dimensionless absorption efficiency calculated based on Mie theory[250] by using modified PyMieScatt[257] Python script. To extract the absorption efficiency of Pt NPs encapsulated in water, the complex refractive index of Pt was extracted from Werner's optical study on platinum[258], and the refractive index of surrounding water was considered to be 1.33. Calculated absorption efficiency of Pt with varying particle and incident beam wavelength is shown in **Figure 4-4 a**. The magnitude of absorption efficiency of Pt NPs shows a prominent feature in the UV region (200–300 nm) with a particle size range in 10-300 nm. Furthermore, the absorption efficiency decays with increasing incident beam wavelength and particle size. The absorption efficiency as a function of particle diameter and typical laser wavelengths (i.e. 248, 355, 532 and 1064 nm) is displayed in **Figure 4-4 b**. An evident elevation in absorption efficiency of Pt NPs (in a range of 1-150 nm) upon 248 nm laser irradiation was found, indicating high proportional laser energy can be deposited by Pt NPs under 248 nm irradiation. The difference in absorption cross-section of Pt NPs against particle diameter upon different wavelength irradiation is shown in **Figure 4-4 c**. It clearly shows the dependency of particle size and applied wavelength on the absorption cross-section. Notably, for Pt NPs size less than 20 nm, the absorption cross-section at 248 nm wavelength was found to be 3.0, 12.1 and 68.2 times higher than that of at wavelength of 355, 532 and 1064 nm, respectively.

The converted energy from an individual pulse by each particle can be described by the following relation:

$$E_{abs} = F C_{abs} \quad (4\text{-}2)$$

With a known amount of absorbed energy, the energy required for phase changes of the particle can be correlated to the materials enthalpy of melting and vaporization[259-260]. With the absorbed energy below the melting point, the particles only experience heating:

$$E_{abs} = m\left[\int_{T_0}^{T_m} C_p^S(T)dT\right] = m[\left(H_{T_m} - H_0\right) \quad (4\text{-}3)$$

When the absorbed energy exceeds the melting temperature, particle melting is expected:

$$E_{abs} = m\left[\int_{T_0}^{T_m} C_p^S(T)dT + \Delta H_m\right] = m\left[\left(H_{T_m} - H_0\right) + \Delta H_m\right] \quad (4\text{-}4)$$

Similarly, when the deposited energy surpasses the vaporization temperature, the particle will start boiling:

$$E_{abs} = m\left[\int_{T_0}^{T_m} C_p^S(T)dT + \Delta H_m + \int_{T_m}^{T_b} C_b^l(T)dT\right]$$

$$= m[(H_{Tm} - H_0) + \Delta H_m + (H_{Tb} - H_{Tm})] \quad (4\text{-}5)$$

Complete vaporization will occur when the converted energy reaches a certain threshold:

$$E_{abs} = m\left[\int_{T_0}^{T_m} C_p^S(T)dT + \Delta H_m + \int_{T_m}^{T_b} C_b^l(T)dT\right]$$

$$= m\left[(H_{Tm} - H_0) + \Delta H_m + (H_{Tb} - H_{Tm}) + \Delta H_{vp}\right] \quad (4\text{-}6)$$

Where m is the mass of Pt NPs, C_P^S and C_P^l are the heat capacitance of Pt in the solid and liquid state, T_0 is the ambient temperature, T_m and T_b are the melting and boiling temperature of Pt, ΔH_m and ΔH_{vp} are the enthalpy of melting and vaporization, (H_{Tm}-H_0) and (H_{Tb}- H_{Tm}) are the relative enthalpy of different states. Meanwhile, the heat dissipation through heat transfer between the heated particles and the solution medium was also considered and the heat. The heat loss term becomes pronounced with decreasing particle dimension, for the small particles have a high specific surface area that promotes the heat transfer with the liquid medium. We applied the MATLAB code provided by Metwally *et al.* [261] used in irradiation heating and cooling gold nanoparticles to analyse the temperature evolution of LPt under UV laser irradiation. The calculation was based on several assumptions: assume the optical characteristics of all particles are the same as the corresponding values of their bulk counterpart; all absorbed photon energy is converted into heat; and assume the properties of water remain constant with regards to the temperature. The physical constants used in the calculation are listed in **Table 4-1**. As the MATLAB script does not consider phase changes of metallic NPs, we converted the calculated temperature into unit enthalpy for better comparison and interpretation.

Table 4-1. Physical constants of water and platinum.

Physical constant	Value	reference
Density of platinum (kg/m^3)	21447	[262]
Density of water (kg/m^3)	1000	[263]
Thermal conductivity of platinum (W/m·K)	71.6	[262]
Thermal conductivity of water (W/m·K)	0.6	[263]
Thermal diffusivity of water (m^2/s)	0.1433*10^{-6}	[263]
Heat capacitance of platinum (J/K·kg)	21450	[262]
Heat capacitance of water (J/K·kg)	4180	[263]
Enthalpy of melting of platinum (KJ/mol)	19.65	[264]
Enthalpy of vaporization of platinum (KJ/mol)	492.33	[264]
H_{Tm}-H_{298} (KJ/mol)	53.216	[264]
H_{Tb}-H_{298} (KJ/mol)	145.87	[264]
Melting temperature of platinum (K)	2042	[264]
Boiling temperature of platinum (K)	4144	[264]

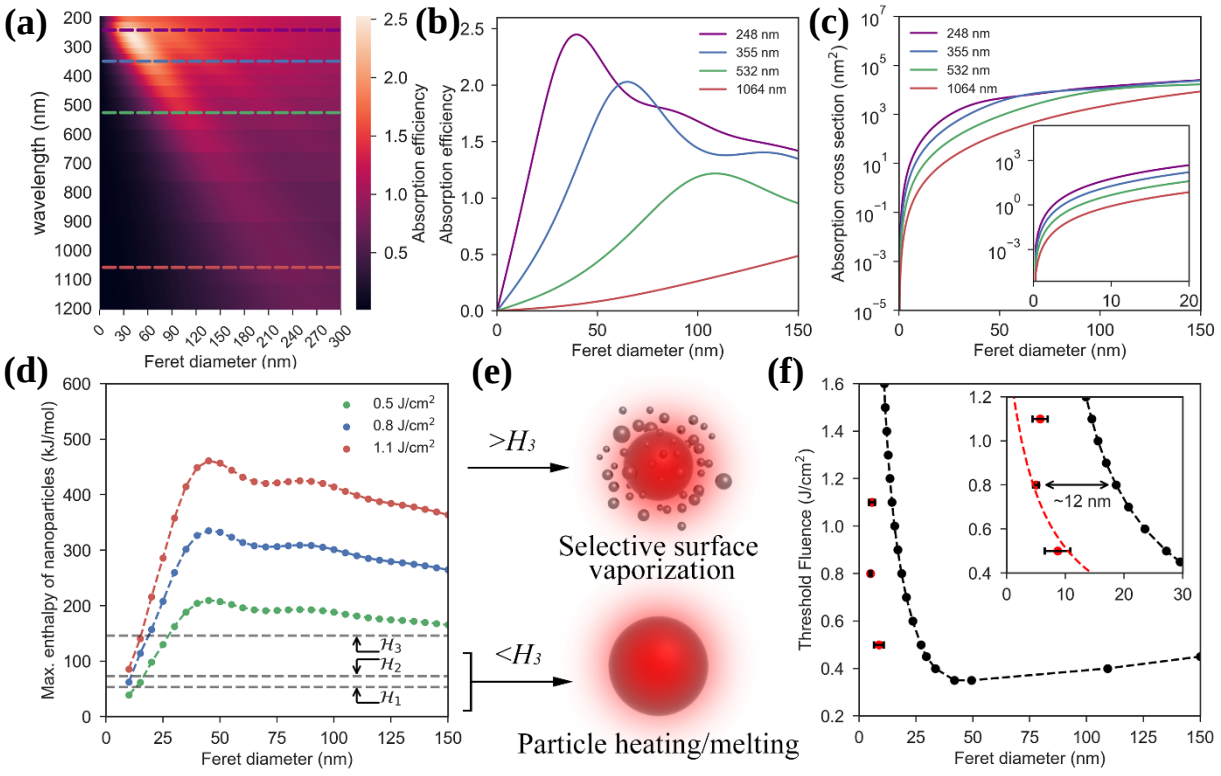

Figure 4-4. (**a**) Absorption efficiency as a function of irradiation wavelength and Feret diameters of spherical Pt NPs calculated using Mie theory, and (**b**) absorption efficiency of spherical Pt NPs at a typical laser wavelength of 248, 355, 532 and 1064 nm. (**c**) The absorption cross-section of Pt NPs with varying particle diameter. (**d**) Max enthalpy absorbed by Pt NPs after a single pulse laser irradiation (248 nm) at fluences of 0.5, 0.8 and 1.1 J/cm^2, (**e**) and the schematic illustration of particle refine mechanism. The H_1, H_2 and H_3 denote the enthalpy required to reach melting temperature, complete melting and start of boiling, respectively. (**f**) The threshold fluence of boiling for Pt NPs calculated by single-pulse irradiation (248 nm) as a function of spherical particle diameter, and the experimental particle diameter (red spot) of Pt NPs irradiated at 0.5, 0.8 and 1.1 J/cm^2 for 10 min.

Figure 4-4 d shows the calculated maximum unit enthalpy of LPt NPs as a function of particle diameters and applied laser fluences. The dotted horizontal lines represent the enthalpy required for phase changes which described in equation (3-5), namely, H_1 particle heating, H_2 particle melting and H_3 particle vaporization. Above the H_1 line, the LPt NPs start to melt, when the absorbed energy surpasses H_2 line, the LPt NPs melts completely, and when the deposited energy exceeds H_3 line, the boiling and surface vaporization of LPt NPs is expected (schematic is shown in **Figure 4-4 e**). The energy needed for complete vaporization of Pt NPs surpasses the calculated maximum unit enthalpy, thus, it is not included in the figure. A prominent peak was found in **Figure 4-4 d** for a particle diameter around 45 nm, which is independent to the incident laser fluence. When the particle size smaller than 45 nm, more heat loss occurs, and less energy absorbed by the LPt NPs results from the damping of the absorption cross-section. In the case of particles size larger than 45 nm, more energy is required for phase changes as the mass of the absorbers increases. For reducing LPt NPs size, the vaporization enthalpy, H_3, is the main criteria to estimate the laser fluence needed for vaporizing NPs. In **Figure 4-4 e**, the black dots represent the vaporization threshold fluence of varying particle diameters, which intersects with the H_3 line in **Figure 4-4 d**. Above the dashed line, surface vaporization of LPt NPs is expected, whereas particles may experience melting if the applied fluence is below the threshold. It is clear that the vaporization threshold increases exponentially with reducing particles size, showing a minimum fragmentation size of ~11 nm can be achieved through UV laser irradiation (at a laser fluence < 1.6 J/cm^2). We also plot the average size of LPt-500, LPt-800 and LPt-1100 NPs after 10 min processing time in the inset plot (shown in red dots). The experimentally derived particle size slightly deviates from the prediction line to a lower fluence value. The overestimation of the vaporization threshold may attribute to other effects that are not considered in the simulation, for examples: 1) a sudden elevation of temperature will cause a bubble formation at the particle-water interface, the bubble acts as a barrier that inhibits the heat dissipation from the heat source to the surrounding[265]. 2) the heat of melting and boiling of metallic NPs decrease compared with their bulk counterpart[266-267]. 3) heat accumulation during the repetitive laser pulse irradiation *etc*. As for the LPt-1100, the increase of average particle size and size dispersion may attribute to the fluctuations of the spatial pulse energy distribution and heat accumulation of the bulk solution, which may accelerate particle fusion and aggregation.

Despite the complexity of the phenomenon, the experiment derived particles size variation shows the same trend as the simulation. And the damping of absorption cross-section and fast heat dissipation of LPt NPs lead to a significantly increased threshold fluence, and inhibit

further size reduction of LPt NPs. Furthermore, the calculation provides a reasonable estimation for finely tuning the Pt particles size by controlling the laser fluence.

4.5.3 Electrocatalytic Performance

To make the catalyst for ORR, the obtained LPt NPs were mixed with carbon black (Vulcan72) to a final catalyst loading of 20 wt_{Pt}%. ORR performance of the refined LPt catalysts was tested in O_2/N_2 saturated 0.1 M KOH electrolyte. For comparison, the pristine LPt and the commercially available Pt/C (20 wt%, HISPEC 3000) were examined under the same experimental condition. The ECSA for the catalysts were determined by integrating the hydrogen adsorption and desorption peaks in a N_2 saturated electrolyte (**Figure 4-5 a**). The ECSA of the LPt-800 was found to be 90.1 m^2/g_{Pt} based on the cyclic voltammetry (CV), which is significantly higher than that of the commercial Pt/C catalysts (ECSA: 74.6 m^2/g_{Pt}). Meanwhile, the ECSAs of the pristine LPt, LPt-500 and LPt-1100 was calculated to be 31.8 m^2/g_{Pt}, 59.4 m^2/g_{Pt} and 80.8 m^2/g_{Pt} respectively, indicating the increased geometric surface area and unified size dispersion benefit the absorption of hydroxyl species on the Pt surface. The catalysts activity in ORR was further analysis through linear sweep voltammetry (LSV) at 1600 rpm, as shown in **Figure 4-4 b**. The LSV curves of all samples show a typical kinetic-diffusion mixed region from 0.6 – 1.0 V versus a reversible hydrogen electrode (RHE), and a clear diffusion-limiting current plateau in the potential range of 0.3 – 0.6 V. Both the onset potential and halfwave potential for the catalysts exhibit a positive shift with the following order: pristine LPt, LPt-500, LPt-1100, commercial Pt/C and LPt-800, with the highest onset potential of 0.97 V (vs RHE) and the halfwave potential of 0.85 V (vs RHE) for LPt-800 catalysts. Furthermore, the diffusion-limiting plateau potential region for the LPt-800 catalysts is wider, suggesting the kinetic current drops slower with increasing potential. The kinetic current was calculated from the LSV curves through the Koutechy-Levich equation, using the measured current and the diffusion-limited current at 0.65 to 0.9 V (vs RHE) (**Figure 4-5 c**). Tafel plot in **Figure 4-5 d** shows the kinetic current of LPt-800 and commercial Pt/C, which reveals a comparable slope of 79.8 mV/dec for LPt-800 and 79.1 mV/dec for Pt/C. Additionally, the calculated average electron transfer number of LPt-800 (**Figure 4-5 e**) via Koutechy-Levich relation was found to be 4.1, suggesting a direct four-electron process was achieved for reducing oxygen to water in alkaline electrolyte. The mass-specific current density, which represents the intrinsic activity of the catalyst and the precious metal utilization was calculated by normalizing the kinetic current to the Pt loading on the electrode. As shown in **Figure 4-5 d**, LPt-800 exhibits a mass activity of 0.28 $mA/\mu g_{Pt}$ at 0.9 V and 0.83 $mA/\mu g_{Pt}$ at 0.85 V, which are ~ 6 times (0.05 $mA/\mu g_{Pt}$

at 0.9 V) and ~ 4.7 (0.18 mA/μg_{Pt} at 0.85 V) times greater than that of the commercial Pt/C catalysts.

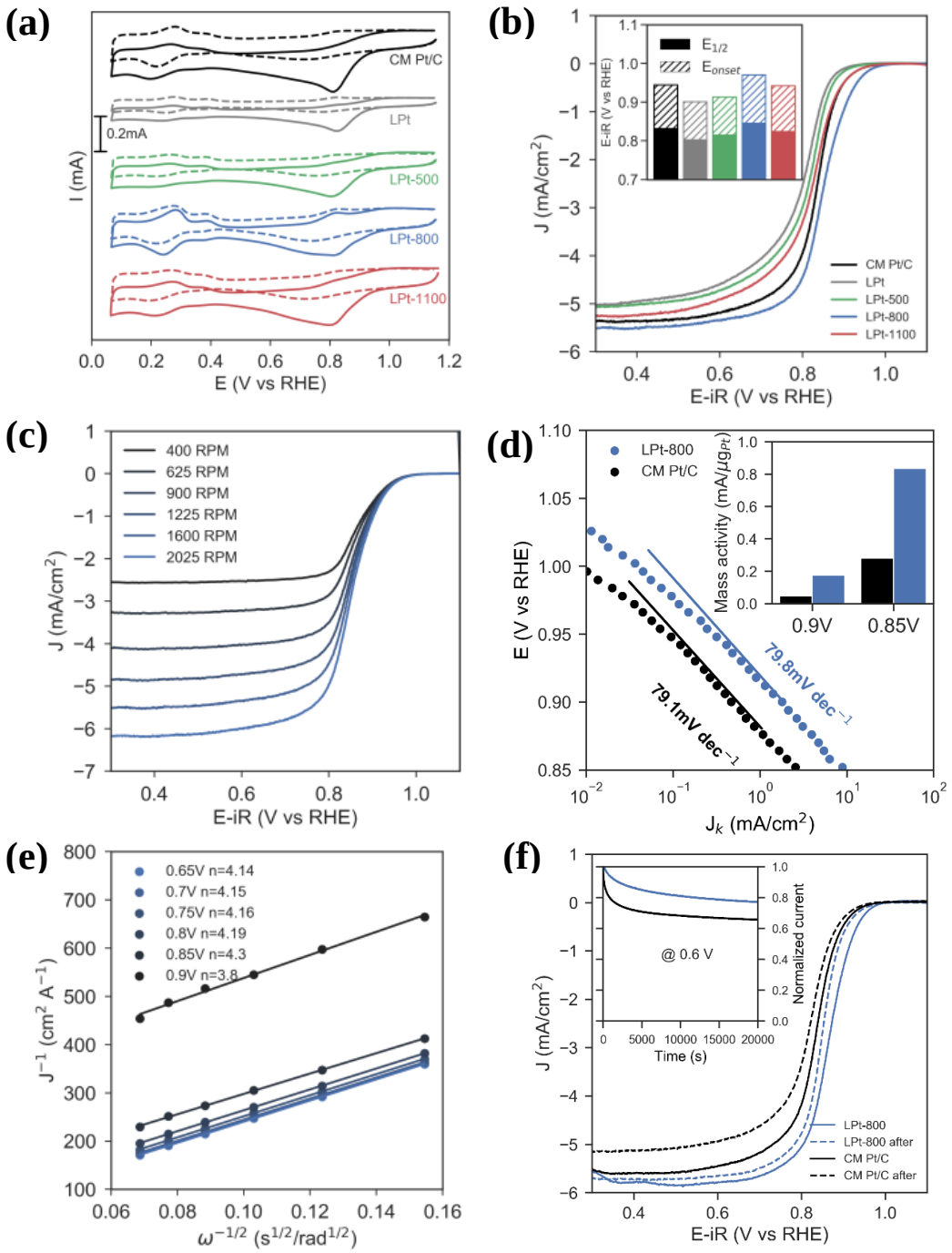

Figure 4-5. (**a**) Cyclic voltammograms of CM Pt/C, LPt, LPt-500, LPt-800 and LPt-1100 measured via RDE in N_2/O_2-saturated 0.1 M KOH. (**b**) Comparison of LSVs of CM Pt/C, pristine LPt, LPt-500, LPt-800 and LPt-1100, respectively, the inset shows the comparison of the onset potential. (**c**) Linear sweep voltammetry of LPt-800 at different rotation speed from 400 to 2025 rpm at a scan rate of 10 mV/s in O_2-saturated 0.1 M KOH electrolyte. (**d**) Comparison of Tafel plot, and mass activity of CM Pt/C and LPt-800 at 0.9 and 0.85 V (vs RHE). (**e**) The Koutechy-Levich plot of LPt-800 and calculated electron transfer number. (**f**) the LSVs before and after ORR 20000 s chronoamperometric test of CM Pt/C and LPt-800 at 0.6 V (vs RHE) in O_2-saturated 0.1 M KOH, inset shows the ORR current-time chronoamperometric responses.

The greatly enhanced ORR activity of LPt-800 in contrast to the commercial Pt/C catalyst may attribute to the high ECSA of LPt-800 catalyst. TEM imaging was performed to reveal the morphology of the commercial Pt/C catalyst (**Figure 4-6 a-c**), which shows an average size of 4.9 nm (σ = 1.2). Despite the similar average size of Pt/C to LPt-800 (**Figure 4-6 d**), the commercial Pt/C displays a broader size distribution which could potentially decrease the exposed Pt area and thus the ECSA. On the other hand, the reference Pt/C appears in a spheroid shape with random facets exposure. While the dominating (111) and (100) facets of LPt-800 possess weaker oxygen binding energy among other low index faces could benefit the ORR performance[268-269].

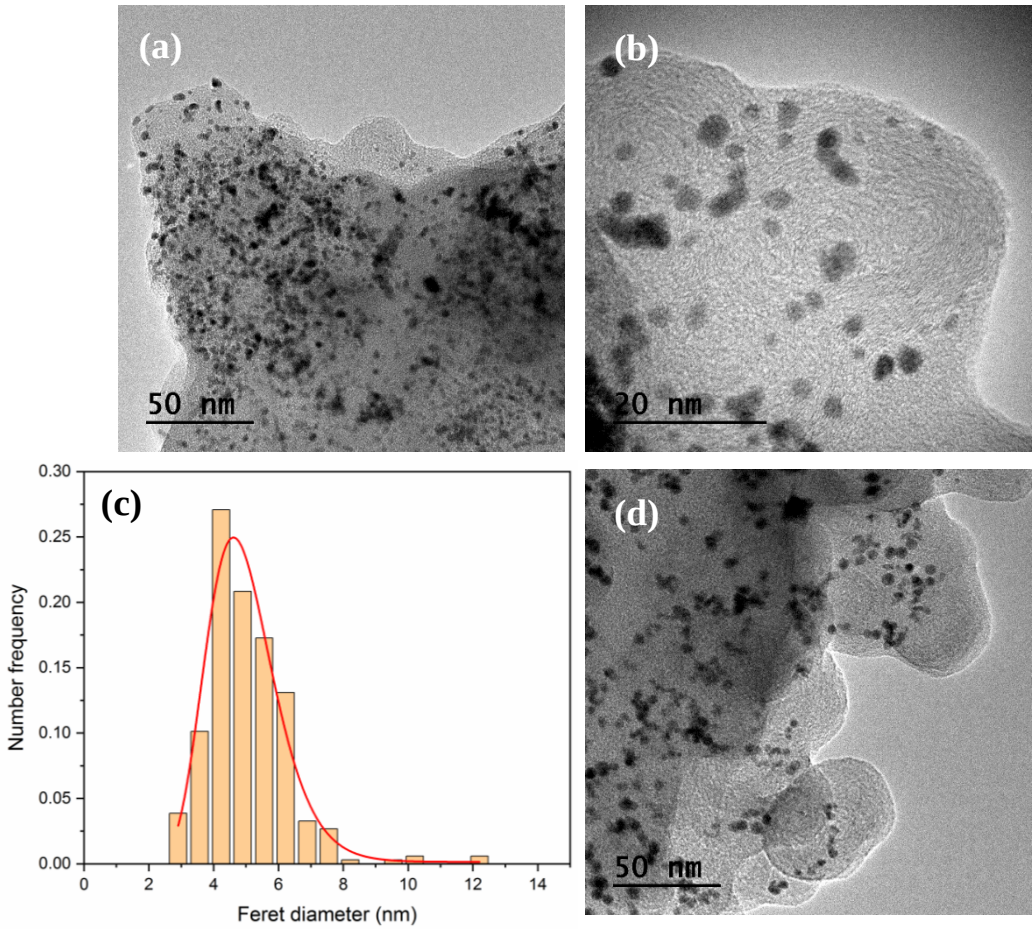

Figure 4-6. (**a**) and (**b**) Representative TEM images of commercial Pt/C (20wt_{Pt}%), and (**c**) the size distribution of Pt/C catalyst was given by counting 673 particles from TEM images in random area, the histogram was fitted with a log-normal function (with an average diameter of 4.9 and standard deviation of 1.2). (**d**) The TEM image of LPt-800 catalyst.

The long-term durability of the LPt-800 catalyst and Pt/C were evaluated in O_2-saturated 0.1 M KOH electrolyte at 1600 rpm through chronoamperometry by holding the potential at 0.6 V (vs RHE) where the diffusion-limited current was achieved. After 20000 seconds (~ 5.5 hours) test, the commercial Pt/C catalyst showed degradation in onset potential (~ 11 mV) and half-wave

potential (~ 12 mV), while the onset and halfwave potential of LPt-800 dropped by 15 mV and 20 mV, respectively (**Figure 4-5 f**). Despite the similar degradation in catalysts activity, the drop in diffusion-limiting current density for the commercial Pt/C catalyst was quite severe (~0.46 mA/cm^2). In sharp contrast, the degradation of LPt-800 in the plateau current density is negligible (~ 0.087 mA/cm^2). Moreover, the LPt-800 catalyst retains 78% of its current density after ~5.5 h chronoamperometry test, while the commercial Pt/C dropped to 66%. The results suggest that LPt-800 possesses higher durability in ORR than that of the commercial Pt/C. Previous Pt/C ORR stability studies indicate the degradation of catalysts stability can be categorized in following reasons: 1) growth of Pt NPs via Ostwald ripening and coalescence, 2) detachment of Pt NPs, 3) dissolution of Pt particles and 4) corrosion of carbon substrate[270-272]. The ECSA of both LPt-800 and commercial Pt/C catalysts decreased after the durability test, with a loss of 13.7 % and 37.9 %, respectively (**Figure 4-7 a and b**). TEM images (**Figure 4-7 c and d**) of the LPt-800 after durability test shows particle aggregation and coalescence via particles migration. The growth of the Pt NPs, therefore, caused the decay of activity, which reflects in the decrease of onset and half-wave potential. However, the significant drop in the diffusion-limiting current density and ECSA for the commercial Pt/C implies the significant loss of active sites and Pt loading[273]. The enhanced stability of the LPt-800, on the one hand, might be attributed to the nanoparticle-support interaction. We carried out zeta potential measurement of the freshly produced LPt NPs dispersed in water, which shows the particles were negatively charged with a potential of -38 mV. The Vulcan 72 carbon black is positively charged in neutral water, and the potential was found to be 29 mV, which is in agreement with the literature[274-275]. Thus, the formed LPt NPs were likely to be absorbed on the carbon black support through electrostatic interaction. On the other hand, the dissolution rate of Pt particles in a smaller size is expected to be higher[270], which hints towards that the stability could be potentially increased by reducing the particles size dispersion. In this case, the commercial Pt/C catalyst with a relatively larger size dispersion (σ = 1.2) is more likely to leach out in the reaction. In contrast, the monodispersed LPt-800 catalyst (σ = 0.3) is expected to have a slower dissolution rate.

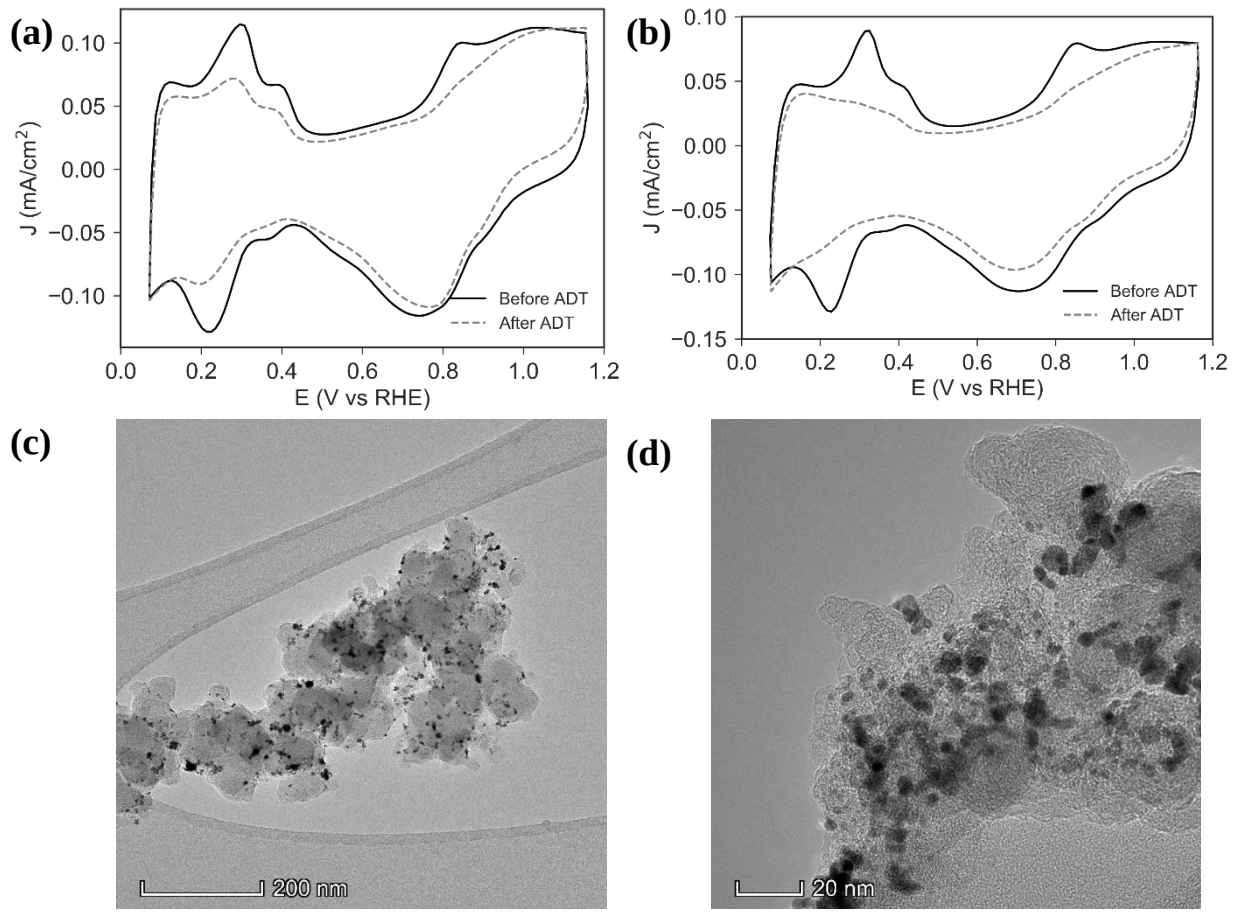

Figure 4-7. CV curves for (**a**) LPt-800 and (**b**) commercial Pt/C catalysts before and after 20000 s chronoamperometry test. (**c**) and (**d**) TEM images of LPt-800 catalysts after 20000 s chronoamperometry test show particle aggregation.

4.6 Conclusion

In conclusion, we developed a facile and free of chemical reagent physical approach for mono-dispersed Pt NPs synthesis. The LPt NPs synthesized through PLAL with an average particles size of 24 nm with a broad size distribution can be further refined by UV laser irradiation. The resulting LPt-800 NPs shows good crystallinity and a significant reduction in size with an average diameter of 4.7 nm and narrow size distribution. For Pt NPs with a LSPR band in the UV region, the use of a 248 nm laser irradiation shows superiority in photon energy absorption by Pt. The mechanism of size refinement of Pt NPs through ns UV laser irradiation follows the metal heating-melting-vaporization model, and a prediction of the vaporization threshold fluence of Pt NPs was provided. Based on the simulation, the average particle size is tuneable by varying the incident laser fluence. However, a limited particle size of ~5 nm was found experimentally with a laser fluence below 1.1 J/cm^2, for the damping of the absorption cross-section and fast heat dissipation of small Pt NPs. For catalytical application in ORR, the LPt-800 catalyst outperforms the commercially available Pt/C, which have a superior performance

that is ~ 6 times and ~ 4.7 times higher in mass activity at 0.9 V and 0.85 V, respectively. And benefit by the mono-dispersity in the particle size and strong electrostatic interaction with the carbon support, the LPt-800 catalyst retains 78% of its current after ~5.5 h durability test and surpasses the commercial Pt/C. Additionally, the straightforward approach can potentially extend to a wide variety of NPs synthesis, and offer the nanomaterials with tuneable size and functionalities.

Chapter 5. Laser Assisted Solution Synthesis of High Performance Graphene Supported Electrocatalysts

5.1 Chapter Introduction

As shown in the previous chapter, a UV laser is a powerful tool to tailor the NPs size even the original NPs have a broad size distribution. These are Attributed to the size-dependent optical properties and heat dissipation rate of NPs in a liquid medium, monodispersed LPt NPs can be produced and exhibit promising catalytic activity and durability in ORR. However, for the low energy absorption efficiency and fast heat loss of small Pt NPs, further size reduction of Pt NPs well below sub-5 nm will come at the cost of exponentially growing laser fluence. Thus, we developed a solution-based synthesis method for NPs decorated graphene composites fabrication. Uniformly distributed Pt and RuO_2 NPs were found on the graphene substrate, with particles size well below sub-5 nm.

This chapter describes a photodeposition method triggered by a UV Excimer laser irradiation on graphene oxide (GO). Many studies in the literature detail the photodeposition of heterogeneous NPs on semiconducting substrates, using light source range from UV to IR. The semiconducting GO has been demonstrated previously as a potential substrate for photodeposition. The simultaneous reduction of GO via photo-excited electrons leads to a single-step synthesis of metal (oxide) NP-functionalized graphene materials. However, the conventional GO produced using chemical approaches is heavily oxidized and defective (> 30 at% oxygen), causing issues including incomplete reduction and photo-degradation. In addition, the approaches previously reported produced particles with relatively large sizes (> 5 nm), which is possibly due to the restricted nucleation rate as the photon energy of used laser (< 3.49 eV) is smaller than the bandgap of heavily oxidized GO (~ 4 eV). To date, there is no report regarding the use of photo deposited NPs on GO/rGO as electrocatalysts.

In this study, we report a UV laser-assisted, continuous, solution route for the simultaneous reduction and modification of GO with ultrafine catalytic NPs. Electrochemical graphene oxide (EGO) prepared using a newly developed approach was used as the starting material due to its low degree of oxidation, which imparts structural integrity and an ability to withstand photo-degradation. Simply by illuminating a stream of EGO and metal salts precursor solutions using a laser beam with a wavelength of 248 nm (4.99 eV), produced extensively reduced EGO (rEGO) flakes, which were modified by uniformly distributed Pt (~ 2 nm) or RuO_2 (~ 2.8 nm)

NPs. The high laser photon energy and fluence correspond to a high current density increase supersaturation of metal precursor on the EGO flakes, resulting in a high heterogeneous nucleation rate and reducing the critical cluster size. Moreover, the RuO_2-rEGO catalyst exhibits superior activity for the oxygen evolution reaction, requiring a small overpotential of 225 mV to reach 10 mA cm^{-2} current density. The Pt-rEGO catalyst shows significantly enhanced mass activity for the hydrogen evolution reaction together with comparable performance for oxygen reduction reaction compared with the commercial 20% Pt/C catalyst. This simple method was further applied to deposit PtPd alloy and MnO_x nanoparticles on the rEGO support, demonstrating its versatility in synthesizing functional nanoparticle-modified graphene materials. These graphene-based functional materials could be used for diverse applications beyond electrochemical energy storage and conversion, such as photocatalytic materials, biomedicine and biotechnology.

In this work, the thesis author conceived this study under the supervision of Dr. Zhu Liu, and carried out materials fabrication, XRD/SEM/TEM/XPS/ICP-OES/UV-Vis/Raman spectroscopy characterization and data analysis, electrochemical measurements and wrote the paper. Dr. Jianyun Cao contributed extensive discussions on problem-solving, and carried out EGO synthesis and Raman spectroscopy characterization. Mr. Jie Yang and Ms. Wenji Yang carried out BET/TGA characterization and analysis of the results. All authors contributed to discussions and manuscript review. The results of this project have been published on Advanced Functional Materials (doi: 10.1002/adfm.202001756). The original manuscript is presented in the following sections.

Paper: Laser Assisted Solution Synthesis of High Performance graphene supported Electrocatalysts

Yudong Peng, Jianyun Cao, Jie Yang, Wenji Yang, Chao Zhang, Xiaohong Li, Robert A.W. Dryfe, Lin Li, Ian A. Kinloch*, Zhu Liu**

Y. Peng, Dr. J. Cao, W. Yang, C. Zhang, Prof. I. A. Kinloch, Dr. Z. Liu

Department of Materials, School of Natural Sciences, University of Manchester, Oxford Road, Manchester, M13 9PL, U.K.

E-mail: jianyun.cao@manchester.ac.uk; ian.kinloch@manchester.ac.uk; zhu.liu@manchester.ac.uk

J. Yang, Prof. R.A.W. Dryfe

Department of Chemistry, School of Natural Sciences, University of Manchester, Oxford Road, Manchester, M13 9PL, U.K.

Dr. J. Cao, J. Yang, Prof. R.A.W. Dryfe, Prof. I. A. Kinloch

National Graphene Institute, University of Manchester, Oxford Road, Manchester, M13 9PL, U.K.

Prof. X. Li

Renewable Energy Group, College of Engineering, Mathematics and Physical Sciences, University of Exeter, Penryn Campus, Cornwall TR10 9FE, U.K.

Prof. L. Li

Laser Processing Research Centre, Department of Mechanical, Aerospace and Civil Engineering, Faculty of Science and Engineering, University of Manchester, Oxford Road, Manchester, M13 9PL, U.K.

Keywords: laser; photodeposition; graphene oxide; nanoparticles; electrocatalysts

5.2 Abstract

Simple, yet versatile, methods to functionalize graphene flakes with metal (oxide) nanoparticles are in demand, particularly for the development of advanced catalysts. Herein, based on light-induced electrochemistry, we report a laser-assisted, continuous, solution route for the simultaneous reduction and modification of graphene oxide with catalytic nanoparticles. Electrochemical graphene oxide (EGO) was used as starting material and electron-hole pair source due to its low degree of oxidation, which imparts structural integrity and an ability to withstand photo-degradation. Simply illuminating a solution stream containing EGO and metal salt (e.g. H_2PtCl_6 or $RuCl_3$) with a 248 nm wavelength laser produced reduced EGO (rEGO, oxygen content 4.0 at.%) flakes, decorated with Pt (~2.0 nm) or RuO_2 (~2.8 nm) nanoparticles. The RuO_2-rEGO flakes exhibited superior catalytic activity for the oxygen evolution reaction, requiring a small overpotential of 225 mV to reach a current density of 10 mA cm^{-2}. The Pt-rEGO flakes (10.2 wt.% of Pt) shows enhanced mass activity for the hydrogen evolution reaction, and similar performance for oxygen reduction reaction compared to a commercial 20 wt.% Pt/C catalyst. This simple production method was also used to deposit PtPd alloy and MnO_x nanoparticles on rEGO, demonstrating its versatility in synthesizing functional nanoparticle-modified graphene materials.

5.3 Introduction

The urgent need for sustainable and clean energy to reduce the usage of traditional fossil fuels has promoted enormous interest in the field of energy storage and conversion.[276] The use of hydrogen as an intermediate for energy storage and power generation has been considered as one of the most promising alternatives to the current non-renewable fossil fuels. Within the hydrogen economy, molecular hydrogen links power grids to other energy sectors through a zero-emission electrochemical pathway.[277-278] In detail, the pathway is the generation of hydrogen as well as oxygen via electrochemical water splitting by the hydrogen evolution reaction (HER) and oxygen evolution reaction (OER) at the generator and then the consumption of hydrogen using a fuel cell system, in which the oxygen reduction reaction (ORR) and hydrogen oxidation reactions convert hydrogen directly into electricity. However, the sluggish kinetics of these electrochemical energy conversion reactions limits seriously the wide application of hydrogen energy.[279] The development of high-performance electrocatalysts, which can reach a designated current density under minimum overpotential, is desirable for maximizing the hydrogen production and utilization efficiency. To-date, platinum group metals and their oxides remain the state-of-the-art catalysts for electrochemical energy conversion.[277] To reduce the cost of electrocatalysts, carbon nanomaterials (e.g. carbon black, carbon nanotubes, graphene, etc.) are widely used as supports for the platinum group metal (oxide) nanoparticles.

Due to its high electrical conductivity and large specific surface area, the two-dimensional (2D) single atom thick graphene has been considered as a promising supporting material for developing advanced electrocatalysts.[280] Compared with the hydrophobic pristine graphene flakes, graphene oxide (GO) with oxygen groups and thus aqueous solution processability has become a more versatile starting material for loading/supporting functional nanoparticles, including electrocatalyst nanoparticles.[281] In the last decade, various methods have been developed to deposit nanoparticles onto the surface of graphene/GO/reduced GO (rGO) flakes, including wet chemical deposition,[282-285] electrochemical deposition,[286-287] and plasma-assisted synthesis,[288] etc. However, several of these techniques require elevated temperatures, harsh chemicals, or high voltage bias. A robust and versatile method which is able to synthesis various types of ultrafine nanoparticles on the surface of graphene in a single-step is still desired.

The use of laser technology to prepare nanomaterials has recently attracted increasing attention due to its simple and fast merits.[217, 289-294] Methods including laser ablation in liquid (PLAL),

[289-290] laser pyrolysis,[217, 291, 294-295] and photodeposition[296-298] have been demonstrated for the synthesis of either carbon-supported or unsupported nanoparticles for the applications in electrochemical energy storage and conversion. Briefly, in laser ablation in liquid, nanoparticles are formed by the rapid cooling of a plasma plume compromised of elements from the solid ablation targets and the surrounding liquid;[289-290] while in laser pyrolysis, the laser-induced carbonization/graphitization of a precursor (e.g. polyimide) and/or decomposition of metal salt precursor leads to the formation of nanoparticles modified graphene/nanocarbon materials.[217, 291, 294-295] Different from the photothermal mechanism of both the laser ablation in liquid and laser pyrolysis, which requires focused and intense laser beam, photodeposition is based on mild light-induced electrochemistry.

Photodeposition of metal (oxide) nanoparticles on the surfaces of semiconductors (metal oxides or sulfides) has been thoroughly studied in the past few decades as indicated in a review paper published recently.[299] Photodeposition is driven by light-induced electron transfer, it occurs simply via illumination of dispersions of semiconductor particles in aqueous solutions containing metal salt precursors.[299] The photoexcitation of semiconductor creates electron-hole pairs, which reduce/oxidize the adsorbed metal ions into metal/metal oxide; the insoluble metal/metal oxide heterogeneously nucleates and grows on the semiconductor substrate.[299-300] In spite of the numerous interests in photodeposition of nanoparticles on the surfaces of metal oxides and sulfides semiconductors, only a few works have studied GO,[296-298] which also behaves as a semiconductor with tuneable bandgap values depending on the content and type of oxygen groups.[301-303] Additionally, the sizes of the photodeposited nanoparticles on rGO reported in these pioneering works using lasers with wavelengths of 355 and 532 nm are relatively large (> 5 nm) and not uniformly distributed.[296-298] To date, there is no report regarding the use of photo deposited nanoparticles on GO/rGO as electrocatalysts. One of the possible reasons for the absence of reports on the use of GO for photodeposition is the simultaneous reduction and degradation of GO when exposed to laser irradiation. The reduction of GO by the photon-excited electrons,[299, 304-305] is accompanied by the undesired oxidative GO degradation by photo-generated holes.[305-306] This generally leads to a partial reduction or even degradation of the GO flakes,[305-307] particularly for the heavily oxidized GO with a large amount of oxygen groups (oxygen composition ≥ 30 at.%).[306] In addition, the existence of electron scavenging metal ions (e.g. Pd^{2+}) during the photodeposition of metal nanoparticles could further impede the full reduction of GO.[298]

A very recent discovery suggests that the use of mildly oxidized, oxygen functionalized graphene as starting material leads to highly reduced high-quality graphene flakes via an ultraviolet (UV) light-induced reduction.[305] Compared with the conventional chemical GO (CGO) produced by Hummers' method, the oxygen functionalized graphene has lower oxygen content and a less disrupted graphene honeycomb lattice structure.[308-309] Electrochemical GO (EGO), produced using a scalable, low-cost and environmentally friendly electrochemical oxidation, has a similar structure with oxygen functionalized graphene with a low content of oxygen groups (~20 at.%), especially the unrestorable C=O and −COO− groups.[310] It has been proved that the reduction of EGO via chemical approaches (e.g. hydrazine) can lead to a higher degree of graphene lattice restoration compared to that can be achieved using CGO.[310] In addition, the photo-degradation of carbon lattice of GO is reported to be dependent on the oxidation level/oxygen content, with a more severe degradation for GO has higher oxygen content.[306] Therefore, the higher structural stability and narrower bandgap of EGO due to the lower oxygen content compared with CGO could potentially allow a rapid and full reduction using lasers with high photon energy and fluence (i.e. laser energy density in mJ cm^{-2}) without causing significant degradation of the carbon lattice. Meanwhile, the use of laser beam with higher photon energy and fluence benefits the generation of electron-hole pairs via a one-photon process, the abundant electrons/holes would potentially lead to a high nucleation rate for the metal/metal oxide particles and thus small particle size.

Herein, in this work, we report a UV (248 nm) laser-induced continuous solution-phase strategy for simultaneous reduction and modification of EGO with uniformly distributed ultrafine catalyst nanoparticles. In a typical experiment (**Figure 5-1 and Figure 5-2**), the aqueous precursor solution of metal salt (e.g. H_2PtCl_6, $RuCl_3$, etc.) and EGO was circulated continuously from a bulk solution tank to a quartz cell reactor, on which a UV laser (KrF excimer; wavelength: 248 nm; pulse width: 10 ns; repetition rate: 100 Hz; photon energy: 4.99 eV) with a beam size of 1.1×0.4 cm^2 and irradiates at various laser fluences. This laser-induced solution approach leads to deeply reduced EGO (rEGO) flakes with a low oxygen content of 4.0 at.% and a partial restoration of the graphene lattice structure evidenced by Raman spectroscopy. The as-formed Pt and RuO_2 nanoparticles distribute uniformly on the rEGO flakes, with ultrafine average diameters of 2.0 nm ($\sigma = 0.5$) and 2.8 nm ($\sigma = 0.6$), respectively. When used as electrocatalysts, the RuO_2-rEGO exhibits superior activity for the OER, with a small overpotential of 225 mV at a current density of 10 mA cm^{-2}, outperforming the majority of the reported Ru based electrocatalysts. In comparison with the commercial (CM) Pt/C catalyst (Pt loading: 20 wt.%; HISPEC 3000; Johnson Matthey), the as-synthesized Pt-rEGO catalyst with

a Pt loading of 10.2 wt.% shows significantly enhanced mass activity for HER, together with a comparable performance for ORR. This simple, scalable and straightforward method has been further applied to the synthesis of other metal (oxide) nanoparticles supported on rEGO flakes, including PtPd alloy and MnO_x, demonstrating its versatility in the production of functional nanoparticle modified graphene materials.

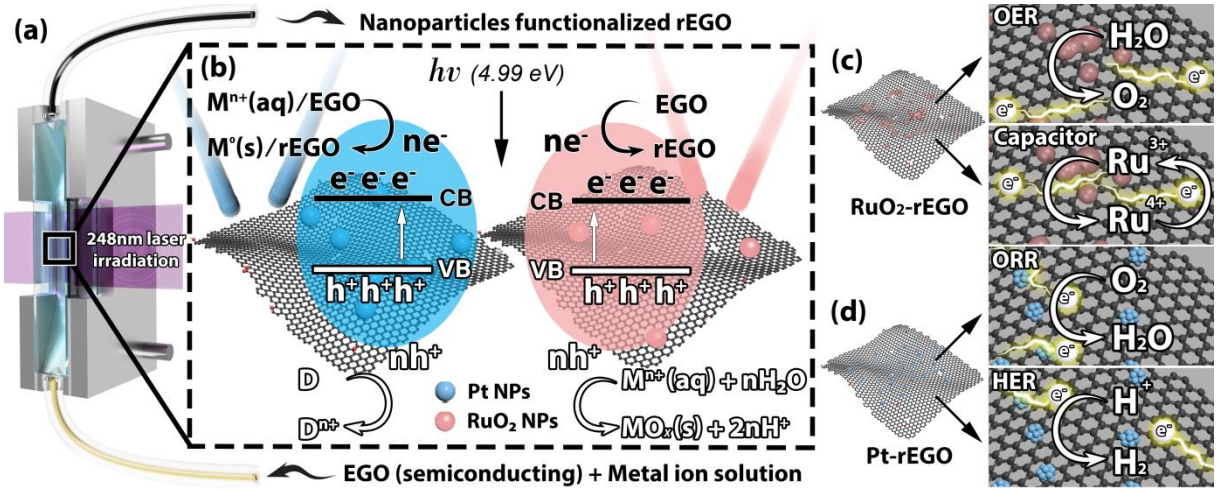

Figure 5-1. Schematic illustration of the laser-assisted synthetic route for rEGO supported nanoparticles. (**a**) The precursor solution of EGO and metal salts (e.g. $RuCl_3$, H_2PtCl_6 etc.) is circulated through the quartz cell reactor, which is irradiated by a 248 nm laser beam (photon energy: 4.99 eV; beam size: 1.1 × 0.4 cm^2). (**b**) The photoexcitation of the semiconducting EGO creates electron-hole pairs, which reduce/oxidize the metal ions (M^{n+}) into metal/metal oxide; the metal/metal oxide nucleates and grows on the EGO substrate as nanoparticles; simultaneously, the EGO is reduced by photo-generated electrons to rEGO; Pt (left) and RuO_2 (right) nanoparticles (NPs) are shown as examples for the reductive and oxidative photodeposition, respectively; the photo-generated holes for reductive photodeposition are consumed by sacrificial electron donor (D). (**c**) and (**d**) The as-synthesized graphene supported RuO_2 and Pt nanoparticles, respectively, are used for electrochemical energy storage and conversion.

5.4 Experiment Details

Materials

Electrochemical graphene oxide (EGO) was prepared using the method reported elsewhere.[310] Chemical graphene oxide (CGO) was prepared using Hummers' method according to the literature.[311-312] Chloroplatinic acid hydrate ($H_2PtCl_6 \cdot xH_2O$, 99.995%), ruthenium(III) chloride hydrate ($RuCl_3 \cdot xH_2O$, 99.98%), sodium tetrachloroplalladate(II) (Na_2PdCl_4, 99.99%), manganese(II) chloride tetrahydrate ($MnCl_2 \cdot 4H_2O$, 99.0%), isopropanol (99%), acetone (99.5%), Nafion (5 wt% in lower alphatic alcohols and water), Potassium hydroxide solution (KOH, 0.1 M and 1.0 M), sulfuric acid (H_2SO_4, 95.5-98.0%), were purchased from Sigma Aldrich. ICP standard solution: platinum (1000 μg ml^{-1}), ruthenium (1000 μg ml^{-1}), were purchased from SPEX CertiPrep. All reagents and chemicals were used as received without

further purification. Commercially available 20 wt% Pt/C (CM Pt/C, Hispec 3000) and RuO_2 anhydrous (CM RuO_2, Premion, 99.95%, Ru 75.2% min) were purchased from Alfa Aesar as reference materials.

Preparation of rEGO composites

The EGO solution was diluted with de-ionized water (15 MΩ cm) to a concentration of 0.1 mg ml^{-1}, and mixed with metal salt (i.e. H_2PtCl_6, $RuCl_3$, Na_2PdCl_4, $MnCl_2$, 50 $\mu g_{metal\ ion}$ ml^{-1}). To accelerate the photoreduction of GO by suppressing the combination of electron-hole pair, small amounts of isopropanol and acetone were added into the solution ($m_{isoporpanol}$:$m_{acetone}$:m_{water} = 2:1:100). The addition of isopropanol and acetone as the hole and electron scavenger, respectively, could form reactive radical species which benefit the reduction of GO.[305]

The mixed solution was purged with Ar gas, stirred vigorously and pumped into a flow cell (with a light path of 1 cm) through a peristaltic tubing pump (FH15, Fisher Scientific) with a volumetric flow rate of 100 ml min^{-1} (**Figure 5-2**). A KrF pulsed excimer laser (Lumonics IPEX-848, LightMachinery) with a wavelength of 248 nm, a pulse width of 10 ns irradiated at the flowing solution. The laser beam (beam size: 1.1 × 0.4 cm^2) irradiating on the liquid channel was operated at a repetition rate of 100 Hz. The laser energy was set to 100, 150, 200, 250 and 300 mJ, which gives laser fluences of 227, 340, 454, 568 and 681 mJ cm^{-2}. The 100 ml solution flowed through the quartz cell with 30 min processing time to ensure the solution was evenly processed. The as-prepared solution was then collected, washed (in water, 3 times) and freeze-dried to obtain the rEGO nanoparticles composites.

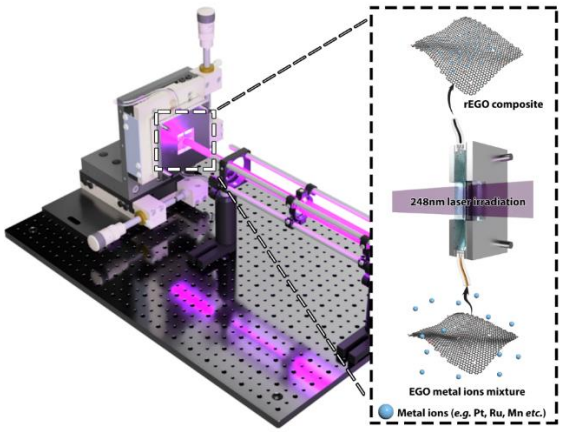

Figure 5-2. Experimental setups for sample preparation. The raw beam with a rectangular shape (L: 1.1 cm, W: 0.4 cm) irradiates on the flow cell, which covers the quartz window with 1 cm light path. The solution was pumped from the bottom of the flow cell and left the cell from the top with a volumetric flow rate of 100 mL min^{-1}.

Materials characterization

The morphologies of the rEGO nanocomposites were captured by scanning electron microscopy (SEM) performed on a field emission Zeiss Sigma VP SEM operating at 3 kV in in-lens mode. The high-resolution transmission electron microscopy (HRTEM) images, and energy dispersive X-ray spectroscopy (EDS) were carried out on a field emission FEI Talos F200X S/TEM operating at 200 kV equipped with a high-efficiency Super-X EDS detector system. The crystalline structures were determined through X-ray diffractometer (XRD) by using a Proto AXRD benchtop powder X-ray diffractometer with a Cu anode (λ = 1.5406 Å) operating at 30 kV. X-ray photoelectron spectroscopy (XPS) was performed with a SPECS NAP-XPS system; the XPS spectra were corrected with respect to the C 1s peak at 284.8 eV and fitted by CasaXPS software. The mass of metal content within the rEGO nanocomposites were determined through inductively coupled plasma optical emission spectrometry (ICP-OES), all samples were weighed and digested in aqua regia for two days, and then diluted and filtered with a PTFE membrane filter. All samples were analysed by using an Analytikjena PlasmaQuant 9000 Elite system. Raman spectroscopy analysis was carried on a Renishaw InVia Raman spectrometer, with a laser wavelength of 633 nm and a laser spot size of 2 μm; curve fitting of the recorded Raman spectra was conducted using Wire 4.2 software with Lorentzian functions after baseline subtraction. The peak intensity ratio of Raman D band to G band (I_D/I_G) for EGO and rEGO was obtained from the fitted peak intensities. The full width at half-maximum (FWHM; Γ) of D and G bands was directly obtained from the curve fitting results. UV-Vis absorption spectra were measured through a Thermo Scientific Evolution 201 spectrophotometer. The pH values of precursor solutions were measured using a pH meter (HI-9813-5 pH/EC/TDS/°C Portable Meter, Hanna Instruments) at room temperature. Nitrogen physisorption analysis at 77 K was carried out on Micromeritics TriStar II Plus. The specific surface area was estimated by using the Brunauer-Emmett-Teller (BET) model.

Electrochemical experiments

Electrochemical measurements were performed using a potentiostat (VersaSTAT4 Potentiostat Galvanostat, AMETEK) and an electrode rotator (636A Electrode Rotator, AMETEK). All experiments were conducted using a three-electrode cell at room temperature. An Ag/AgCl (saturated KCl filling solution) was used as the reference electrode, a platinum wire was used as the counter electrode. All composites catalysts were drop-cast on a glassy carbon rotating disk electrode (RDE, Pine research) with a diameter of 5 mm (0.196 cm^2), the coated RDE was

used as the working electrode. The RDE was polished on a microfiber polishing cloth with a small volume of 0.05 μm alumina slurry until mirror finish prior to all experiments. To prepare the catalyst ink, 5 mg catalyst was mixed with 450 μL deionized water, 500 μL isopropanol (99%, Aldrich), and 50 μL Nafion (5 wt% in lower alphatic alcohols and water, Aldrich) to a final catalyst concentration of 5 mg mL^{-1}.[230, 313] The catalyst ink was ultrasonicated in an ice bath for 1 hour. For the OER, HER and capacitance measurements, 10 μL of well-mixed ink was drop-cast on the glassy carbon electrode, resulting in a total catalyst loading of 50 μg (255.1 μg cm^{-2}). For the ORR measurement, 2 μL of the ink (10 μg, 51 μg cm^{-2}) was deposited on the glassy carbon electrode, as the rational evaluation of ORR performance highly depends on the film thickness and quality.[227, 273]

The measured potential corresponding to the Ag/AgCl reference electrode was converted and versus the reverse hydrogen electrode (RHE) by using the Nernst equation:

$$E_{RHE} = E_{Ag/AgCl} + 0.059\,pH + E^{0}_{Ag/AgCl} \qquad (5\text{-}1)$$

Where E_{RHE} is the potential in RHE scale, $E_{Ag/AgCl}$ is the measured potential against the Ag/AgCl reference electrode, $E^{0}_{Ag/AgCl}$ = 0.197 V at 25 °C.

The OER performance of the catalysts was measured in an O_2 saturated 1.0 M KOH electrolyte. The catalyst was activated using cyclic voltammetry (CV) in the range of 0 to 0.7 V vs Ag/AgCl at a scan speed of 50 mV s^{-1}, with a rotation speed of 2000 rpm, for 20 cycles until the CV loops overlapped. The Ohmic losses within the system were compensated by applying *iR*-correction. The uncompensated system resistance was determined by electrochemical impedance spectroscopy (EIS) at the open circuit potential. The EIS was measured in a range of 100 kHz to 1 Hz, with a perturbation of 10 mV. The system resistance was determined at the x-intercept of the Nyquist plot. The OER raw data was estimated through CV scans between 0 to 0.7 V (vs Ag/AgCl, equiv 1.023 to 1.723 V vs RHE) at a scanning speed of 10 mV s^{-1}, and rotation rate of 2000 rpm to remove the generated oxygen bubbles. The OER activity was extracted through background-correction and *iR*-correction of the collected raw data. The background-correction was conducted by averaging the forward and backward scan, the system ohmic-losses then being compensated through *iR*-correction: $E_{corr} = E - iR$. EIS was measured at 0.5 V vs Ag/AgCl (equiv 1.523 V vs RHE) in a frequency range of 100000 to 0.1 Hz.

The turnover frequency (TOF) of the OER catalysts was estimated based on the total amount of Ru atoms deposited on the GC electrode. The TOF value was calculated using the following equation:[314]

$$TOF(S^{-1}) = \frac{I}{4nF} \quad (5\text{-}2)$$

Where I is the current from the LSV curves at a certain potential, n is mole of metal atoms loaded on the electrode, F is the Faraday constant (96485.332 C mol^{-1}).

The electrochemically active surface area (ECSA) of OER catalysts were estimated by the double-layer capacitance of the catalysts loaded GC electrode.[315] The ECSA was calculated by the following equation:

$$ECSA = \frac{C_{DL}}{C_s} \quad (5\text{-}3)$$

$$i_c = C_{DL} v \quad (5\text{-}4)$$

Where C_{DL} is the double-layer capacitance of loaded materials in a non-Faradaic potential range, C_{DL} is the slope of the charging current, i_c, with respect to scan rate, ν, the C_s defines the specific capacitance of RuO_2 which is in a range between 0.013 to 0.019 mF cm^{-2} in the alkaline environment according to prior literature:[316] a mean value of 0.016 mF cm^{-2} was used to estimate ECSA in the study.

The HER activities of the catalyst were measured through CV in a 0.5 M N_2-saturated H_2SO_4 electrolyte at 2000 rpm and scan rate 10 mV s^{-1} in the range of −0.5 to 5 V (vs Ag/AgCl, equiv −0.303 to 0.197 V vs RHE). The background-correction and *iR*-correction were processed in the same manner as mentioned in the OER section. The mass activities of OER and HER were calculated by normalizing the measured current at given overpotential to the RuO_2 and Pt mass loadings, respectively.[313]

Catalysts ORR behaviour was evaluated in 0.1 M KOH electrolyte in N_2 and O_2 saturated condition. ECSA was quantified by integrating the coulombic charge of the hydrogen underpotential deposition (HUPD) region from a CV scan (−0.9 to 0.2 V vs Ag/AgCl) at a scan speed of 50 mV s^{-1} in the N_2 saturated electrolyte. For determining the ORR activity, cathodic scan (−0.9 to 0.2 V vs Ag/AgCl, 10 mV s^{-1}) was carried out at varying rotating speed (400 to 2025 rpm) in the O_2 saturated electrolyte. All measurements were corrected by compensating

the ohmic-drop and the capacitive current. The number of electrons transferred (n) and the kinetic current density (J_k) were extracted by using the Koutecky-Levich (K-L) equation:

$$\frac{1}{J} = \frac{1}{B\omega^{1/2}} + \frac{1}{J_k} \quad (5\text{-}5)$$

$$B = 0.62nFC_0(D_0)^{2/3}\nu^{-1/6} \quad (5\text{-}6)$$

where J is the measured current density, ω is the angular velocity of the RDE, F is the Faraday constant (F = 96485 C mol^{-1}), C_0 is the bulk concentration of O_2 in 0.1 M KOH aqueous solution (C_0 = 1.2 × 10^{-6} mol cm^{-3}),[229] D_0 is the diffusion coefficient of O_2 in KOH solution (1.9 × 10^{-5} cm^2 s^{-1}),[5] ν is the kinematic viscosity of KOH (0.01 m^2 s^{-1}).[230] The number of electrons transferred (n) is found from the slope of the linear fit lines of the K-L equation, and the kinetic current density (J_k) is the current density-intercept of the fitted lines. The mass activities of ORR were calculated by normalizing the measured current at given overpotential to the Pt mass loading.

To evaluate the OER durability of RuO_2-rEGO catalyst, chronopotentiometric measurement at a constant current density of 10 mA cm^{-2} was carried out in O_2 saturated 1.0 M KOH electrolyte at a rotation speed of 2000 rpm. The durability of HER was tested through chronopotentiometry at a current density of −10 mA cm^{-2} in N_2-saturated 0.5 M H_2SO_4 solution and at a rotation speed of 2000 rpm to avoid bubble accumulation. The durability of Pt-rEGO catalyst for ORR was evaluated by chronoamperometric test in O_2 saturated 0.1 M KOH solution at 0.55 V vs RHE with a rotation speed of 1600 rpm to achieve the diffusion-limit current density.

For capacitance analysis, CV was conducted between 0.2 and 1.0 V (vs Ag/AgCl) at various scan rates (10, 20, 50, 100, 200, 500, 1000 mV s^{-1}) in an N_2 saturated 1.0 M H_2SO_4 electrolyte. The gravimetric capacitance was estimated based on the galvanostatic discharge and calculated as follows:

$$C = \frac{I\Delta t}{m\Delta V} \quad (5\text{-}7)$$

Where C (F g^{-1}) is the capacitance per total mass of material loaded on the RDE, I is the discharge current (A), Δt is the discharge time span (s), ΔV is the potential range excluding the iR drop (V), and m is the total mass of materials loaded on the working electrode.

5.5 Results and Discussion

5.5.1 Characterization of Reduced EGO

The optical bandgap of EGO and their fragments dispersed in water has been estimated by applying the Tauc plot[317] through the UV-Vis absorption spectrum (**Figure 5-3 a and b**). The combination of the π-state (sp^2 bonded) carbons, and the σ-state (sp^3 bonded) carbons in GO makes it a semiconductor with a bandgap in a range from 2 to 7 eV.[302] The absorption at ~4 eV caused by n-π* transitions of C=O, and the peak at approximately 5 eV is attributed to π-π* transitions of C=C.[318-319] The bandgap values of EGO has been approximated from the linear extrapolation using the Tauc plot,[320] which gives a direct bandgap range from 3.25 to 3.95 eV (**Figure 5-3 a**), and an indirect bandgap from 2.04-2.4 eV (**Figure 5-3 b**). Therefore, the photon energy of 248 nm laser (4.99 eV) is sufficiently high to excite EGO and thus create electron-hole pairs. In contrast, due to the higher degree of oxidation compared with EGO,[310] CGO exhibits larger bandgap values for both direct (3.25 to 4.31 eV) and indirect (2.04 to 3.38 eV) bandgaps **(Figure 5-4)**.

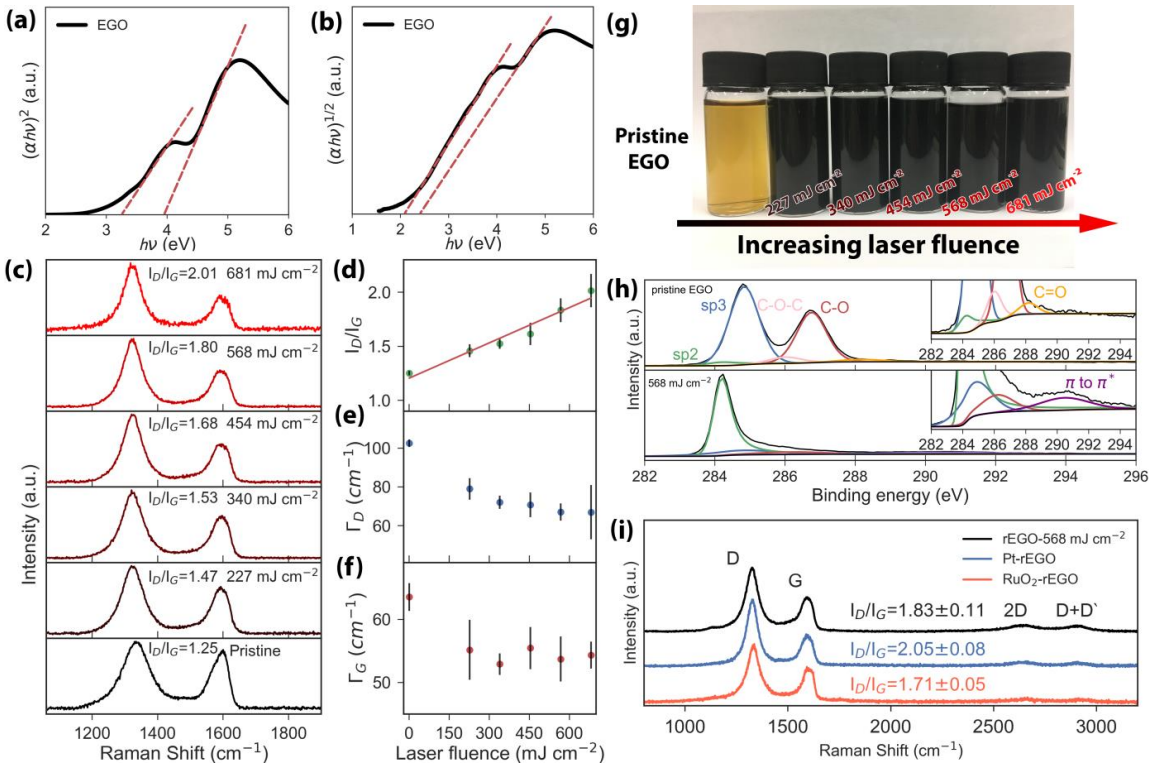

Figure 5-3. (**a**) and (**b**) Tauc plots derived from the UV-vis spectra of pristine EGO for determination of bandgaps for direct and indirect transitions, respectively. (**c**) Typical Raman spectra of EGO after 248 nm laser irradiation at various fluences, (**d**) the evolution of I_D/I_G ratio with the increase of laser fluence. (**e**) and (**f**) FWHM values of D and G band for EGO treated with various laser fluences. (**g**) Photographs of pristine EGO and rEGO after laser irradiation at various fluences. (**h**) XPS high-resolution C 1s spectra of pristine EGO and rEGO reduced by laser irradiation at 568 mJ cm^{-2}. (**i**) Comparison of typical Raman spectra for pure rEGO, RuO_2-rEGO and Pt-rEGO composites prepared using laser irradiation at 568 mJ cm^{-2}, the I_D/I_G ratio displayed is an average value of five spectra.

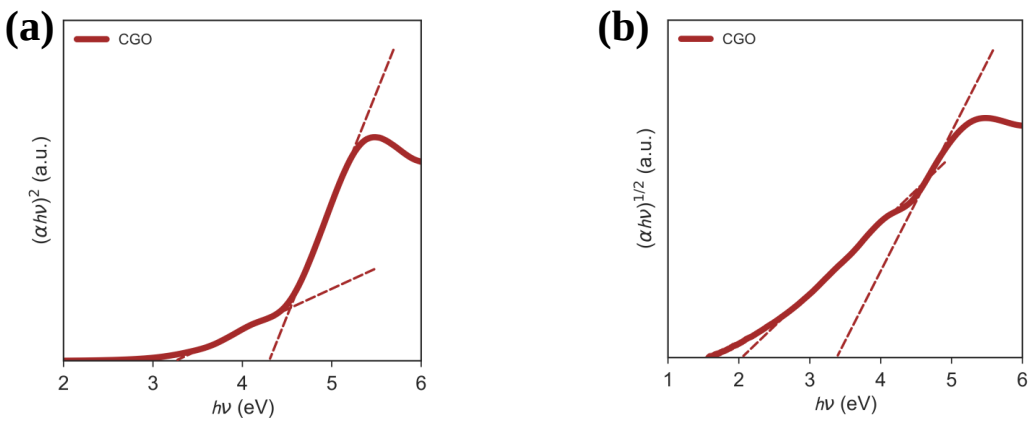

Figure 5-4. Tauc plots of CGO for (**a**) the direct (3.25 to 4.31 eV) and (**b**) the indirect (2.04 to 3.38 eV) bandgap transitions.

Raman spectroscopy was used to characterize the quality of the graphene lattice and defect density of rEGO. The excitation laser (He-Ne; 633 nm) output power for recording the Raman spectra was limited to < 0.5 mW to avoid any laser-induced structure alteration. **Figure 5-3 c** shows typical Raman spectral of EGO and rEGO. Spectra of all samples show a D band at 1333 cm^{-1} representing the edge planes and disordered structures, and the characteristic G band at 1595 cm^{-1} ascribed to the ordered sp^2 bonded carbon.[321] The Raman spectra were further analysed by fitting the D and G bands with Lorentzian function after baseline subtraction (**Figure 5-5**). For Raman analysis, the baseline of the recorded spectrum was subtracted followed by Lorentzian function curve fitting. The I_D/I_G ratio was calculated from the fitted peak intensities of D and G bands, and Γ_D and Γ_G were extracted from the FWHM of the fitted D and G bands, respectively.

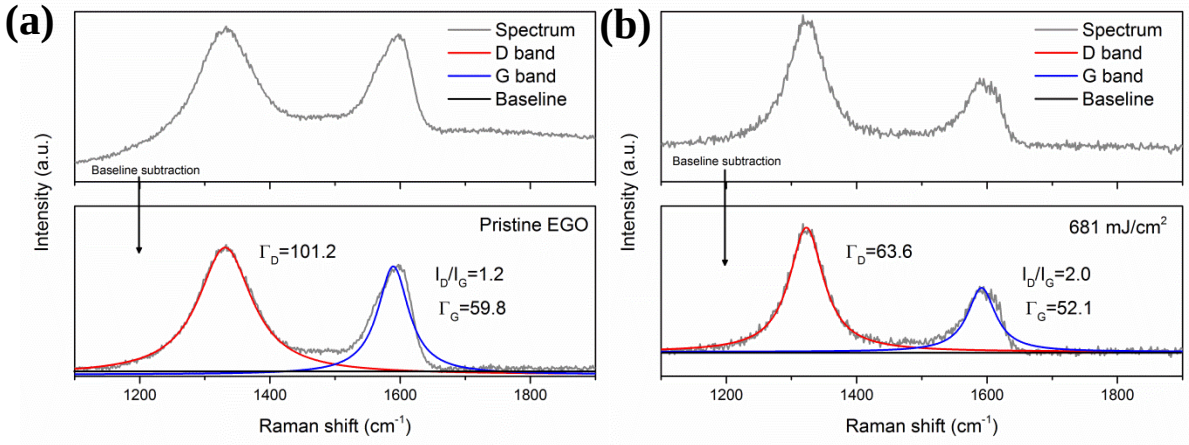

Figure 5-5. Examples of baseline subtraction and curve fitting for the as-recorded Raman spectra. (**a**) pristine EGO; (**b**) rEGO treated by laser irradiation at 681 mJ cm^{-2}.

The intensity ratio of D to G band (I_D/I_G) is closely related to the density of defect/functionality in the graphene lattice,[322-324] the I_D/I_G ratio of rEGO increases linearly from 1.25 to 2.01 with

the increasing of laser fluence (0 to 681 mJ cm^{-2}, Note: zero fluence represents pristine EGO) (**Figure 5-3 d**). Using the model proposed by Lucchese et al.[322] and Cançado et al.,[323] the defect distance (L_D) can be determined from the Raman I_D/I_G ratio (**Figure 5-6 a** and **Table 5-1**). The amount of disorder is measured by characterising the defect distance and the degree of functionalization. The quantitative model correlates the defect distance (L_D) and the I_D/I_G ratio is given as follows: [310, 325-326]

$$\frac{I_D}{I_G} = C_A\left(\frac{r_A^2 - r_S^2}{r_A^2 - 2r_S^2}\right)\left[e^{-\pi r_S^2/L_D^2} - e^{-\pi(r_A^2 - r_S^2)/L_D^2}\right] \quad (5\text{-}8)$$

where r_S = 1 nm and r_A = 3.1 nm, define the radii of the structurally disordered area and "activated" area caused by a point defect, respectively, both areas contribute to the D band scattering; the electron-phonon matrix elements, $C_A = 160E_L^{-4}$, where E_L is defined by the laser energy (1.96 eV for 633 nm wavelength); L_D is the average distance between defects. In the example, the rEGO (treated at 681 mJ cm^{-2}) with an I_D/I_G ratio of 2.01 ± 0.15 has a L_D value of 1.32 ± 0.03 nm (**Figure 5-6 a**).

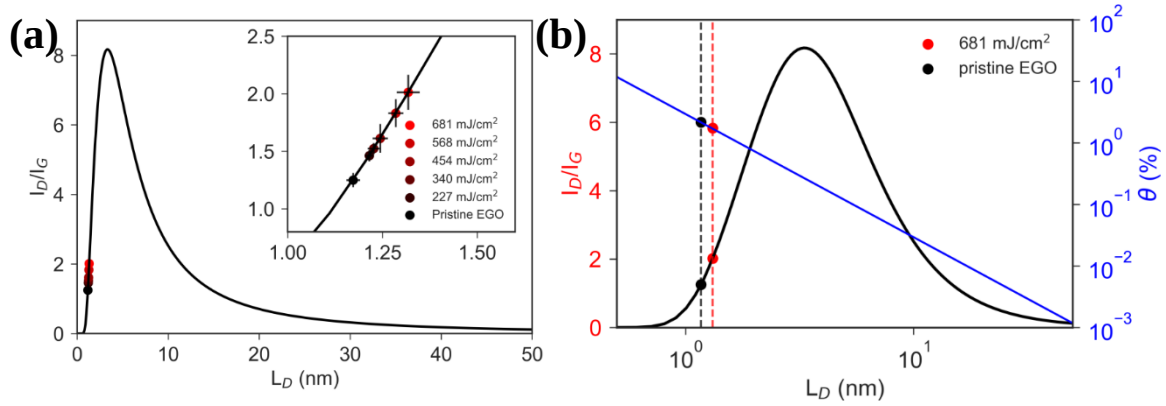

Figure 5-6. Example of defect distance and degree of functionalization analysis for the rEGO treated at 681 mJ cm^{-2}: (**a**) the Raman I_D/I_G ratio versus the defect distance (L_D); (**b**) correlation of L_D with the degree of functionalization (θ) and I_D/I_G ratio. The I_D/I_G ratio was obtained from Raman spectra recorded using a He-Ne laser with a wavelength of 633 nm.

The degree of functionalization (θ) defines the ratio of sp^3 hybridized carbon atoms to the total carbon atoms, which can be correlated with the I_D/I_G ratio at a given wavelength of excitation laser:[224]

$$\theta = \frac{a^2}{2L_D^2} \quad (5\text{-}9)$$

where a is the graphene lattice unit cell vector, and $|a|$=0.242 nm. The blue line in **Figure 5-6 b** is the correlation of L_D with the degree of functionalization θ under an excitation laser wavelength of 633 nm. In the example, the rEGO (treated at 681 mJ cm^{-2}) with the L_D of 1.32

± 0.03 nm corresponds to a θ of 1.68 ± 0.06 %. Detailed L_D and θ values for pristine EGO and rEGO treated at various laser fluences are shown in **Table 5-1**.

Table 5-1. Summary of statistical Raman analysis of pristine EGO and EGO after 248 nm laser irradiation at various laser fluences.

Laser fluence (mJ cm^{-2})	Γ_D (cm^{-1})	Γ_G (cm^{-1})	I_D/I_G	L_D (nm)	θ (%)
0	102.46±1.89	63.52±2.19	1.25±0.02	1.17±0.01	2.13±0.03
227	78.92±5.52	55.14±4.75	1.46±0.06	1.22±0.01	1.98±0.03
340	72.02±3.35	52.89±1.70	1.52±0.05	1.23±0.01	1.94±0.02
454	70.65±6.38	55.43±3.21	1.61±0.10	1.24±0.02	1.89±0.05
568	67.01±4.44	53.69±3.55	1.83±0.11	1.29±0.02	1.77±0.04
681	66.89±13.93	54.29±2.14	2.01±0.15	1.32±0.03	1.68±0.06

With the increasing laser fluence, L_D rises from 1.17 to 1.32 nm, suggesting a partial restoration of the graphene lattice. Quantification of defect density (θ), defined as the ratio of C(sp^3) to C(sp^2), using the calculated L_D values,[324] suggests a gradual reduction of θ from 2.13% to 1.68% with the increase of laser fluences (**Figure 5-6 b** and **Table 5-1**). The lattice restoration after laser reduction is also confirmed by the narrowing of full width at half-maximum (FWHM; Γ) of D and G bands (**Figure 5-3 e and f**).[327] In addition, the photographs of EGO solutions (**Figure 5-3 g)** indicate that the colour of EGO dispersions turned from brown into the black after laser irradiation at various fluences of 227, 340, 454, 568 and 681 mJ cm^{-2}, respectively. X-ray diffraction (XRD) further confirms the increased reduction of EGO at higher laser fluence. The diffraction peak of EGO at ~10° vanished gradually with the increase of laser fluence (**Figure 5-7 a**).

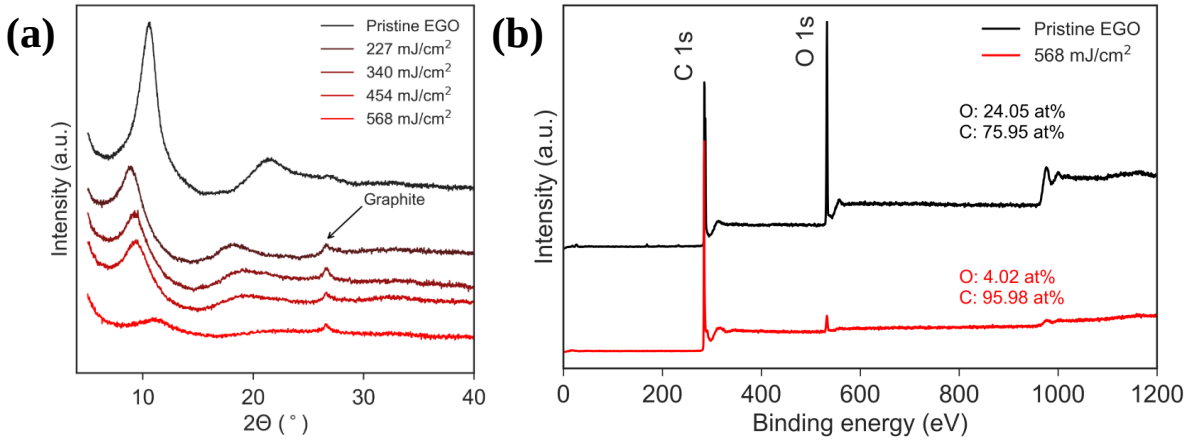

Figure 5-7. (**a**) XRD patterns of pristine EGO and EGO irradiated at various laser fluences. All samples were drop-cast on a zero background Si wafer and dried at room temperature. The shift of the (001) peak of graphene

oxide from 10.55° to 8.95° was caused by swelling of graphene oxide in humid air[328]. The small peak at 26.62° is ascribed to a small amount of graphite in the pristine EGO. (**b**) XPS survey spectra of the pristine EGO and the rEGO that was reduced at 568 mJ cm^{-2} irradiation.

The X-ray photoelectron spectroscopy (XPS) survey spectra collected with pristine EGO and rEGO after irradiation at a laser energy density of 568 mJ cm^{-2} reveal a significant decrease in oxygen content, from 24.0 at.% (EGO) to 4.0 at.% (rEGO) **(Figure 5-7 b**). **Figure 5-3 h** compares the C 1s spectra for pristine EGO and rEGO. The deconvolution of the C 1s spectrum of pristine EGO shows five distinctive components, which are assigned to sp^2 carbon (284.2 eV), sp^3 carbon (284.9 eV), C−O (286.0 eV), C−O−C (287.0 eV) and C=O/−COO− (288.2 eV),[329] (details in **Table 5-2**). In contrast, the C 1s of rEGO shows an effective removal of oxygen groups and restoration of sp^2 carbon structure. Notably, the sp^2 carbon content increases dramatically from 2.5 at.% for pristine EGO to 61.9 at.% for rEGO. Both the Raman and XPS results indicate an efficient restoration of the sp^2 bonded graphene lattice from the sp^3 oxygenated sites via the facile laser-induced reduction. In comparison, the reduction of EGO by thermal annealing up to 250 °C removes oxygen functionalities but leaves the defects unrestored. The XRD diffraction peak of EGO at ~ 10° decreases in its intensity and disappears after annealing at temperature > 200 °C, revealing the removal of the majority of the oxygen functionalities (**Figure 5-8 a**). Previous reports also suggested that thermal annealing at 200 °C effectively reduced EGO film as evidenced by the dramatic recovery of electrical conductivity.[310] However, the decrease of Raman I_D/I_G ratio (**Figure 5-8 b and c**) for thermal annealed EGO suggests the sp^2 bonded graphene lattice structure is not restored. Quantification and comparison of defect distance and density using Raman I_D/I_G ratio indicate that thermal annealing leads to a slightly increased defect density compared with pristine EGO (**Figure 5-8 d**). This is due to the thermal decomposition of oxygen functional groups to CO_2/CO products, thereby removing oxygen and carbon atoms simultaneously, leaving permanent defects and vacancies in the graphene lattice.[330] The results from thermally reduced EGO also suggest that the UV laser-induced reduction of EGO in aqueous solution follows a dominating photochemical mechanism with minimum photothermal effect.

Table 5-2. Summary of XPS characterization of pristine EGO and photo-reduced EGO after laser irradiation at 568 mJ cm^{-2} for 30 min.

Sample	Oxygen content (at.%)	C 1s components (at.%)					
		C−C (sp^3) 284.9 eV	C−C (sp^2) 284.2 eV	C−O 286.0 eV	C=O, −COO− 288.2 eV	C−O−C 286.0 eV	π to π* 290.5 eV
Pristine EGO	24.0	55.1	2.5	35.4	2.2	4.8	0
rEGO (568 mJ cm^{-2})	4.0	17.1	61.9	8.8	0	0	12.2

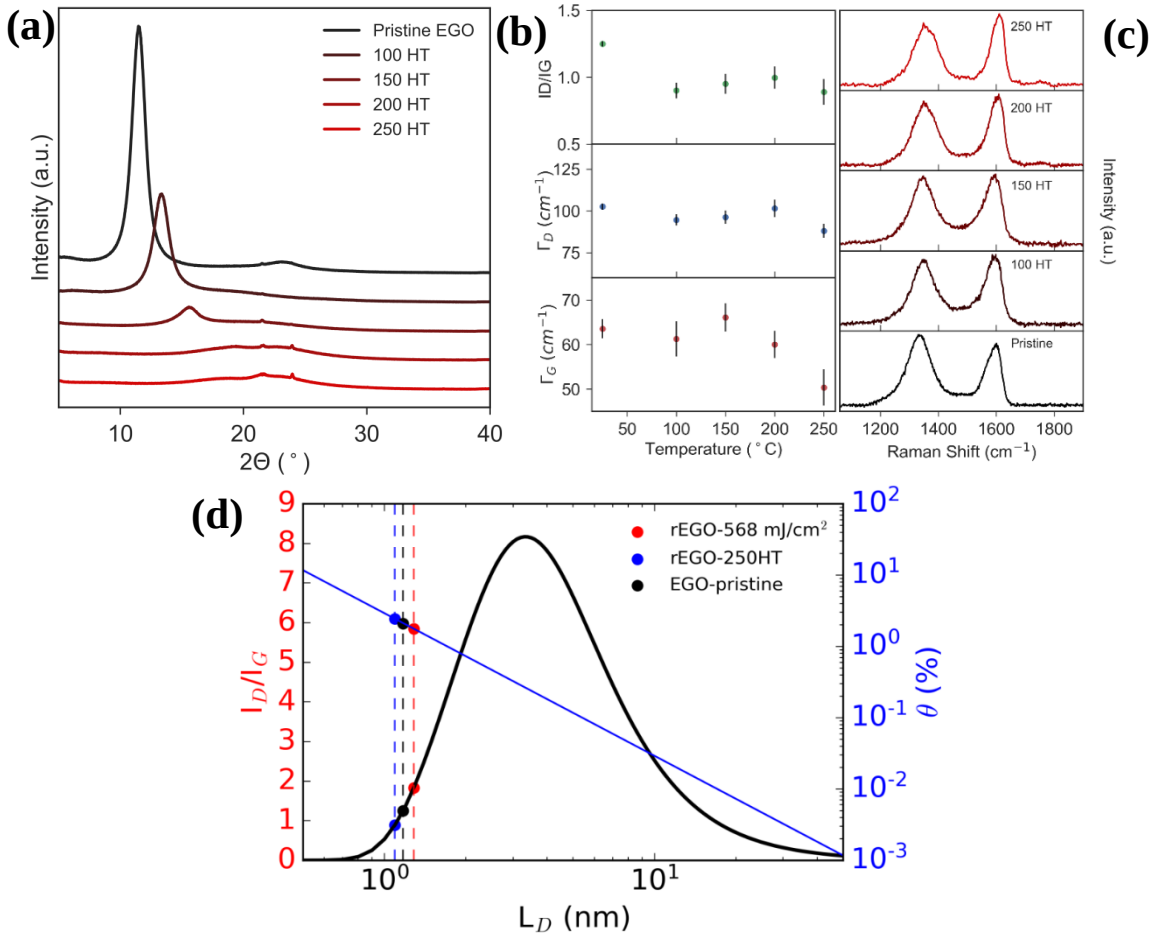

Figure 5-8. (**a**) XRD patterns of pristine EGO and EGO heat-treated in air at 100, 150, 200 and 250 °C for 8 hours. The EGO (002) peak shifts to higher angle with increasing temperature, which is attributed to the drastic vaporization of intercalated water.[331] The evolution of D and G bands of EGO with increasing annealing temperature in air at 100, 150, 200 and 250 °C for 8 hours. (**b**) I_D/I_G ratio, FWHM for D band (Γ_D) and G band (Γ_D). (**c**) typical Raman spectra of EGO annealed at various temperature. (**d**) Comparison of the defect distance (L_D) and degree of functionalization (θ) for pristine EGO, rEGO treated at 568 mJ cm^{-2} and thermally reduced EGO at 250 °C.

Due to the hydrophobic nature of graphene, the rEGO dispersion agglomerated and settled at the bottom of the water within 2 hours (**Figure 5-9 a**). Additionally, there is a gradual increase in weight loss (26.8 to 79.1 wt.%) and Raman I_D/I_G ratio (1.46 to 2.01) for rEGO irradiated using a laser beam with increasing fluence from 227 to 568 mJ cm^{-2} (**Figure 5-9 b**). This suggests a more efficient removal of oxygen groups and restoration of graphene lattice at higher

laser fluence. Further increase of the laser fluence to 681 mJ cm^{-2} causes a sudden drop in the remaining weight of rEGO to 22.4% compared to the starting EGO (**Figure 5-9 b**), indicating photodegradation occurs at such high laser fluence. In comparison with EGO, there are much less apparent changes in weight loss, Raman I_D/I_G ratio, Γ_D and Γ_G for CGO after laser irradiation at increasing fluence from 227 to 681 mJ cm^{-2} (**Figure 5-9 c**), but a more severe photodegradation (13.8% remaining weight) at the laser fluence of 681 mJ cm^{-2}. In comparison to the rEGO, the laser-treated CGO under the same condition yields a brownish suspension indicating insufficient reduction (**Figure 5-9 d**). The less efficient reduction and restoration of conventional CGO using the laser-assisted solution approach are consistent with the recent report.[305] To avoid severe photodegradation, the laser fluence of 568 mJ cm^{-2} was selected to be optimal for the simultaneous reduction of EGO and deposition of catalyst nanoparticles.

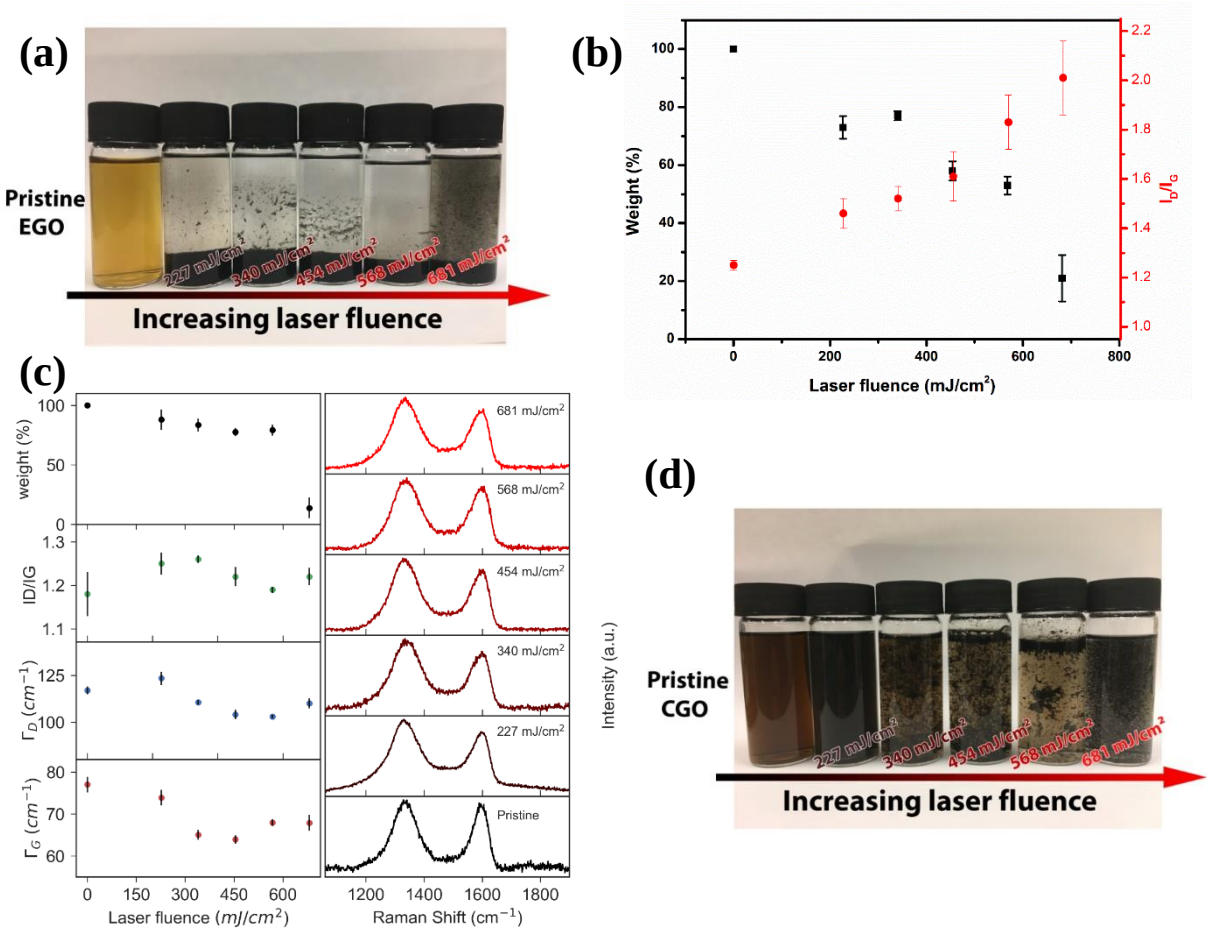

Figure 5-9. (**a**) Photograph of pristine EGO and rEGO aqueous suspensions after laser irradiation at various laser fluences. The suspensions were settled at ambient conditions for 2 hours. (**b**) Weight changes, and Raman D and G bands intensity ratio of EGO after UV laser irradiation at various laser fluences, all samples were weighed after freeze-drying. (**c**) The evolution of weight and Raman spectral characteristics for CGO after 248 nm laser irradiation at various laser fluences. Change of weight, I_D/I_G ratio, Γ_D and Γ_G with the increasing laser fluence. Representative Raman spectra of CGO after laser irradiation at various fluences. (**d**) Photograph of pristine CGO and rCGO after laser irradiation at various laser fluences.

5.5.2 Characterization of Reduced EGO Modified with Metal (Oxide) Nanoparticles

Metal salts of chloroplatinic acid (H_2PtCl_6) and ruthenium chloride ($RuCl_3$) were selected as precursors for metal (Pt) and metal oxide (RuO_2) nanoparticles, respectively. **Figure 5-3i** shows the Raman spectra of RuO_2-rEGO and Pt-rEGO in comparison with pure rEGO reduced by UV laser irradiation. All samples exhibit sharp D and G bands with broad 2D and D + D` bands. The I_D/I_G ratios for RuO_2-rEGO, Pt-rEGO and rEGO are 1.71, 2.05 and 1.83, respectively, which are significantly different from the ratio of the original EGO (I_D/I_G = 1.25), indicating the laser-induced reduction of EGO remains effective after the addition of metal salts in the dispersion. Interestingly, the RuO_2-rEGO sample shows a reduced I_D/I_G ratio compared with that of rEGO, suggesting more defects/functionalities. This indicates a possible bond formation (oxygen bridges) between rEGO and RuO_2. In addition, the G band position of RuO_2-rEGO sample upshifts by 5.7 cm^{-1} to 1597.8 cm^{-1} (**Figure 5-10 a and b**) compared with that of rEGO (1592.1 cm^{-1}), indicating charge transfer occurred between rEGO and RuO_2 via doping effect and/or bond formation.[332] Therefore, the reduced I_D/I_G ratio and shift of G band position of RuO_2-rEGO compared with rEGO suggests the formation of oxygen bridges. The complete reduction of EGO in the Pt-rEGO was confirmed by XPS C 1s spectrum (**Figure 5-10 c**). In contrast, according to literature,[298] the photodeposition of Pd nanoparticles from Pd^{2+} inhibited the complete reduction of CGO. As the reduction potential vs standard hydrogen electrode (SHE) for $PdCl_4^{2-}$/Pd (0.591 V) is not significantly different from that of $PtCl_6^{2-}$/$PtCl_4^{2-}$ (0.68 V) and $PtCl_4^{2-}$/Pt (0.755 V).[333] The effective laser-induced reduction of EGO in the presence of competing reactions (reduction of $PtCl_6^{2-}$ to Pt) suggests EGO with low contents of oxygen (~20 at.%) and unrestorable C=O/−COO− groups as a promising platform for the laser-assisted synthesizing of nanoparticle-functionalized graphene materials.

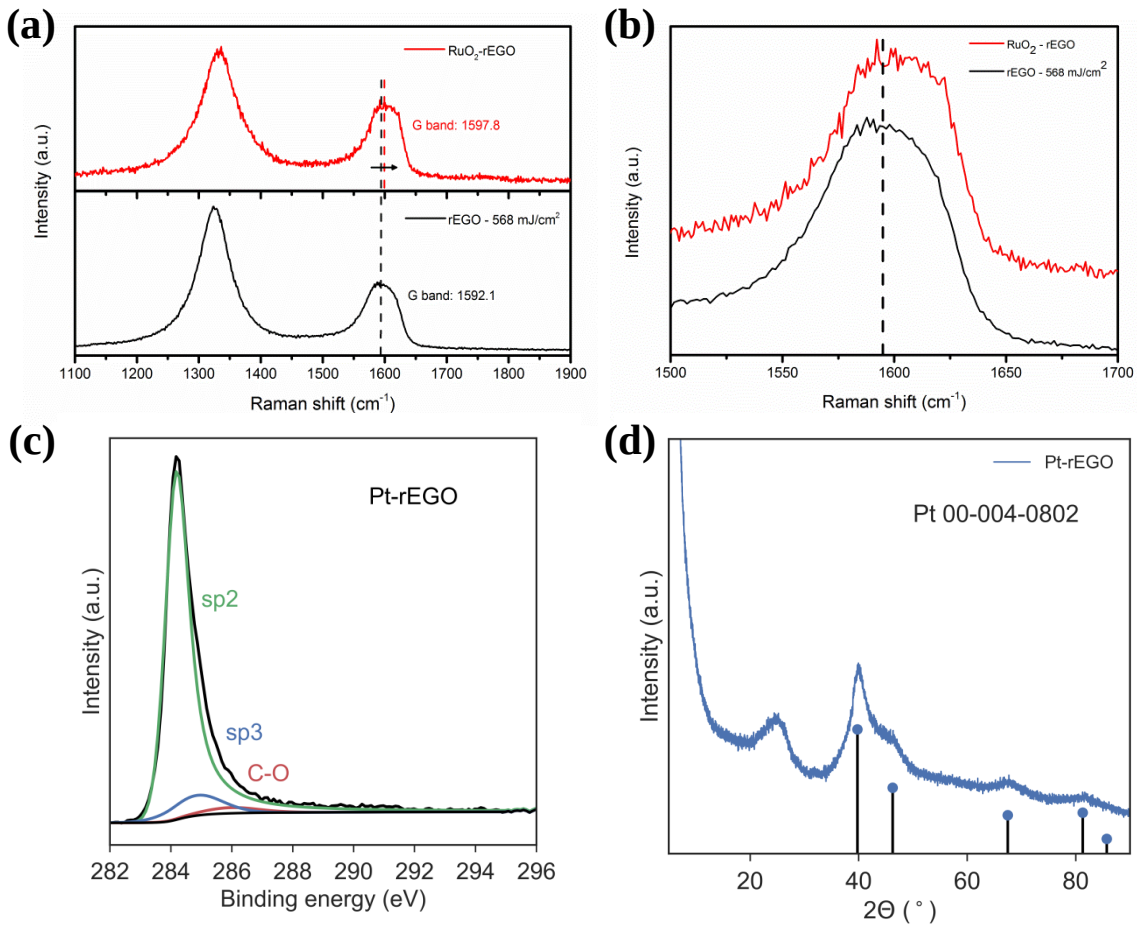

Figure 5-10. Raman G band upshift of the RuO_2-rEGO sample compared with rEGO. (**a**) Typical Raman spectra of RuO_2-rEGO and rEGO. (**b**) Raman spectra of RuO_2-rEGO and rEGO in G band region. (**c**) High-resolution XPS C 1s spectrum recorded from the Pt-rEGO sample, (**d**) XRD patterns of the as-synthesized Pt-rEGO sample.

Both the Raman spectrum and XRD pattern (**Figure 5-11 a and b**) of the as-synthesized RuO_2-rEGO indicate an amorphous structure of the freshly deposited hydrous RuO_2 (RuO_2 with structural water, $RuO_2{\cdot}xH_2O$). As the degree of crystallinity of RuO_2 affects its OER[334-335] and pseudo-capacitance[336-338] performance, heat treatment was performed with the RuO_2-rEGO in air at various temperatures ranging from 100 to 250 °C. The Raman spectra of samples annealed at 200 and 250 °C (**Figure 5-11 a**) show characteristic vibrational peaks at 515, 630 and 703 cm^{-1}, corresponding to E_g, A_{1g} and B_{2g} modes of crystalline RuO_2, respectively. The transition from amorphous to crystalline structure for the RuO_2-rEGO composite was further confirmed by XRD (**Figure 5-11 b**). The diffraction peaks at 28.0° and 35.0° corresponding to (110) and (101) planes of rutile RuO_2 (ICDD No 00-040-1290) appear after annealing at 200 and 250 °C. Interestingly, apart from the RuO_2 peaks, weak peaks at 39.4°, 42.2° and 44.1° corresponding to metallic Ru are also observed, indicating the formation of minor metallic Ru phases with the prevailing RuO_2 phase. The XRD pattern of Pt-rEGO (**Figure 5-10 d**) shows that all of the diffraction peaks match with Pt (ICDD No. 00-004-0802), suggesting that the successful

photodeposition of Pt on the rEGO sheets had occurred. According to the standard reduction potentials of aqueous Ru and Pt solutions,[299, 333] the reduction potential vs SHE decreases in the order: $PtCl_4^{2-}$/Pt (0.755 V) > $PtCl_6^{2-}$/$PtCl_4^{2-}$ (0.68 V) > Ru^{2+}/Ru (0.455 V) > Ru^{3+}/Ru^{2+} (0.249 V). The deposition of metallic Ru requires a more negative potential than that of Pt, which is probably one of the reasons for the formation of RuO_2 as the dominant phase rather than metallic Ru. Note that the pH values of EGO-H_2PtCl_6 (3.18) and EGO-$RuCl_3$ (3.32) precursor solutions are comparable. At this pH range, according to the Pourbaix diagram, the reduction potential for $Ru(OH)_3$/Ru is ~ 0.5 V vs SHE, lower than that of $Pt(OH)_2$/Pt (~0.8 V vs SHE).[339] In addition, Ru is known to be much less noble than other Pt group metals and thus has a stable oxidation state of +4 in the presence of oxygen.[339] Electrochemical investigation of Ru metal electrodes indicated that the surface oxidation of Ru already begins at the potentials in, or close to, the H region, 0.05 to 0.2 V vs reversible hydrogen electrode (RHE) in 0.5 M H_2SO_4.[340] In contrast, the surface oxidation of Pt starts at a high potential of 0.8 V vs RHE in 0.5 M H_2SO_4.[341] Hence, another possible reason for the formation of RuO_2 as dominating phase is due to the as-formed metallic Ru is prone to be oxidized by photo-generated holes.

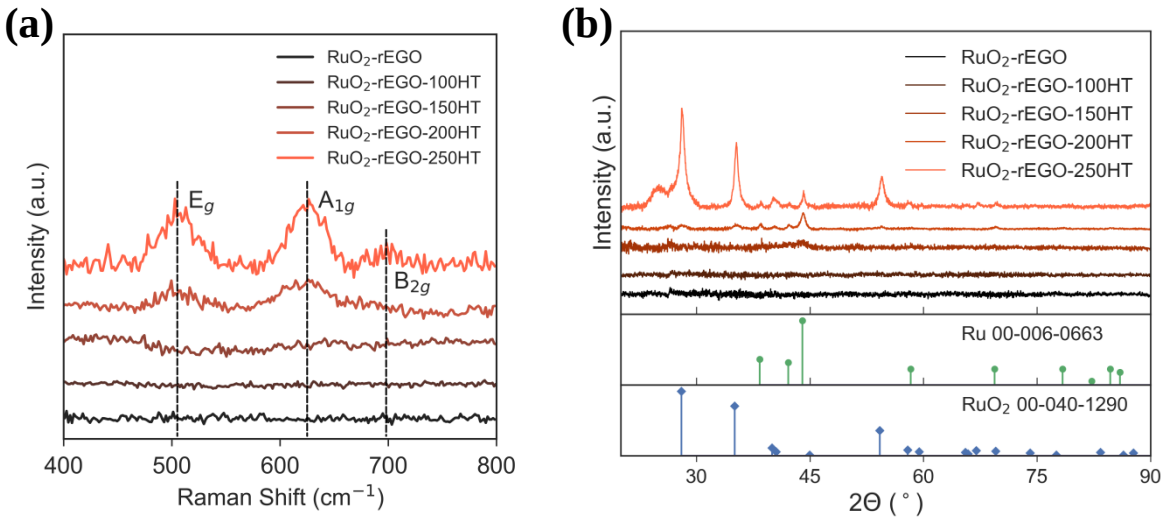

Figure 5-11. (**a**) Raman spectra and (**b**) XRD patterns of as-synthesized RuO_2-rEGO sample and samples after heat treatment (HT) at 100, 150, 200 and 250 °C, respectively.

Transmission electron microscopy (TEM) and scanning transmission electron microscopy with high angle annular dark field (STEM-HAADF) were used to characterize the particle size and crystal structure of the RuO_2-rEGO and Pt-rEGO composites. The TEM and STEM-HAADF images for both the RuO_2-rEGO-250HT (heat-treated in air at 250 °C; **Figure 5-12a and c**) and Pt-rEGO (**Figure 5-12 b and d**) show uniformly distributed ultrafine nanoparticles on the rEGO support. Compared with the TEM images of the as-synthesized RuO_2-rEGO without heat

treatment (**Figure 5-13**), annealing at 250 °C shows minor effects in the morphology of RuO_2-rEGO sample. Statistical particle size analysis was conducted for the Pt and RuO_2 nanoparticles, with 1000 and 833 particles in random areas being analysed, respectively, and a log-normal function being used for data fitting. The results show mono-dispersed particle sizes of 2.0 nm (standard deviation: $\sigma = 0.5$) for Pt-rEGO and 2.8 nm ($\sigma = 0.6$) for RuO_2-rEGO-250HT. One of the possible reasons, that the smaller size of nanoparticles (2~3 nm) in this work compared with the sizes of photo deposited nanoparticles (> 5 nm) on rGO in the previous reports,[296-298] is due to the use of a laser with higher photon energy and fluence. Analog to electrodeposition, higher laser photon energy and fluence correspond to larger current density (overpotential) and thus increased supersaturation, leading to higher nucleation rate and reduced critical cluster size, therefore smaller particle size.[342] In addition, the possible bond formation (e.g. oxygen bridges) between rEGO and nanoparticles would provide anchoring effect and thus inhibit the agglomeration and growth of small particles. Nevertheless, factors affecting the nanoparticle size of a laser-induced photodeposition process are complicated, the potential factors include but not limited to: concentrations of EGO and metal ions, type and concentration of sacrificial electron donor/acceptor, temperature, pH, laser wavelength (photon energy), fluence, irradiation time, pulse repetition rate, mass diffusion related variables (e.g. stirring, flow rate), etc. Full understanding of the nanoparticle formation mechanism and precise control of nanoparticle size require future and in-depth studies.

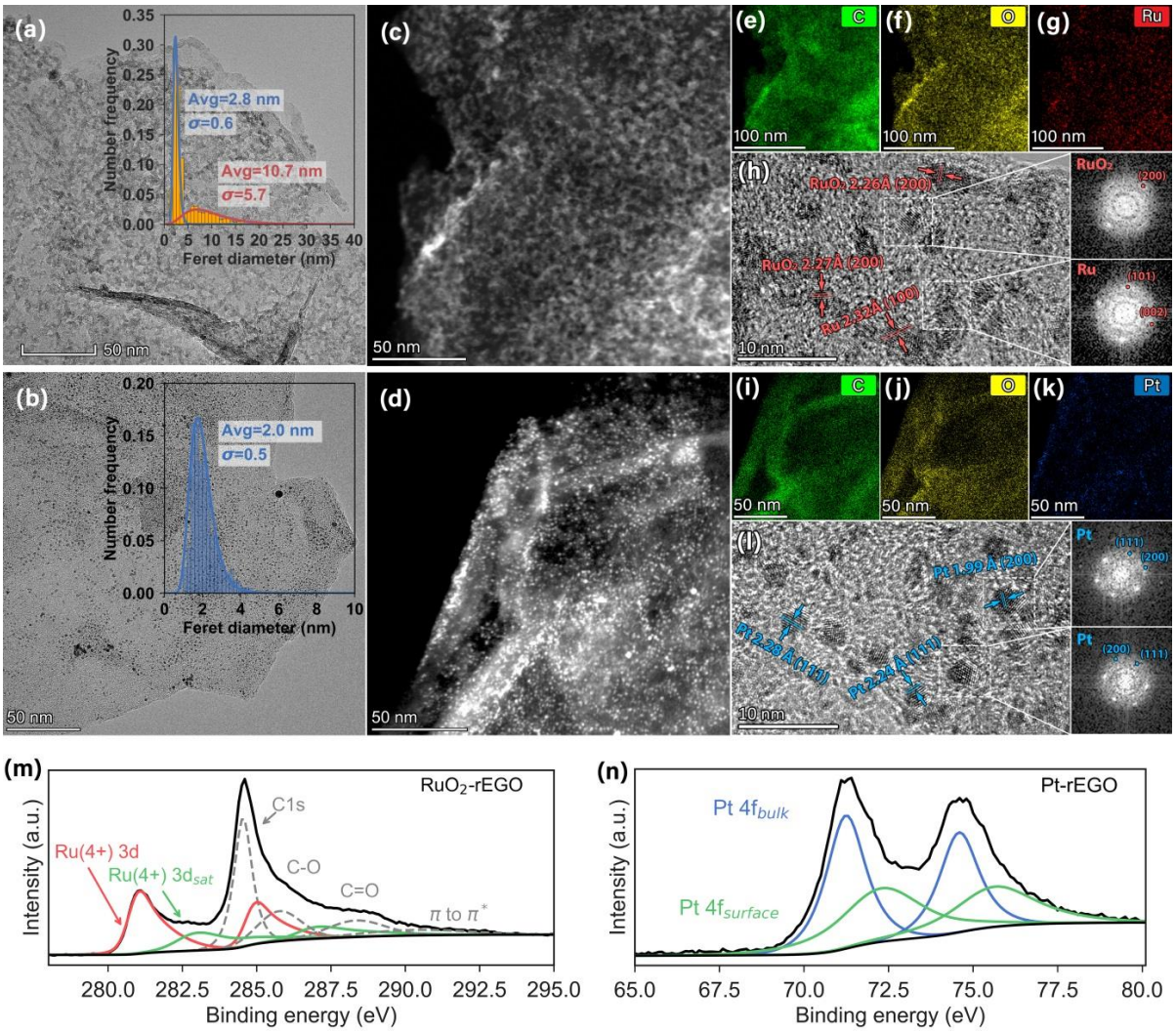

Figure 5-12. TEM images of (**a**) RuO_2-rEGO-250HT (heat-treated at 250 °C) and (**b**) Pt-rEGO prepared via laser irradiation at 568 mJ cm^{-2}, insets: size distribution of two samples by counting 833 and 1000 particles, respectively. STEM-HAADF images of c) RuO_2-rEGO-250HT and (**d**) Pt-rEGO. (**e-g**) STEM-EDS elemental mappings of C, O and Ru in the RuO_2-rEGO-250HT sample. (**h**) HRTEM image of RuO_2-rEGO-250HT shows lattice fringes of Ru and RuO_2, inset: representative FFT of selected particles. (**i-k**) STEM-EDS elemental mappings of C, O and Pt in the Pt-rEGO. (**l**) HRTEM image of Pt-rEGO shows lattice fringes of Pt, inset: representative FFT of selected particles. (**m**) and (**n**) High-resolution XPS Ru 3d and Pt 4f spectra recorded from the as-synthesized RuO_2-rEGO and Pt-rEGO samples, respectively.

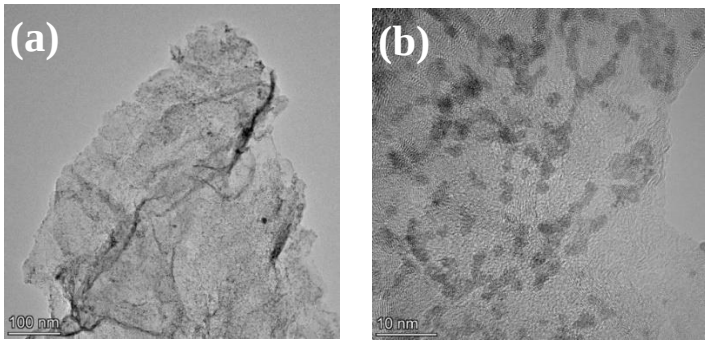

Figure 5-13. (**a**) and (**b**) Representative TEM images of the as-synthesised RuO_2-rEGO without heat treatment.

Energy-dispersive X-ray spectroscopy (EDS) was employed to analyse the distribution of Ru and Pt elements in the rEGO support. The EDS mapping data (**Figure 5-12 e to g and i to k,**

respectively) indicates that both the Ru and Pt are evenly distributed over the entire rEGO support. The HRTEM image of Pt-rEGO (**Figure 12l**) shows the Pt nanoparticles have a single-crystalline feature with clear lattice fringes. The labelled Pt nanoparticles in **Figure 12l** show lattice spacing values of 0.224 and 0.199 nm, which are indexed to the (111) and (200) facets of Pt, respectively. The nanoparticles on RuO_2-rEGO-250HT sample show clear lattice fringes (**Figure 12h**) with a spacing value of 0.227 nm, corresponding to the (200) facet of RuO_2. In addition, secondary metallic Ru nanoparticles are also observed from the TEM image of RuO_2-rEGO sample (**Figure 12h**). The TEM images of RuO_2-rEGO-200HT (**Figure 14a and d**) and RuO_2-rEGO-250HT (**Figure 14d and e**) reveal that the rEGO flakes are decorated with both primary fine particles (2.8 nm; $\sigma = 0.6$) and secondary nanoparticles with relatively larger average size (10.7 nm; $\sigma = 5.7$) and higher contrast. The HRTEM images and the fast Fourier transfer pattern (FFT) (insets in **Figure 14b and e**) of these large particles show the lattice spacing of 0.201 and 0.210 nm corresponding to the (101) and (002) planes of metallic Ru. Further characterization of > 5 randomly selected large particles all show a metallic Ru phase, indicating that the majority of the large particles are metallic Ru. The observation of a secondary metallic Ru phase from TEM characterization is consistent with the XRD results. Scanning electron microscope (SEM) images of the drop casted RuO_2-rEGO and Pt-rEGO composite films on silicon wafers indicate a thick porous structure (**Figure 15a, c and e**). At higher magnifications, the SEM images of the composite films (**Figure 15b, d and f**) all exhibit a typical wrinkled flake-like morphology of stacked graphene flakes.

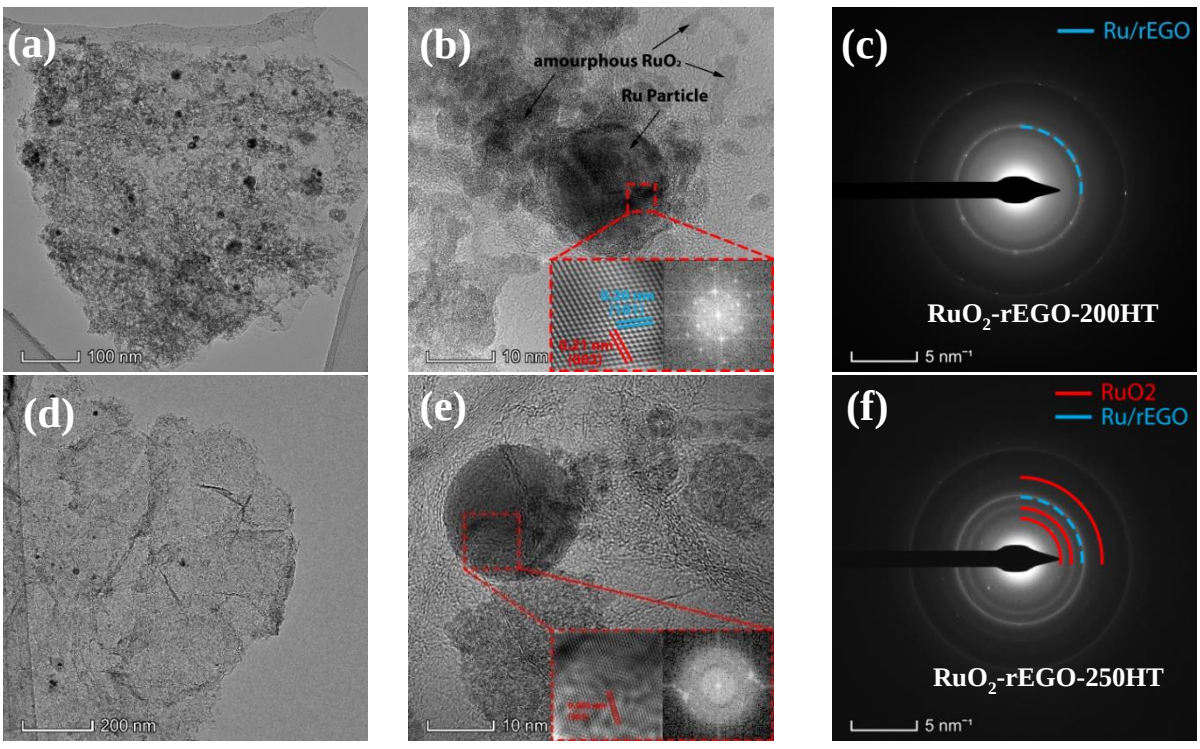

Figure 5-14. (**a**) and (**b**) TEM images of RuO_2-rEGO-200HT the insert image shows the lattice fringes and FFT corresponding to metallic Ru, (**c**) selected area diffraction pattern (SADP) of RuO_2-rEGO-200HT shows metallic Ru and amorphous RuO_2, which is consistent with the XRD characterization, the blue dashed line is corresponding to the overlapped diffraction ring/pattern of metallic Ru and graphene (rEGO). (**d**) and (**e**) TEM images of RuO_2-rEGO-250HT and (**f**) its SADP reveal the co-existence of crystalline RuO_2 and Ru after annealing at 250 °C.

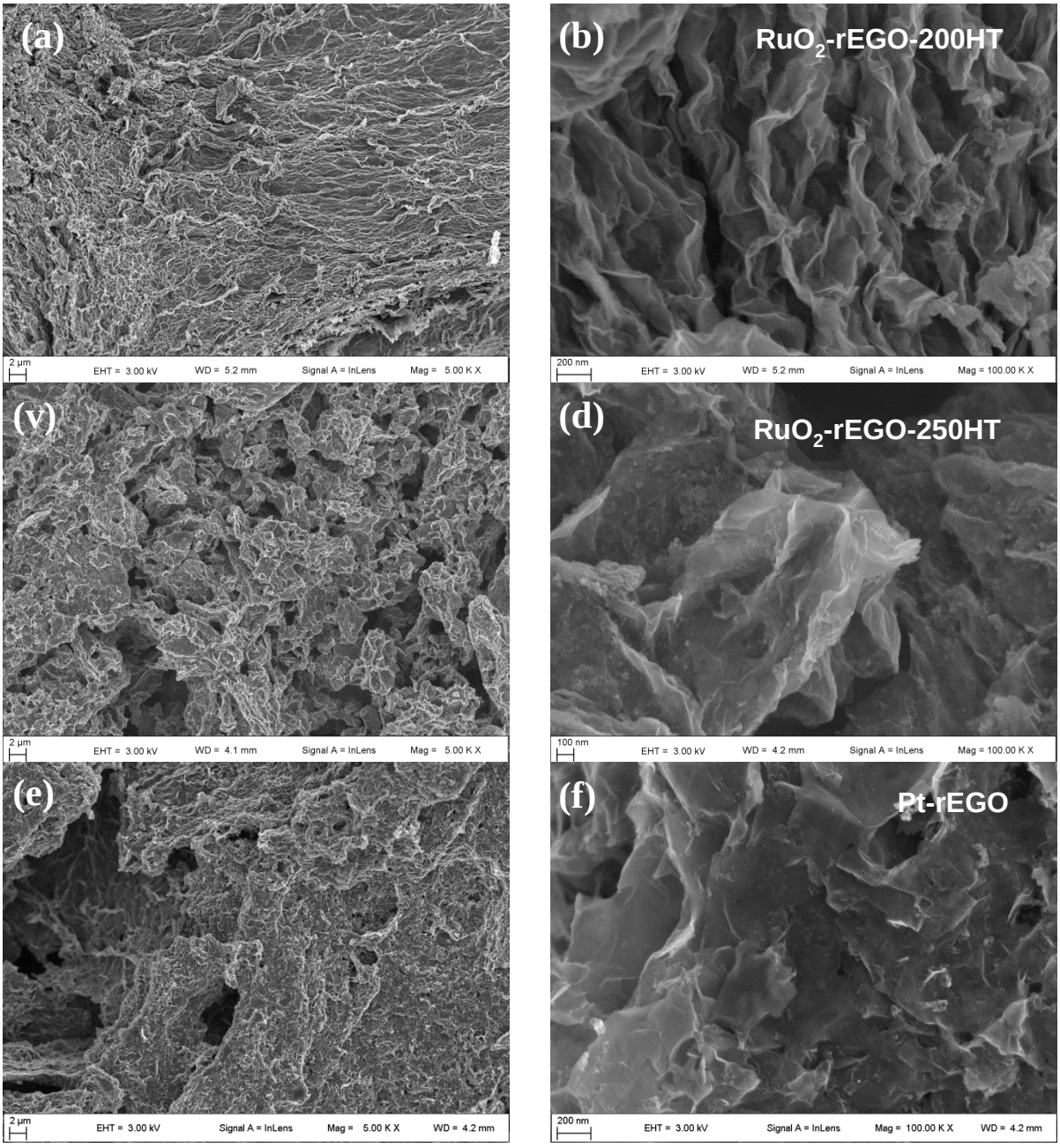

Figure 5-15. SEM images of (**a**) and (**b**)RuO_2-rEGO-200HT, (**c**) and (**d**)RuO_2-rEGO-250HT, (**e**) and (**f**) Pt-rEGO.

XPS was performed to investigate the oxidation state of the elements in the as-formed nanoparticles, and their coupling with the rEGO support. As shown in **Figure 5-12 m,** the Ru 3d high-resolution spectrum of the as-synthesized RuO_2-rEGO without heat treatment shows a set of doublet peaks located at 280.9 and 284.9 eV, corresponding to the doublet peaks for Ru (IV) $3d_{5/2}$ and $3d_{3/2}$, respectively.[343] Owing to the strong interference of Ru 3d and C 1s signals, the comparison of the survey, Ru 4d and Ru 3p spectra (**Figure 5-16 a, b and c, respectively**)

for RuO_2-rEGO, commercial RuO_2 (CM RuO_2) and metallic Ru was conducted to identify the oxidation state of Ru. In comparison to the Ru $3p_{3/2}$ peaks of CM RuO_2 at 462.5 eV and metallic Ru at 461.5 eV (**Figure 5-16 c**), the Ru $3p_{3/2}$ of RuO_2-rEGO contains only Ru (IV) with Ru $3p_{3/2}$ peak located at 462.7 eV. This indicates that the RuO_2-rEGO is dominated by Ru (IV) with a negligible amount of Ru (0) (details in **Table 5-3**). The comparison of Ru 3d (**Figure 5-16 b**) also indicates the dominance of Ru (IV) in RuO_2-rEGO.

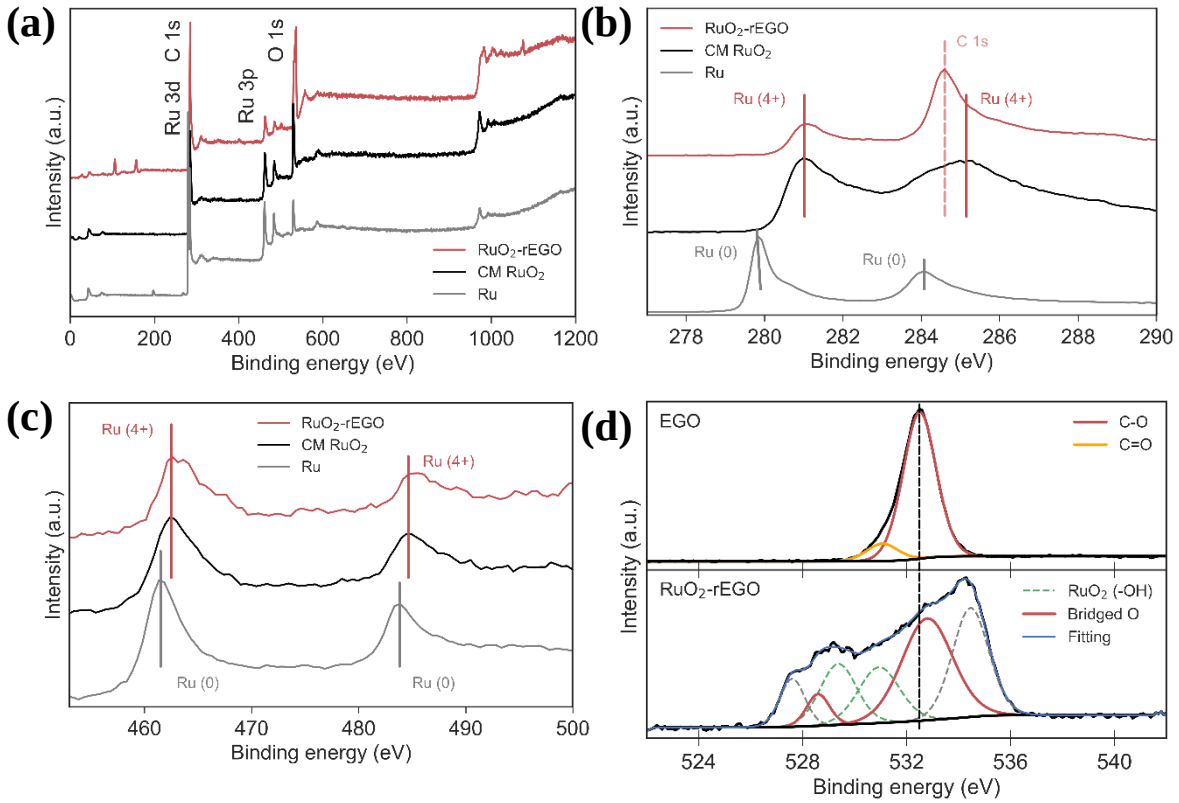

Figure 5-16. XPS characterization of the RuO_2-rEGO sample. (**a**) XPS survey, (**b**) Ru 3d, (**c**) Ru 3p, and (**d**) O 1s spectra of RuO_2-rEGO, CM RuO_2 and metallic Ru. The peaks observed at 104.3 and 155.1 eV in the survey spectrum of RuO_2-rEGO are assigned to the silicon substrate.

Table 5-3. Comparison of the binding energies of XPS Ru 3d and Ru 3p for the RuO_2-rEGO, CM RuO_2 and Ru samples.

Sample	Ru 3d		Ru 3p	
	Ru 3d5/2	Ru 3d3/2	Ru 3p3/2	Ru 3p1/2
RuO_2-rEGO-250HT	280.9	284.9	462.7	484.9
CM RuO_2	280.8	284.8	462.5	484.6
Ru	279.9	284.0	461.5	483.8

In addition, although the C 1s signal is overlapped with that of Ru $3d_{3/2}$, three components can be deconvoluted as shown in **Figure 5-12 m**, namely, C−C at 284.6 eV, C−O at 285.6 eV and C=O at 288.6 eV. The existence of C−O bond is possibly due to the strong coupling between

rEGO and RuO_2 via oxygen bridges instead of insufficient reduction of EGO. The evidence for the formation oxygen bridges includes: (1) the relative lower I_D/I_G ratio and the upshift of G band position for RuO_2-rEGO compared with the rEGO indicate possible bond formation via oxygen bridges; (2) deconvolution of overlapped Ru $3d_{3/2}$ and C 1s spectra of RuO_2-rEGO shows that percentage of C−O component in total C 1s spectrum is 19.8 at.%, much higher than that of rEGO (8.8 at.%, Table S2), this high percentage of C−O component in RuO_2-rEGO is thereby unlikely from the unreduced functional groups but oxygen bridges between RuO_2 and rEGO; (2) the component corresponding to C−O in the O 1s spectrum of RuO_2-rEGO is shifted to higher energy compared with that of EGO (**Figure 5-16 d**), suggesting a lower electron density at the oxygen sites due to the electron transfer from the oxygen to Ru atoms;[314] (3) the peak identified at 528.6 eV in O 1s spectrum is in agreement with the bridged O connecting Ru and C as-reported in the literature.[344] For the Pt 4f high-resolution spectrum of Pt-rEGO (**Figure 5-12 n**), the set of doublet peaks located at 71.2 and 74.6 eV are ascribed to the bulk Pt atoms, while the doublet peaks at higher binding energies of 72.3 and 75.6 eV correspond to the surface atoms of Pt.[345] Further, inductively coupled plasma-optical emission spectrometry (ICP-OES) reveals that the mass loadings of RuO_2 and Pt in the as-prepared composites are 41.6 ± 0.9 wt.% and 10.2 ± 1.0 wt.%, respectively.

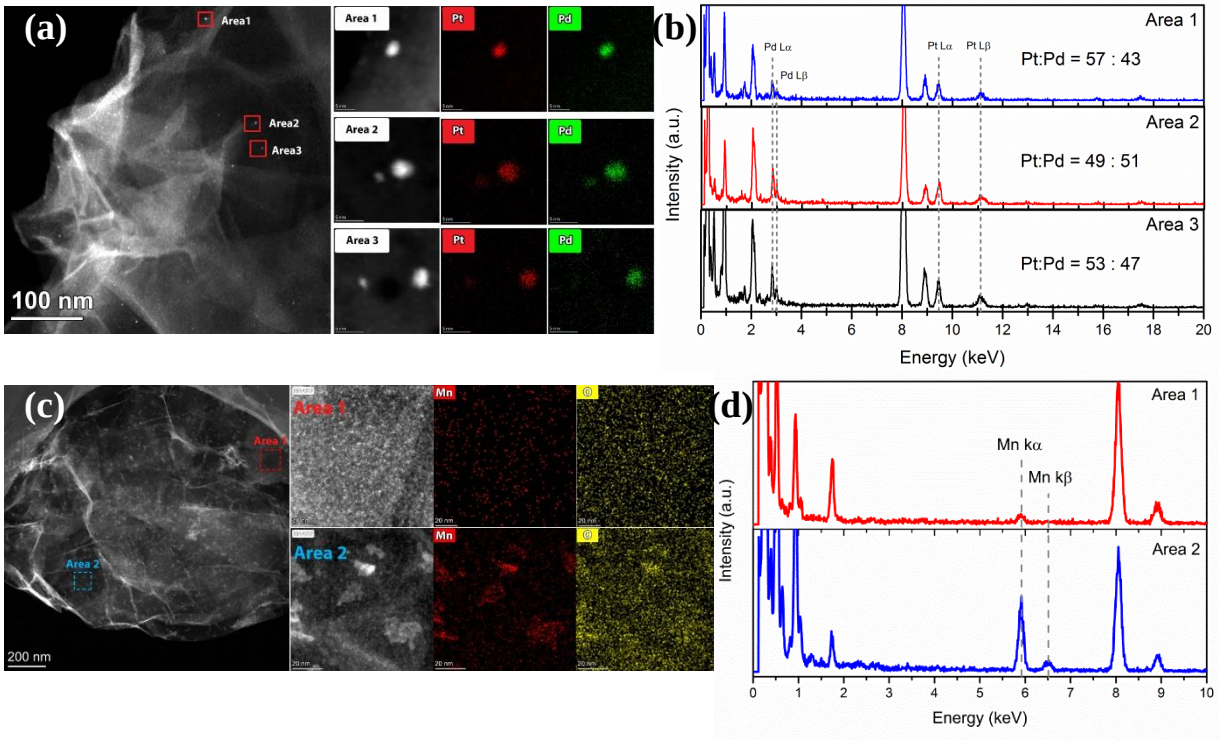

Figure 5-17. (**a**) Representative STEM image of PtPd-rEGO, high magnification HAADF images and STEM-EDS mappings of PtPd nanoparticles. (**b**) Details EDS spectra of corresponding mapping areas, the EDS elemental quantification based on Pt Lα and Pd Lα shows the nanoparticles is in accordance with the composition ratio of

added precursor. (**c**) Representative HAADF image of MnO_x-rEGO, images and STEM-EDS mappings of MnO_x nanoparticles and flakes. (**d**) The EDS spectra of the areas marked by dashed rectangles.

The laser-induced solution approach leads to deeply reduced rEGO modified with ultrafine catalyst nanoparticles in a single step, as demonstrated above using RuO_2 and Pt as model materials. To further prove the versatility of this laser-assisted approach in the deposition of various types of functional nanoparticles on the surface of rEGO sheets, PtPd alloy and MnO_x nanoparticles have also been successfully deposited using H_2PtCl_6/Na_2PdCl_4 and $MnCl_2$ as precursor metal salts, respectively. The corresponding TEM characterizations for PtPd/rEGO and MnO_x/rEGO are shown in **Figure 5-17 a and b** and **Figure 5-17 c and d**, respectively. Based on the experimental results and literature knowledge,[297, 299, 305] possible reactions behind this laser-induced solution approach have been proposed. The photon excitation of EGO creates electron-hole pairs as:

$$\mathrm{EGO} + \mathrm{h}\nu \rightarrow \mathrm{EGO} + \mathrm{h}_{\mathrm{vb}}^{+} + \mathrm{e}_{\mathrm{cb}}^{-} \quad (1)$$

where h_{vb}^+ and e_{cb}^- are photo-generated holes and electrons, respectively. The subsequent reduction of EGO by photo-generated electrons occurs following:

$$\mathrm{EGO} + \mathrm{e}_{\mathrm{cb}}^{-} \rightarrow \mathrm{rEGO} + \mathrm{OH}^{-} \quad (2)$$

For reductive photodeposition of metal (M) nanoparticles, the reduction of metal ions happens as:

$$\mathrm{M}^{\mathrm{n}+}(\mathrm{aq}) + \mathrm{ne}_{\mathrm{cb}}^{-} \rightarrow \mathrm{M}(\mathrm{s}) \quad (3)$$

While for the oxidative photodeposition of metal oxide nanoparticles, the reaction could occur through:

$$\mathrm{M}^{\mathrm{n}+}(\mathrm{aq}) + \mathrm{nh}_{\mathrm{vb}}^{+} + \mathrm{nH_2O} \rightarrow \mathrm{MO}_n(\mathrm{s}) + 2\mathrm{nH}^{+} \quad (4)$$

The excess photo-generated holes and electrons are consumed by the sacrificial electron donor (D) and acceptor (A), respectively, as follow:

$$\mathrm{nh}_{\mathrm{vb}}^{+} + \mathrm{D} \rightarrow \mathrm{D}^{\mathrm{n}+} \quad (5)$$

$$\mathrm{ne}_{\mathrm{cb}}^{-} + \mathrm{A} \rightarrow \mathrm{A}^{\mathrm{n}-} \quad (6)$$

In an actual photodeposition process, the consumption of excess electrons leads to the reduction of protons to form H_2 gas, while the consumption of excess holes could oxidize water to from O_2.[299] If sacrificial organic agents (e.g. methanol, isopropanol) are added, their reactions with

photo-generated holes/electrons form highly reducing radical species, which participate in the reduction of metal ions.[299, 305] In the present work, isopropanol and acetone were added as sacrificial electron donor and acceptor, respectively, leading to the formation of highly reducing carbon-centred isopropanol radicals,[305] which further benefit a fast and thorough reduction of EGO and metal ions. In addition, these highly reducing radicals could also be the reason that metallic Ru is present in the RuO_2-rEGO product.

5.5.3 Electrocatalytic Performance

To demonstrate the applications of the as-prepared RuO_2-rEGO and Pt-rEGO composites, their performances as electrocatalysts have been measured and evaluated. To obtain the intrinsic catalytic activities of the samples for OER, HER and ORR, the ohmic-drop correction was carried out to minimize the effects of solution resistance (**Figure 18**).

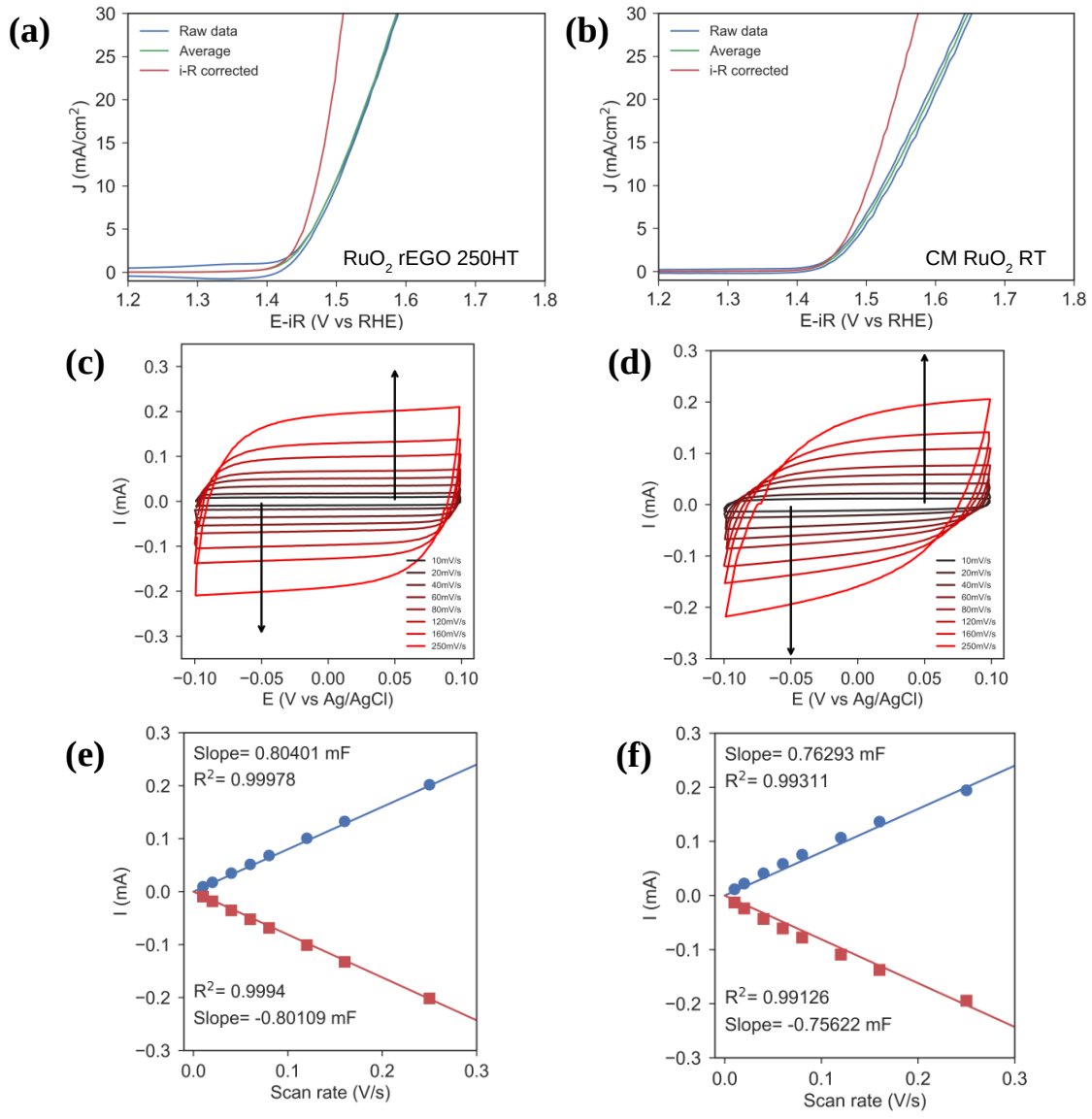

Figure 5-18. (**a**) Capacitive and the ohmic-drop corrected CVs of RuO_2-rEGO-250HT, (**b**) and CM RuO_2 deposited on the 5 mm GC electrode. (**c**) CVs of RuO_2-rEGO-250HT, (**d**) and CM RuO_2 measured in the non-Faradaic potential range of −0.1 to 0.1 V (vs Ag/AgCl) at a scan speed of 10, 20, 40, 60, 80, 120, 160, 250 mV s^{-1}. The anodic (blue) and cathodic (red) charging current measured at 0.05 V and −0.05 V vs Ag/AgCl, respectively for (**e**) RuO_2-rEGO-250HT and (**f**) CM RuO_2, the double-layer capacitance determined by linear fitting the charge value.

For RuO_2-rEGO, the OER polarization voltammogram was obtained at a scan rate of 10 mV s^{-1} in O_2-saturated 1.0 M KOH aqueous electrolyte using a rotating disk electrode (RDE) at a rotating speed of 2000 rpm. As shown in **Figure 5-19 a**, the RuO_2-rEGO-250HT possesses a superior catalytic activity with a small overpotential of 225 mV at 10 mA cm^{-2}, compared to the overpotential for the sample heat-treated at 200 °C (RuO_2-rEGO-200HT), which is significantly larger (310 mV). There is no obvious catalytic activity for the sample annealed at 150 °C (**Figure 5-20 a**). In addition, there is a noticeable drop in the Tafel slope for the RuO_2-rEGO composites with the increase of heat treatment temperature from 200 to 250 °C (**Figure 5-19 b**). These results suggest the OER activity is profoundly affected by the crystallinity of RuO_2. Note that it is known that metallic Ru nanoparticles are unstable and dissolve completely during the first OER polarization,[346] and this dissolution of Ru is more severe in alkaline electrolytes than in acidic electrolytes.[347]] Therefore, the small content of Ru nanoparticles in RuO_2-rEGO catalyst would dissolve rapidly in the first OER polarization and have minimum influence on the subsequent evaluation of the catalytic activity. This has been confirmed by the first 11 OER CV scans recorded with the RuO_2-rEGO catalyst (**Figure 5-20 b and c**), the current due to Ru oxidation/dissolution appears only in the first anodic scan, and the CVs overlap with each other after the second cycle. As a benchmark, the OER performance of CM RuO_2 (Premion, Alfa Aesar) was measured under the same conditions. Notably, CM RuO_2 requires an overpotential of 283 mV to reach the current density of 10 mA cm^{-2} (**Figure 5-19 a**), with RuO_2 loading 2.4 times higher than that of RuO_2-rEGO (42.5 wt.% of RuO_2). In addition, as shown in **Figure 5-9 b,** the RuO_2-rEGO-250HT shows a smaller Tafel slope (50 mV dec^{-1}) than that of CM RuO_2 (53 mV dec^{-1}). Chronopotentiometric testing at 10 mA cm^{-2} was used to evaluate the durability of RuO_2-rEGO-250HT catalyst, as shown in the inset of **Figure 5-19 a**, the overpotential of RuO_2-rEGO-250HT increased by only 14.1 mV after 3 hours testing. The comparison of linear sweep voltammograms (LSVs) (**Figure 5-21 a**) and Tafel plots (**Figure 5-21 b**) for the RuO_2-rEGO-250HT catalyst before and after chronopotentiometric test shows only slight degradation of catalytic activity. The LSVs after chronopotentiometric measurements show a slight degradation of the OER performance (**Figure 5-21 a**), possibly due to the dissolution of the RuO_2 and electrochemical oxidation of rEGO. However, despite the slight decrease in current density, the change in the Tafel slope is

negligible (**Figure 5-21 b**), which indicates a similar level of activity for the catalysts before and after the durability test.

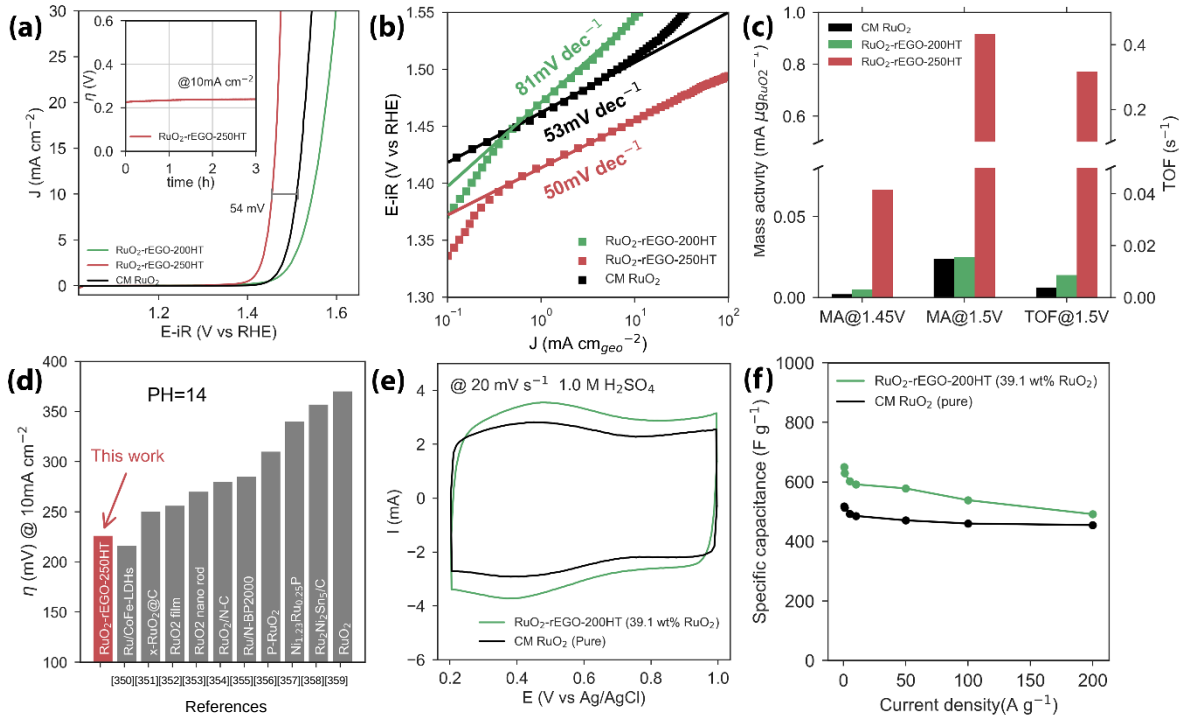

Figure 5-19. (**a**) LSVs of RuO_2-rEGO-200HT, RuO_2-rEGO-250HT and CM RuO_2 measured at a scan rate of 10 mV s^{-1} in 1.0 M KOH electrolyte at 2000 rpm (inset: chronopotentiometry of RuO_2-rEGO-250HT catalyst at a current density of 10 mA cm^{-2}). (**b**) Tafel plots derived from LSV curves. (**c**) Comparison of mass activities at current densities of 1.45 V and 1.5 V, respectively, the comparison of TOF values at 1.5 V is also included. (**d**) Comparison of the overpotentials required to achieve a 10 mA cm^{-2} current density for various types of literature reported Ru based electrocatalysts. Note: the bibliographic information of the reference numbers can be found in **Table 5-4**. (**e**) CVs recorded at 20 mV s^{-1} and (**f**) specific capacitances at various current densities for the RuO_2-rEGO-200HT and CM RuO_2 electrodes in 1 M H_2SO_4 aqueous electrolyte.

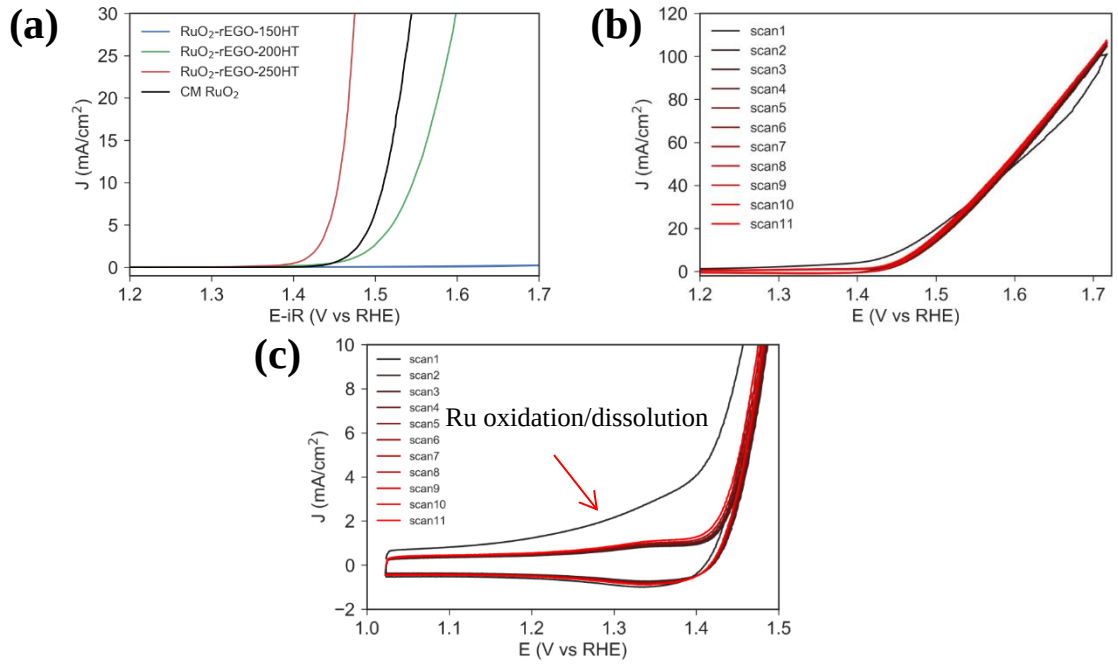

Figure 5-20. (**a**) Polarization curves of RuO_2-rEGO-150HT, RuO_2-rEGO-200HT, RuO_2-rEGO-250HT and CM RuO_2 in O_2-saturated 1.0 M KOH electrolyte at 10 mV s^{-1}. It is clear that the RuO_2-rEGO-150HT shows poor OER activity. The first 11 OER CV scans recorded with the RuO_2-rEGO-250HT catalyst. (**b**) and (**c**) are the same CV scans shown in different potential ranges. The current corresponding to oxidation/dissolution of Ru nanoparticles in the first anodic scan is marked by a red arrow.

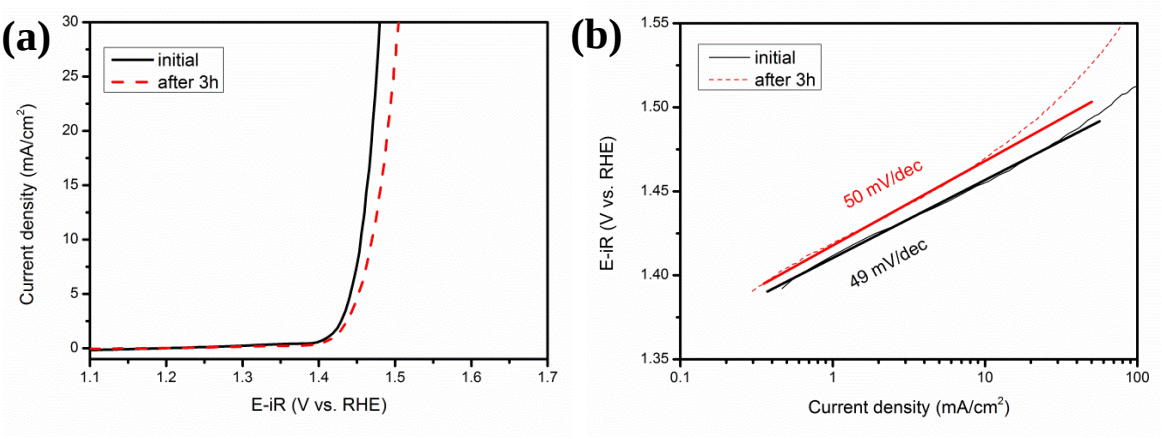

Figure 5-21. (**a**) The ohmic-drop corrected LSVs of RuO_2-rEGO-250HT before and after OER chronopotentiometric test at a current density of 10 mA cm^{-2} in O_2-saturated 1.0 M KOH; (**b**) and the corresponding Tafel plots.

The electrochemically active surface area (ECSA) of the catalysts has been estimated by measuring the double-layer capacitance as reported in the literature.[348] The C_{DL} was determined from the cyclic voltammetry (CV) scans in the non-Faradaic region between −0.1 and 0.1 V vs Ag/AgCl in 1 M KOH aqueous electrolyte (**Figure 5-18 c and d**). The ECSA was estimated to be 50.2 and 47.4 cm^2 for RuO_2-rEGO-250HT and CM RuO_2, respectively, indicating that the RuO_2-rEGO composite with 42.5 wt.% of RuO_2 has a slightly higher accessible surface area to the electrolyte in comparison with CM RuO_2 (100 wt.% RuO_2 loading). In addition, the specific surface areas derived from nitrogen adsorption/desorption isotherms (**Figure 5-22 a and b**) also suggest that the RuO_2-rEGO has a higher specific surface area (261.8 m^2 g^{-1}) than that of CM RuO_2 (49.1 m^2 g^{-1}). Electrochemical impedance spectroscopy (EIS) was conducted at 1.5 V vs RHE for the as-prepared catalysts (**Figure 5-22 c**). Interestingly, the charge transfer resistances derived from the Nyquist plots for RuO_2-rEGO composites (6.72 and 10.59 Ω for RuO_2-rEGO-250HT and RuO_2-rEGO-200HT, respectively) are significantly smaller than that of CM RuO_2 (18.05 Ω). The enhanced charge transfer in the RuO-rEGO composites is attributed to the highly conductive rEGO support, which provides fast electron transfer routes. In addition, the smaller charge transfer resistance for RuO_2-rEGO composite annealed at 250 °C, compared to that annealed at 200 °C, is probably due to increased electrical conductivity of RuO_2 itself at higher annealing temperatures.[349]

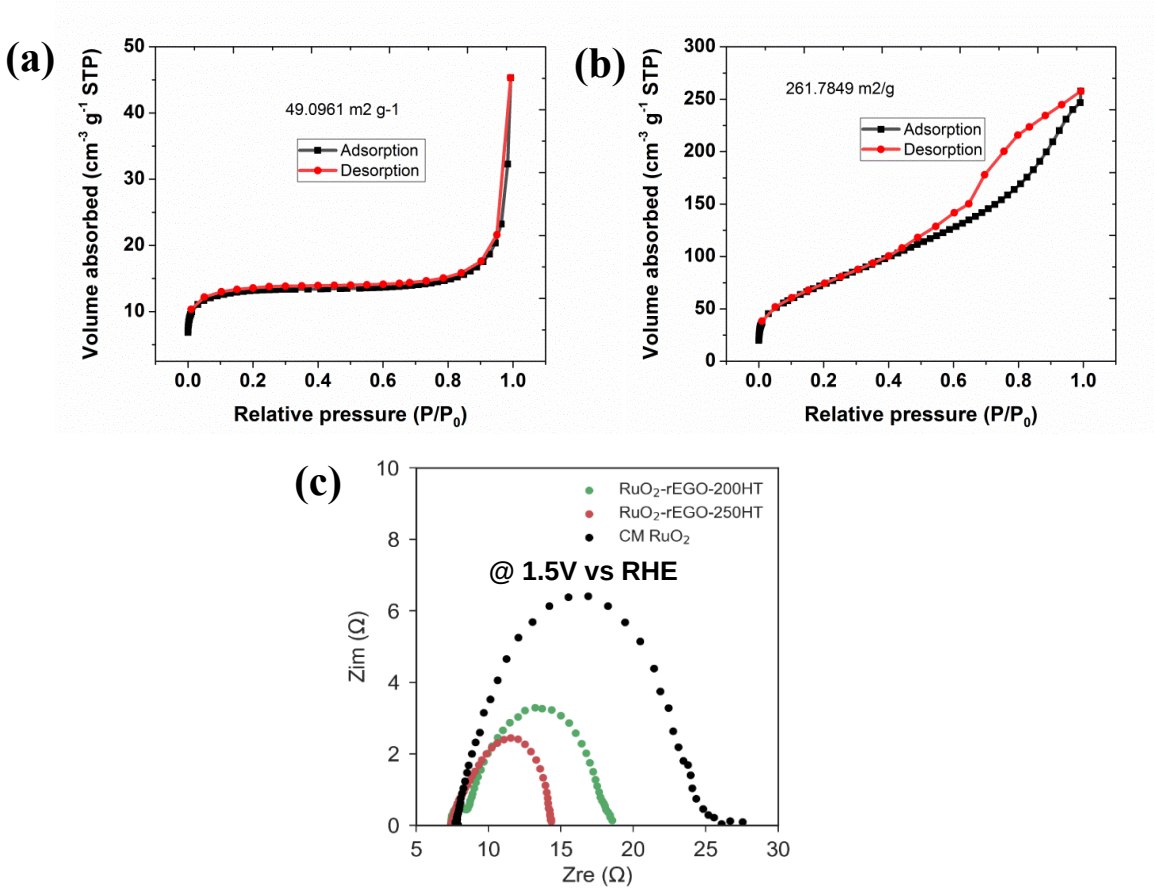

Figure 5-22. BET adsorption and desorption isotherms of (**a**) CM-RuO_2, and (**b**) RuO_2-rEGO-250HT. (**c**) Nyquist plot of RuO_2-rEGO-250HT, RuO_2-rEGO-200HT and CM RuO_2 at 1.5 V vs RHE in 1.0 M O_2-saturated KOH electrolyte.

As revealed in **Figure 5-19 c**, the RuO_2-rEGO-250HT exhibits much higher (one order of magnitude) mass activity and turnover frequency (TOF) than that of the CM RuO_2 (A detailed TOF calculation is given in Supporting Information). This further confirms the enhancement of intrinsic catalyst activity for the RuO_2-EGO composites. The OER performance of RuO_2-rEGO-250HT has been further compared with the state-of-the-art Ru-based catalysts reported in the literature. The overpotential of RuO_2-rEGO-250HT at 10 mA cm^{-2} and the Tafel slope is outperforming the majority of the literature values (**Figure 5-19 d** and **Table 5-4**). The low overpotential, small Tafel slope, high mass activity and TOF, together with the good durability of the RuO_2-rEGO composites indicate their great potential as electrocatalysts for OER.

Table 5-4. OER overpotentials and Tafel slopes of RuO_2-rEGO-250HT and other reported ruthenium-based catalysts in an alkaline electrolyte.

Catalysts	Electrode	Electrolyte	Loading (total) (mg cm^{-2})	Overpotential @ 10mA cm^{-2} (mV)	Tafel slope (mV dec^{-1})	Ref.
RuO_2-rEGO-250HT	GCE[a)]	1.0 M KOH	0.255	226	50	This work
Ru/CoFe-LDHs	Carbon paper	1.0 M KOH	1	198	39	[350]
	Carbon paper	1.0 M KOH	0.25	216	N/A	[350]
	GCE	1.0 M KOH	0.25	213	N/A	[350]
x-RuO_2@C	GCE	1.0 M KOH	0.612	250	68	[351]
RuO_2 film	Ti plate	1.0 M NaOH	N/A	256	60	[352]
RuO_2 nano rod	GCE	1.0 M NaOH	0.357	270	78.31	[353]
RuO_2/N-C	GCE	1.0 M KOH	0.306	280	56	[354]
Ru/N-BP2000-4wt%	GCE	1.0 M KOH	0.285	285	70	[355]
P-RuO_2	GCE	1.0 M KOH	0.2	310	60.7	[356]
$Ni_{1.25}Ru_{0.25}P$	GCE	1.0 M KOH	0.284	340	N/A	[357]
Ru_2Ni_2 SNs/C	GCE	1.0 M KOH	0.1	357	75	[358]
RuO_2	GCE	1.0 M KOH	0.2	370	105	[359]

[a)] GCE: glassy carbon electrode

RuO_2 is known to be a very promising electrode material for supercapacitors due to its large specific capacitance (experimental values up to 720 F g^{-1}) and good rate capability.[349] However, the rarity of Ru in Earth's crust results in the high cost of RuO_2, which limits its wider application in the real world. This challenge could be possibly solved by developing composites of RuO_2 and carbon, which can reduce the usage of RuO_2 while maintaining high specific capacitance. Hence, the electrochemical capacitance of RuO_2-rEGO composites (RuO_2 loading: 41.6 ± 0.9 wt.%) has been measured and evaluated.

Initially, the effect of annealing temperature on the electrochemical capacitance of the RuO_2-rEGO composite was investigated (**Figure 5-23**). The specific capacitance increases with the rise of annealing temperature and maximize at 200 °C, further increase of the annealing temperature causes deterioration of the specific capacitance. This phenomenon is consistent with previous works and can be explained by the balancing of ionic (proton), and electronic conductivity of hydrous RuO_2 during annealing (**Figure 5-23**)[349]. The same trend was also reported by pioneering works.[337, 360-361] Different from the amorphous RuO_2 with nano-porous morphology, the crystalline RuO_2 possesses a compact and dense surface, which minimizes the utilization of active material. The gradual loss of confined water with the increasing of annealing temperature also deteriorates the proton mobility of hydrous RuO_2. As a result, the

capacitance drops with increasing temperature above 200 °C. However, when the annealing temperature was below 200 °C, the partial removal of confined water in the hydrous RuO_2 increased the specific surface area and enhanced the electron mobility. Hence, the balanced electron and proton conduction at 200 °C leads to the highest specific capacitance. **Figure 5-19 e** shows the CVs of RuO_2-rEGO composite annealed at 200 °C at a scan rate of 20 mV s^{-1} in 1 M H_2SO_4 electrolyte. The CV of CM RuO_2 recorded under the same conditions is added for comparison. Both the CVs show a typical rectangular shape corresponding to capacitive behaviour. A pair of broad redox peaks appear at around 0.4 V vs Ag/AgCl due to the Ru (III)/Ru (IV) transition. **Figure 5-19 f** compares the gravimetric specific capacitances of RuO_2-rEGO-200HT composite and the CM RuO_2. Note that the specific capacitance of RuO_2-rEGO-200HT is normalized by the total mass of the composite. The RuO_2-rEGO-200HT shows higher specific capacitance of 649.7 F g^{-1} at a current density of 0.5 A g^{-1} with good rate capability, outperforming the CM RuO_2 (518.2 F g^{-1} at 0.5 A g^{-1}).

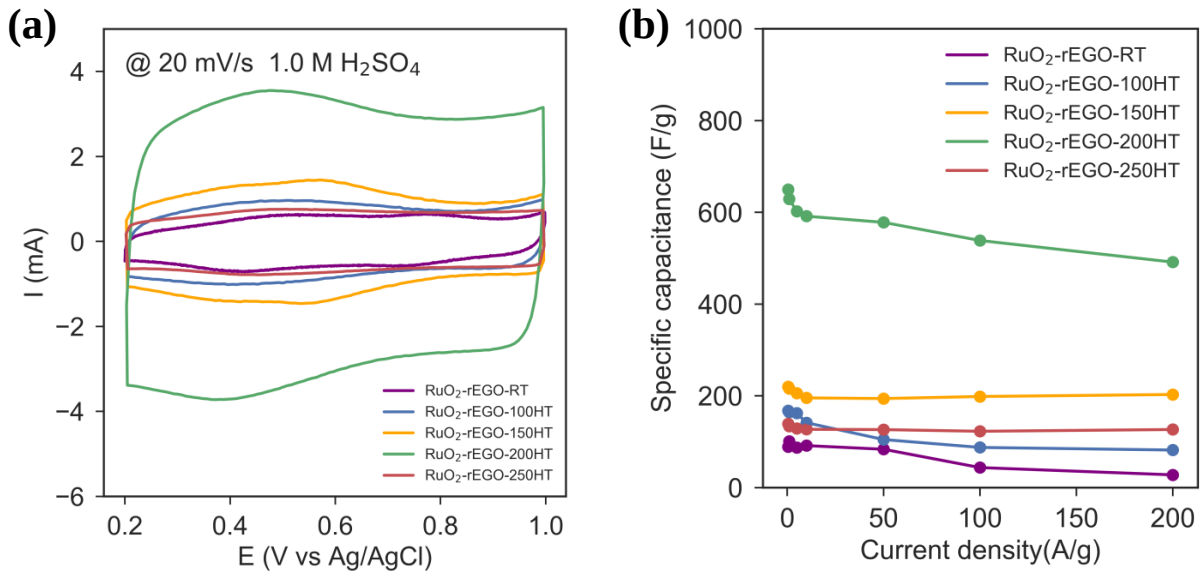

Figure 5-23. (**a**) CV responses, and (**b**) specific capacitance of RuO_2-rEGO heat-treated at 100, 150,200 and 250 °C tested in 1.0 M H_2SO_4 electrolyte at a scan speed of 20 mV s^{-1}.

For the Pt nanoparticle modified rEGO (Pt loading 10.2 ± 1.0 wt.%), the catalytic performances with respect to ORR and HER have been measured and compared with CM Pt/C (20 wt.%, HISPEC 3000, Johnson Matthey). **Figure 5-24 a** shows the LSV response of Pt-rEGO catalyst as a function of rotation speed in an O_2 saturated 0.1 M KOH aqueous electrolyte. The Koutechy-Levich (K-L) relation of the LSV curves (inset of Figure 5a) exhibits good linearity with an average electron transfer number (*n*) of 3.93, suggesting a four-electron reduction to water is largely operative. In addition, the Pt-rEGO catalyst shows a higher double layer capacitance in comparison with CM Pt/C according to the CVs recorded in N_2-saturated electrolyte (**Figure**

5-25), possibly due to the large surface area of rEGO. The ECSA of the catalysts were further determined through integration of the charge for hydrogen adsorption and desorption in a N_2 saturated environment. Due to the ultrafine size of the Pt nanoparticles (2.0 ± 0.5 nm), the Pt-rEGO provides an enhanced ECSA of 97.2 m^2 g_{Pt}^{-1} compared with that of CM Pt/C (73.9 m^2 g_{Pt}^{-1}).

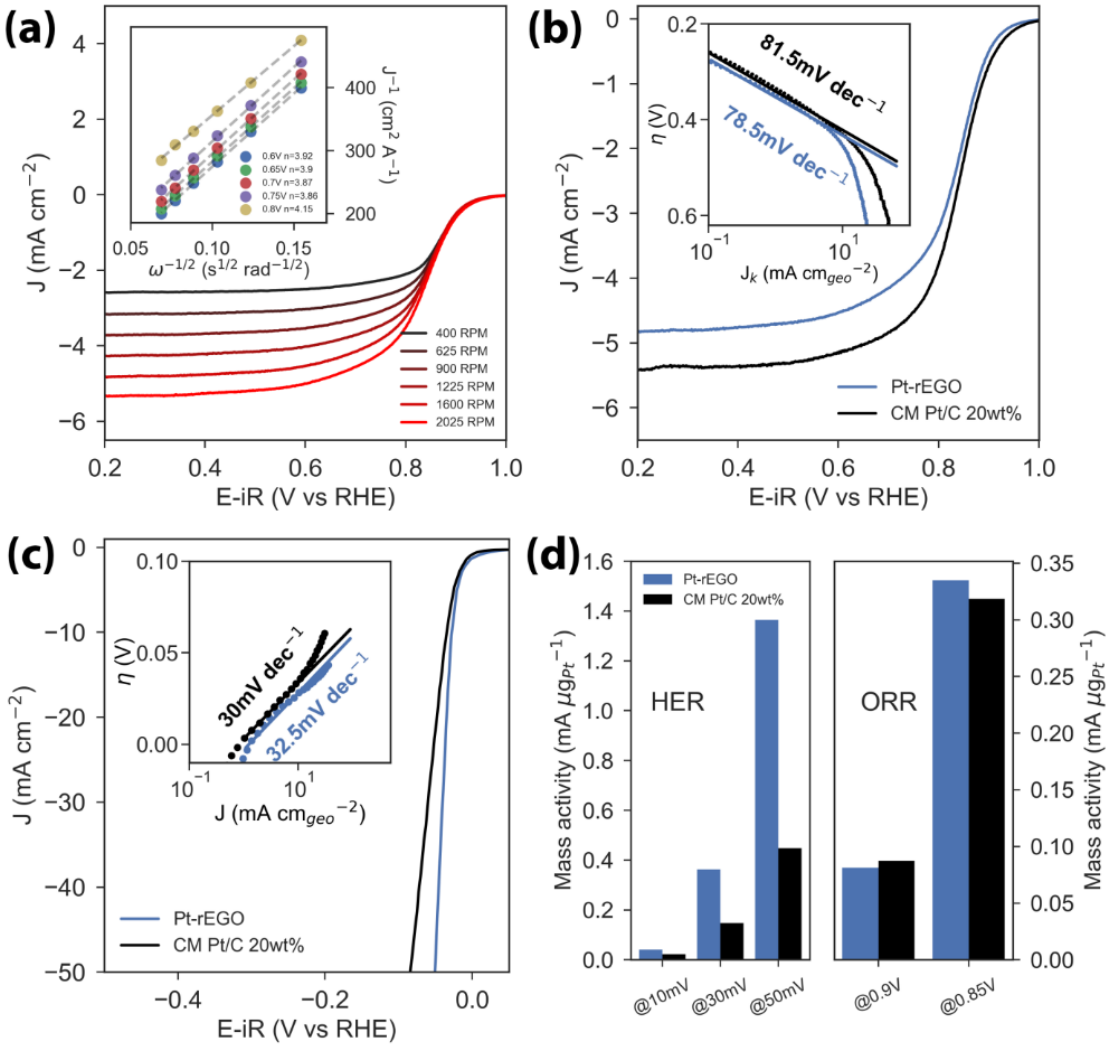

Figure 5-24. (**a**) LSVs of Pt-rEGO tested at different rotation speed from 400 to 2025 rpm at a scan rate of 10 mV s^{-1} in O_2-saturated 0.1 M KOH electrolyte, the inset shows the corresponding Koutechy-Levich plots. (**b**) Comparison of LSVs for Pt-rEGO and 20 wt.% Pt/C at 1600 rpm, the inset shows the corresponding Tafel plots. (**c**) LSVs of Pt-rEGO and CM Pt/C 20 wt.% in N_2-saturated 0.5 M H_2SO_4 electrolyte at a scan rate of 10 mV s^{-1} and a rotation speed of 2000 rpm, and the inset image shows the corresponding Tafel plots. (**d**) Comparison of mass activities of Pt-rEGO and CM Pt/C 20 wt.% catalysts for both HER (left panel) and OER (right panel) at different overpotentials.

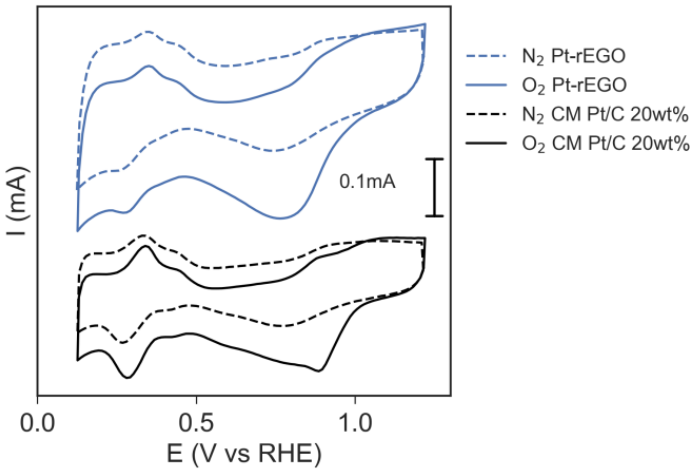

Figure 5-25. CVs of Pt-rEGO 10.2 wt.% and CM Pt/C 20 wt.% in N_2 and O_2-saturated 0.1 M KOH electrolyte.

As displayed in **Figure 5-24 b**, Pt-rEGO exhibits a similar onset potential (0.95 V), and half-wave potential (0.83 V) to that of the CM Pt/C, indicating comparable activities of Pt-rEGO and CM Pt/C in spite of the much lower Pt loading (10.2 wt.% vs 20 wt.%). Tafel plots (inset of Figure 5b) suggest a slightly enhanced Tafel value of 78.5 mV dec^{-1} for Pt-rEGO compared with that of the Pt/C (81.5 mV dec^{-1}), indicating fast kinetics of ORR with Pt-rEGO catalyst. However, the diffusion-limited current density of ORR for Pt-rEGO (4.89 mA cm^{-2}) is slightly smaller than that of CM Pt/C (5.36 mA cm^{-2}). This is caused by retarded diffusion of dissolved O_2 through the stacked graphene sheets.[362] Effective prevention of graphene restacking could lead to further enhancement in performance, but it remains a big challenge. Nevertheless, the 2D rEGO flakes act as barriers to prevent the leaching and dissolution of Pt,[362] leading to significantly improved ORR durability for Pt-rEGO catalyst (76% retention after ca. 5.6 hours test) compared with that of CM Pt/C (63% retention after ca. 5.6 hours; see **Figure 5-26 a** for details).

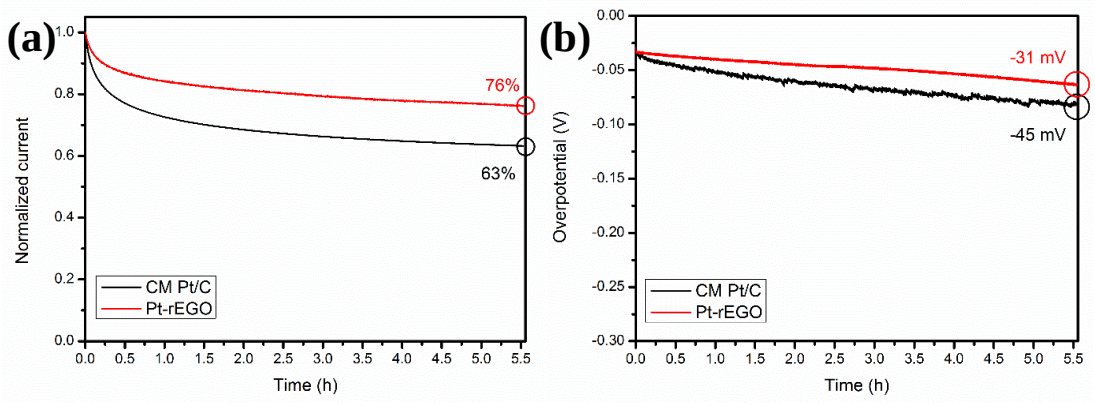

Figure 5-26. (**a**) ORR current-time chronoamperometric responses of CM Pt/C and Pt-rEGO at 0.55 V (vs RHE) in O_2-saturated 0.1 M KOH. (**b**) HER chronopotentiometry of CM Pt/C and Pt-rEGO at a current density of 10 mA cm^{-2} in N_2-saturated 0.5 M H_2SO_4.

For both ORR and HER, the Pt-rEGO catalyst displayed better durability than that of CM Pt/C. The durability of Pt-rEGO as ORR catalyst was evaluated by chronoamperometric test in 0.1 M KOH solution saturated with O_2 at 0.55 V vs RHE at a rotation rate of 1600 rpm to achieve the diffusion-limit current density. It is clear that Pt-rEGO catalyst with current retention of 76% obviously outperforms that of CM Pt/C, which only retains 63% of its initial current after ca. 5.6 hours (20000 s) of chronoamperometric test. The durability of Pt-rEGO as HER catalyst was tested using chronopotentiometry at a current density of −10 mA cm^{-2} in N_2-saturated 0.5 M H_2SO_4 electrolyte at a rotation rate of 2000 rpm to avoid bubble accumulation. After ca. 5.6 hours (20000 s) of chronopotentiometry test, the Pt-rEGO sample exhibits an overpotential increase of –31 mV compared with the initial value, while CM Pt/C shows a more significant increase of –45 mV in overpotential to maintain the current density of 10 mA cm^{-2}. These results suggest that the Pt-rEGO exhibits better durability for both HER and ORR than that of the CM Pt/C 20 wt.%. The enhanced stability is primarily due to the two-dimensional structure of rEGO, which acts as a barrier to prevent the leaching and dissolution of Pt into the electrolyte.

The Pt-rEGO exhibits superior catalytic activity for HER when compared with the CM Pt/C. The HER activity of Pt-rEGO was measured in N_2 saturated 0.5 M H_2SO_4 electrolyte. **Figure 5-24 c** shows the polarization curves of Pt-rEGO and CM Pt/C catalysts after ohmic-drop correction. To drive 10 mA cm^{-2} current density, the Pt-rEGO only required a small overpotential of 28.27 mV which is superior to that of CM Pt/C (33.13 mV). The Tafel plots (inset of **Figure 5-24 c**) show comparable kinetics of Pt-rEGO (32.5 mV dec^{-1}) and CM Pt/C (30 mV dec^{-1}). Similar to ORR, the barrier effects of 2D rEGO leads to an obviously improved durability of Pt-rEGO for HER compared with that of CM Pt/C (**Figure 5-26 b**). Figure 5d reveals the mass activities of Pt-rEGO catalyst for both HER and ORR, in comparison with that of CM Pt/C. Since the Pt loading Pt-rEGO (10.2 wt.%) is around half the value of CM Pt/C (20 wt.%), it shows more than double the mass activity for HER at overpotentials of 10, 30 and 50 mV. The statistics of the Pt particles in CM Pt/C shows an average size of 4.3 nm (σ = 1.0) (**Figure 5-27**), which is twice the size of Pt particles in Pt-rEGO (2.0 nm σ=0.5). The results imply that the facilitated catalytic performance of Pt-rEGO can be possibly ascribed to smaller particle size and thus higher utilization of Pt atoms. For ORR, the Pt-rEGO exhibits comparable mass activity with CM Pt/C at both 0.85 and 0.9 V vs RHE, in spite of the slightly lower diffusion-limited current density due to the inhibited oxygen diffusion in the restacked graphene layers.

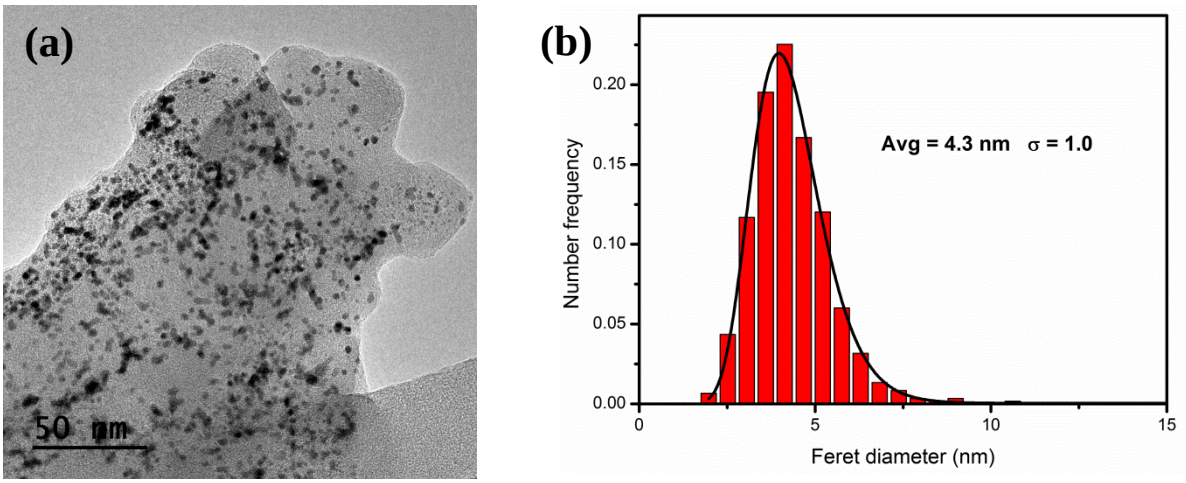

Figure 5-27. (**a**) Representative TEM image of CM Pt/C 20 wt.% catalyst, and (**b**) the size distribution of Pt nanoparticles. The statistics of particles size was conducted by counting 600 particles, and fitted with a log-normal function.

The RuO_2 and Pt modified rEGO show superior catalytic activity for the water splitting processes (OER and HER) compared with the commercial catalysts and literature values, together with comparable ORR activity (**Table 5-5 and 5-6**). The better performance of the Pt modified rEGO catalysts for HER compared with ORR is possible because that the diffusion limitation in the restacked rEGO layers has a lower effect on HER due to the high concentration of H^+ in the acidic electrolyte.[363]

Table 5-5. HER overpotentials and Tafel slopes of Pt-rEGO and other reported platinum-based catalysts tested in 0.5 M H_2SO_4.

Catalysts	Electrode	Electrolyte	Loading (total) (mg cm^{-2})	Overpotential @ -10mA cm^{-2} (mV)	Tafel slope (mV dec^{-1})	Ref.
Pt-rEGO	GCE	0.5 M H_2SO_4	0.255	28.3	32.5	This work
Pt_5/HMCS	GCE	0.5 M H_2SO_4	0.319	20.7	28.3	[364]
Pd/Cu-Pt	GCE	0.5 M H_2SO_4	0.041	22.8	25	[365]
400-SWNT/Pt	GCE	0.5 M H_2SO_4	~0.19	27	38	[366]
Pt/MoS_2	Stainless steel sheet	0.5 M H_2SO_4	~3.066	31	52	[367]
PtCoFe@CN	GCE	0.5 M H_2SO_4	0.285	45	32	[368]
Pt/def-WO_3@CFC	GCE	0.5 M H_2SO_4	N/A	42	61	[369]
Pt ML/AuNF/Ni foam	Ni foam	0.5 M H_2SO_4	N/A	~68	53	[370]
Pt-MoS_x	GCE	0.5 M H_2SO_4	N/A	80	48	[371]
Pt/WS_2	GCE	0.5 M H_2SO_4	~0. 094	80	55	[372]

Table 5-6. ORR onset potential, halfwave potential and Tafel slope of Pt-rEGO and other reported platinum-based catalysts in 0.1 M KOH electrolyte.

Catalysts	Electrode	Electrolyte	Loading (total) (mg cm^{-2})	E_{onset} [a] (V vs RHE)	$E_{1/2}$ [b] (V vs RHE)	Tafel slope (mV dec^{-1})	Ref.
Pt-rEGO	GCE	0.1 M KOH	0.051	0.95	0.833	78.5	This work
PtCo@NC	GCE	0.1 M KOH	N/A	~1.01	0.925	N/A	[373]
Pt-Pd core-island shell NCs	GCE	0.1 M KOH	0.03	~1	0.884	N/A	[374]
PtPd@Pt	GCE	0.1 M KOH	0.13	0.98	0.88	N/A	[375]
Co@Pt-NC	GCE	0.1 M KOH	0.32	0.99	0.87	71.4	[376]
Pt/TiO_2-FGS	GCE	0.1 M KOH	0.051	~1.0	0.85	76	[377]
$Pt_{0.1}$-PGR	GCE	0.1 M KOH	0.714	~0.98	~0.84	N/A	[378]
PtCo-NW/CF	GCE	0.1 M KOH	N/A	~0.91	~0.79	N/A	[379]
Ni@Pd/Pt-2h	GCE	0.1 M KOH	0.225	0.898	~0.85	N/A	[380]
1-PtNP/MWCNT	GCE	0.1 M KOH	~0.097	N/A	0.77	61	[381]

[a] E_{onset}: onset potential; [b] $E_{1/2}$: half-wave potential.

5.6 Conclusion

In summary, a simple, yet versatile, UV laser-assisted method based on photo-induced redox processes has been demonstrated in this work for continuous solution reduction and modification of EGO with functional nanoparticles. The use of EGO with a lower degree of oxidation, and thus narrower bandgap, and better structural integrity compared with conventional CGO leads to deeply reduced rEGO with a low oxygen content of 4.0 at.%. Various types of ultrafine metal (oxide) nanoparticles (Pt, PtPd, RuO_2, MnO_x) have been uniformly deposited on the rEGO support simply by using different metal salts precursor solutions. The RuO_2-rEGO composite with an average RuO_2 particle size of 2.8 nm shows an extraordinary activity for OER. The overpotential required to reach the current density of 10 mA cm^{-2} is as small as 225 mV for the RuO_2-rEGO-250HT catalyst, outperforming the majority of Ru based catalysts reported in the literature. The Pt-rEGO catalyst with a Pt loading of 10.2 wt.% exhibits enhanced performance for HER compared with the CM Pt/C catalyst with a Pt loading of 20 wt.%, leading to more than tripled mass activity. This versatile, simple and scalable method can be easily adapted for the synthesis of various types graphene-based functional nanocomposites, for diverse applications beyond electrochemical energy storage and conversions, such as photocatalytic materials, biomedicine and biotechnology.

Acknowledgements

Y.P. and J.C. contributed equally to this work. This work made use of the facilities at the University of Manchester Electron Microscopy Center, Y.P. thanks Matthew Smith for the TEM training and technical support. The authors acknowledge the use of the Department of Materials X-ray Diffraction Suite at the University of Manchester and are grateful for the technical support and advice by Dr. John E. Warren. J.Y. thanks The University of Manchester for the award of a Presidential Doctoral Scholarship. The authors acknowledge support for equipment funded via EPSRC (UK) grants to the Sir Henry Royce Institute, grant references EP/S019367/1 and EP/P025021/1. R.A.W.D acknowledges further support from EPSRC (grant reference EP/N032888/1). J.C. and I.A.K. acknowledge the European Union's Horizon 2020 research and innovation program under grant agreement No 785219. I.A.K. also acknowledges the Royal Academy of Engineering and Morgan Advanced Materials for his Chair.

Received: February 24, 2020
Revised: May 3, 2020
Published online: June 25, 2020

Graphene supported electrocatalysts, including RuO_2 and Pt, have been synthesized by laser (248 nm) irradiation of semiconducting electrochemical graphene oxide (EGO) and metal salts precursor solutions. The catalysts show superior activity for oxygen evolution reaction (OER) and hydrogen evolution reaction (HER), which is attributed to the homogeneous distribution of ultrafine nanoparticles (~2 nm) on the deeply reduced EGO support.

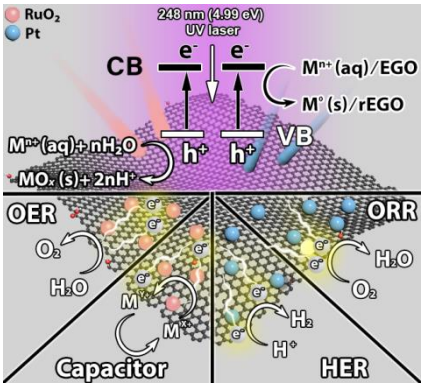

Chapter 6. Laser Enabled Synthesis of Single Atom Catalysts

6.1 Chapter Introduction

Due to the maximised atom utilisation and unique coordination environments, single atom catalysts (SACs) have emerged as a new frontier in heterogeneous catalysis, showing outstanding catalytic performance in a wide variety of reactions. This chapter dedicates to develop a SACs synthesis method through a rapid laser pyrolysis process, and to investigate the key factors to fabricate homogeneous distributed isolated Pt atoms on the graphene support.

One of the key aspects to successfully produce the SACs is to immobilize the metal ions and atoms. However, the solution synthesis strategies as described in chapter 3 and 4 are limited for the high mobility of ions and atoms in a liquid medium, which inevitably leads to the aggregation of metal atoms and clusters and forms NPs. In order to compensate the migration of metallic atoms during laser processing, we used freeze drying to sublimate the metal precursors after the metal salts filtration through a hydrophilic EGO film. It was also found the precursor types, so as the laser parameters have significant impacts on the distribution of the isolated atoms on EGO flakes. This chapter also considers the effect of laser wavelength on the SACs formation on the EGO substrate, investigation of both IR and UV laser irradiation was conducted for optimizing the EGO substrate conductivity, Pt single atoms catalytic performance and stability.

In this work, the thesis author conceived the idea, and carried out materials fabrication, TEM/SEM/ICP-OES/XRD/XPS/thermal camera/Raman spectroscopy characterization and data analysis, COMSOL modelling and electrochemical measurements and wrote the manuscript. Dr. Jianyun Cao carried out EGO synthesis and Raman spectroscopy characterization. Mr. Yang Sha and Ms. Wenji Yang contributed partly to the sample pre-treatment, including film preparation and freeze-drying of the precursors filtered EGO films. All authors contributed to the discussion and review of the manuscript. The original manuscript is presented in the following sections.

Paper: Laser Enabled Synthesis of Single atom Catalysts

Yudong Peng[1], Jianyun Cao[1,2], Yang Sha[1], Wenji Yang[1], Lin Li[3], Zhu Liu[3]

[1]: Department of Materials, School of Natural Sciences, University of Manchester, Oxford Road, Manchester, M13 9PL, U.K

[2]: National Graphene Institute, University of Manchester, Oxford Road, Manchester, M13 9PL, UK.

[3]: Laser Processing Research Centre, Department of Mechanical, Aerospace and Civil Engineering, Faculty of Science and Engineering, University of Manchester, Oxford Road, Manchester, M13 9PL, U.K.

Keywords: Laser; Photoreduction; Single-atom Catalysts; Graphene oxide; Electrocatalysts

6.2 Abstract

Single atom catalysts (SACs) with atomically dispersed catalytic sites have shown outstanding catalytic performance in a variety of reactions. However, the development of facile and high-yield techniques for the fabrication of SACs remains challenging. In this paper, we report a laser-induced solid-phase strategy for simultaneous reduction of metal salt precursors and reduction/graphitisation of electrochemical graphene oxide (EGO) to syntheses Pt single atoms supported on reduced electrochemical graphene oxide (rEGO); this has been achieved by laser irradiation of freeze-dried chloroplatinic acid (H_2PtCl_6) on EGO flakes via rapid galvanometric scanning. The sublimation by freeze-drying was essential to form "isolated dispersion" of $[PtCl_6]^{2-}$ ions on negatively charged EGO. Two types of lasers, including nanosecond pulsed infrared (IR) Nd:YAG laser with a wavelength of 1064 nm and a picosecond pulsed ultraviolet (UV) laser with a wavelength of 355 nm were used to investigate the effects of laser wavelength and pulse duration on photoreduction mechanisms. The atomically dispersed Pt on reduced EGO exhibits a small overpotential of -42.3 mV at -10 mA cm^{-2} in hydrogen evolution reaction (HER) and a mass activity tenfold higher than that of the commercial Pt/C. This new method is simple, ultrafast and potentially versatile and scalable for mass production of SACs.

6.3 Introduction

Single-atom catalysts (SACs) are a class of catalysts in which individual and isolated metal atoms are anchored to supports. Due to their maximised atom utilisation and unique coordination environments, SACs have emerged as a new frontier in heterogeneous catalysts, showing outstanding catalytic performance in a variety of reactions[382-387], including electrochemical reactions, water-gas shift reactions, hydrogenation reactions, etc. The SACs have shown a wide range of applications in synthetic organic chemistry[388], solar hydrogen technologies[389-390] and low-platinum fuel cells[391-392].

However, the production of well-dispersed isolated atoms as heterogeneous catalysts remain challenging due to that the high surface energy of individual atoms tends to aggregate. Various methods have been developed for the fabrication of SACs. The high-vacuum physical deposition technologies, such as atomic layer deposition[386, 393], provides ideal model catalysts for fundamental studies of the metal-support interaction[394]. However, these high vacuum methods are difficult for large-scale production due to the complex and costly equipment and low yield. Meanwhile, a variety of wet-chemical routes, including co-precipitation[395-396], impregnation[397] and acid leaching[398-399], through delicate control of nucleation, strong atom-supporting materials interaction or de-alloying[400], respectively, are commonly used for catalyst synthesis. Yet, the adaptation of these methods in the production of SACs remains limited, for the complexity, poor versatility, long processing time and high waste cost[401]. Additionally, the defect engineering[402-403] and organic synthesis (e.g. metal-organic framework[404-405]) also suffer from low versatility and tedious substrate modifications.

On the other hand, facile fabrication of heterogeneous SACs has been achieved by high-temperature pyrolysis and thermal activation of precursors on a wide variety of supports. For instance, single atom Fe, Co or Ni on carbon nanotube was obtained by multistep pyrolysis of the mixture of dicyandiamide with iron, cobalt and nickel acetylacetonate, respectively[406]. Very recently, Yao *et al.* demonstrated the use of high-temperature shockwaves generated form pulsed electrical Joule heating of the H_2PtCl_6-loaded activated carbon nanofiber to synthesise and stabilise single Pt atoms[407]. In this research, proper controls of the heating period and temperature (~ 1500 K) is critical to avoid agglomeration and provide sufficient activation energy for the formation of

thermodynamically stable Pt-C bond. This synthetic method extends the previous high temperature atom trapping, and pyrolysis routes,[408-410] improves processing efficiency and can be easily scaled up. Despite the simplicity and versatility of this method, several flaws may inhibit its wide application in industrial production: 1) the method is substrate-specific, for non-conductive substrate (e.g. C_3N_4, TiO_2) radiative/conductive heating is necessary to elevate the temperature; 2) the processing temperature is in a range of ~1100 to 3300 K[411-412], may inhibit the application in temperature-sensitive materials. 3) limited capability in the fabrication of microelectronics and small-scale patterns.

Lasers, as a state-of-art manufacturing tool benefits from tuneable wavelength, high energy density, rapid scanning speed and high spatial resolution[413], have been used to fabricate various kinds of nanoparticles (NPs), including metal, alloy and metal oxide NPs, semiconductor quantum dots, and core-shell NPs[1, 112], offering a powerful and flexible alternative to the purely chemical approaches for the synthesis of NPs. Laser-induced synthesis of NPs mainly based on two different mechanisms. The first mechanism is based on laser ablation in liquid to produce colloidal NPs with particle size typically above 5 nm to hundreds of nm[1]. The second mechanism is based on laser-assisted photochemical processes to generate metal (Au, Ag, and Pd) NPs down to sub-5 nm through photochemical reduction of metal salt precursors in aqueous solution, e.g. using ultra-short laser pulses to induce solvated electron from the liquid medium or excite electron-hole pairs in the semiconducting solute that are capable of reducing soluble metal ions to neutral atoms, which then coalesce into NPs[414-415]. Recently, we demonstrated a laser-induced continuous solution-phase strategy for simultaneous reduction and modification of EGO to synthesis uniformly dispersed Pt (or RuO_2) NPs on the reduced-graphene oxide support using a KrF Excimer laser with a wavelength of 248 nm[416]. The size of Pt and RuO_2 NPs was 2.0 nm ± 0.5 and 2.8 nm ± 0.6 respectively, and the resultant products showed significantly enhanced mass activity for the hydrogen evolution reaction together with comparable performance for oxygen reduction reaction compared with the commercial 20% Pt/C catalyst[416]. However, synthesis of atomically dispersed species via liquid phase laser photo-deposition remains challenging, as the nucleation and crystal growth can hardly be prevented without effective confinement of the reactants.

In this paper, for the first time, we report a laser-induced solid-phase strategy for the synthesis of atomically dispersed Pt on the rEGO support by simultaneous pyrolysis of metal salt precursor and

reduction/graphitisation of EGO. Prior to laser irradiation, Pt-EGO samples were prepared by freeze-drying to form an "isolated-dispersion" of $[PtCl_6]^{2-}$ ions on the negatively charged EGO. In order to establish laser synthesis mechanisms, two types of lasers, i.e. a picosecond pulsed ultraviolet (UV) laser with a wavelength of 355 nm and nanosecond pulsed infrared (IR) Nd:YAG laser with a wavelength of 1064 nm were used, and temperature evolution was recorded during laser irradiation. For the use of the ns IR laser, the localised temperature reached up to ca. 1350.2 K with a calculated peak temperature of 1692.6 K, suggesting thermal decomposition route via photothermal effect, while the use of the ps UV laser resulted in less high temperature of 953.2 K, implying that photochemical reduction also played an important role. After the laser irradiation, single Pt atoms decorated on laser-reduced EGO (LrEGO) with a metal loading of 0.41 wt.% were successfully synthesised. As electrocatalysts, the Pt-LrEGO presented a small overpotential of -42.3 mV at -10 mA cm^{-2} in hydrogen evolution reaction (HER) with the mass activity which was over tenfold increase compared with the commercial Pt/C. In addition, the HER stability of the Pt-LrEGO fabricated by the ns IR laser increased significantly with increasing the processing temperatures as the laser fluences increase, indicating that a stronger metal-support interaction facilitates the electrocatalytic stability. This ambient laser synthesis method is one-step, simple, ultrafast and potentially scalable, which can be readily extended to other metals and supporting materials for mass production of functional SACs for various applications.

6.4 Experiment Details

Materials

Electrochemically exfoliated graphene oxide (EGO) was prepared using the previously reported method.[218] Chloroplatinic acid hydrate ($H_2PtCl_6 \cdot xH_2O$, 99.995%), platinum (IV) chloride hydrate ($PtCl_4 \cdot xH_2O$, 99.9%), Nafion (5% in lower alphatic alcohols and water) were purchased from Sigma-Aldrich and used as received. Platinum (1000 μg ml^{-1}) ICP standard solution was purchased from SPEX CertiPrep. All chemicals were used as received without further purification, except dilution using deionized water (15 MΩ·cm).

Preparation of LrEGO composites film

To prepare the GO film, 4 mL of 1 mg mL^{-1} EGO water dispersion was vacuum filtered through a PTFE filtration membrane (0.2 μm pore size, Millipore), the dimension of the EGO film was 3.2 cm in diameter and 1.5 ± 0.2 μm in thickness. In the case of Pt/Ir-EGO film, 1 mL metal precursor

solution (H_2PtCl_6 or $PtCl_4$, 0.1 – 10 mmol L^{-1}) was vacuum filtered through the EGO membrane. The EGO or Pt-EGO films were then immersed in liquid nitrogen and freeze-dried to reduce localized precipitation of metal salts. The dried GO and Pt-EGO films were subjected to direct laser beam patterning in constant Ar flow (**Figure 6-1**). Two laser sources were used to study the temperature-dependent SAC synthesis and electrolysis stability:

an infrared laser system of 1064 nm central wavelength (IPG Photonics, USA), 5 ns pulse width, 30 kHz repetition rate and average power 3-10 W was focused into the EGO film with a spot size of ~ 1 mm. an ultraviolet laser system (355 nm, 10 ps pulse duration, EdgeWave GmbH, Germany) with pulse energy up to 54.4 μJ, a repetition rate of 404 kHz, a spot size of ~ 1 mm. A raster scanner with a line spacing of 0.5 mm, which equal to the radius of the laser spot, was scanned across the Pt-EGO film with a dimension of 3 cm × 3 cm. The galvo head scanning speed of both lasers was set to 1000 mm/s.

The Pt-LrEGO were peeled off from the filtration membrane, the collected film samples were then sonicated in water, repeatedly washed (in deionized water, 3 times) and finally freeze-dried to obtain the catalyst powder for further electrochemical experiments.

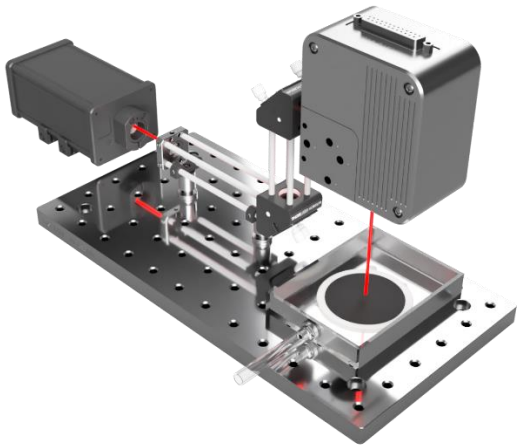

Figure 6-1. Schematic illustration of the fabrication of LrEGO and M-LrEGO films. The laser beam was scanned across the EGO or M-EGO film by varing laser output and with constant Ar gas flow.

Materials characterization

Images of the LrEGO films after laser irradiation were characterized using scanning electron microscopy (SEM) performed on a field emission Zeiss Ultra 55 SEM operating at 3 kV in lens mode. The high-resolution scanning transmission electron microscopy (HR-STEM) images, and

energy dispersive X-ray spectroscopy (EDS) of Pt-LrEGO were captured by a C_s-corrected FEI Titan G2 80-200 S/TEM ChemiSTEM operating at 200 kV equipped with a high-efficiency Super-X EDS detector system. To prepare TEM samples, the Pt-LrEGO were dispersed and sonicated in ethanol as a dilution solution, then drop-casted onto a copper grid with a lacy carbon film. Raman spectroscopy was conducted using a Renishaw InVia Raman spectrometer, with a laser wavelength of 633 nm and a spot size of 2 μm; Raman spectra were analyzed using Wire 4.2 software, with Lorentzian function fitting after baseline subtraction. X-ray diffraction (XRD) was performed using a Proto AXRD benchtop powder X-ray diffractometer (XRD) with a Cu anode (λ = 1.5406 Å) operating at 30 kV. X-ray photoelectron spectroscopy (XPS) was performed with a SPECS NAP-XPS system; XPS spectra curve fittings were accomplished by CasaXPS software. The time-dependent temperature profile of the samples under laser irradiation was recorded using a FLIR T650sc infrared camera with a measurement range up to 2000 °C. The calibration of the infrared camera was conducted by the following steps[417]: an EGO film was adhered on a 3M black electrical insulation tape and attached to a hotplate (Fisherbrand Isotemp, Fisher Scientific). The temperature was measured by a thermocouple (Model 88106-IEC, Omega) and controlled by the hotplate. The emissivity was calibrated through the infrared camera until the IR temperature is in accordance with the thermocouple measurement. The temporal temperature profile was recorded by averaging 5 individual points in each measurement. 4-point probe resistance measurements of the GO and LrEGO films were carried out using a 4-point probe system (Janedel Engineering Ltd., Linslade, UK) equipped with a Keithley 2182A nano voltmeter and a Keithley 6220 current source (Keithley Instruments, Cleveland, OH, USA). To determine the mass of metal content within the Pt/Ir-LrEGO catalysts, an inductively coupled plasma optical emission spectrometry (ICP-OES) was conducted by using a Analytikjena PlasmaQuant 9000 Elite system. All samples were weighed and digested in aqua regia for two days, the solution was then diluted and filtered with a 0.2 μm pore size Whatman syringe filter (Fisher Scientific, UK).

FE simulations

The time-dependent FE simulations of the pulsed-laser patterning process on the EGO film was performed using COMSOL modelling to acquire a better understanding of the effects of laser fluences and NOPs on the temporal temperature elevation. An EGO film with 2 μm thick and dimensions of 1 cm by 1 cm was modelled as a candidate material, where its temperature-dependent material properties are acquired by taking typical values from literature (**Table 6-1**).

The pulsed laser with a Gaussian power distribution is modelled as a heat flux on the surface of the EGO film. The heat transfer within the materials is governed by the COMSOL built-in general heat equation:

$$\rho C_p \frac{\partial T}{\partial t} + \rho C_p u \cdot \nabla T + \nabla \cdot (-k \nabla T) = Q \tag{6-1}$$

Where the first, second and third terms on the left-hand side are the time derivative of thermal energy per unit volume, convection energy and conduction energy, respectively. T is the local temperature, t is the time span, Q is the converted energy from the laser beam to the material through photothermal conversion. ρ, C_p and k are mass density, specific heat capacitance and thermal conductivity, respectively. The geometric model was set to a 5×5 mm^2 square thin film with a thickness of 2 μm. The upper boundary of the film was set to expose to the boundary conditions of heat flux, natural convection and irradiative convection. The lower boundary was subjected to an insulated boundary.

The pulsed laser heat source with a Gaussian profile is shown in the following equation[418-419]:

$$Q = A \cdot P \cdot Beam(x, y, t) \cdot Pulsetrain(t) \tag{6-2}$$

Where, A is the absorption absorptivity at given incident radiation wavelength, P is the laser output power density, Beam (x,y,t) describe the Gaussian laser beam shape and its displacement, and Pulsetrain (t) describes the laser time-dependent pulse parameter. The Gaussian power distribution of the laser beam was described as the following expression:

$$Beam(x, y, t) = \exp\left\{-\frac{[x-(x_0-v_x t)]^2}{2\phi^2} + \frac{y^2}{2\phi^2}\right\} \tag{6-3}$$

Where, x and y are the coordinates of the laser beam centre, v_x is the beam travel velocity along the x-direction, t is the time span, and ϕ is the standard deviation of the Gaussian laser beam. The thermal and optical properties of EGO used in the calculation were listed in **Table 6-1**.

Table 6-1 Material properties of the simulated EGO under IR laser irradiation.

Material Properties	EGO	Units	Ref.
Density	2200	Kg m^{-3}	[420-421]
Heat capacitance	2000	J $kg^{-1}K^{-1}$	[422-423]
In-plane thermal conductivity	8.8	W $m^{-1}K^{-1}$	[424-426]
Cross-plane thermal conductivity	0.09	W $m^{-1}K^{-1}$	[426]
Absorptivity @ 1064 nm	0.6		[427-428]
Scanning speed	1000	mm s^{-1}	
Initial temperature	25	°C	

Electrochemical experiments

All electrochemical experiments were performed in a conventional three-electrode system at a VersaSTAT4 Potentiostat (AMETEK, USA) and a 636A electrode rotator system (AMETEK, USA) with an Ag/AgCl (saturated KCl solution) electrode as the reference electrode, a coiled platinum wire as the counter electrode, and a glassy carbon rotating disk electrode (RDE, Pine research) with a diameter of 5 mm (0.196 cm^2) as the working electrode. All potential was converted to the RHE by using the following equation: $E_{RHE} = E_{Ag/AgCl} + 0.197 + 0.059$ pH. The RDE was polished with a microfiber polishing cloth with 0.05 μm alumina slurry until mirror finish prior to all experiments. 10 mg catalyst was mixed with deionized water, isopropanol (99%, Aldrich) and Nafion (5%, Aldrich) with a volume ratio of 9:10:1, respectively, to a final concentration of 5 mg mL^{-1}. After ultrasonication in an ice bath for 1 hour, 10 μL homogeneous ink was drop-casting on the RDE and dried under ambient, with a final loading of 50 μg (~0.255 mg cm^{-2}). The Ohmic losses within the system were compensated by applying *IR*-correction. The uncompensated system resistance was determined by electrochemical impedance spectroscopy (EIS) at the open circuit potential. The EIS was measured in a range of 100 kHz to 1 Hz, with a perturbation of 10 mV. The system resistance was then determined at the x-intercept of the Nyquist plot. The Nyquist plot during HER was based on EIS measurements at an overpotential of 30 mV in a frequency range of 10^{-2} to 10^6 Hz with 10 mV sinusoidal perturbations in 0.5 M H_2SO_4. Linear sweep voltammetry with a scan rate of 10 mV s^{-1} was conducted in N_2 or O_2 saturated 0.5 M H_2SO_4

at a rotating speed of 1600 rpm. Chronopotentiometry measurements (at ± 10 mA cm^{-2}) were conducted to evaluate the long term HER/OER stability.

6.5 Results and Discussion

The laser synthesis is described in **Figure 6-2**. Firstly, the electrochemical graphene oxide (EGO) film was prepared by vacuum filtration of the EGO aqueous dispersion through a PTFE membrane filter, then 1 mL of the chloroplatinic acid (H_2PtCl_6) solution with desired concentration (1, 2, 3, 5 or 10 mM) was filtered through the EGO film to obtain the Pt-EGO film. The freshly filtered Pt-EGO film supported by the PTFE membrane filter was immediately frozen in liquid nitrogen, followed by freeze-drying in vacuum to sublimate the ice. The purpose of this direct sublimation of solid ice to water vapour was to immobilise the $[PtCl_6]^{2-}$ anion complex on negatively charged EGO flakes to avoid localised precipitation of the metal precursor. The as-prepared Pt-EGO films were subject to laser irradiation under Ar atmosphere via rapid scanning. After the laser treatment, the laser reduced EGO (LrEGO) film loaded with Pt single atoms were separated from the PTFE membrane filter by sonication in water, followed by washing and freeze-drying to obtain the final materials in powder state. According to the concentration of H_2PtCl_6 precursor solution, the as-formed graphene supported Pt SACs are denoted as Pt*x*-LrEGO (e.g. Pt5-LrEGO represents a concentration of H_2PtCl_6 precursor solution of 5 mM). To distinguish the IR laser-treated LrEGO, the UV fabricated reduced graphene was denoted as $LrEGO_{UV}$.

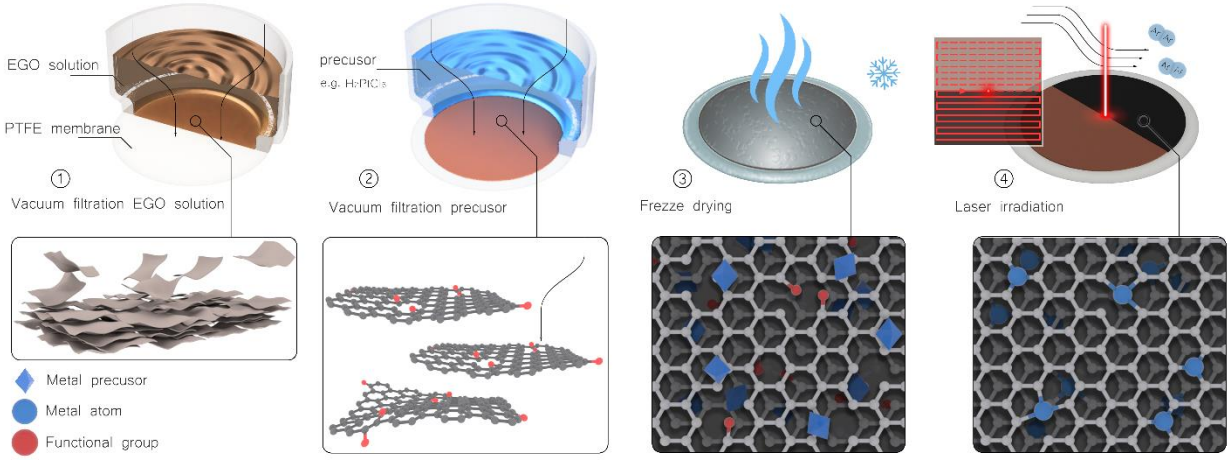

Figure 6-2. Schematic illustration of the formation of Pt-LrEGO. (**a**) Preparation of EGO film from 1.0 mg ml^{-1} EGO solution through vacuum filtration; (**b**) metal precursor filter through the EGO film and followed by (**c**) immediate freeze in liquid nitrogen and freeze-drying; (**d**) direct 1064 nm laser writing of the Pt-EGO to form Pt-LrEGO, inset

shows the schematic of the laser scanning zigzag path, the laser beam spot size was 1 mm in diameter and overlap ratio between the tracks was 50%.

6.5.1 Characterisation of Pt Single Atoms

The samples were characterised with aberration-corrected high-angle annular dark field-scanning transmission electron microscopy (HAADF-STEM). For the sample prepared by the, **Figure 6-3 a** shows the HAADF-STEM images of the Pt5-LrEGO sample prepared by the ns IR Nd:YAG laser, revealing an intact 2D flake without the presence of Pt nanoparticles or clusters. Energy-dispersive X-ray (EDX) elemental maps (**Figure 6-3 b**) indicate homogeneous dispersion of Pt over the LrEGO support in an atomic scale. The HAADF-STEM image at high magnification (**Figure 6-3 c**) clearly shows the presence of densely populated Pt particles (appeared as bright dots) on the LrEGO support. The intensity line profile shows a spot diameter of ~ 0.34 nm, corresponding to the size of an individual Pt atom. The HAADF-STEM characterisation clearly suggests the presence of single Pt atoms on EGO support.

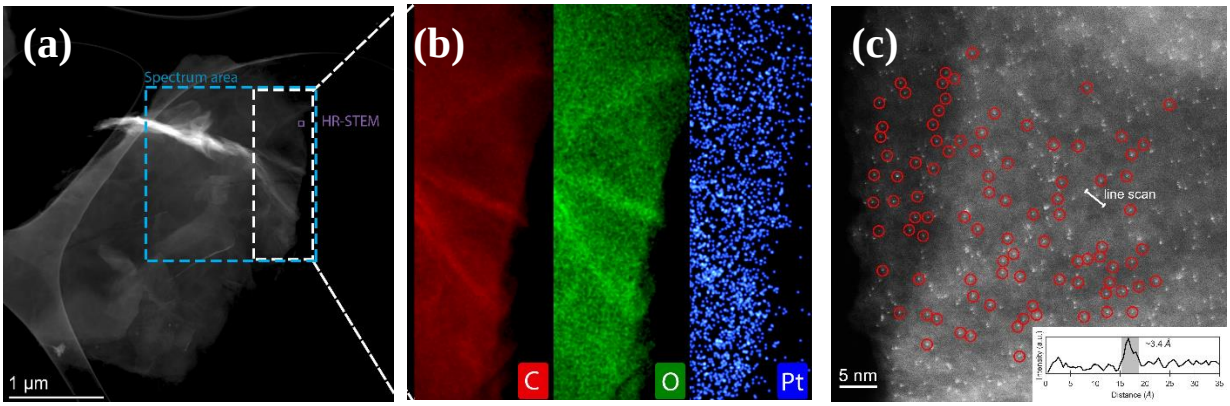

Figure 6-3 (**a**) HAADF-STEM image of Pt-LrEGO after 1064 nm laser irradiation at a laser fluence of 7.66 mJ cm^{-2} and (**b**) EDS mapping of C, O and Pt of the selected area. (**c**) representative HAADF-STEM image showing isolated Pt atoms deposited on LrEGO support (inset shows the representative line scan of the bright spot).

In addition to the HAADF-STEM characterisation, X-ray diffraction (XRD) and X-ray photoelectron spectroscopy (XPS) further confirms that the Pt species exist in the Pt-LrEGO as uniformly dispersed single atoms. In detail, the XRD pattern of Pt5-LrEGO in **Figure 6-4 a** indicates the absence of crystallised Pt nanoparticles, as the characteristic peaks of Pt (111), (200), (220) and (311) (ICDD No. 00-004-0802) that clearly appears in the XRD pattern of CM Pt/C are missing in the XRD pattern recorded from the Pt5-LrEGO sample. XPS Pt 4f high-resolution

spectra provide further evidence for the single atomic dispersion of Pt in the Pt5-LrEGO sample. As shown in **Figure 6-4 b**, the Pt 4f high-resolution spectra of the CM Pt/C show a set of doublet peaks located at 71.4 and 74.7 eV, corresponding to the doublet peaks of Pt (0) $4f_{7/2}$ and $4f_{5/2}$ respectively[93, 429-430]. For the laser-treated Pt-5-LrEGO, the doublet peaks shifted to the higher binding energy of 72.6 and 75.8 eV, corresponding to Pt (2+)[93, 429-430]. The lack of detectable Pt (0) signal implies that the Pt nanoparticle/clusters were unlikely to exist or with a negligible content in the sample, conforming to the absence of crystallised Pt signals in the XRD patterns. The 2+ valence of Pt (2+) originates from the interaction between the single Pt atoms and substrates[93]. The Pt loading for the Pt-5-LrEGO is 0.40 ± 0.01 wt.% as determined by ICP-OES.

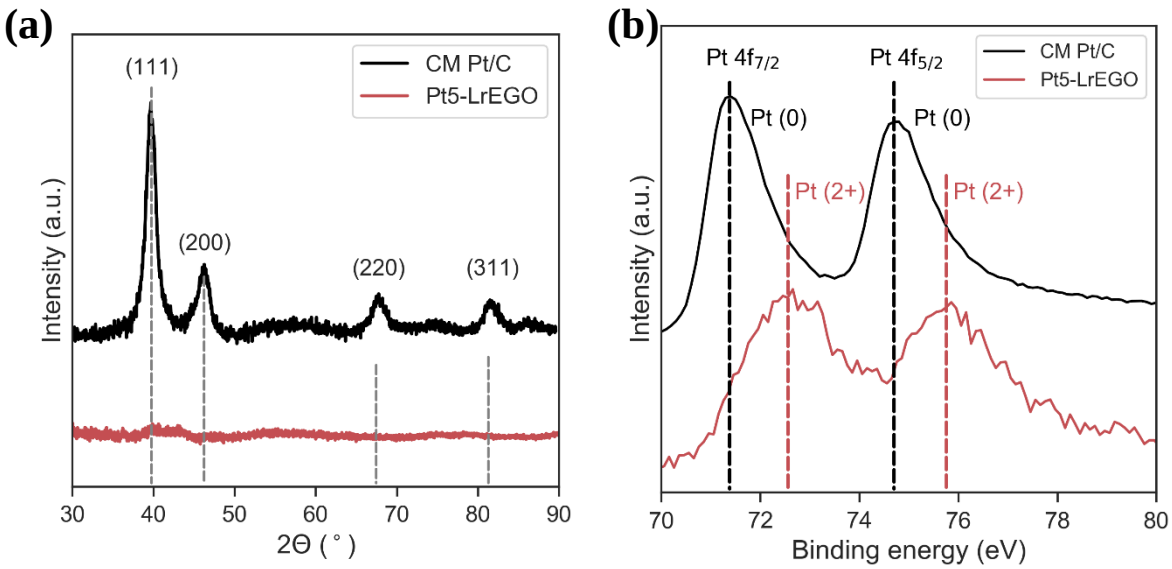

Figure 6-4. (**a**) XRD pattern and (**b**) XPS spectra of the commercial Pt and Pt5-LrEGO fabricated by 1064 nm laser at 7.66 mJ cm^{-2}.

6.5.2 Effect of Precursor Concentration and Precursor Type

The variation in the concentration of H_2PtCl_6 solution filtered through the EGO film (**Figure 6-2 a**) showed a strong influence on the as-formed Pt species. As shown in **Figure 6-5 a and b**, the laser-treated Pt1-LrEGO using the 1 mM of H_2PtCl_6 solution shows atomically dispersive Pt species in a similar size of ~ 0.34 nm but having a low Pt loading of ~ 0.03 wt.%. With the increase of the H_2PtCl_6 concentration to 5 mM, the Pt species remains atomically dispersed on the LrEGO flake (**Figure 6-5 c**) while the Pt loading increases to 0.41 wt.% without noticeable aggregation. Further increase of the concentration of H_2PtCl_6 to 10 mM leads to clear aggregation of the Pt

single atoms (**Figure 6-5 d**). The weight percentage of Pt species increased from 0.03 wt.% to 1.40 wt.% with increasing the H_2PtCl_6 concentration from 1 to 10 mM (**Figure 6-5 a**).

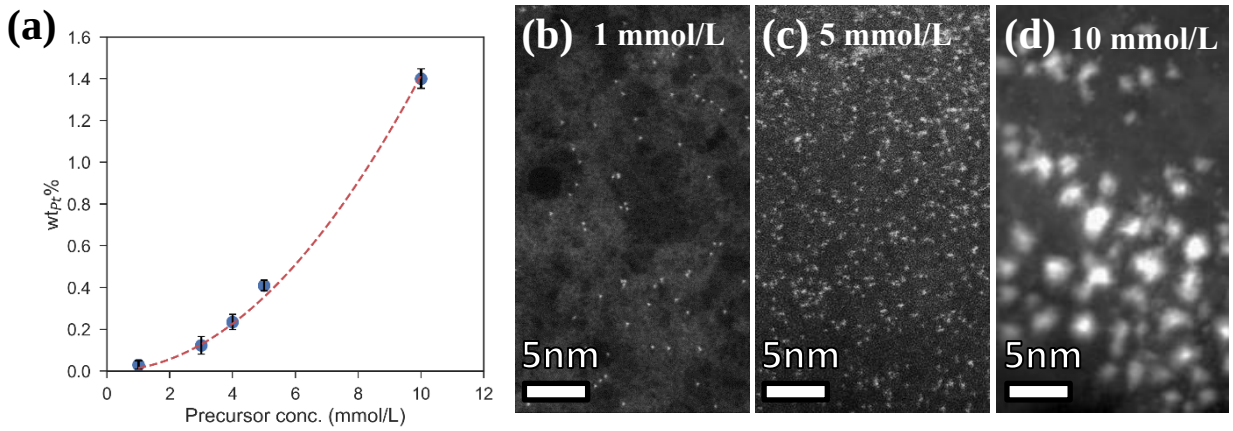

Figure 6-5 (a) ICP-OES result of Pt loading within Pt-LrGO with various precursor concentration, and representative STEM images of (**b**) Pt1-LrGO, (**c**) Pt5-LrGO and (**d**) Pt10-LrGO fabricated by 1064 nm laser at 7.66 mJ cm^{-2}.

In addition to the concentration of precursor solution, the type of platinum precursor compounds, namely, H_2PtCl_6 or $PtCl_4$, shows a significant impact on the as-formed Pt species on the LrEGO support. Unlike the H_2PtCl_6 solution that leads to atomically dispersed Pt on the LrEGO flakes, the STEM images (**Figure 6-6)** of the Pt-LrEGO synthesised from the $PtCl_4$ precursor via same lasing parameters show prevailing the formation of Pt nanoparticles for all the concentrations used (from 1 to 10 mM).

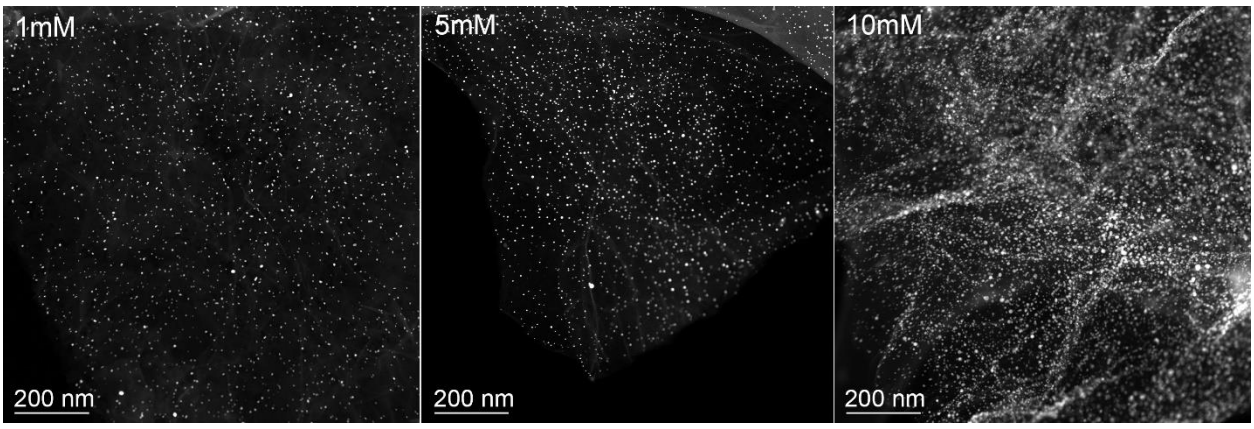

Figure 6-6. STEM image of the Pt-LrEGO synthesized via 1064 nm laser irradiation at a fluence of 7.66 mJ cm^{-2} on $PtCl_4$ (with a concetration of 1, 5 and 10 mM respectively) filtered EGO films.

We then performed XPS analysis for the precursor adsorbed EGO to understand the interfacial interaction between $PtCl_4$, H_2PtCl_6 and EGO support. **Figure 6-7 a** presents the XPS survey of the pristine EGO, and EGO after $PtCl_4$ (5 mM) and H_2PtCl_6 (5 mM) precursor treatment. Except the C 1s and O 1s peaks exist in all samples, the Pt 4f and Cl 2p peaks were found in the precursor filtered EGO films. Through comparison of the relative areas of the integrated intensity of Pt, Cl, C and O, the percentage of Pt species in the spectral are ~0.69 at_{Pt}% and ~0.06 at_{Pt}% for EGO-$PtCl_4$ and EGO-H_2PtCl_6, respectively. The adsorbed Pt species on the EGO-$PtCl_4$ is one order magnitude higher than that of the EGO-H_2PtCl_6 clearly indicates the difference in interfacial interaction and adsorption tendency. Besides, in exploring the remaining Cl ions within the samples, we found that the Pt:Cl ratio for EGO-H_2PtCl_6 is 1:5 which is close to the original compound, while the ratio for EGO-$PtCl_4$ is ~ 2:3. **Figure 6-7 b** shows the Pt 4f spectra of the EGO-$PtCl_4$ and EGO-H_2PtCl_6, each Pt 4f peaks can be deconvoluted into two pairs of doublets and were assigned into Pt (IV) ($PtCl_4$/ H_2PtCl_6), Pt (II) ($PtCl_4$) and $PtO/Pt(OH)_2$ (binding energy summarised in **Table 6-2**)[431-434]. Apart from the Pt (IV) peaks from the precursors, the existence of $PtO/Pt(OH)_2$ peaks attributes to the hydrolysis of the metal salts by humid air[431, 435]. Furthermore, the dominating Pt (II) components of EGO-$PtCl_4$ are possibly caused by the reduction of Pt^{4+}. Owing to the electrophilic nature of Pt (IV), the Pt (IV) can oxidise hydrocarbon and itself turns to $PtCl_2$ and HCl[436-437]. In our study, the oxidation of EGO caused by $PtCl_4$ is more pronounced than H_2PtCl_6, this explains the disproportion of Pt:Cl in the samples. By examining the O1s spectra (**Figure 6-7 c**), the integrated area of C-O peak of EGO-$PtCl_4$ among the deconvoluted O1s signal is 11.6%, which is 2 times larger than 5.4% of EGO-H_2PtCl_6. Moreover, the binding energies corresponded to C-O are 533.5, 533.3 and 533.6 eV for the pristine EGO, EGO-$PtCl_4$ and EGO-H_2PtCl_6, the clear negative shift of EGO-$PtCl_4$ C-O bond provides evidence that adsorption of Pt species on O and/or OH functional groups of EGO[432, 438].

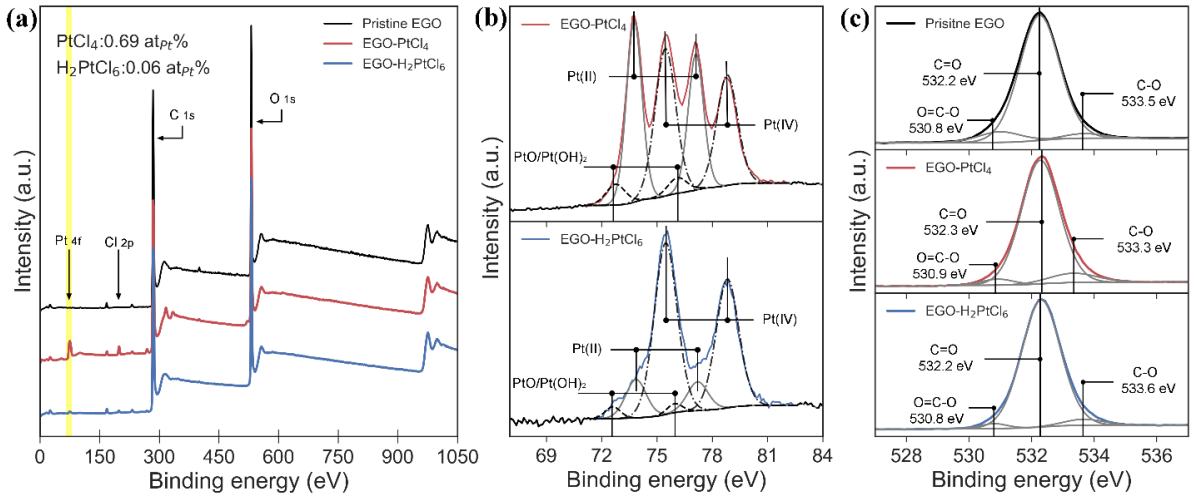

Figure 6-7. XPS characterisation of the pristine EGO, and $PtCl_4$ (5 mM) and H_2PtCl_6 (5 mM) filtered EGO films. (**a**) XPS survey, (**b**) high-resolution XPS Pt 4f spectra and (**c**) O 1s spectra.

Table 6-2 Summary of XPS high resolution Pt 4f spectra of EGO after $PtCl_4$ and H_2PtCl_6 sorption.

Component	Pt(IV)		Pt(II)		$PtO/Pt(OH)_2$	
Assignment	$PtCl_4/H_2PtCl_6$		$PtCl_2$		$PtO/Pt(OH)_2$	
	4f5	4f7	4f5	4f7	4f5	4f7
EGO-$PtCl_4$	78.8	75.5	77.1	73.8	76.1	72.8
EGO-H2$PtCl_6$	78.8	75.5	77.2	73.9	76.0	72.6

The excellent hydrophilicity of EGO in water primarily due to the negative charge oxygen-containing groups on the surface, where hydrated cation tends to interact with the oxidised groups through coupling between the oxygen atoms and the empty orbitals of metal cations[439-440]. Previous research[441] on quantification of Pt uptake by oxidised carbon substrate indicates the amount of $PtCl_6^{2-}$ taken up was negligible compared to $Pt(NH_3)_2^{+}$. Similarly, the positively charged Pt^{4+} from $PtCl_4$ is most likely absorbed on EGO via electronic interaction and form EGO-Pt (II/IV) complex before freeze-drying, which might adversely affect the dispersion of Pt^{4+} on the EGO substrate, and thus unlikely to form Pt single atoms.

Therefore, the successful formation of single Pt atoms anchored on the LrEGO support in this case, strongly relied on controlling the ion distribution on the supporting materials and the precursor concentration and types. On the one hand, reducing the precipitation of metal precursors and physical increasing of the ions/single atoms distance would minimise the supersaturation level of

metals on the supporting materials, and thus suppress aggregation and formation of clusters/nanoparticles. On the other hand, anchoring the single atoms also highly relied on the substrate or the strong metal-support interaction between supporting materials and metal atoms, thus the type of substrates and the amount of anchoring site, e.g. vacancies, edges, steps and heterogeneous elements doping etc., are important factors determining the loading of metal atoms[442-444].

6.5.3 Characterization of Laser Reduced EGO

In addition to the single Pt atoms, reduction of the EGO by the laser treatment also plays an essential role on supporting the single atoms, to maximise the exposure of active points to the electrolyte and reactants, and build up an electrical conduction network. **Figure 6-8** shows Scanning electron microscopy (SEM) images of the laser-treated Pt5-LrEGO using the ns IR laser. A significant expansion of the EGO film was observed in the laser-irradiated area with the film thickness increased ~ 27 times from 1.3 μm to 35 μm, reflecting a drastic explosive degassing during the laser reduction process. The XRD patterns of the Pt5-LrEGO irradiated by the ns IR laser (**Figure 6-9 a**) show the disappearance of the characteristic diffraction peak of EGO at 2θ = 11.9° for all the laser fluences and the peaks centred at 2θ = 26.2°, representing (002) planes of restacked graphene, raised gradually with increasing the laser fluences, indicating the occurrence of reduction of the EGO.

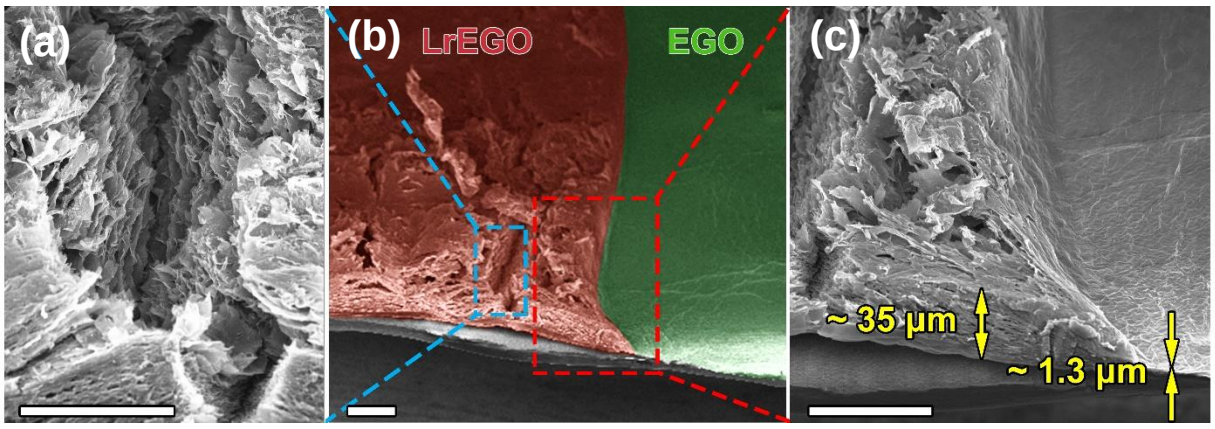

Figure 6-8. SEM images of (**a**) and (**b**) representative SEM images of LrGO revealing the reduction of LrGO and (**c**) the interface of GO and LrGO after 1064 nm laser irradiation at a pulse energy of 7.66 mJ cm^{-2}.

The XPS high-resolution C1s spectra collected from the pristine EGO film and the Pt5-LrEGO after films after the IR laser irradiation at 7.66 mJ cm^{-2} reveal a significant decrease in oxygen

functional groups (**Figure 6-10**). The deconvolution of the C 1s spectrum of the pristine EGO shows four characteristic components, which are assigned to C1s (284.5 eV), C−O (286.4 eV), C=O (287.9 eV) and −COO− (289.2 eV) respectively (details in **Table 6-3**).[218, 329] In comparison, the C1s spectrum of the LrEGO film shows a significant decrease in the oxygen components peak intensity, the oxygen contents dropped from 20.04 at.% to 5.08 at.%, and the π to π* peak at (290.8 eV) appears, showing an effective removal of oxygen contents and restoration of the graphitic structure.

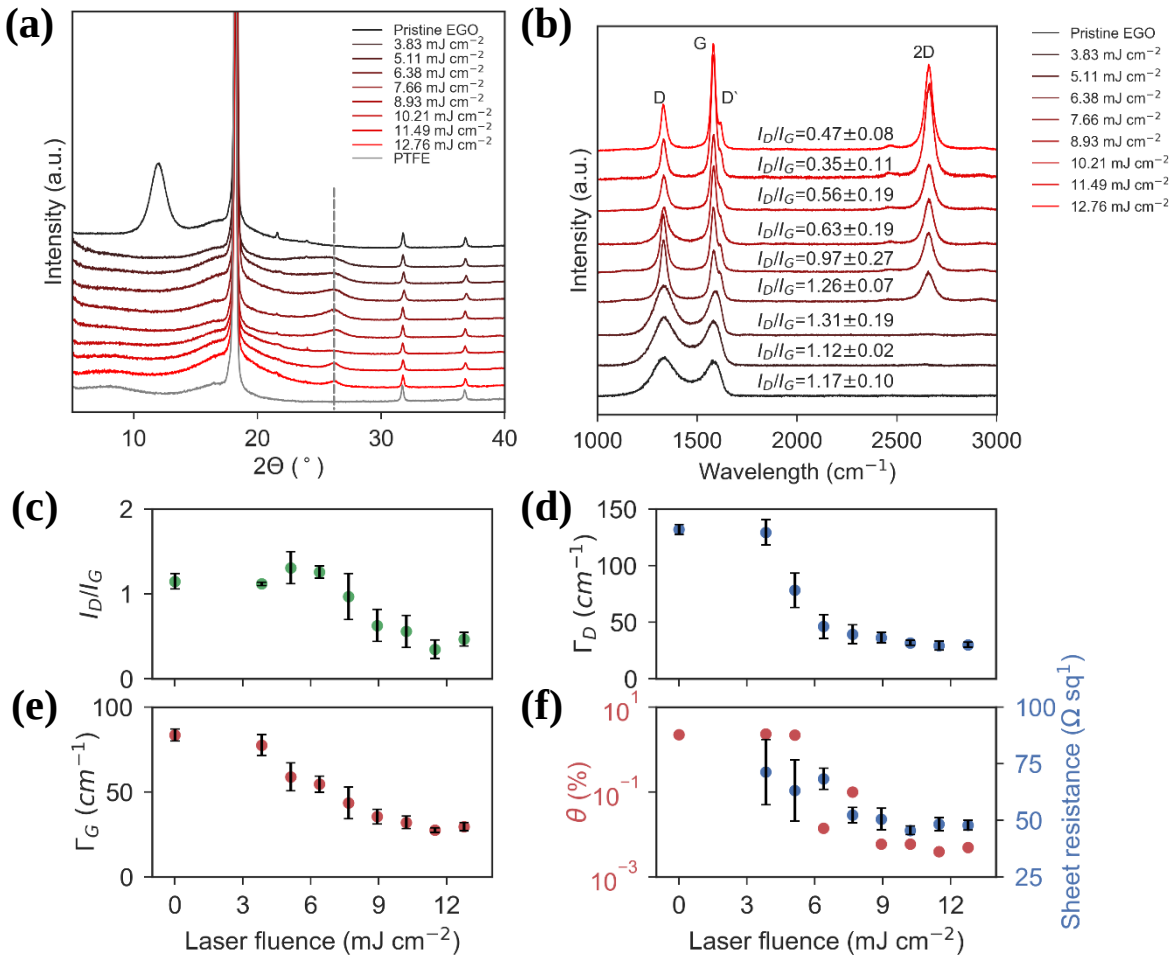

Figure 6-9. (**a**) XRD patterns and (**b**) Raman spectra of the pristine EGO and LrEGO after 1064 nm laser irradiation at various laser fluences (the diffraction peaks centred at 2θ= 18.1°, 31.7° and 36.8° originated from the PTFE film). The evolution of (**c**) I_D/I_G ratio, (**d**) and (**e**) FWHM values of D and G bands, and (**f**) defect density and sheet resistance of EGO and LrEGO samples.

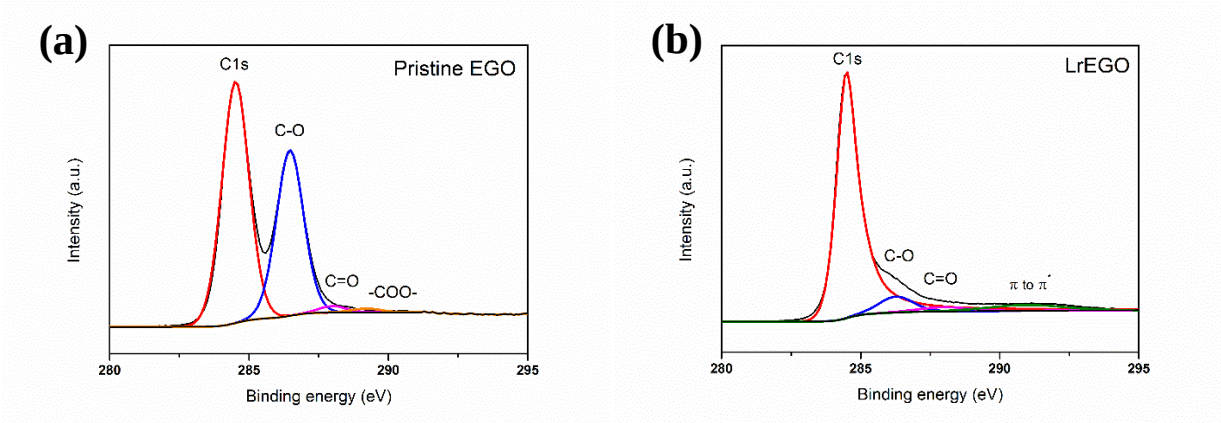

Figure 6-10. XPS high resolution C1s spectra of (**a**) pristine EGO and (**b**) LrEGO.

Table 6-3 Summary of XPS characterization of pristine EGO and LrEGO.

Sample	Oxygen content (at%)	Carbon content (at%)	C 1s components (at%)				
			C1s 284.5 eV	C−O 286.4 eV	C=O, 287.9 eV	−COO− 289.2 eV	π to π* 290.8 eV
Pristine EGO	20.04	79.96	57.88	39.94	1.53	0.98	0
LrGO	5.08	94.92	90.90	8.89	3.56	0	6.70

Raman spectroscopy with an excitation wavelength of 633 nm was used to characterise the graphitisation degree of Pt5-LrEGO, the acquired spectra were fitted with Lorentzian function after baseline subtraction for further analysis. **Figure 6-9 b** shows the typical Raman spectra of the pristine EGO and LrEGO samples: the D band located at ~1332 cm^{-1} representing the edge planes and disordered structures, the G band at ~1581 cm^{-1} induced by the ordered sp^2 bonded carbon, the D` peak centred at ~1619 cm^{-1} originated from an intravalley double resonance process, the peak at ~2660 cm^{-1} is assigned to be the 2D band which is the second order of the D peak.[223, 325] To monitor the evolution of defect density in the Pt5-LrEGO sample after laser irradiation, the I_D/I_G ratio as a function of irradiation fluence was plotted (**Figure 6-9 c**). The values I_D/I_G ratio are closely related to the density of defect/functionality within the graphene basal plane.[322, 325] For the use of the ns IR laser as shown in Figure 5c, the D and G bands intensity ratio increased initially from 1.17 ± 0.10 to 1.31 ± 0.19, followed by a drastic drop down to 0.35 ± 0.11 with the increasing the laser fluences, which fits Ferrari and Robertson's classification of disorder transition from

amorphous carbons to graphite[222], indicating the decrease of structure disorder. The reduction degree and restoration of graphene structure in the Pt5-LrEGO was also supported by the observation of the narrowing the full width at half-maximum (FWHM: Γ) of D and G bands with the increase of laser fluence (**Figure 6-9 d and e**), and the trends are accordant with the I_D/I_G ratio. The model proposed by Lucchese et al.[322] and Cançado et al.[325] was then applied to quantify the development of defect distance (L_D) and defect density (θ) of the LrEGO films from the Raman I_D/I_G ratios (**Table 6-4**). **Figure 6-9 f** shows the defect density retained ~ 2.20% at the laser fluence of 5.11 mJ cm^{-2}, and then dropped precipitously and down to ~ 0.01% at the laser fluence of 7.66 mJ cm^{-2}. This observation provides clear evidence confirming that efficient removal of oxygen groups along with the restoration of the graphene structure under the ns IR laser reduction. The probe of sheet resistance change after laser irradiation provides further evidence for the reduction and restoration electrically conductive sp2 structure. The sheet resistance of the Pt5-LrEGO film (**Figure 6-9 f**) decreases with the increase of laser fluences from 3.83 to 6.38 mJ cm^{-2} and remains nearly constant at higher fluences up to 12.76 mJ cm^{-2}. A minimum sheet resistance value of 45.6 **Ω** sq^{-1} was achieved at the laser fluence of 10.21 mJ cm^{-2} (Note: the pristine EGO is a good insulator and the resistance value is beyond the instrument detection limit).

Table 6-4. Summary of statistical Raman analysis of pristine EGO and EGO after 1064 nm laser irradiation at various laser fluences.

Laser fluence (mJ cm^{-2})	Γ_D (cm^{-1})	Γ_G (cm^{-1})	I_D/I_G	L_D (nm)	θ (%)
0	132.12±4.32	83.61±3.58	1.17±0.10	1.16	2.25
3.83	129.56±11.20	77.72±6.04	1.12±0.02	1.14	2.36
5.11	78.27±15.24	58.98±8.24	1.31±0.19	1.18	2.20
6.38	46.38±10.52	54.70±4.76	1.26±0.07	14.81	0.014
7.66	39.50±8.43	43.64±9.39	0.97±0.27	16.92	0.010
8.93	36.36±4.59	35.56±4.38	0.63±0.19	21.21	0.006
10.21	31.89±2.25	32.09±3.64	0.56±0.19	22.53	0.006
11.49	29.34±3.94	27.70±1.34	0.35±0.11	28.70	0.004
12.76	30.13±2.13	29.60±2.45	0.47±0.08	24.65	0.005

The Pt5-LrEGO$_{UV}$ films treated with a relatively narrow fluence range and dense pulse overlap conditions also shows a similar trend in I_D/I_G ratio, Γ_D and Γ_G values with increasing the laser fluences (**Figure 6-11**). The ordered crystalline structure occurred in a fluence range of 1.8 to 2.00 mJ cm^{-2}. However, at fluences below 1.8 mJ cm^{-2}, broadened and relatively high I_D/I_G ratio, Γ_D

and Γ_G values appeared (**Table 6-5**), indicating the reduction degree of EGO is low and uneven. The poor reduction degree also reflects in the resistance of Pt5-LrEGO$_{UV}$. **Figure 6-11 e** shows the Pt5-LrEGO$_{UV}$ decrease in sheet resistance with increased laser fluences, but with much less extent than seen in the IR irradiated LrEGO. The unevenness in reduction degree was further verified by XRD (**Figure 6-12**). The Pt5-LrEGO$_{UV}$ films treated by the ps UV laser show a clear peak at 2θ=11.9°**,** and the peak intensity gradually decreased and completely disappeared when the laser fluence reached 2.0 mJ cm^{-2}, while the graphene (002) peaks increased progressively at the laser fluence exceeding 1.45 mJ cm^{-2}. When the laser fluence reached 2.09 mJ cm^{-2}, the EGO film was ablated completely from the PTFE membrane.

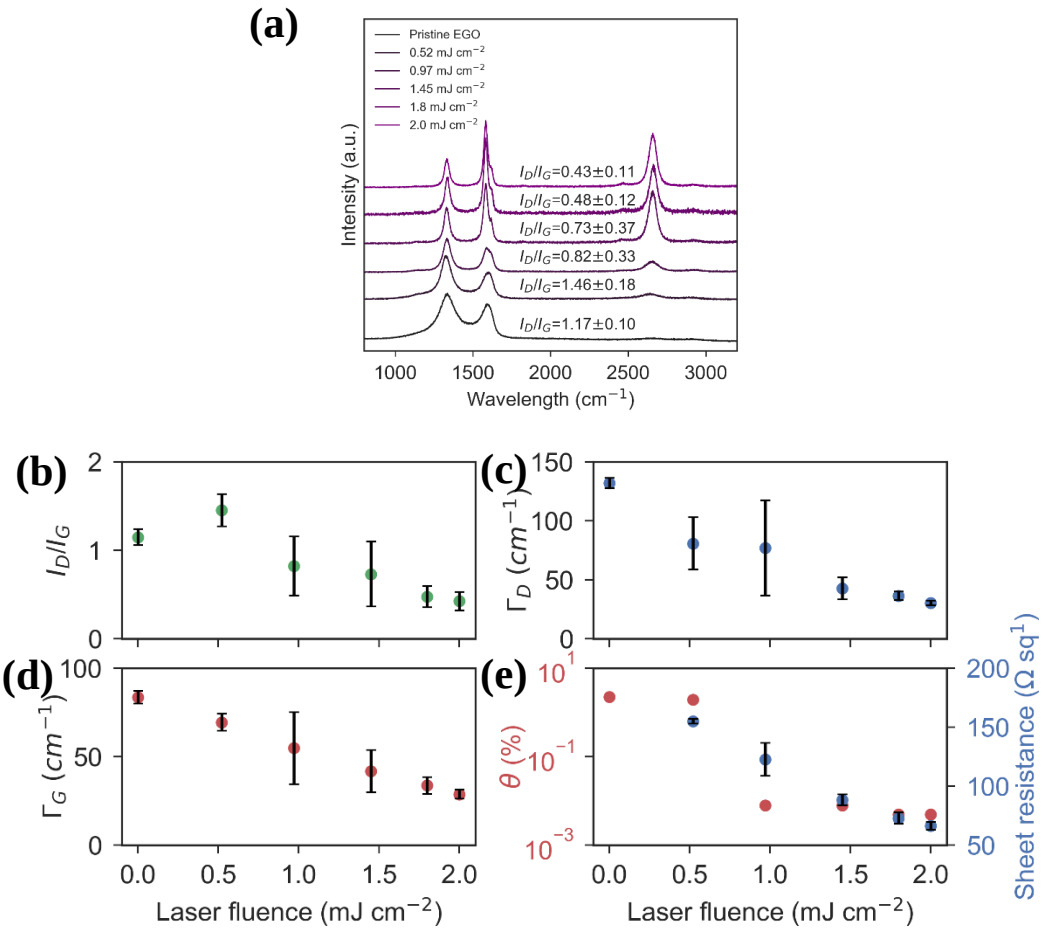

Figure 6-11. (a) Raman spectra of the pristine EGO, and 355 nm laser treated samples at various laser fluences. The evolution of (**b**) I_D/I_G ratio, (**c**) and (**d**) FWHM values of D and G bands, and **e**) defect density and sheet resistance of EGO and LrEGO samples.

Table 6-5 Summary of statistical Raman analysis of pristine EGO and EGO after 355 nm laser irradiation at various laser fluences.

Laser fluence (mJ cm^{-2})	Γ_D (cm^{-1})	Γ_G (cm^{-1})	I_D/I_G	θ (%)
0	132.12±4.32	83.61±3.58	1.17±0.10	2.25
0.52	80.86±22.25	69.45±4.81	1.46±0.18	1.96
0.97	77.02±40.27	54.90±20.32	0.82±0.33	0.008
1.45	42.68±9.29	41.88±11.96	0.73±0.37	0.008
1.80	36.36±3.57	33.75±4.79	0.48±0.12	0.005
2.00	30.37±1.89	28.78±2.61	0.43±0.11	0.005

Taken together, the Raman, XRD and sheet resistance results together strongly suggest the photo-reduction of EGO through IR and UV radiation occurs in different photoinitiated manner. From a practical perspective, efficient and even reduction of EGO film was found in IR irradiation, which also showed high crystallinity and low sheet resistance.

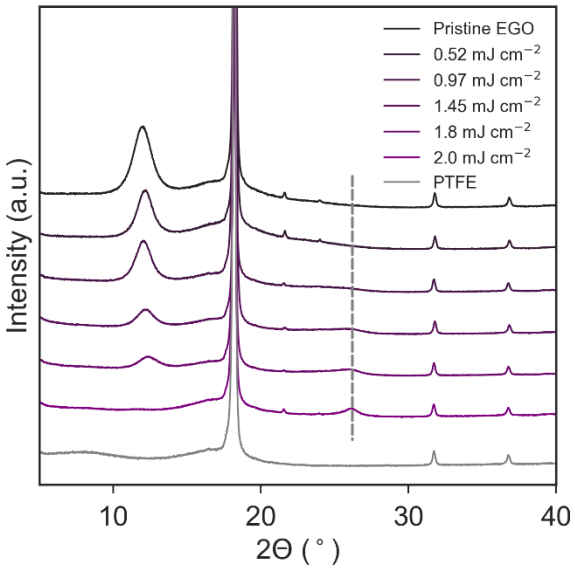

Figure 6-12. XRD patterns of the pristine EGO and LrEGO films after 1064 nm laser irradiation at various laser fluences (the diffraction peaks centred at 2θ= 18.1°, 31.7° and 36.8° originated from the PTFE film).

6.5.4 SACs Laser Synthesis Mechanisms

The laser synthesis method introduced in this work was based on the photo-reduction of metal precursor and EGO simultaneously. Unlike other chemical and thermal reduction of GO processes, laser reduction is characterised by energy absorption by the GO films dependent on radiation wavelength and pulse width. From the wavelength perspective, the photo-reduction of GO generally can be achieved photochemically with radiation wavelength in the UV region[416] and

photothermally using radiation from visible to IR[445-446]. From the temporal perspective, the laser-matter interaction occurs in a clear time sequence[419]: excitation of an electron by incident photon occurs in the first ~ 100 fs, following by electron-phonon coupling from 100 fs to 10 ps, finally from 100 ps or longer heat dissipate to the surrounding matrix. Therefore, thermal analysis is invalid for fs laser irradiation. In our current study, the pulse width of 5 ns is sufficient for heat-conducting to the bulk materials.

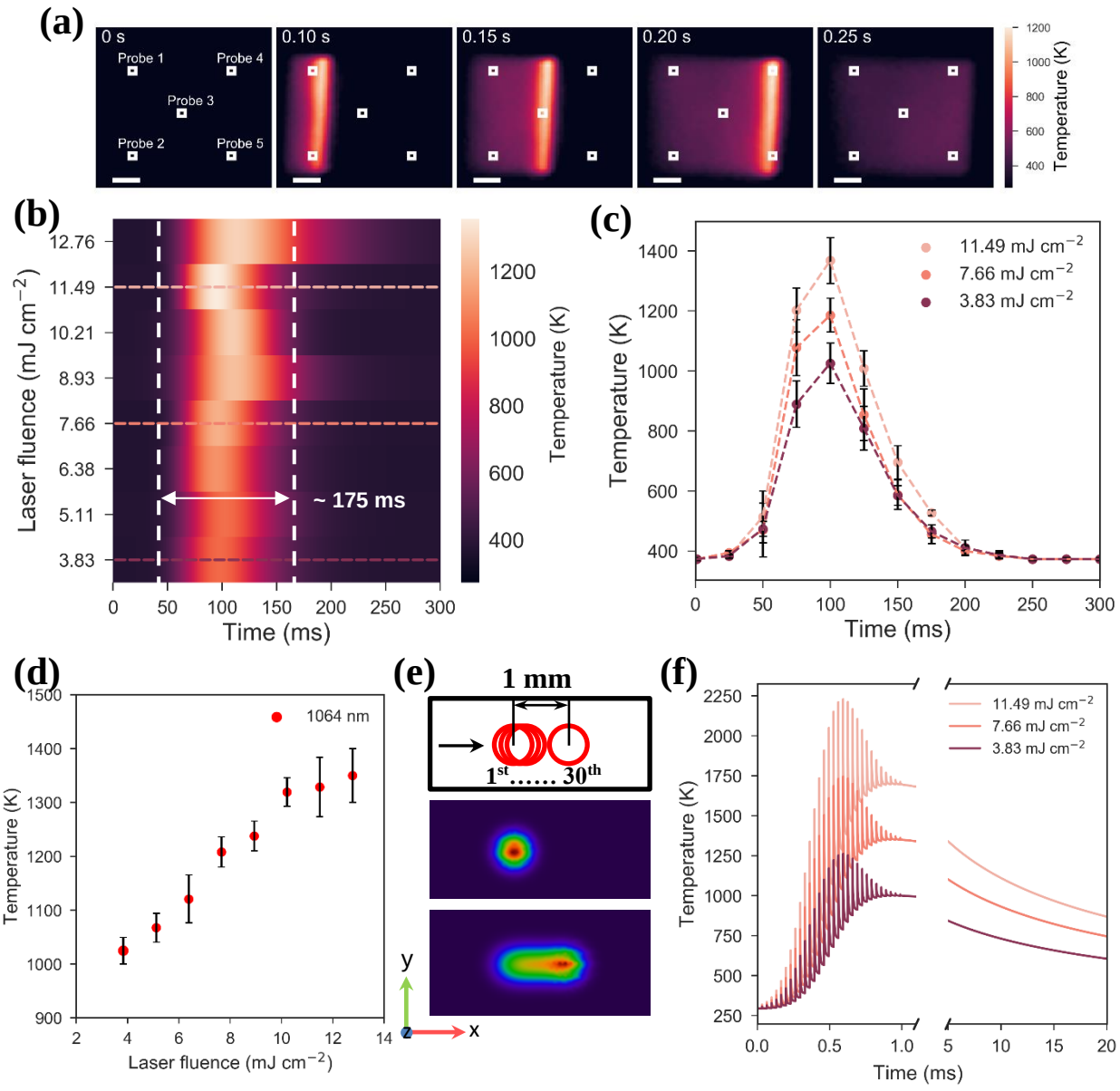

Figure 6-13. (**a**) The infrared images of EGO under 1064nm laser patterning at an average power of 6 W and at a scanning speed of 1000 mm/s (the scale is 25 mm); (**b**) Measured temporal thermal profile during Nd:YAG 1064 nm laser treatment at different laser average power and (**c**) typical temperature history with incident laser beam average

power of 3.83, 7.66 and 11.49 mJ cm^{-2}, respectively. (**d**) The change of temperatures with the variation of laser fluences under the same NOP (i.e. 30). (**e**) Schematic of 30 successive laser pulse train irradiated on the EGO surface, and the temperature fields in the top surface of EGO film after the first and the thirtieth pulse irradiation. (**f**) COMSOL modelling of the EGO film process by 1064 nm laser at various laser fluence.

When the ns IR laser with a photon energy of 1.17 eV irradiated on the Pt-EGO surface, the absorbed laser energy was rapidly converted into local heat via photothermal effect and raise the local temperature, depending on the laser processing conditions i.e. laser fluences and number of pulses per point (NOPs) determined by the beam size, scanning speed and repetition rate. To evaluate the elevated temperature profile of EGO film under laser patterning, we conducted thermal camera measurement of EGO to record the temperature images of EGO scanned by 1064 nm laser at various fluences. The temporal temperature profile captured by a FLIR high-resolution IR thermal camera represented averaged time trace temperatures (averaged from 5 individual points, **Figure 6-13 a** and **Figure 6-14**) rather than peak temperatures reached for each pulse. **Figure 6-13 b** and **c** show the temperature evolution of the Pt-EGO surface and **Figure 6-13 d** shows the change of temperatures with the variation of laser fluences under the same NOP (i.e. 30) using the ns IR laser at various laser fluences. As shown in **Figure 6-13 c and d**, increasing the laser fluences resulted in the increase of temperatures up to 1350.2 ± 50 K at the laser fluence of 11.49 mJ cm^{-2}. In addition, due to the high repetition rate (30 kHz), the generated spike heat induced by each pulse was not able to cool down to the initial temperature between pulses. Therefore, the heat accumulation effect lasted up to ~150 ms above the temperature of 493.2 K. However, owing to fast temperature elevation and limited frame rate of the infrared camera, the observed time trace temperature profiles was a result of heat accumulation rather than an actual heating pattern.

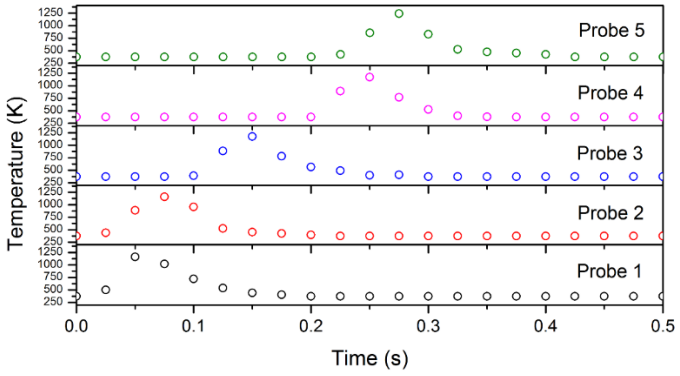

Figure 6-14 Time trace of the surface temperature of 5 individual probe points across the patterned area, the temporal temperature profile in the manuscript was processed by averaging those individual probes dataset.

Thus, in order to reveal the thermal evolution, COMSOL Multiphysics software was used to simulate the EGO film temperature dynamics undergoing 1064 nm laser irradiation at varying laser fluences. Owing to the extremely small duty cycle of 1/6660 (5 ns, 30 kHz), the calculation of the entire process requires tremendous computing time. Thus, the simulation was conducted by depositing 30 successive pulses scanned across the surface probe at 1000 mm s^{-1} with an interval of ~ 33.3 μs (**Figure 6-13 e**). Each individual pulse possesses a Gaussian energy distribution and has a laser ON time of 5 ns. The simulations shown in **Figure 6-13 f** represents the temporal temperature profile in a dynamic fashion with ~ 1 ms heating time and ~ 19 ms thermal relaxation time. At a given laser fluence, the rapid heating and cooling during and after the laser ON period were clearly shown, and the peak temperature gradually rises with increasing accumulated heat and spatial energy density. When the laser beam bypassed the probe, the accumulated heat reached the highest value of 998.9, 1348.2 and 1692.6 K corresponds to the laser fluences of 3.83, 7.66 and 11.49 mJ cm^{-2}. The residual temperature decades in 20 – 30 ms depending on the incident laser fluences.

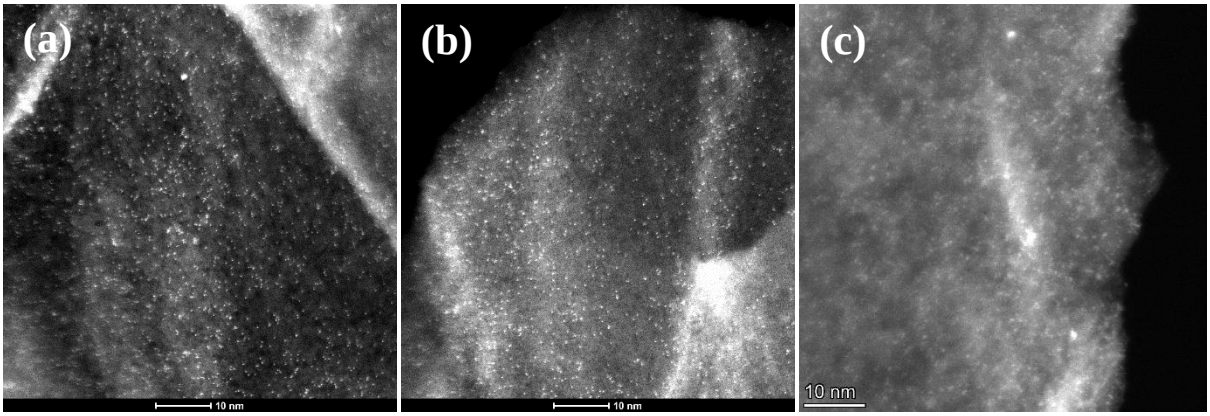

Figure 6-15 Representative HR-STEM images of Pt5-LrEGO fabricated via 1064 nm laser at (**a**) 3.83, (**b**) 7.66 and (**c**) 11.49 mJ cm^{-2}.

As described in Schweizer and Kerr's work[447], the thermal breakdown of H_2PtCl_6 to form platinum metal takes place through several steps as follows: $H_2PtCl_6 \rightarrow PtCl_4 + 2HCl$ at 423.2 – 453.2 K, $PtCl_4 \rightarrow PtCl_2 + Cl_2$ at 574.2-594.2 K, $PtCl_2 \rightarrow Pt + Cl_2$ at 648.2 – 783.2 K. Therefore, the temperature of 1025 K achieved during the 1064 nm laser irradiation at the lowest laser fluence (3.83 mJ cm^{-2}) was sufficient to induce *in situ* thermal decomposition of adsorbed H_6PtCl_2 molecules in the EGO film to form Pt single atoms. The rapid heating and cooling during

processing inhibit the diffusion and aggregation of the Pt atoms, and the short thermal pulse at temperatures up to 1692.2 K is likely to promote the formation of stable bonding between the Pt single atoms and the graphene support[407]. Interestingly, at the H_2PtCl_6 concentration of 5 mM, the as-formed Pt species remain as atomically dispersed single atoms with the increase of laser fluence from 3.83 mJ cm^{-2} to 11.49 mJ cm^{-2} (**Figure 6-15**), indicating that the rise in temperatures had not promoted the diffusion of the single atoms, which suggested stable metal–substrate bonding and high stability of the atomic dispersion.

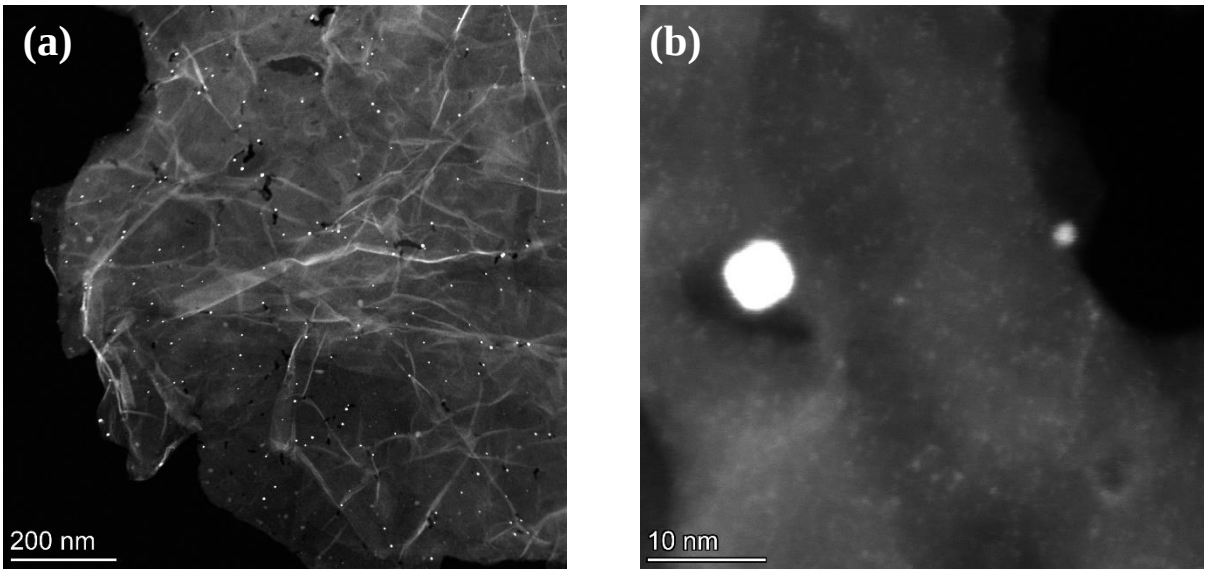

Figure 6-16 Representative (**a**) STEM and (**b**) HR-STEM images of Pt5-LrEGO synthesised via 1064 nm laser irradiation at 7.66 mJ cm^{-2}, with a scanning speed of 800 mm/s. The co-existence of Pt nanoparticles and single atoms were clearly presented.

This can be further supported by the consideration of two types of overlapping involved in the beam scanning. One is that as described in **Figure 6-2**, the laser beam spot size was 1 mm in diameter and overlap ratio between the tracks was 50%. This means that 50% of the laser track with already formed Pt single atoms was re-treated and a portion adjacent to the successive track was re-heated. However, no Pt aggregation/clusters were evident. The ultra-short heating time (~ 1 ms) and a rapid quenching time of ~ 108 ms under the laser settings may inhibit the migration of reduced Pt single atoms. The re-heating by the successive track was not significant at a scanning speed of 1000 mm/s, the simulated peak temperature caused by the successive laser tracks is ~ 538.2 K at a laser fluence of 11.49 mJ/cm^2 with 50% overlap ratio between the tracks. Additionally, strong metal-substrate bonding can be formed, which can anchor single atoms at a temperature of

1073 - 1173 K[407]. Thus, the absence of Pt aggregation during the successive laser track may attribute to the fast quenching, mild temperature evaluation and strong metal-support interaction during the direct laser irradiation. The other type of overlapping is always present in pulsed laser scanning. For instance, with the beam size of 1 mm, the scanning speed of 1000 mm/s and repetition rate of 30 kHz, the number of pulses per point (NOPs) is 30, which means that the Pt single atoms were exposed to the successive pulses, but no Pt aggregation was observed. On the other hand, thermal reduction of EGO involves removal of functional groups and restoration of carbon structures. Although the reduction of carboxyl groups with low stability starts at 100–150°C[448], total elimination of all the functional groups including highly stable carbonyl groups need a very high temperature (>1000°C)[330], and carbon structural evolution is temperature-dependent. During the laser irradiation, the temperature range achieved was sufficient to induce *in situ* photothermal reduction of the EGO, and the re-heating caused by overlapping should be beneficial to the reduction degree. Nevertheless, the rapid heating and quenching are also critical to prevent aggregation of atomic Pt dispersion. In order to investigate the effect of the laser heating, the scanning speed was set to be 800 mm/s with the same laser fluence to 7.66 mJ cm^{-2} to avoid damage of the Pt-EGO layer. In this case, the Pt particles/clusters were found in **Figure 6-16**, implying that the duration, which also enhances degree of overlapping, played an important role on atomic diffusion/aggregation of Pt single atoms.

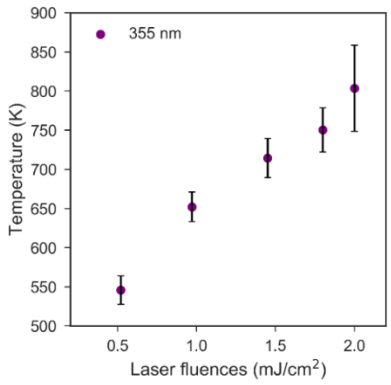

Figure 6-17 The change of temperatures with the variation of laser fluences under 355 nm laser irradiation at a scanning speed of 1000 mm/s.

When the ps UV laser, i.e. photon energy of 3.49 eV, was applied, the photochemical effect was expected. However, the temperature raises of the Pt-EGO surface monitored by the thermal camera (**Figure 17**) reached 803.7 K, suggesting that both photochemical and photothermal mechanisms

took place simultaneously. Although the direct bond-breaking led by the photochemical effect occurred ahead of thermal conduction, the photoreduction of the EGO via combined mechanisms may follow the sub-processes of removal of oxygen-containing functional groups, conversion of reduced carbon sp^3 into sp^2 structure and restoration of sp^2 network. The removal of functional groups and the conversion of sp^2 structure can be achieved by both photochemical and photothermal routes, but the restoration of sp^2 network might be dominated by thermal effect. Since the temperature measured on the Pt-EGO film at the laser fluence of 2.0 mJ cm^{-2} and the number of pulses of ~404 reached ~803.7 K, the reduction of the EGO may attribute to the combination of both photochemical and photothermal effects. In addition, the defect density of the LrEGO by the ps UV laser was higher than that by the ns IR laser as the higher temperature in the ns IR laser irradiation might be attributed more towards the restoration of sp^2 carbon network.

Since the EGO films contain multiple layers of EGO flakes, one of the reasons might be from anisotropy of thermal conductivity for two-dimensional materials, and GO has over 100-fold anisotropy of heat flow between the in-plane and out-of-plane directions[426]. In addition, laser beam conversion into thermal energy depends on not only the wavelength, pulse width, but also the stacked layers[418]. The penetration depth of the UV laser is smaller than that of the IR laser, and the ns pulse width also enhances heat conduction deeper than the ps pulse width. Therefore, the depth of the reduced Pt5-LrEGO layer by the ns IR laser should be deeper than that by the ps UV laser. This was reflected by the XRD patterns (**Figure 12**) that the signals from the EGO were still present for the ps UV treated Pt5-LrEGO, particularly for the low end of the laser fluences. This was also supported by the observation of the large error bars from 10 measurements for various Raman parameters (**Figure 11 b-d**), suggesting that less uniform and smaller penetration of heating by the ps UV laser. Therefore, despite the effective removal of oxygen via dominating photochemical mechanism by the UV laser, reduction and structure restoration of the beneath layers are most likely achieved by thermal conduction with limited heat transport. Increasing the laser fluence of the ps UV laser caused ablation of GO which accompanies endothermic phase changes and further impedes heat conduction. It could be concluded that the ns IR laser irradiation promotes an effective and uniform reduction of EGO throughout the EGO film in the thickness of 1.3 μm via a photothermal route.

In a comparison of other chemical and physical methods for fabrication of single atom catalysts, the laser photoreduction method is one-step, ultrafast laser manufacturing technique for fabrication of Pt single atoms on LrEGO support. Since the processing temperature by the ns IR laser can readily reach over 1350.2 K, which is sufficient to decompose most of metal precursors thermally.

6.5.5 Electrocatalytic Performance

The electrocatalytic HER activities of the Pt-5-LrEGO treated by the ns IR laser was evaluated using a typical three-electrode system with a rotating disk electrode (RDE). The measurement was conducted in a N_2-saturated 0.5 M H_2SO_4 electrolyte at a rotating speed of 1600 rpm. To reveal the intrinsic catalytic performance, an ohmic-drop correction was conducted in order to minimise the solution resistance. The linear sweep voltammograms (LSVs) curves of the purchased commercial Pt/C (20 wt.%, Johnson Matthew, HISEPC 3000), LrEGO and Pt-LrEGO samples with varying Pt loading are shown in **Figure 18a**. Note that both Pt1-LrEGO and Pt5-LrEGO have Pt in the form of single atoms, while the Pt species in the Pt10-LrEGO consist of Pt clusters.

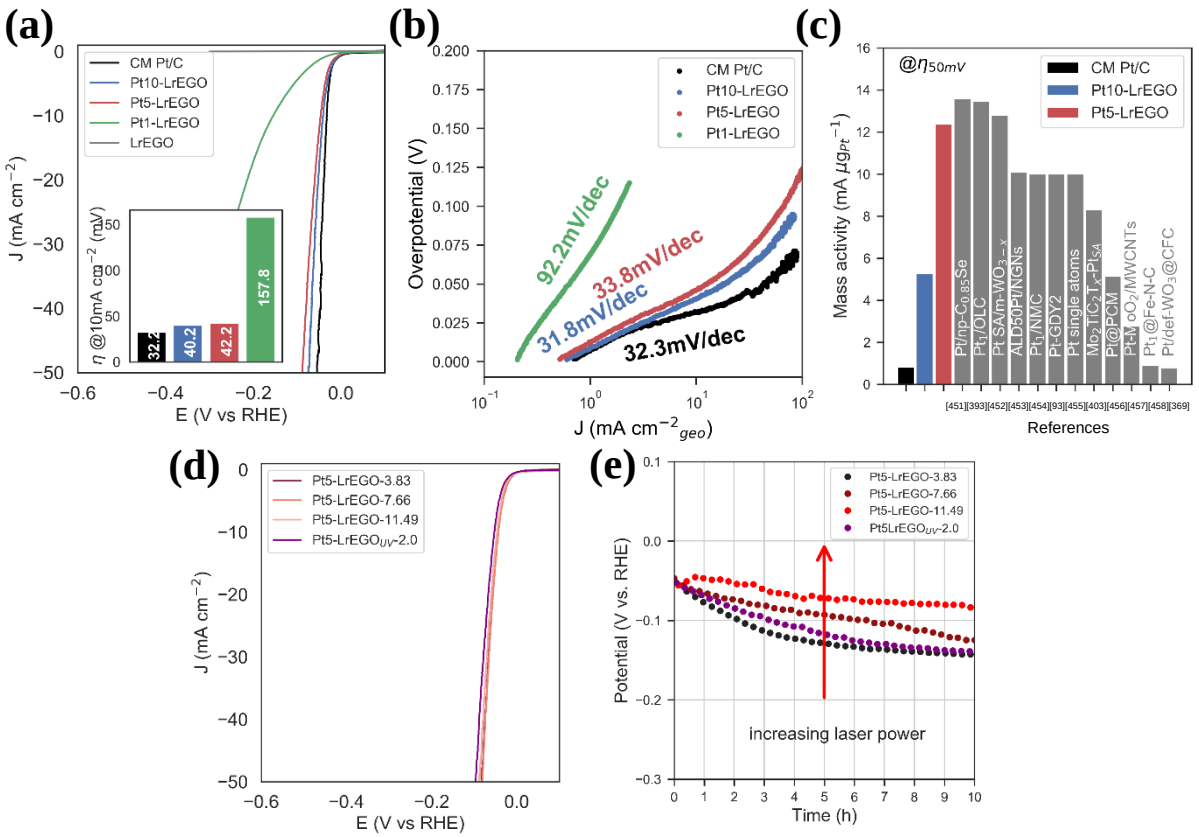

Figure 6-18. (**a**) LSV (after ohmic-drop correction) of the commercial Pt/C (20 wt_{Pt}%) and Pt-LrEGO fabricated by 1064 nm laser at 7.66 mJ cm^{-2} and treated with various precursor concentration at a scan rate of 10 mV s^{-1} in N_2-saturated 0.5 M H_2SO_4 at a rotation speed of 1600 rpm (inset: the overpotential of samples at a current density of 10 mA cm^{-2}). (**b**) Tafel slopes of the commercial Pt/C and Pt10-LrEGO, Pt5-LrEGO and Pt1-LrEGO. (**c**) Mass activities of the commercial Pt/C, Pt-LrEGO and the literature reported Pt-based SACs at an overpotential 50 mV. The bibliographic information of the reference numbers can be found in **Table 6-6**. (**d**) LSV of Pt-5-LrEGO samples obtained by 1064 laser writing at various laser fluences. (**e**) Chronopotentiometry of the commercial Pt/C and Pt-LrEGO treated at various laser power at a current density of 10 mA cm^{-2}.

The results showed that the incorporation of Pt into LrEGO in the form of either single atoms or clusters enhances its HER activity, as the pure LrEGO exhibits negligible current change under the applied voltage of - 0.3 V vs RHE. Using the thermodynamic HER potential E_0 (H^+/H_2 = 0 V vs RHE) as a reference, the Pt10-LrEGO and Pt5-LrEGO exhibited small overpotentials of 40.2 mV and 42.2 mV to drive a 10 mA cm^{-2} current density, respectively, which are comparable to that of the commercial Pt/C catalyst (32.2 mV). With the further decrease of the Pt loading, the Pt-1-LrEGO shows a large HER overpotential of 157.8 mV at 10 mA cm^{-2}, indicating the lack of active sites on the LrEGO support. Electrochemical impedance spectroscopy (EIS) analysis was performed at an overpotential of 30 mV to evaluate the electrode kinetics for HER (**Figure 6-19**).[393, 449] The Nyquist plot shows the Pt-5-LrEGO possess a low charge transfer resistance (R_{ct}) of 5.46 **Ω** implying a fast Faradaic process between the catalysts and electrolyte have been achieved.

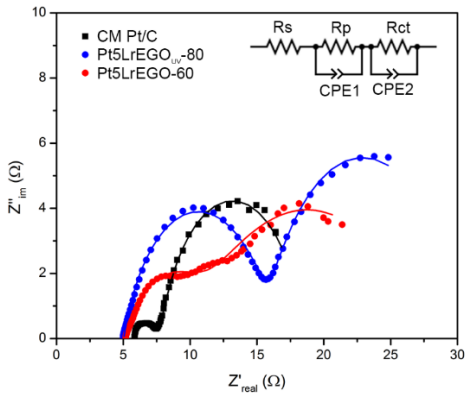

Figure 6-19 The Nyquist plots of Pt5-LrEGO fabricated via 1064 nm laser irradiation at 7.66 mJ cm^{-2}, Pt5-$LrEGO_{UV}$ treated through 355 nm laser at 2.00 mJ cm^{-2} and the commercial Pt/C at an overpotential of 30 mV with 10 mV sinusoidal perturbations from 0.01 to 10^6 Hz. The inset shows the equivalent circuit models, where R_s represents the solution resistance, R_p represents the surface absorption resistance and R_{ct} is the charge transfer resistance.

The HER catalysis kinetics of all samples were assessed by Tafel plot, as shown in **Figure 6-18 b**. The resultant Tafel slope of Pt10-LrEGO (31.8 mV dec^{-1}) and Pt5-LrEGO (33.8 mV dec^{-1}) are comparable to the CM Pt/C (32.3 mV dec^{-1}), signifying superior HER kinetics in spite of the

extremely low Pt loading (1.4 wt_{Pt}.% and 0.4 wt_{Pt}.% vs 20 wt_{Pt}.%). As expected, the Pt1-LrEGO shows a large Tafel slope of 92.2 mV dec^{-1} due to the lack of active sites. The mass activities of the catalysts were evaluated by normalising the measured current at given overpotential to the Pt mass loading, and an overpotential of 50 mV was chosen to compare with the literature reported values. As shown in Figure 3c, because of the significantly lower Pt loading in the Pt5-LrEGO (0.4 wt_{Pt}%) compared to the CM Pt/C (20 wt_{Pt}%), the Pt5-LrEGO shows an order of magnitude higher mass activity (12.36 mA μg_{Pt}^{-1}) than the CM Pt/C (0.83 mA μg_{Pt}^{-1}) at an overpotential of 50 mV. The superior HER mass activity of Pt5-LrEGO outperforms the majority of literature values (**Figure 6-18 c**, a detailed comparison is given in **Table 6-6**), and demonstrating an ultrahigh Pt utilisation and great promise for the practical application. Compared to the Pt5-LrEGO, the Pt10-LrEGO shows a moderate enhancement in mass activity versus CM Pt/C, which is likely because of a fraction of inert Pt atoms embedded in the clusters.

We subsequently studied the influence of laser fluence on the HER performance of Pt single atoms decorated LrEGO. The Pt5-LrEGO treated by the ns 1064 nm laser at 3.83, 7.66 and 11.49 mJ/cm^2 are denoted as Pt5LrEGO-3.83, Pt5LrEGO-7.66 and Pt5-LrEGO-11.49 respectively, and sample fabricated via ps 355 nm laser at a laser fluence of 2.0 mJ/cm^2 is named as Pt5-$LrEGO_{UV}$-2.0. **Figure 6-18 d** shows the LSVs of above-mentioned catalysts tested in 0.5 M H_2SO_4 electrolyte, the overpotential at 10 mA cm^{-2} of Pt5-LrEGO-3.83, Pt5-LrEGO-7.66 and Pt5-LrEGO-11.49 were 43.3, 42.2 and 43.1 mV respectively, demonstrating the HER activity and kinetics remain unchanged with various laser output under this fabrication conditions. The Pt5-$LrEGO_{UV}$-2.0 samples show a slightly increased overpotential of 52.6 mV at 10 mA cm^{-2}, possibly owing to the unevenly reduced LrEGO which leads to a relatively larger charge transfer resistance (R_{ct} = 14.2 **Ω** at an overpotential of 30 mV, **Figure 6-19**). Chronopotentiometric test at 10 mA cm^{-2} has been performed to evaluate the HER durability of Pt5LrEGO samples. As shown in **Figure 6-18 e**, among these catalysts, the Pt5LrEGO-11.49 maintains a stable HER performance with a slight increase 39 mV after 10 h testing. Nevertheless, the HER activity of Pt5LrEGO-7.66 and Pt5LrEGO-3.83 degraded remarkably after 10 h with the final potential of -0.1 and -0.13 V vs RHE to drive 10 mA cm^{-2} current density, indicating the Pt5LrEGO HER durability increased with increasing laser power. Electrochemical perturbation is involved in HER process, which may cause damage to the basal plane of graphene[450]. The conductive pathways of 3D-interconnected graphene substrates will be destroyed after long-term testing, thus leading to the degradation of

electrocatalytic activity in HER. Therefore, graphene substrate with less structural defects and better mechanical property may exhibit superior stability during HER test. Additionally, it was found that at a high temperature (> 1500 K), Pt atoms can coordinate with carbon supports and form a strong and stable metal-substrate bonding[407]. The enhanced metal-support interaction may also play an important role in the enhancement of catalytical durability.

Table 6-6. HER experimental conditions and activity of Pt-5-rEGO, CM Pt/C and other reported platinum-based SACs tested in 0.5 M H_2SO_4 electrolyte.

Catalysts	Electrode	Electrolyte	Catalyst loading[b] (mg cm^{-2})	η[c] @ 10mA cm^{-2} (mV)	Tafel slope (mV dec^{-1})	Pt mass activity (mA μg_{Pt}^{-1})	Ref.
Pt5-LrEGO	GCE[a]	0.5 M H_2SO_4	~0.255	42.3	33.8	12.36 @ $\eta_{50\ mV}$	This work
CM Pt/C (20 wt.%)				32.2	32.3	0.83 @ $\eta_{50\ mV}$	
Pt/np-$Co_{0.85}Se$	Pt/np-$Co_{0.85}Se$	0.5 M H_2SO_4	N/A	58	26	13.57 @ $\eta_{50\ mV}$	[451]
Pt_1/OLC	GCE	0.5 M H_2SO_4	0.51	~38	36	~13.46 @ $\eta_{50\ mV}$	[393]
Pt_1/graphene				~56.6	42	~4.93 @ $\eta_{50\ mV}$	
Pt SA/m-WO_{3-x}	GCE	0.5 M H_2SO_4	~0.204	47	45	12.8 @ $\eta_{50\ mV}$	[452]
ALD50Pt/NGNs	GCE	0.5 M H_2SO_4	~0.077	~41	29	10.1 @ $\eta_{50\ mV}$	[453]
Pt_1/NMC	GCE	0.5 M H_2SO_4	~0.204	29	26	10 @ $\eta_{50\ mV}$	[454]
Pt-GDY2	Ti foil	0.5 M H_2SO_4	4.65 (μg_{Pt} cm^{-2})	N/A	N/A	~10 @ $\eta_{50\ mV}$	[93]
Pt single atoms	GCE	0.5 M H_2SO_4	~0.153	~39	33.2	10 @ $\eta_{50\ mV}$	[455]
$Mo_2TiC_2T_x$-Pt_{SA}	Carbon paper	0.5 M H_2SO_4	1	~32.8	30	8.3 @ $\eta_{77\ mV}$	[403]
Pt@PCM	GCE	0.5 M H_2SO_4	~0.107	105	65.3	~5.13 @ $\eta_{50\ mV}$	[456]
Pt-MoO_2/MWCNTs	GCE	0.5 M H_2SO_4	0.47	60	43	~2.77 @ $\eta_{50\ mV}$	[457]
Pt_1@Fe-N-C	GCE	0.5 M H_2SO_4	~0.3	60	42	~0.9 @ $\eta_{50\ mV}$	[458]
Pt/def-WO_3@CFC	GCE	0.5 M H_2SO_4	~0.255	42	61	~0.8 @ $\eta_{50\ mV}$	[369]

[a] Glassy carbon electrode. [b] The catalyst loading, if not specific noted, denotes the total mass of catalysts loaded on the working electrode. [c] Overpotential.

6.6 Conclusion

In summary, for the first time, we have developed a rapid, versatile, solid-phase laser manufacturing technique for synthesising graphene supported Pt SAC for HER application. In this approach, sublimation of the precursor solution contains anionic metal complex ($PtCl_6^{2-}$) promotes the uniform distribution of metal ions on the EGO substrate surface and prevents localised aggregation by minimising the electrostatic interaction between EGO and the metal ions. The influence of the laser fluence and the heating time on the SACs production of the Pt-LrEGO was determined. The pronounced photothermal effect of the 1064 nm laser irradiation via fast scanning enables a high-temperature synthesis (up to ~1700 K) with an ultra-short heating time (~19 ms), which not only guarantees the through-thickness thermal reduction of both EGO and Pt ions at once, but also prevents the migration of metal atoms. We also demonstrated the Pt-LrEGO exhibits promising activity and high Pt utilisation in HER with mass activity with an overpotential of 42.3 mV at 10 mA/cm^2 and mass activity of 12.36 $mA/\mu g_{Pt}$ at 50mV. This method opens up a versatile avenue for a variety of graphene-based catalysts and smart electronics preparation of a set of single atoms.

Chapter 7 Conclusions and Perspectives

7.1 Conclusions

Development of laser-assisted synthesis methods for electrocatalysts fabrication was conducted in the project, in which different synthesis strategies, various laser parameters and processing mechanisms studies were employed. The project explored the potential of laser techniques in synthesizing precious metal nanocatalysts from monodispersed sub 5 nm NPs, to ~ 2 nm NPs decorated graphene composites and finally down to homogeneously distributed single atoms. Furthermore, the electrocatalysts produced in each approach demonstrate their promising performance in various catalytic applications, including ORR, OER, HER and supercapacitor. Although the catalytic activities of precious nanocatalysts depend on various factors and differ between reactions. But size reduction of catalytic species from NPs to atomic scale displays its importance in maximizing the active site exposure and precious metal utilization and reducing the cost. Additionally, the laser-assisted approaches are not materials specific, *i.e.* the methods are not designed for specific elements/materials, which can be easily extended to a wide variety of nanomaterials fabrication. Thus, the present work opens up new opportunities for homogeneous NPs decorated electrocatalysts and SACs production. The main findings and conclusions presented in the thesis are summarized as follows:

7.1.1 UV Laser Assisted Pt Nanoparticles Size Refinement for Enhanced Oxygen Reduction Reaction

Admittedly, the widely studied PLAL method for NPs synthesis demonstrates its advantage in producing ligand-free NPs, its feasibility for a wide range of nanomaterials fabrication, and its potential in large-scale production. However, the lack of particles size control limits its catalytical applications, for the large particles size consists of ineffective atoms beneath the surface, and the broad size distribution inhibits the performance stability and reproducibility. In order to refine the pristine Pt NPs produced via PLAL method, and to enhance the ORR activity, a UV laser laser-assisted size tailoring step was employed. The main conclusions of this work include:

- Statistics particles size analysis through TEM imaging showed the Pt NPs size distribution and average size rapidly narrowed and decreased with increasing laser fluence and irradiation time. As the irradiation time prolongs, the variation in the size

distribution of all samples was minimized. In detail, the PLAL produced pristine Pt NPs with an average size of 24 nm (σ = 8.2) significantly reduced down to 9.3 nm (σ = 1.3), 4.7 nm (σ = 0.3) and 5.2 nm (σ = 1.3) after laser irradiation with fluences of 0.5, 0.8 and 1.1 J/cm^2, respectively.

- The UV-Vis spectra of the size tailored Pt NPs samples were compared with Mie theory calculated extinction efficiency. The predicted LSPR bands of the refined LPt NPs exhibit clear blueshift and drop in intensity with decreasing particles size, which was in agreement with the experimental result. However, it was also found, at a higher laser fluence of 1.1 J/cm^2 irradiation, the size of Pt NPs was not further reduced compared to the sample treated at 0.8 J/cm^2.
- Based on Mie theory calculation, the magnitude of absorption efficiency of Pt NPs shows a prominent feature in the UV region for Pt NPs size range in 10 – 300 nm. Additionally, for Pt NPs size less than 20 nm, the absorption cross-section at 248 nm was found to be 3.0, 12.1 and 68.2 times higher than that of the wavelength of 355, 532 and 1064 nm, respectively. The high absorption-cross section of Pt NPs at 248 nm is beneficial for laser energy deposition.
- Through numerical simulations, it has been found that Pt NPs size refinement attributes to surface vaporization of Pt. A vaporization threshold fluence was plotted based on the interplay between size-dependent energy deposition and heat dissipation. Owing to the low energy absorption efficiency and fast heat loss of small Pt NPs, further size reduction of Pt NPs well below sub-5 nm will come at the cost of exponentially growing laser fluence.
- When employed as an oxygen reduction reaction (ORR) catalyst, the refined Pt NPs exhibits excellent catalytic performance with an onset potential of 0.97 V and a mass activity of 0.83 mA/μg_{Pt} at 0.85 V, which outperforms the commercial Pt/C catalysts. Additionally, benefit by the negatively charged surface and mono size dispersion of the refined Pt NPs, the laser assisted Pt NPs show enhanced stability with only 13.7 % current loss after 5.5 h durability test.

7.1.2 Laser Assisted Solution Synthesis of High Performance Graphene Supported Electrocatalysts

The UV laser irradiation of NPs colloids has shown its efficient size tailoring of Pt NPs. However, for the low energy absorption efficiency and fast heat loss of small Pt NPs, further

size reduction of Pt NPs well below sub-5 nm will come at the cost of exponentially growing laser fluence. Thus, we developed a solution-based synthesis method for NPs decorated graphene production. Uniformly distributed Pt and RuO_2 NPs were found on the graphene substrate, with particles size well below sub-5 nm. The main findings are summarized as follows:

- The direct photoexcitation energy for EGO was estimated to be ~ 3.25 to 3.95 eV. Therefore, the photon energy of 248 nm laser (4.99 eV) is sufficiently high to excite EGO and thus create electron-hole pairs. In contrast. The conventional GO synthesized via Hummers' method exhibits a direct transition energy of ~ 3.25 – 4.31 eV for its high oxygen contents, indicating a less efficient excitation under UV irradiation than that of EGO.
- Photon-induced reduction of the EGO dispersion was found with the presence of electron donors. With increasing laser fluence, the removal of oxygen groups and restoration of sp2 carbon structure became more pronounced. Meanwhile, at a higher laser fluence (681 mJ/cm^2), EGO bleached out due to photodegradation at such high laser fluence. Thus, the optimal laser fluence of 568 mJ/cm^2 in the study guarantees an efficient reduction of EGO and the integrity of rEGO flakes.
- Simultaneous can be achieved via UV laser irradiation of metal salts contained EGO precursor solution. Within the current study, RuO_2 and Pt NPs were homogeneously deposited on rEGO flakes, with a particles size of 2.8 nm ($\sigma = 1.3$) and 2 nm ($\sigma = 0.5$). Additionally, the method demonstrates its versatility in producing various types of functional nanoparticles on the surface of rEGO sheets, such as alloy (PtPd) and metal oxide (MnO_x) NPs.
- The mechanism of the laser induced photochemical reaction was proposed. The photon excitation of EGO creates electron-hole pairs. The photoinduced electrons reduce EGO and metal ions, while the photogenerated holes participate in oxidative reactions with the reduced metal NPs or the electron donors.
- Further electrochemical performance measurements indicate the crystalline RuO_2-rEGO exhibits excellent OER activity with a small overpotential of 225 mV at 10 mA/cm^2, and outperforms the commercial RuO_2 catalyst (283 mV). Additionally, when used in electrochemical capacitance, the amorphous RuO_2-rEGO composite shows higher specific capacitance of 649.7 F/g at a current density of 0.5 A/g with good rate

capability, outperforming the commercial reference. The great performance of RuO_2-rEGO composite attributes to the high ECSA and good electrical conductivity.

- Owing to the small size distribution and high Pt utilization, the Pt-rEGO composite shows superior catalytical activities in HER and ORR. For HER catalysis, the Pt-rEGO shows more than double the mass activity at overpotentials of 10, 30 and 50 mV than that of the commercial Pt/C. In the case of ORR, a lower diffusion-limited current was found in the Pt-rEGO sample, which caused by the restacking of graphene sheets that inhibits the diffusion of solvated O_2.
- This versatile, simple and scalable method can be easily adapted for the synthesis of various types graphene-based functional nanocomposites, for diverse applications beyond electrochemical energy storage and conversion.

7.1.3 Laser Enabled Synthesis of Single Atom Catalysts

The isolated dispersion of metallic atoms on solid support represents the ultimate limit of nanoscale catalysts. At such an atomic scale, the atom utilization is maximized, and the catalytic activity can be tuned via different metal-support interaction. However, for SACs synthesis, the solution synthesis strategies are limited for the high mobility of ions and atoms in a liquid medium, which inevitably leads to the aggregation of metal atoms and clusters and forms NPs. Thus, this work develops a solid-phase synthesis of SACs via rapid laser treatment, and investigate key aspects for successfully fabricating Pt SACs. The main conclusions are summaries as follows:

- After filtration of metal precursor solution through the EGO films, water sublimation through freeze-drying is essential to immobilise the metal ions and to avoid localised precipitation of the metal precursor.
- The Pt loading of the laser reduced Pt-LrEGO composites exponentially increases with increasing precursor concentration. An optimal precursor concentration of 5mM in this study allows an atomically dispersed Pt on LrEGO flakes with a Pt loading of 0.41 wt%. However, further increase of the concentration leads to clear aggregation of Pt atoms.
- The precursor types show a significant impact on the as-formed Pt species ($PtCl_4$ and H_2PtCl_6). The XPS results indicate the Pt cations tend to couple with the oxygen-containing groups within EGO which adversely affect the dispersion of metal cations on the EGO substrate, and thus unlikely to form isolated atom after laser irradiation.

The interaction tendency of the Pt anionic complex is less pronounced, which helps the isolated dispersion of Pt species on EGO.

- The laser wavelength should be carefully chosen. For both IR and UV irradiation, the elevated temperature is sufficient to decompose the H_2PtCl_6 and form metallic Pt species. However, the low penetration depth and low ablation threshold of UV (355 nm) irradiation together with the anisotropic thermal conductivity of EGO flakes leads to an inhomogeneous reduction and restoration of graphene structure, and accelerates the ablation of EGO. In contrast, effective and homogenous graphitization of EGO was observed after ns IR laser irradiation. Through simulations and experiments, the temporal accumulated heat during ns IR laser scanning can reach up to ~ 1692.6 K. High temperature and relatively high ablation threshold of IR (1064 nm) processing guarantee a thorough thermal reduction of the EGO film.
- To prevent atom migration during the high temperature process, the high scanning speed of the laser probe plays an important role. It has been found that high scanning speed at 1000 mm/s with a repetition rate of 30 kHz is beneficial to prevent Pt atoms migration.
- For HER catalysis, the Pt5-LrEGO SAC shows a comparable activity (33.8 mV/dec) than the commercial Pt/C (32.3 mV/dec) but with extremely low precious loading. Benefit by the high Pt utilization, the Pt5-LrEGO displays an order of magnitude high mass activity (12.36 mA μg_{Pt}^{-1}) than the CM Pt/C (0.83 mA μg_{Pt}^{-1}) at an overpotential of 50 mV. Additionally, the HER stability increases with increasing applied laser fluence, which may attribute to the decrease in structural defects within the graphene support and the enhanced metal-support interaction after high temperature process.

7.2 Perspectives

The present studies have detailed the laser-assisted approach for precious metal electrocatalysts synthesis. Different approaches were employed to produce nanocatalysts size from monodispersed sub 5 nm NPs, to ~ 2 nm NPs decorated graphene composites and ultimately down to homogeneously distributed single atoms. Even though, the study focused on single element precious metal catalysts (*e.g.* Pt and Ru), the developed methods can be easily extended to a wide variety of materials and substrates, and can be potentially scaled up.

Alloy and precious metal-free electrocatalysts

Owing to the valuable features of laser refinement for monodisperse colloids generation, such as tunable size, naked surface and free of contamination, the synthesized NPs are excellent model catalyst candidates. The free of ligands surface minimizes unexpected effects caused by the attached ligands and chemical contamination. The tunable size of NPs provides an opportunity to investigate the size-dependent catalysis behaviors and reaction mechanisms. Furthermore, it is also possible to screen catalysts with various mixed oxides and alloying elements with tunable composition. Such characteristics of being a reference candidate are not limited in electrocatalysis, but can be potentially extended to other applications, such as biomedicine, optical devices and chemical detection. However, challenges remain for alloy NPs synthesis, as well as size tailoring. One of the issues is to keep the stoichiometry of the original target or NPs. Although, noble materials such as Pt remain stable under intense laser-induced vaporization and condensation in a liquid environment, transient elements on the opposite side tend to react with the solvent or solvent decomposed species. As demonstrated in **Figure 7-1** from the early study, when ablating a FePt alloy target (Fe:Pt = 50:50) in water, clear element segregation was found. The as-synthesized FePt NPs exhibit two distinct morphologies, one is a core-shell structure with Fe_3O_4 shell and a Fe deficient alloy core, another one is an iron-depleted alloy $Fe_{25}Pt_{75}$ NPs. The severe element segregation hints towards a different reactivity of two elements in the aqueous environment. The reactive Fe tends to react with water and form oxides covers on the Pt core. Thus, avoid element segregation and oxidation is critical for successfully synthesizing alloyed NPs in future work.

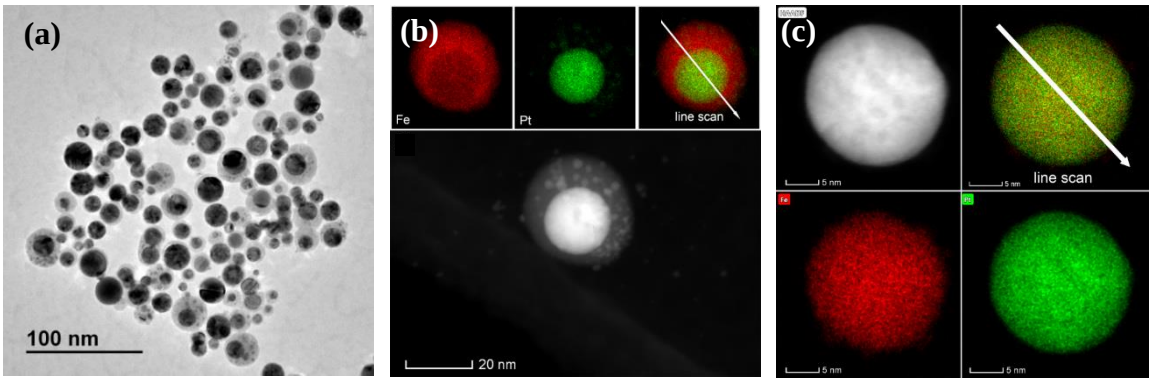

Figure 7-1 (**a**) TEM image of FePt NPs synthesized via PLAL in de-ionized water, and representative STEM images and EDS mappings of the coexisting (**b**) core-shell and (**c**) alloy FePt NPs. Within the EDS mapping, Fe is marked in red, and Pt is marked in green.

On the other hand, towards replacing the expensive platinum-based catalysts, recent work has highlighted the promise of transition metal catalysts as a highly active alternative to the existing precious metal-based materials. The laser assisted technique shows promising versatility can potentially fit non-precious metal catalysts synthesis, materials screening and development.

Metal-support interactions for tuning the stability and activity of the catalyst

Heterogeneous catalysts are widely adopted in various catalytic applications, such as fuel cell, electrolysis and CO_2 reduction *etc*. The interplay between the catalytic species and supporting materials has a significant impact on the catalyst's stability and activity. For instance, the nitrogen-doped carbon materials were frequently used to support catalytical NPs or single atoms. Precious elements, such as Pt, can be anchored at the nitrogen-doped site, and thus enhance the catalytical durability. Additionally, the interaction of catalytically active species onto various support also provides a chance to tune the electron configuration of the electrocatalysts, which can potentially adjust the adsorption energy of active site to the reactants and hence, promote the intrinsic catalytic activity. In addition to the graphic support used in this study, other newly developed 2D supporting materials, such as MoS_2 and Mxene, with unique properties could potentially modify the catalysts performance. However, challenges in high-power pulsed laser irradiation may modify the supporting materials photothermally or photochemically. Thus, fundamental studies on the physical and chemical phenomena, such as elements segregation, defect development, particles ejection *etc*. may benefit the control of the supporting materials' morphology, composition and functionality.

Meanwhile, the high temperature and high-pressure process during laser-matter interaction can potentially trigger atom re-arrangement as found in this study, which offers a chance for heterogeneous doping in the graphic support. Moreover, the formation of porous structure through fierce laser-matter interaction may lead to an increased surface area of the support. Therefore, the future work on the heterogeneous catalysts through laser irradiation can focus on the metal-support interaction and the construction of supporting materials with heterogeneous atom doping and porous structure.

Theoretical modelling of atoms migration and metal-support interaction

For laser assisted fabrication of SACs, the origin of materials atomic dispersion under high temperature, and the interaction between metal atoms with substrates, and hence the resulting catalytic performance should be investigated by the novel numerical technique. The effects of many parameters, such as, the shape, size, defects development of nanocatalysts and their response to adsorbents and adatoms during catalytic reactions, are difficult to determine

experimentally. To date, the molecular dynamic simulation would be an ideal tool to understand the migration of metal atoms/clusters in the laser-irradiated area, which is instructive to understand the single atom formation mechanisms and to optimize the processing parameters. As for the catalytic activity, density function theory as an emerging tool can provide insights about the electron configuration of the active sites and the adsorption mechanisms between reactants and catalysts interface. Thus, the simulations open up new opportunities to reveal the reactivity and reaction mechanisms, and provide a pathway for catalysts screening and design.

Scale-up production

The production rate for electrocatalysts synthesis of the current study is still limited. Efficient scale-up from lab to pilot production is beneficial for large scale catalyst's applications such as fuel cell, electrolyzer and organic fuel production. For the laser-assisted photodeposition method, higher photodeposition efficiency could be optimized by adjusting the liquid flow, optical pathway, and laser parameters *etc*. In the case of laser pyrolysis for SACs production, a focused line beam would benefit the production rate for it can reduce the scanning path and mitigate the repeated heating.

Reference

[1] D. Zhang, B. Gökce, S. Barcikowski, *Chem. Rev.* **2017**, *117*, 3990.
[2] S. Jendrzej, B. Gökce, M. Epple, S. Barcikowski, *ChemPhysChem* **2017**, *18*, 1012.
[3] T. Tsuzuki, *Nanotechnology Commercialisation*, Singapore Pan Stanford Publishing, **2016**.
[4] A. Nel, T. Xia, L. Mädler, N. Li, *Science (New York, N.Y.)* **2006**, *311*, 622.
[5] R. Lux, 2014.
[6] W. G. Kreyling, M. Semmler-Behnke, Q. Chaudhry, *Nano Today* **2010**, *5*, 165.
[7] *Nature Nanotechnology* **2019**, *14*, 193.
[8] *BSI Standards Publication Nanoparticles – Vocabulary*, PAS 71:2011, British Standards Institution, **2011**.
[9] M. A. Kebede, T. Imae, in *Advanced Supramolecular Nanoarchitectonics*, DOI: https://doi.org/10.1016/B978-0-12-813341-5.00001-2 (Eds: K. Ariga, M. Aono), William Andrew Publishing **2019**, p. 3.
[10] S. Dang, Q.-L. Zhu, Q. Xu, *Nature Reviews Materials* **2017**, *3*, 17075.
[11] L. A. Bauer, N. S. Birenbaum, G. J. Meyer, *Journal of Materials Chemistry* **2004**, *14*, 517.
[12] C. Buzea, I. I. Pacheco, K. Robbie, *Biointerphases* **2007**, *2*, MR17.
[13] C. Altavilla, E. Ciliberto, *Inorganic Nanoparticles: Synthesis, Applications, and Perspectives*, CRC Press, **2016**.
[14] K. K. Nanda, *Physics Letters A* **2012**, *376*, 1647.
[15] W. H. Qi, M. P. Wang, *Materials Chemistry and Physics* **2004**, *88*, 280.
[16] P. Buffat, J. P. Borel, *Physical Review A* **1976**, *13*, 2287.
[17] in *Nanoparticle Technology Handbook (Third Edition)*, DOI: https://doi.org/10.1016/B978-0-444-64110-6.00001-9 (Eds: M. Naito, T. Yokoyama, K. Hosokawa, K. Nogi), Elsevier **2018**, p. 3.
[18] R. C. Garvie, *The Journal of Physical Chemistry* **1965**, *69*, 1238.
[19] R. C. Garvie, *Journal of Physical Chemistry* **1978**, *82*, 218.
[20] T. Chraska, A. H. King, C. C. Berndt, *Materials Science and Engineering: A* **2000**, *286*, 169.
[21] R. Nitsche, M. Winterer, H. Hahn, *Nanostructured Materials* **1995**, *6*, 679.
[22] R. C. Garvie, R. H. Hannink, R. T. Pascoe, *Nature* **1975**, *258*, 703.
[23] T. Tsuzuki, *International Journal of Nanotechnology* **2009**, *6*, 567.
[24] H. Zhang, J. F. Banfield, *Journal of Materials Chemistry* **1998**, *8*, 2073.
[25] K.-R. Zhu, M.-S. Zhang, J.-M. Hong, Z. Yin, *Materials Science and Engineering: A* **2005**, *403*, 87.
[26] J. M. McHale, *Science* **1997**, *277*, 788.
[27] M. C. Roco, *Journal of Nanoparticle Research* **1999**, *1*, 1.
[28] B. D. Begg, E. R. Vance, J. Nowotny, *Journal of the American Ceramic Society* **1994**, *77*, 3186.
[29] K. Ishikawa, T. Uemori, *Phys. Rev. B* **1999**, *60*, 11841.
[30] K. Ishikawa, K. Yoshikawa, N. Okada, *Phys. Rev. B* **1988**, *37*, 5852.
[31] S. Chattopadhyay, P. Ayyub, V. R. Palkar, M. Multani, *Phys. Rev. B* **1995**, *52*, 13177.
[32] J. a. Scholl, A. L. Koh, J. a. Dionne, *Nature* **2012**, *483*, 421.
[33] G. Mie, *Annalen der Physik* **1908**, *330*, 377.
[34] K. L. Kelly, E. Coronado, L. L. Zhao, G. C. Schatz, *The Journal of Physical Chemistry B* **2003**, *107*, 668.

[35] G. Cao, *Nanostructures & Nanomaterials : Synthesis, Properties & Applications*, Imperial College Press, London **2004**.
[36] D. R. Dreyer, S. Park, C. W. Bielawski, R. S. Ruoff, *Chemical Society Reviews* **2010**, *39*, 228.
[37] M. Naguib, V. N. Mochalin, M. W. Barsoum, Y. Gogotsi, *Advanced Materials* **2014**, *26*, 992.
[38] C. Suryanarayana, *Progress in Materials Science* **2001**, *46*, 1.
[39] B. L. Cushing, V. L. Kolesnichenko, C. J. O'Connor, *Chemical Reviews* **2004**, *104*, 3893.
[40] M. Rycenga, C. M. Cobley, J. Zeng, W. Li, C. H. Moran, Q. Zhang, D. Qin, Y. Xia, *Chemical Reviews* **2011**, *111*, 3669.
[41] K. Wenderich, G. Mul, *Chem. Rev.* **2016**, *116*, 14587.
[42] N. Osterwalder, C. Capello, K. Hungerbühler, W. J. Stark, Vol. 8, 2006, 1.
[43] F. J. Heiligtag, M. Niederberger, *Materials Today* **2013**, *16*, 262.
[44] S.-Y. Lin, Y.-T. Tsai, C.-C. Chen, C.-M. Lin, C.-h. Chen, *The Journal of Physical Chemistry B* **2004**, *108*, 2134.
[45] P. Lee, D. Meisel, *The Journal of Physical Chemistry* **1982**, *86*, 3391.
[46] C. Zhu, S. Guo, Y. Zhai, S. Dong, *Langmuir* **2010**, *26*, 7614.
[47] Z. S. Pillai, P. V. Kamat, *The Journal of Physical Chemistry B* **2004**, *108*, 945.
[48] N. G. Bastús, F. Merkoçi, J. Piella, V. Puntes, *Chemistry of Materials* **2014**, *26*, 2836.
[49] S. Sun, C. B. Murray, D. Weller, L. Folks, A. Moser, *Science* **2000**, *287*, 1989.
[50] Y. Sun, B. Mayers, T. Herricks, Y. Xia, *Nano Letters* **2003**, *3*, 955.
[51] H.-G. Liao, D. Zherebetskyy, H. Xin, C. Czarnik, P. Ercius, H. Elmlund, M. Pan, L.-W. Wang, H. Zheng, *Science* **2014**, *345*, 916.
[52] D. Li, C. Wang, D. Tripkovic, S. Sun, N. M. Markovic, V. R. Stamenkovic, *ACS Catalysis* **2012**, *2*, 1358.
[53] M. Luo, Y. Hong, W. Yao, C. Huang, Q. Xu, Q. Wu, *Journal of Materials Chemistry A* **2015**, *3*, 2770.
[54] L. Rodríguez-Sánchez, M. C. Blanco, M. A. López-Quintela, *The Journal of Physical Chemistry B* **2000**, *104*, 9683.
[55] N. Tian, Z.-Y. Zhou, S.-G. Sun, Y. Ding, Z. L. Wang, *Science* **2007**, *316*, 732.
[56] Z. Zhang, C. Feng, C. Liu, M. Zuo, L. Qin, X. Yan, Y. Xing, H. Li, R. Si, S. Zhou, J. Zeng, *Nature Communications* **2020**, *11*, 1215.
[57] J. Lee, W. Choi, *The Journal of Physical Chemistry B* **2005**, *109*, 7399.
[58] P. Sen, J. Ghosh, A. Abdullah, P. Kumar, Vandana, *Journal of Chemical Sciences* **2003**, *115*, 499.
[59] Vandana, P. Sen, *Journal of Physics: Condensed Matter* **2005**, *17*, 5327.
[60] T. Suzuki, K. Keawchai, W. Jiang, K. Yatsui, *Japanese Journal of Applied Physics* **2001**, *1073*, 1073.
[61] W. Jiang, K. Yatsui, *IEEE Transactions on Plasma Science* **1998**, *26*, 1498.
[62] Y. A. Kotov, *Journal of Nanoparticle Research* **2003**, *5*, 539.
[63] J. Muñoz-García, L. Vázquez, R. Cuerno, J. A. Sánchez-García, M. Castro, R. Gago, DOI: 10.1007/978-0-387-77717-7_10, Springer US, New York, NY **2009**, p. 323.
[64] O. K. Alekseeva, A. I. Mikhalev, E. K. Lutikova, V. I. Porembsky, M. Y. Presnyakov, V. N. Fateev, B. L. Shapir, S. A. Grigoriev, *Catalysts* **2018**, *8*.
[65] H. R. Rezaie, A. Shokuhfar, F. Arianpour, Vol. 77 **2012**, p. 171.
[66] S. Mende, F. Stenger, W. Peukert, J. Schwedes, *Journal of Materials Science* **2004**, *39*, 5223.
[67] H. Hao, Y. Geng, J. E. Tate, F. Liu, K. Chen, X. Sun, Z. Liu, F. Zhao, *Nature Communications* **2019**, *10*, 5398.

[68] Z. A. Needell, J. McNerney, M. T. Chang, J. E. Trancik, *Nature Energy* **2016**, *1*, 16112.
[69] Z. W. Seh, J. Kibsgaard, C. F. Dickens, I. Chorkendorff, J. K. Nørskov, T. F. Jaramillo, *Science* **2017**, *355*, eaad4998.
[70] J. M. Campos-Martin, G. Blanco-Brieva, J. L. G. Fierro, *Angewandte Chemie International Edition* **2006**, *45*, 6962.
[71] R. O'hayre, S.-W. Cha, W. Colella, F. B. Prinz, *Fuel cell fundamentals*, John Wiley & Sons, **2016**.
[72] T. Yoshida, K. Kojima, *Electrochemical Society Interface* **2015**, *24*, 45.
[73] F. Ning, X. He, Y. Shen, H. Jin, Q. Li, D. Li, S. Li, Y. Zhan, Y. Du, J. Jiang, H. Yang, X. Zhou, *ACS Nano* **2017**, *11*, 5982.
[74] T. Aicher, B. Lenz, F. Gschnell, U. Groos, F. Federici, L. Caprile, L. Parodi, *Journal of Power Sources* **2006**, *154*, 503.
[75] M. K. Debe, *Nature* **2012**, *486*, 43.
[76] C. Song, J. Zhang, in *PEM Fuel Cell Electrocatalysts and Catalyst Layers: Fundamentals and Applications*, DOI: 10.1007/978-1-84800-936-3_2 (Ed: J. Zhang), Springer London, London **2008**, p. 89.
[77] S. Sui, X. Wang, X. Zhou, Y. Su, S. Riffat, C.-j. Liu, *Journal of Materials Chemistry A* **2017**, *5*, 1808.
[78] J.-C. Dong, X.-G. Zhang, V. Briega-Martos, X. Jin, J. Yang, S. Chen, Z.-L. Yang, D.-Y. Wu, J. M. Feliu, C. T. Williams, Z.-Q. Tian, J.-F. Li, *Nature Energy* **2019**, *4*, 60.
[79] J. K. Nørskov, J. Rossmeisl, A. Logadottir, L. Lindqvist, J. R. Kitchin, T. Bligaard, H. Jónsson, *The Journal of Physical Chemistry B* **2004**, *108*, 17886.
[80] B. Pivovar, *Nat. Catal.* **2019**, *2*, 562.
[81] F. J. Perez-Alonso, D. N. McCarthy, A. Nierhoff, P. Hernandez-Fernandez, C. Strebel, I. E. L. Stephens, J. H. Nielsen, I. Chorkendorff, *Angewandte Chemie International Edition* **2012**, *51*, 4641.
[82] B. Garlyyev, K. Kratzl, M. Rück, J. Michalička, J. Fichtner, J. M. Macak, T. Kratky, S. Günther, M. Cokoja, A. S. Bandarenka, A. Gagliardi, R. A. Fischer, *Angewandte Chemie International Edition* **2019**, *58*, 9596.
[83] M. Shao, Q. Chang, J. P. Dodelet, R. Chenitz, *Chem Rev* **2016**, *116*, 3594.
[84] Y. Jiao, Y. Zheng, M. Jaroniec, S. Z. Qiao, *Chem Soc Rev* **2015**, *44*, 2060.
[85] X. Huang, Z. Zhao, L. Cao, Y. Chen, E. Zhu, Z. Lin, M. Li, A. Yan, A. Zettl, Y. M. Wang, X. Duan, T. Mueller, Y. Huang, *Science* **2015**, *348*, 1230.
[86] M. Carmo, D. L. Fritz, J. Mergel, D. Stolten, *International Journal of Hydrogen Energy* **2013**, *38*, 4901.
[87] Denmark, (Ed: E. a. B. t. t. D. P. Ministry of Climate), 2012.
[88] J. P. Barton, D. G. Infield, *IEEE Transactions on Energy Conversion* **2004**, *19*, 441.
[89] P. Lettenmeier, S. Kolb, N. Sata, A. Fallisch, L. Zielke, S. Thiele, A. S. Gago, K. A. Friedrich, *Energy & Environmental Science* **2017**, *10*, 2521.
[90] E. Antolini, *ACS Catalysis* **2014**, *4*, 1426.
[91] I. C. Man, H.-Y. Su, F. Calle-Vallejo, H. A. Hansen, J. I. Martínez, N. G. Inoglu, J. Kitchin, T. F. Jaramillo, J. K. Nørskov, J. Rossmeisl, *ChemCatChem* **2011**, *3*, 1159.
[92] Y. Zheng, Y. Jiao, Y. Zhu, L. H. Li, Y. Han, Y. Chen, A. Du, M. Jaroniec, S. Z. Qiao, *Nature Communications* **2014**, *5*, 3783.
[93] X.-P. Yin, H.-J. Wang, S.-F. Tang, X.-L. Lu, M. Shu, R. Si, T.-B. Lu, *Angewandte Chemie International Edition* **2018**, *57*, 9382.
[94] *Optics and photonics. Lasers and laser-related equipment. Vocabulary and symbols*, BS EN ISO 11145:2016, British Standards Institution, **2016**.
[95] W. M. Steen, J. Mazumder, *Laser Material Processing*, Springer London, London **2010**.

[96] P. W. Milonni, J. H. Eberly, *Laser Physics*, John Wiley & Sons, Inc., Hoboken, NJ, USA **2010**.
[97] C. B. Hitz, J. J. Ewing, H. Jeff, DOI: 10.1002/9781118219492.ch11, John Wiley & Sons, Inc., Hoboken, NJ, USA **2012**, p. 129.
[98] P. K. Gupta, *Laser Physics and Technology*, **2012**.
[99] H. Kogelnik, T. Li, *Proceedings of the IEEE* **1966**, *54*, 1312.
[100] J. G. Walter, S. Petersen, F. Stahl, T. Scheper, S. Barcikowski, *Journal of Nanobiotechnology* **2010**, *8*, 21.
[101] A. Barchanski, P. Wagener, S. Klein, S. Barcikowski, **2011**, 5094.
[102] G. Yang, *Progress in Materials Science* **2007**, *52*, 648.
[103] R. Kumar, R. K. Singh, D. P. Singh, E. Joanni, R. M. Yadav, S. A. Moshkalev, *Coordination Chemistry Reviews* **2017**, *342*, 34.
[104] M. B. Agranat, S. I. Anisimov, S. I. Ashitkov, V. V. Zhakhovskii, N. A. Inogamov, K. Nishihara, Y. V. Petrov, V. E. Fortov, V. A. Khokhlov, *Applied Surface Science* **2007**, *253*, 6276.
[105] D. Perez, L. K. Béland, D. Deryng, L. J. Lewis, M. Meunier, *Physical Review B* **2008**, *77*, 014108.
[106] J. P. Sylvestre, A. V. Kabashin, E. Sacher, M. Meunier, *Applied Physics A* **2005**, *80*, 753.
[107] V. Amendola, M. Meneghetti, *Phys. Chem. Chem. Phys.* **2013**, *15*, 3027.
[108] N. Aguiló-Aguayo, Z. Liu, DOI: 10.1201/b19568-22, CRC Press **2016**, p. 401.
[109] S. Barcikowski, G. Compagnini, *Phys. Chem. Chem. Phys.* **2013**, *15*, 3022.
[110] K. Sasaki, N. Takada, *Pure and Applied Chemistry* **2010**, *82*, 1317.
[111] D. Tan, S. Zhou, J. Qiu, N. Khusro, *Journal of Photochemistry and Photobiology C: Photochemistry Reviews* **2013**, *17*, 50.
[112] H. Zeng, X.-W. Du, S. C. Singh, S. A. Kulinich, S. Yang, J. He, W. Cai, *Advanced Functional Materials* **2012**, *22*, 1333.
[113] P. P. Patil, D. M. Phase, S. A. Kulkarni, S. V. Ghaisas, S. K. Kulkarni, S. M. Kanetkar, S. B. Ogale, V. G. Bhide, *Physical Review Letters* **1987**, *58*, 238.
[114] S. B. Ogale, P. P. Patil, D. M. Phase, Y. V. Bhandarkar, S. K. Kulkarni, S. Kulkarni, S. V. Ghaisas, S. M. Kanetkar, V. G. Bhide, S. Guha, *Physical Review B* **1987**, *36*, 8237.
[115] J. Neddersen, G. Chumanov, T. M. Cotton, *Applied Spectroscopy* **1993**, *47*, 1959.
[116] V. Amendola, M. Meneghetti, *Physical Chemistry Chemical Physics* **2009**, *11*, 3805.
[117] D. Bäuerle, *Laser Processing and Chemistry*, Springer Berlin Heidelberg, Berlin, Heidelberg **2011**.
[118] M. Stafe, A. Marcu, N. N. Puscas, *Pulsed Laser Ablation of Solids*, Springer Berlin Heidelberg, Berlin, Heidelberg **2014**.
[119] K.-H. Leitz, B. Redlingshöfer, Y. Reg, A. Otto, M. Schmidt, *Physics Procedia* **2011**, *12*, 230.
[120] T. Tsuji, K. Iryo, Y. Nishimura, M. Tsuji, *Journal of Photochemistry and Photobiology A: Chemistry* **2001**, *145*, 201.
[121] J. Byskov-Nielsen, J.-M. Savolainen, M. S. Christensen, P. Balling, *Applied Physics A* **2010**, *101*, 97.
[122] B. C. Stuart, M. D. Feit, S. Herman, A. M. Rubenchik, B. W. Shore, M. D. Perry, *Journal of the Optical Society of America B* **1996**, *13*, 459.
[123] *Lasers and laser-related equipment. Test methods for laser-induced damage threshold*, BS EN ISO 21254-1:2011, British Standards Institution, **2011**.
[124] M. J. Liu, *Opt. Lett.* **1982**, *7*, 196.
[125] Y. Di Maio, J. P. Colombier, P. Cazottes, E. Audouard, *Optics and Lasers in Engineering* **2012**, *50*, 1582.

[126] N. Sanner, O. Utéza, B. Bussiere, G. Coustillier, A. Leray, T. Itina, M. Sentis, *Applied Physics A* **2009**, *94*, 889.
[127] M. López-Claros, J. M. Vadillo, J. J. Laserna, *J. Anal. At. Spectrom.* **2015**, *30*, 1730.
[128] N. Singh, *International Journal of Modern Physics B* **2010**, *24*, 1141.
[129] S. I. Anisimov, B. L. Kapeliovich, T. L. Perel-man, *Journal of Experimental and Theoretical Physics* **1974**, *66*, 375.
[130] J. Cheng, W. Perrie, B. Wu, S. Tao, S. P. Edwardson, G. Dearden, K. G. Watkins, *Applied Surface Science* **2009**, *255*, 8171.
[131] B. N. Chichkov, C. Momma, S. Nolte, F. Alvensleben, A. Tünnermann, *Applied Physics A Materials Science & Processing* **1996**, *63*, 109.
[132] R. Tanabe, T. T. P. Nguyen, T. Sugiura, Y. Ito, *Applied Surface Science* **2015**, *351*, 327.
[133] A. De Giacomo, M. Dell'Aglio, A. Santagata, R. Gaudiuso, O. De Pascale, P. Wagener, G. C. Messina, G. Compagnini, S. Barcikowski, *Phys. Chem. Chem. Phys.* **2013**, *15*, 3083.
[134] T. Tsuji, Y. Okazaki, Y. Tsuboi, M. Tsuji, *Japanese Journal of Applied Physics* **2007**, *46*, 1533.
[135] Z. Yan, D. B. Chrisey, *Journal of Photochemistry and Photobiology C: Photochemistry Reviews* **2012**, *13*, 204.
[136] M. H. Mahdieh, B. Fattahi, *Optics & Laser Technology* **2015**, *75*, 188.
[137] V. P. Veiko, V. I. Konov, *Fundamentals of Laser-Assisted Micro- and Nanotechnologies*, Springer International Publishing, Cham **2014**.
[138] W. Soliman, N. Takada, K. Sasaki, *Applied Physics Express* **2010**, *3*, 035201.
[139] A. Menéndez-Manjón, B. N. Chichkov, S. Barcikowski, *The Journal of Physical Chemistry C* **2010**, *114*, 2499.
[140] R. Lachaine, E. Boulais, E. Bourbeau, M. Meunier, *Applied Physics A* **2013**, *112*, 119.
[141] X. Chen, R. Q. Xu, Z. H. Shen, J. Lu, X. W. Ni, *Optics & Laser Technology* **2004**, *36*, 197.
[142] K. Sasaki, T. Nakano, W. Soliman, N. Takada, *Applied Physics Express* **2009**, *2*, 046501.
[143] C. L. s. Sajti, R. Sattari, B. N. Chichkov, S. Barcikowski, *The Journal of Physical Chemistry C* **2010**, *114*, 2421.
[144] T. Tsuji, D. H. Thang, Y. Okazaki, M. Nakanishi, Y. Tsuboi, M. Tsuji, *Applied Surface Science* **2008**, *254*, 5224.
[145] F. Mafune, J. Kohno, Y. Takeda, T. Kondow, H. Sawabe, *Journal of Physical Chemistry B* **2000**, *104*, 9111.
[146] F. Mafuné, J. Y. Kohno, Y. Takeda, T. Kondow, H. Sawabe, *Journal of Physical Chemistry B* **2001**, *105*, 5114.
[147] J.-P. Sylvestre, A. V. Kabashin, E. Sacher, M. Meunier, J. H. T. Luong, *Journal of the American Chemical Society* **2004**, *126*, 7176.
[148] S. b. Besner, A. V. Kabashin, F. o. M. Winnik, M. Meunier, *The Journal of Physical Chemistry C* **2009**, *113*, 9526.
[149] Z. Yan, R. Bao, D. B. Chrisey, *Nanotechnology* **2010**, *21*, 145609.
[150] Z. Yan, R. Bao, C. M. Busta, D. B. Chrisey, *Nanotechnology* **2011**, *22*, 265610.
[151] Z. Yan, R. Bao, Y. Huang, D. B. Chrisey, *The Journal of Physical Chemistry C* **2010**, *114*, 11370.
[152] Z. Yan, R. Bao, D. B. Chrisey, *Phys. Chem. Chem. Phys.* **2013**, *15*, 3052.
[153] Z. Yan, R. Bao, R. N. Wright, D. B. Chrisey, *Applied Physics Letters* **2010**, *97*, 124106.
[154] Z. Yan, R. Bao, Y. Huang, A. N. Caruso, S. B. Qadri, C. Z. Dinu, D. B. Chrisey, *The Journal of Physical Chemistry C* **2010**, *114*, 3869.

[155] D. C. Schinca, L. B. Scaffardi, F. A. Videla, G. A. Torchia, P. Moreno, L. Roso, *Journal of Physics D: Applied Physics* **2009**, *42*, 215102.
[156] W. T. Nichols, T. Sasaki, N. Koshizaki, *Journal of Applied Physics* **2006**, *100*, 114913.
[157] H. Muto, K. Yamada, K. Miyajima, F. Mafuné, *The Journal of Physical Chemistry C* **2007**, *111*, 17221.
[158] H. Zeng, W. Cai, Y. Li, J. Hu, P. Liu, *The Journal of Physical Chemistry B* **2005**, *109*, 18260.
[159] J.-P. Sylvestre, S. Poulin, A. V. Kabashin, E. Sacher, M. Meunier, J. H. T. Luong, *The Journal of Physical Chemistry B* **2004**, *108*, 16864.
[160] N. Takada, T. Sasaki, K. Sasaki, *Applied Physics A* **2008**, *93*, 833.
[161] J. S. Golightly, A. W. Castleman, *The Journal of Physical Chemistry B* **2006**, *110*, 19979.
[162] P. V. Kamat, *The Journal of Physical Chemistry B* **2002**, *106*, 7729.
[163] H. Hada, Y. Yonezawa, M. Saikawa, *Bulletin of the Chemical Society of Japan* **1982**, *55*, 2010.
[164] A. Wood, M. Giersig, P. Mulvaney, *The Journal of Physical Chemistry B* **2001**, *105*, 8810.
[165] Z. Sheykhifard, M. Ranjbar, H. Farrokhpour, H. Salamati, *The Journal of Physical Chemistry C* **2015**, *119*, 9534.
[166] N. Mottaghi, M. Ranjbar, H. Farrokhpour, M. Khoshouei, A. Khoshouei, P. Kameli, H. Salamati, M. Tabrizchi, M. Jalilian-Nosrati, *Applied Surface Science* **2014**, *292*, 892.
[167] H. Hada, Y. Yonezawa, A. Yoshida, A. Kurakake, *The Journal of Physical Chemistry* **1976**, *80*, 2728.
[168] S. Eustis, H.-Y. Hsu, M. A. El-Sayed, *The Journal of Physical Chemistry B* **2005**, *109*, 4811.
[169] K. Kurihara, J. Kizling, P. Stenius, J. H. Fendler, *Journal of the American Chemical Society* **1983**, *105*, 2574.
[170] E. Jiménez, K. Abderrafi, R. Abargues, J. L. Valdés, J. P. Martínez-Pastor, *Langmuir* **2010**, *26*, 7458.
[171] P. Liu, H. Chen, H. Wang, J. Yan, Z. Lin, G. Yang, *The Journal of Physical Chemistry C* **2015**, *119*, 1234.
[172] D. Zhang, B. Gökce, C. Notthoff, S. Barcikowski, *Scientific Reports* **2015**, *5*, 13661.
[173] M. Chen, D. Wang, X. Liu, *RSC Advances* **2016**, *6*, 9549.
[174] R. Mahfouz, F. J. Cadete Santos Aires, A. Brenier, E. Ehret, M. Roumié, B. Nsouli, B. Jacquier, J. C. Bertolini, *Journal of Nanoparticle Research* **2010**, *12*, 3123.
[175] S. Sebastian, C. L. Linslal, C. P. G. Vallbhan, V. P. N. Nampoori, P. Radhakrishnan, M. Kailasnath, *Chemical Physics Letters* **2015**, *628*, 25.
[176] H. Han, Y. Fang, Z. Li, H. Xu, *Applied Physics Letters* **2008**, *92*, 023116.
[177] A. A. Serkov, M. E. Shcherbina, P. G. Kuzmin, N. A. Kirichenko, *Applied Surface Science* **2015**, *336*, 96.
[178] R. Singh, R. K. Soni, *Applied Physics A* **2014**, *116*, 955.
[179] K. D. Malviya, K. Chattopadhyay, *The Journal of Physical Chemistry C* **2014**, *118*, 13228.
[180] S. Petrović, B. Salatić, D. Milovanović, V. Lazović, L. Živković, M. Trtica, B. Jelenković, *Journal of Optics* **2015**, *17*, 025402.
[181] R. Singh, R. K. Soni, *Applied Physics A* **2015**, *121*, 261.
[182] Y. Zhao, S. Li, Y. Zeng, Y. Jiang, *APL Materials* **2015**, *3*, 086103.
[183] A. Santagata, A. Guarnaccio, D. Pietrangeli, Á. Szegedi, J. Valyon, A. De Stefanis, A. De Bonis, R. Teghil, M. Sansone, D. Mollica, G. P. Parisi, *Journal of Physics D: Applied Physics* **2015**, *48*, 205304.

[184] T. Salminen, M. Honkanen, T. Niemi, *Physical Chemistry Chemical Physics* **2013**, *15*, 3047.
[185] M. Ganjali, M. Ganjali, S. Khoby, M. A. Meshkot, *Nano-Micro Letters* **2011**, *3*, 256.
[186] O. R. Musaev, E. A. Sutter, J. M. Wrobel, M. B. Kruger, *Journal of Nanoparticle Research* **2012**, *14*, 654.
[187] Z. Li, J.-Y. Fu, Y. Feng, C.-K. Dong, H. Liu, X.-W. Du, *Nature Catalysis* **2019**, *2*, 1107.
[188] P. Wagener, J. Jakobi, C. Rehbock, V. S. K. Chakravadhanula, C. Thede, U. Wiedwald, M. Bartsch, L. Kienle, S. Barcikowski, *Scientific Reports* **2016**, *6*, 23352.
[189] V. Amendola, S. Scaramuzza, L. Litti, M. Meneghetti, G. Zuccolotto, A. Rosato, E. Nicolato, P. Marzola, G. Fracasso, C. Anselmi, M. Pinto, M. Colombatti, *Small* **2014**, *10*, 2476.
[190] Y. Ishikawa, K. Kawaguchi, Y. Shimizu, T. Sasaki, N. Koshizaki, *Chemical Physics Letters* **2006**, *428*, 426.
[191] A. A. Serkov, E. V. Barmina, A. V. Simakin, P. G. Kuzmin, V. V. Voronov, G. A. Shafeev, *Applied Surface Science* **2015**, *348*, 71.
[192] J. Jakobi, S. Petersen, A. Menéndez-Manjón, P. Wagener, S. Barcikowski, *Langmuir* **2010**, *26*, 6892.
[193] M. Chakif, A. Essaidi, E. Gurevich, A. Ostendorf, O. Prymak, M. Epple, *Journal of Materials Engineering and Performance* **2014**, *23*, 2482.
[194] N. Patra, K. Akash, S. Shiva, R. Gagrani, H. S. P. Rao, V. R. Anirudh, I. A. Palani, V. Singh, *Applied Surface Science* **2016**, *366*, 104.
[195] M. I. Mendivil, L. V. García, B. Krishnan, D. Avellaneda, J. A. Martinez, S. Shaji, *Materials Research Bulletin* **2015**, *72*, 106.
[196] N. G. Semaltianos, E. Hendry, H. Chang, M. L. Wears, G. Monteil, M. Assoul, V. Malkhasyan, V. Blondeau-Patissier, B. Gauthier-Manuel, V. Moutarlier, *Journal of Colloid and Interface Science* **2016**, *469*, 57.
[197] V. Švrček, D. Mariotti, R. A. Blackley, W. Z. Zhou, T. Nagai, K. Matsubara, M. Kondo, *Nanoscale* **2013**, *5*, 6725.
[198] K. Hagedorn, B. Liu, A. Marcinkevicius, *Journal of The Electrochemical Society* **2012**, *160*, F106.
[199] J. Jakobi, S. Petersen, A. Menéndez-Manjón, P. Wagener, S. Barcikowski, *Langmuir* **2010**, *26*, 6892.
[200] M. P. Navas, R. K. Soni, *Applied Physics A* **2014**, *116*, 879.
[201] R. G. Nikov, N. N. Nedyalkov, A. S. Nikolov, P. A. Atanasov, M. T. Alexandrov, D. B. Karashanova, 2015/01//.
[202] J. Zhang, D. N. Oko, S. Garbarino, R. Imbeault, M. Chaker, A. C. Tavares, D. Guay, D. Ma, *The Journal of Physical Chemistry C* **2012**, *116*, 13413.
[203] D. N. Oko, J. Zhang, S. Garbarino, M. Chaker, D. Ma, A. C. Tavares, D. Guay, *Journal of Power Sources* **2014**, *248*, 273.
[204] J. Jakobi, A. Menéndez-Manjón, V. S. K. Chakravadhanula, L. Kienle, P. Wagener, S. Barcikowski, *Nanotechnology* **2011**, *22*, 145601.
[205] V. Amendola, M. Meneghetti, O. M. Bakr, P. Riello, S. Polizzi, D. H. Anjum, S. Fiameni, P. Arosio, T. Orlando, C. De Julian Fernandez, F. Pineider, C. Sangregorio, A. Lascialfari, *Nanoscale* **2013**, *5*, 5611.
[206] V. Amendola, S. Scaramuzza, S. Agnoli, S. Polizzi, M. Meneghetti, *Nanoscale* **2014**, *6*, 1423.
[207] L. Gan, C. Cui, M. Heggen, F. Dionigi, S. Rudi, P. Strasser, *Science* **2014**, *346*, 1502.
[208] H. Lee, S. E. Habas, S. Kweskin, D. Butcher, G. A. Somorjai, P. Yang, *Angewandte Chemie International Edition* **2006**, *45*, 7824.

[209] C. Gumeci, A. Marathe, R. L. Behrens, J. Chaudhuri, C. Korzeniewski, *The Journal of Physical Chemistry C* **2014**, *118*, 14433.
[210] Z.-C. Zhang, J.-F. Hui, Z.-G. Guo, Q.-Y. Yu, B. Xu, X. Zhang, Z.-C. Liu, C.-M. Xu, J.-S. Gao, X. Wang, *Nanoscale* **2012**, *4*, 2633.
[211] I. A. Safo, M. Oezaslan, *Electrochimica Acta* **2017**, *241*, 544.
[212] S.-I. Choi, S. Xie, M. Shao, J. H. Odell, N. Lu, H.-C. Peng, L. Protsailo, S. Guerrero, J. Park, X. Xia, J. Wang, M. J. Kim, Y. Xia, *Nano Letters* **2013**, *13*, 3420.
[213] Z. Li, Y. Feng, Y.-L. Liang, C.-Q. Cheng, C.-K. Dong, H. Liu, X.-W. Du, *Advanced Materials* **2020**, *32*, 1908521.
[214] M. Yu, F. Waag, C. K. Chan, C. Weidenthaler, S. Barcikowski, H. Tüysüz, *ChemSusChem* **2020**, *13*, 520.
[215] S. Kohsakowski, R. Streubel, I. Radev, V. Peinecke, S. Barcikowski, G. Marzun, S. Reichenberger, *Applied Surface Science* **2019**, *467-468*, 486.
[216] S. Hu, M. Tian, E. L. Ribeiro, G. Duscher, D. Mukherjee, *Journal of Power Sources* **2016**, *306*, 413.
[217] M. Ren, J. Zhang, J. M. Tour, *Carbon* **2018**, *139*, 880.
[218] J. Cao, P. He, M. A. Mohammed, X. Zhao, R. J. Young, B. Derby, I. A. Kinloch, R. A. W. Dryfe, *J. Am. Chem. Soc.* **2017**, *139*, 17446.
[219] D. B. Williams, C. B. Carter, *Transmission Electron Microscopy - A Textbook for Materials Science*, Springer US, **2009**.
[220] *X - Ray Photoelectron Spectroscopy* **2011**, DOI: https://doi.org/10.1002/9781118162897.ch213.
[221] B. Charles, K. J. Fredeen.
[222] A. C. Ferrari, D. M. Basko, *Nature Nanotechnology* **2013**, *8*, 235.
[223] A. Eckmann, A. Felten, A. Mishchenko, L. Britnell, R. Krupke, K. S. Novoselov, C. Casiraghi, *Nano Lett.* **2012**, *12*, 3925.
[224] J. M. Englert, P. Vecera, K. C. Knirsch, R. A. Schäfer, F. Hauke, A. Hirsch, *ACS Nano* **2013**, *7*, 5472.
[225] N. Elgrishi, K. J. Rountree, B. D. McCarthy, E. S. Rountree, T. T. Eisenhart, J. L. Dempsey, *Journal of Chemical Education* **2018**, *95*, 197.
[226] M. Lu, F. Beguin, E. Frackowiak, *Supercapacitors: Materials, Systems, and Applications*, Wiley, **2013**.
[227] C. Wei, R. R. Rao, J. Peng, B. Huang, I. E. L. Stephens, M. Risch, Z. J. Xu, Y. Shao-Horn, *Adv Mater* **2019**, *31*, e1806296.
[228] J. B. Allen, R. F. Larry, *Electrochemical methods fundamentals and applications*, John Wiley & Sons, **2001**.
[229] R. E. Davis, G. L. Horvath, C. W. Tobias, *Electrochim. Acta* **1967**, *12*, 287.
[230] Y. Liang, Y. Li, H. Wang, J. Zhou, J. Wang, T. Regier, H. Dai, *Nat. Mater.* **2011**, *10*, 780.
[231] S. Sharma, B. G. Pollet, *Journal of Power Sources* **2012**, *208*, 96.
[232] E. Alonso, F. R. Field, R. E. Kirchain, *Environmental Science & Technology* **2012**, *46*, 12986.
[233] M. Li, Z. Zhao, T. Cheng, A. Fortunelli, C.-Y. Chen, R. Yu, Q. Zhang, L. Gu, B. V. Merinov, Z. Lin, E. Zhu, T. Yu, Q. Jia, J. Guo, L. Zhang, W. A. Goddard, Y. Huang, X. Duan, *Science* **2016**, *354*, 1414.
[234] D. Y. Chung, S. W. Jun, G. Yoon, S. G. Kwon, D. Y. Shin, P. Seo, J. M. Yoo, H. Shin, Y.-H. Chung, H. Kim, B. S. Mun, K.-S. Lee, N.-S. Lee, S. J. Yoo, D.-H. Lim, K. Kang, Y.-E. Sung, T. Hyeon, *Journal of the American Chemical Society* **2015**, *137*, 15478.
[235] X. Ge, L. Chen, J. Kang, T. Fujita, A. Hirata, W. Zhang, J. Jiang, M. Chen, *Advanced Functional Materials* **2013**, *23*, 4156.

[236] K. A. Kuttiyiel, K. Sasaki, Y. Choi, D. Su, P. Liu, R. R. Adzic, *Nano Letters* **2012**, *12*, 6266.
[237] H. Zhang, M. Jin, J. Wang, W. Li, P. H. C. Camargo, M. J. Kim, D. Yang, Z. Xie, Y. Xia, *Journal of the American Chemical Society* **2011**, *133*, 6078.
[238] X. Teng, S. Maksimuk, S. Frommer, H. Yang, *Chemistry of Materials* **2007**, *19*, 36.
[239] M. Nesselberger, S. Ashton, J. C. Meier, I. Katsounaros, K. J. J. Mayrhofer, M. Arenz, *Journal of the American Chemical Society* **2011**, *133*, 17428.
[240] G. Marzun, A. Levish, V. Mackert, T. Kallio, S. Barcikowski, P. Wagener, *Journal of Colloid and Interface Science* **2017**, *489*, 57.
[241] G. González-Rubio, A. Guerrero-Martínez, L. M. Liz-Marzán, *Accounts of Chemical Research* **2016**, *49*, 678.
[242] P. V. Kamat, M. Flumiani, G. V. Hartland, *The Journal of Physical Chemistry B* **1998**, *102*, 3123.
[243] W. T. Nichols, T. Sasaki, N. Koshizaki, *Journal of Applied Physics* **2006**, *100*, 114911.
[244] D. Li, M. H. Nielsen, J. R. I. Lee, C. Frandsen, J. F. Banfield, J. J. De Yoreo, *Science* **2012**, *336*, 1014.
[245] M. Kauranen, A. V. Zayats, *Nature Photonics* **2012**, *6*, 737.
[246] S. Jendrzej, B. Gökce, V. Amendola, S. Barcikowski, *Journal of Colloid and Interface Science* **2016**, *463*, 299.
[247] N. C. Bigall, T. Härtling, M. Klose, P. Simon, L. M. Eng, A. Eychmüller, *Nano Letters* **2008**, *8*, 4588.
[248] N. Zhang, C. Han, Y.-J. Xu, J. J. Foley Iv, D. Zhang, J. Codrington, S. K. Gray, Y. Sun, *Nature Photonics* **2016**, *10*, 473.
[249] J. A. Creighton, D. G. Eadon, *J. Chem. Soc., Faraday Trans.* **1991**, *87*, 3881.
[250] C. F. Bohren, D. R. Huffman, *Absorption and Scattering of Light by Small Particles*, Wiley, **2008**.
[251] A. Henglein, B. G. Ershov, M. Malow, *The Journal of Physical Chemistry* **1995**, *99*, 14129.
[252] J. F. Rivadulla, M. C. Vergara, M. C. Blanco, M. A. López-Quintela, J. Rivas, *The Journal of Physical Chemistry B* **1997**, *101*, 8997.
[253] C. Davis-Wheeler Chin, S. Akbarian-Tefaghi, J. Reconco-Ramirez, J. B. Wiley, *MRS Communications* **2018**, *8*, 71.
[254] I. Zorić, M. Zäch, B. Kasemo, C. Langhammer, *ACS Nano* **2011**, *5*, 2535.
[255] G. Marzun, J. Nakamura, X. Zhang, S. Barcikowski, P. Wagener, *Applied Surface Science* **2015**, *348*, 75.
[256] H. Neff, S. Henkel, E. Hartmannsgruber, E. Steinbeiss, W. Michalke, K. Steenbeck, H. G. Schmidt, *Journal of Applied Physics* **1996**, *79*, 7672.
[257] B. J. Sumlin, W. R. Heinson, R. K. Chakrabarty, *Journal of Quantitative Spectroscopy and Radiative Transfer* **2018**, *205*, 127.
[258] W. S. M. Werner, K. Glantschnig, C. Ambrosch-Draxl, *Journal of Physical and Chemical Reference Data* **2009**, *38*, 1013.
[259] A. Pyatenko, H. Wang, N. Koshizaki, T. Tsuji, *Laser & Photonics Reviews* **2013**, *7*, 596.
[260] A. Pyatenko, M. Yamaguchi, M. Suzuki, *The Journal of Physical Chemistry C* **2009**, *113*, 9078.
[261] K. Metwally, S. Mensah, G. Baffou, *The Journal of Physical Chemistry C* **2015**, *119*, 28586.
[262] G. W. C. Kaye, T. H. Laby, *Tables of physical and chemical constants and some mathematical functions*, **1966**.
[263] J. Y, A. Degiovanni, *Physical Properties of Air and Water*, **2018**.

[264] M. W. Chase, J. L. Curnutt, A. T. Hu, H. Prophet, A. N. Syverud, L. C. Walker, *Journal of Physical and Chemical Reference Data* **1974**, *3*, 311.
[265] S. Hashimoto, T. Katayama, K. Setoura, M. Strasser, T. Uwada, H. Miyasaka, *Physical Chemistry Chemical Physics* **2016**, *18*, 4994.
[266] S. L. Lai, J. Y. Guo, V. Petrova, G. Ramanath, L. H. Allen, *Physical Review Letters* **1996**, *77*, 99.
[267] A. Jiang, N. Awasthi, A. N. Kolmogorov, W. Setyawan, A. Börjesson, K. Bolton, A. R. Harutyunyan, S. Curtarolo, *Physical Review B* **2007**, *75*, 205426.
[268] M. Shao, A. Peles, K. Shoemaker, *Nano Letters* **2011**, *11*, 3714.
[269] W. Wang, Z. Wang, M. Yang, C.-J. Zhong, C.-J. Liu, *Nano Energy* **2016**, *25*, 26.
[270] Y. Shao-Horn, W. C. Sheng, S. Chen, P. J. Ferreira, E. F. Holby, D. Morgan, *Topics in Catalysis* **2007**, *46*, 285.
[271] Y. Zhang, S. Chen, Y. Wang, W. Ding, R. Wu, L. Li, X. Qi, Z. Wei, *Journal of Power Sources* **2015**, *273*, 62.
[272] J. Willsau, J. Heitbaum, *Journal of Electroanalytical Chemistry and Interfacial Electrochemistry* **1984**, *161*, 93.
[273] G. Zhang, Q. Wei, X. Yang, A. C. Tavares, S. Sun, *Appl. Catal. B-Environ.* **2017**, *206*, 115.
[274] H. Schmies, E. Hornberger, B. Anke, T. Jurzinsky, H. N. Nong, F. Dionigi, S. Kühl, J. Drnec, M. Lerch, C. Cremers, P. Strasser, *Chemistry of Materials* **2018**, *30*, 7287.
[275] M. Carmo, M. Linardi, J. G. R. Poco, *Applied Catalysis A: General* **2009**, *355*, 132.
[276] C. Barrington-Leigh, J. Baumgartner, E. Carter, B. E. Robinson, S. Tao, Y. Zhang, *Nat. Energy* **2019**, *4*, 416.
[277] B. Pivovar, *Na. Catal.* **2019**, *2*, 562.
[278] JapanGov, Creating a "Hydrogen Society" to Protect the Global Environment, https://www.japan.go.jp/tomodachi/2017/spring-summer2017/creating_a_hydrogen_society.html, accessed: 02, 2020.
[279] X. X. Wang, M. T. Swihart, G. Wu, *Nat. Catal.* **2019**, *2*, 578.
[280] Y. Sun, Q. Wu, G. Shi, *Energy Environ. Sci.* **2011**, *4*, 1113.
[281] V. Georgakilas, J. N. Tiwari, K. C. Kemp, J. A. Perman, A. B. Bourlinos, K. S. Kim, R. Zboril, *Chem. Rev.* **2016**, *116*, 5464.
[282] Y. Liang, Y. Li, H. Wang, J. Zhou, J. Wang, T. Regier, H. Dai, *Nat. Mater.* **2011**, *10*, 780.
[283] Z. S. Wu, S. Yang, Y. Sun, K. Parvez, X. Feng, K. Mullen, *J. Am. Chem. Soc.* **2012**, *134*, 9082.
[284] D. Higgins, M. A. Hoque, M. H. Seo, R. Wang, F. Hassan, J.-Y. Choi, M. Pritzker, A. Yu, J. Zhang, Z. Chen, *Adv. Funct. Mater.* **2014**, *24*, 4325.
[285] S. D. Perera, R. G. Mariano, K. Vu, N. Nour, O. Seitz, Y. Chabal, K. J. Balkus, *ACS Catal.* **2012**, *2*, 949.
[286] P. S. Toth, M. Velický, M. A. Bissett, T. J. A. Slater, N. Savjani, A. K. Rabiu, A. M. Rakowski, J. R. Brent, S. J. Haigh, P. O'Brien, R. A. W. Dryfe, *Adv. Mater.* **2016**, *28*, 8256.
[287] P. S. Toth, Q. M. Ramasse, M. Velický, R. A. W. Dryfe, *Chem. Sci.* **2015**, *6*, 1316.
[288] S. Dou, L. Tao, R. Wang, S. El Hankari, R. Chen, S. Wang, *Adv. Mater.* **2018**, *30*, 1705850.
[289] J. D. Blakemore, H. B. Gray, J. R. Winkler, A. M. Müller, *ACS Catal.* **2013**, *3*, 2497.
[290] B. M. Hunter, J. D. Blakemore, M. Deimund, H. B. Gray, J. R. Winkler, A. M. Müller, *J. Am. Chem. Soc.* **2014**, *136*, 13118.

[291] J. Sourice, A. Quinsac, Y. Leconte, O. Sublemontier, W. Porcher, C. Haon, A. Bordes, E. De Vito, A. Boulineau, S. Jouanneau Si Larbi, N. Herlin-Boime, C. Reynaud, *ACS Appl. Mater. Interfaces* **2015**, *7*, 6637.
[292] J. Wang, Y. Lin, M. Pinault, A. Filoramo, M. Fabert, B. Ratier, J. Bouclé, N. Herlin-Boime, *ACS Appl. Mater. Interfaces* **2015**, *7*, 51.
[293] R. Ye, D. K. James, J. M. Tour, *Acc. Chem. Res.* **2018**, *51*, 1609.
[294] X. Mo, K. C. Chan, E. C. M. Tse, *Chem. Mater.* **2019**, *31*, 8230.
[295] R. Ye, Z. Peng, T. Wang, Y. Xu, J. Zhang, Y. Li, L. G. Nilewski, J. Lin, J. M. Tour, *ACS Nano* **2015**, *9*, 9244.
[296] S. Moussa, V. Abdelsayed, M. Samy El-Shall, *Chem. Phys. Lett.* **2011**, *510*, 179.
[297] S. Moussa, G. Atkinson, M. SamyEl-Shall, A. Shehata, K. M. AbouZeid, M. B. Mohamed, *J. Mater. Chem.* **2011**, *21*, 9608.
[298] S. Moussa, A. R. Siamaki, B. F. Gupton, M. S. El-Shall, *ACS Catal.* **2012**, *2*, 145.
[299] K. Wenderich, G. Mul, *Chem. Rev.* **2016**, *116*, 14587.
[300] B. Kraeutler, A. J. Bard, *J. Am. Chem. Soc.* **1978**, *100*, 4317.
[301] K. P. Loh, Q. Bao, G. Eda, M. Chhowalla, *Nat. Chem.* **2010**, *2*, 1015.
[302] G. Eda, Y. Y. Lin, C. Mattevi, H. Yamaguchi, H. A. Chen, I. S. Chen, C. W. Chen, M. Chhowalla, *Adv. Mater.* **2010**, *22*, 505.
[303] Abid, P. Sehrawat, S. S. Islam, P. Mishra, S. Ahmad, *Sci. Rep.* **2018**, *8*, 3537.
[304] C. Mattevi, G. Eda, S. Agnoli, S. Miller, K. A. Mkhoyan, O. Celik, D. Mastrogiovanni, G. Granozzi, E. Garfunkel, M. Chhowalla, *Adv. Funct. Mater.* **2009**, *19*, 2577.
[305] R. Flyunt, W. Knolle, A. Kahnt, C. E. Halbig, A. Lotnyk, T. Haupl, A. Prager, S. Eigler, B. Abel, *Nanoscale* **2016**, *8*, 7572.
[306] M. Shams, L. M. Guiney, L. Huang, M. Ramesh, X. Yang, M. C. Hersam, I. Chowdhury, *Environ.-Sci. Nano* **2019**, *6*, 2203.
[307] L. Huang, Y. Liu, L.-C. Ji, Y.-Q. Xie, T. Wang, W.-Z. Shi, *Carbon* **2011**, *49*, 2431.
[308] S. Eigler, M. Enzelberger-Heim, S. Grimm, P. Hofmann, W. Kroener, A. Geworski, C. Dotzer, M. Rockert, J. Xiao, C. Papp, O. Lytken, H. P. Steinruck, P. Muller, A. Hirsch, *Adv. Mater.* **2013**, *25*, 3583.
[309] S. Eigler, *Chem.-Eur. J.* **2016**, *22*, 7012.
[310] J. Cao, P. He, M. A. Mohammed, X. Zhao, R. J. Young, B. Derby, I. A. Kinloch, R. A. W. Dryfe, *J. Am. Chem. Soc.* **2017**, *139*, 17446.
[311] W. S. Hummers, R. E. Offeman, *J. Am. Chem. Soc.* **1958**, *80*, 1339.
[312] N. I. Kovtyukhova, P. J. Ollivier, B. R. Martin, T. E. Mallouk, S. A. Chizhik, E. V. Buzaneva, A. D. Gorchinskiy, *Chem. Mater.* **1999**, *11*, 771.
[313] D. Liu, X. Li, S. Chen, H. Yan, C. Wang, C. Wu, Y. A. Haleem, S. Duan, J. Lu, B. Ge, P. M. Ajayan, Y. Luo, J. Jiang, L. Song, *Nat. Energy* **2019**, *4*, 512.
[314] J. Chen, P. Cui, G. Zhao, K. Rui, M. Lao, Y. Chen, X. Zheng, Y. Jiang, H. Pan, S. X. Dou, W. Sun, *Angew. Chem. Int. Edit.* **2019**, *58*, 12540.
[315] C. C. McCrory, S. Jung, J. C. Peters, T. F. Jaramillo, *J. Am. Chem. Soc.* **2013**, *135*, 16977.
[316] S. Anantharaj, M. Jayachandran, S. Kundu, *Chem. Sci.* **2016**, *7*, 3188.
[317] J. Tauc, *Mater. Res. Bull.* **1968**, *3*, 37.
[318] S. R. M. Santiago, T. N. Lin, C. T. Yuan, J. L. Shen, H. Y. Huang, C. A. J. Lin, *Phys. Chem. Chem. Phys.* **2016**, *18*, 22599.
[319] S. Saxena, T. A. Tyson, S. Shukla, E. Negusse, H. Chen, J. Bai, *Appl. Phys. Lett.* **2011**, *99*, 013104.
[320] H.-C. Hsu, I. Shown, H.-Y. Wei, Y.-C. Chang, H.-Y. Du, Y.-G. Lin, C.-A. Tseng, C.-H. Wang, L.-C. Chen, Y.-C. Lin, K.-H. Chen, *Nanoscale* **2013**, *5*, 262.
[321] F. Tuinstra, J. L. Koenig, *J. Chem. Phys.* **1970**, *53*, 1126.

[322] M. M. Lucchese, F. Stavale, E. H. M. Ferreira, C. Vilani, M. V. O. Moutinho, R. B. Capaz, C. A. Achete, A. Jorio, *Carbon* **2010**, *48*, 1592.
[323] L. G. Cançado, A. Jorio, E. H. Ferreira, F. Stavale, C. A. Achete, R. B. Capaz, M. V. Moutinho, A. Lombardo, T. S. Kulmala, A. C. Ferrari, *Nano Lett.* **2011**, *11*, 3190.
[324] J. M. Engiert, P. Vecera, K. C. Knirsch, R. A. Schafer, F. Hauke, A. Hirsch, *ACS Nano* **2013**, *7*, 5472.
[325] L. G. Cancado, A. Jorio, E. H. Ferreira, F. Stavale, C. A. Achete, R. B. Capaz, M. V. Moutinho, A. Lombardo, T. S. Kulmala, A. C. Ferrari, *Nano Lett.* **2011**, *11*, 3190.
[326] J. H. Zhong, J. Zhang, X. Jin, J. Y. Liu, Q. Li, M. H. Li, W. Cai, D. Y. Wu, D. Zhan, B. Ren, *J Am Chem Soc* **2014**, *136*, 16609.
[327] L. G. Cancado, A. Jorio, E. H. Ferreira, F. Stavale, C. A. Achete, R. B. Capaz, M. V. Moutinho, A. Lombardo, T. S. Kulmala, A. C. Ferrari, *Nano Lett.* **2011**, *11*, 3190.
[328] A. Iakunkov, J. Sun, A. Rebrikova, M. Korobov, A. Klechikov, A. Vorobiev, N. Boulanger, A. V. Talyzin, *J. Mater. Chem. A* **2019**, *7*, 11331.
[329] L. Stobinski, B. Lesiak, A. Malolepszy, M. Mazurkiewicz, B. Mierzwa, J. Zemek, P. Jiricek, I. Bieloshapka, *J. Electron. Spectrosc. Relat. Phenom.* **2014**, *195*, 145.
[330] A. Bagri, C. Mattevi, M. Acik, Y. J. Chabal, M. Chhowalla, V. B. Shenoy, *Nat. Chem.* **2010**, *2*, 581.
[331] H.-K. Jeong, Y. P. Lee, M. H. Jin, E. S. Kim, J. J. Bae, Y. H. Lee, *Chem. Phys. Lett.* **2009**, *470*, 255.
[332] G. Zhou, D.-W. Wang, L.-C. Yin, N. Li, F. Li, H.-M. Cheng, *ACS Nano* **2012**, *6*, 3214.
[333] W. M. Haynes, *CRC Handbook of Chemistry and Physics, 95th Edition*, CRC Press LLC, Oakville, United Kingdom **2014**.
[334] E. Tsuji, A. Imanishi, K.-i. Fukui, Y. Nakato, *Electrochim. Acta* **2011**, *56*, 2009.
[335] Y. Lee, J. Suntivich, K. J. May, E. E. Perry, Y. Shao-Horn, *J. Phys. Chem. Lett.* **2012**, *3*, 399.
[336] Y. Chen, X. Zhang, D. Zhang, Y. Ma, *J. Alloy. Compd.* **2012**, *511*, 251.
[337] W.-C. Fang, J.-H. Huang, L.-C. Chen, Y.-L. O. Su, K.-H. Chen, *J. Power Sources* **2006**, *160*, 1506.
[338] H. Kim, B. N. Popov, *J. Power Sources* **2002**, *104*, 52.
[339] M. Pourbaix, *Atlas of electrochemical equilibria in aqueous solutions*, National Association of Corrosion Engineers, Huston, Texas **1974**.
[340] S. Hadži-Jordanov, H. Angerstein-Kozlowska, M. Vukovič, B. E. Conway, *J. Electrochem. Soc.* **1978**, *125*, 1471.
[341] M. Tian, C. Cousins, D. Beauchemin, Y. Furuya, A. Ohma, G. Jerkiewicz, *ACS Catal.* **2016**, *6*, 5108.
[342] P. Vanden Brande, A. Dumont, R. Winand, *J. Appl. Electrochem.* **1994**, *24*, 201.
[343] D. J. Morgan, *Surf. Interface Anal.* **2015**, *47*, 1072.
[344] K. Qadir, S. H. Joo, B. S. Mun, D. R. Butcher, J. R. Renzas, F. Aksoy, Z. Liu, G. A. Somorjai, J. Y. Park, *Nano Lett.* **2012**, *12*, 5761.
[345] G. Zhang, D. Yang, E. Sacher, *J. Phys. Chem. C* **2007**, *111*, 565.
[346] T. Reier, M. Oezaslan, P. Strasser, *ACS Catal.* **2012**, *2*, 1765.
[347] S. Cherevko, S. Geiger, O. Kasian, N. Kulyk, J.-P. Grote, A. Savan, B. R. Shrestha, S. Merzlikin, B. Breitbach, A. Ludwig, K. J. J. Mayrhofer, *Catal. Today* **2016**, *262*, 170.
[348] C. C. L. McCrory, S. Jung, J. C. Peters, T. F. Jaramillo, *J. Am. Chem. Soc.* **2013**, *135*, 16977.
[349] J. P. Zheng, P. J. Cygan, T. R. Jow, *J. Electrochem. Soc.* **1995**, *142*, 2699.
[350] P. Li, M. Wang, X. Duan, L. Zheng, X. Cheng, Y. Zhang, Y. Kuang, Y. Li, Q. Ma, Z. Feng, W. Liu, X. Sun, *Nat. Commun.* **2019**, *10*, 1711.

[351] H.-S. Park, J. Yang, M. K. Cho, Y. Lee, S. Cho, S.-D. Yim, B.-S. Kim, J. H. Jang, H.-K. Song, *Nano Energy* **2019**, *55*, 49.
[352] M. P. Browne, H. Nolan, B. Twamley, G. S. Duesberg, P. E. Colavita, M. E. G. Lyons, *ChemElectroChem* **2016**, *3*, 1847.
[353] R. Nazir, U. Basak, S. Pande, *Colloids Surf., A* **2019**, *560*, 141.
[354] C.-Z. Yuan, Y.-F. Jiang, Z.-W. Zhao, S.-J. Zhao, X. Zhou, T.-Y. Cheang, A.-W. Xu, *ACS Sustain. Chem. Eng.* **2018**, *6*, 11529.
[355] H. Hu, F. M. D. Kazim, Q. Zhang, K. Qu, Z. Yang, W. Cai, *ChemCatChem* **2019**, *11*, 4327.
[356] T. Qiu, Z. Liang, W. Guo, S. Gao, C. Qu, H. Tabassum, H. Zhang, B. Zhu, R. Zou, Y. Shao-Horn, *Nano Energy* **2019**, *58*, 1.
[357] D. R. Liyanage, D. Li, Q. B. Cheek, H. Baydoun, S. L. Brock, *J. Mater. Chem. A* **2017**, *5*, 17609.
[358] J. Ding, Q. Shao, Y. Feng, X. Huang, *Nano Energy* **2018**, *47*, 1.
[359] S. Fu, J. Song, C. Zhu, G.-L. Xu, K. Amine, C. Sun, X. Li, M. H. Engelhard, D. Du, Y. Lin, *Nano Energy* **2018**, *44*, 319.
[360] J. H. Jang, A. Kato, K. Machida, K. Naoi, *J. Electrochem. Soc.* **2006**, *153*, A321.
[361] N. Yoshida, Y. Yamada, S.-i. Nishimura, Y. Oba, M. Ohnuma, A. Yamada, *J. Phys. Chem. C* **2013**, *117*, 12003.
[362] Y. Li, Y. Li, E. Zhu, T. McLouth, C.-Y. Chiu, X. Huang, Y. Huang, *J. Am. Chem. Soc.* **2012**, *134*, 12326.
[363] J. Zheng, Y. Yan, B. Xu, *Journal of The Electrochemical Society* **2015**, *162*, F1470.
[364] X.-K. Wan, H. B. Wu, B. Y. Guan, D. Luan, X. W. Lou, *Adv. Mater.* **2020**, *32*, 1901349.
[365] T. Chao, X. Luo, W. Chen, B. Jiang, J. Ge, Y. Lin, G. Wu, X. Wang, Y. Hu, Z. Zhuang, Y. Wu, X. Hong, Y. Li, *Angew. Chem.-Int. Edit.* **2017**, *56*, 16047.
[366] M. Tavakkoli, N. Holmberg, R. Kronberg, H. Jiang, J. Sainio, E. I. Kauppinen, T. Kallio, K. Laasonen, *ACS Catal.* **2017**, *7*, 3121.
[367] W. Ren, H. Zhang, C. Cheng, *Electrochim. Acta* **2017**, *241*, 316.
[368] J. Chen, Y. Yang, J. Su, P. Jiang, G. Xia, Q. Chen, *ACS Appl. Mater. Interfaces* **2017**, *9*, 3596.
[369] H. Tian, X. Cui, L. Zeng, L. Su, Y. Song, J. Shi, *J. Mater. Chem. A* **2019**, *7*, 6285.
[370] M. Li, Q. Ma, W. Zi, X. Liu, X. Zhu, S. Liu, *Sci. Adv.* **2015**, *1*, e1400268.
[371] X. Chia, N. A. A. Sutrisnoh, M. Pumera, *ACS Appl. Mater. Interfaces* **2018**, *10*, 8702.
[372] Y. Zhang, J. Yan, X. Ren, L. Pang, H. Chen, S. Liu, *Int. J. Hydrog. Energy* **2017**, *42*, 5472.
[373] N. Du, C. Wang, R. Long, Y. Xiong, *Nano Res.* **2017**, *10*, 3228.
[374] K. Qi, W. Zheng, X. Cui, *Nanoscale* **2016**, *8*, 1698.
[375] Y. Chen, G. Fu, Y. Li, Q. Gu, L. Xu, D. Sun, Y. Tang, *J. Mater. Chem. A* **2017**, *5*, 3774.
[376] L. Wang, Z. Tang, W. Yan, Q. Wang, H. Yang, S. Chen, *J. Power Sources* **2017**, *343*, 458.
[377] K. Tiido, N. Alexeyeva, M. Couillard, C. Bock, B. R. MacDougall, K. Tammeveski, *Electrochim. Acta* **2013**, *107*, 509.
[378] Y. Zhang, H. Liu, H. Wu, Z. Sun, L. Qian, *Mater. Des.* **2016**, *96*, 323.
[379] M. Liu, S. He, W. Chen, *Electrochim. Acta* **2016**, *199*, 218.
[380] D. Bhalothia, J.-P. Chou, C. Yan, A. Hu, Y.-T. Yang, T.-Y. Chen, *ACS Omega* **2018**, *3*, 8733.
[381] K. Jukk, J. Kozlova, P. Ritslaid, V. Sammelselg, N. Alexeyeva, K. Tammeveski, *J. Electroanal. Chem.* **2013**, *708*, 31.
[382] S. Liang, C. Hao, Y. Shi, *ChemCatChem* **2015**, *7*, 2559.

[383] Z. Pu, I. S. Amiinu, R. Cheng, P. Wang, C. Zhang, S. Mu, W. Zhao, F. Su, G. Zhang, S. Liao, S. Sun, *Nano-Micro Letters* **2020**, *12*, 21.
[384] M. Yang, M. Flytzani-Stephanopoulos, *Catalysis Today* **2017**, *298*, 216.
[385] M. Yang, L. F. Allard, M. Flytzani-Stephanopoulos, *J Am Chem Soc* **2013**, *135*, 3768.
[386] H. Yan, H. Cheng, H. Yi, Y. Lin, T. Yao, C. Wang, J. Li, S. Wei, J. Lu, *J Am Chem Soc* **2015**, *137*, 10484.
[387] L. Lin, S. Yao, R. Gao, X. Liang, Q. Yu, Y. Deng, J. Liu, M. Peng, Z. Jiang, S. Li, Y. W. Li, X. D. Wen, W. Zhou, D. Ma, *Nat Nanotechnol* **2019**, *14*, 354.
[388] H. Yan, C. Su, J. He, W. Chen, *Journal of Materials Chemistry A* **2018**, *6*, 8793.
[389] H. Fei, J. Dong, M. J. Arellano-Jimenez, G. Ye, N. Dong Kim, E. L. Samuel, Z. Peng, Z. Zhu, F. Qin, J. Bao, M. J. Yacaman, P. M. Ajayan, D. Chen, J. M. Tour, *Nat Commun* **2015**, *6*, 8668.
[390] J. Liu, M. Jiao, L. Lu, H. M. Barkholtz, Y. Li, Y. Wang, L. Jiang, Z. Wu, D. J. Liu, L. Zhuang, C. Ma, J. Zeng, B. Zhang, D. Su, P. Song, W. Xing, W. Xu, Y. Wang, Z. Jiang, G. Sun, *Nat Commun* **2017**, *8*, 15938.
[391] N. Cheng, L. Zhang, K. Doyle-Davis, X. Sun, *Electrochemical Energy Reviews* **2019**, *2*, 539.
[392] X.-F. Yang, A. Wang, B. Qiao, J. Li, J. Liu, T. Zhang, *Accounts of Chemical Research* **2013**, *46*, 1740.
[393] D. Liu, X. Li, S. Chen, H. Yan, C. Wang, C. Wu, Y. A. Haleem, S. Duan, J. Lu, B. Ge, P. M. Ajayan, Y. Luo, J. Jiang, L. Song, *Nature Energy* **2019**, *4*, 512.
[394] Y. Chen, Z. Huang, Z. Ma, J. Chen, X. Tang, *Catalysis Science & Technology* **2017**, *7*, 4250.
[395] H. Wei, X. Liu, A. Wang, L. Zhang, B. Qiao, X. Yang, Y. Huang, S. Miao, J. Liu, T. Zhang, *Nature Communications* **2014**, *5*, 5634.
[396] J. Lin, B. Qiao, J. Liu, Y. Huang, A. Wang, L. Li, W. Zhang, L. F. Allard, X. Wang, T. Zhang, *Angewandte Chemie International Edition* **2012**, *51*, 2920.
[397] L. Lin, W. Zhou, R. Gao, S. Yao, X. Zhang, W. Xu, S. Zheng, Z. Jiang, Q. Yu, Y.-W. Li, C. Shi, X.-D. Wen, D. Ma, *Nature* **2017**, *544*, 80.
[398] M. Li, K. Duanmu, C. Wan, T. Cheng, L. Zhang, S. Dai, W. Chen, Z. Zhao, P. Li, H. Fei, Y. Zhu, R. Yu, J. Luo, K. Zang, Z. Lin, M. Ding, J. Huang, H. Sun, J. Guo, X. Pan, W. A. Goddard, P. Sautet, Y. Huang, X. Duan, *Nature Catalysis* **2019**, *2*, 495.
[399] L. Zhang, Y. Jia, G. Gao, X. Yan, N. Chen, J. Chen, M. T. Soo, B. Wood, D. Yang, A. Du, X. Yao, *Chem* **2018**, *4*, 285.
[400] H. Fei, J. Dong, D. Chen, T. Hu, X. Duan, I. Shakir, Y. Huang, X. Duan, *Chemical Society Reviews* **2019**, *48*, 5207.
[401] Y. Chen, S. Ji, C. Chen, Q. Peng, D. Wang, Y. Li, *Joule* **2018**, *2*, 1242.
[402] J. Zhang, X. Wu, W.-C. Cheong, W. Chen, R. Lin, J. Li, L. Zheng, W. Yan, L. Gu, C. Chen, Q. Peng, D. Wang, Y. Li, *Nature Communications* **2018**, *9*, 1002.
[403] J. Zhang, Y. Zhao, X. Guo, C. Chen, C.-L. Dong, R.-S. Liu, C.-P. Han, Y. Li, Y. Gogotsi, G. Wang, *Nature Catalysis* **2018**, *1*, 985.
[404] S. Zhao, Y. Wang, J. Dong, C.-T. He, H. Yin, P. An, K. Zhao, X. Zhang, C. Gao, L. Zhang, J. Lv, J. Wang, J. Zhang, A. M. Khattak, N. A. Khan, Z. Wei, J. Zhang, S. Liu, H. Zhao, Z. Tang, *Nature Energy* **2016**, *1*.
[405] W. Cheng, X. Zhao, H. Su, F. Tang, W. Che, H. Zhang, Q. Liu, *Nature Energy* **2019**, *4*, 115.
[406] Y. Cheng, S. Zhao, B. Johannessen, J.-P. Veder, M. Saunders, M. R. Rowles, M. Cheng, C. Liu, M. F. Chisholm, R. De Marco, H.-M. Cheng, S.-Z. Yang, S. P. Jiang, *Advanced Materials* **2018**, *30*, 1706287.

[407] Y. Yao, Z. Huang, P. Xie, L. Wu, L. Ma, T. Li, Z. Pang, M. Jiao, Z. Liang, J. Gao, Y. He, D. J. Kline, M. R. Zachariah, C. Wang, J. Lu, T. Wu, T. Li, C. Wang, R. Shahbazian-Yassar, L. Hu, *Nat Nanotechnol* **2019**, *14*, 851.
[408] J. Jones, H. Xiong, A. T. DeLaRiva, E. J. Peterson, H. Pham, S. R. Challa, G. Qi, S. Oh, M. H. Wiebenga, X. I. Pereira Hernández, Y. Wang, A. K. Datye, *Science* **2016**, *353*, 150.
[409] Y. Qu, B. Chen, Z. Li, X. Duan, L. Wang, Y. Lin, T. Yuan, F. Zhou, Y. Hu, Z. Yang, C. Zhao, J. Wang, C. Zhao, Y. Hu, G. Wu, Q. Zhang, Q. Xu, B. Liu, P. Gao, R. You, W. Huang, L. Zheng, L. Gu, Y. Wu, Y. Li, *Journal of the American Chemical Society* **2019**, *141*, 4505.
[410] K. Jiang, S. Siahrostami, T. Zheng, Y. Hu, S. Hwang, E. Stavitski, Y. Peng, J. Dynes, M. Gangisetty, D. Su, K. Attenkofer, H. Wang, *Energy Environ. Sci.* **2018**, *11*, 893.
[411] C. Wang, W. Ping, Q. Bai, H. Cui, R. Hensleigh, R. Wang, A. H. Brozena, Z. Xu, J. Dai, Y. Pei, C. Zheng, G. Pastel, J. Gao, X. Wang, H. Wang, J.-C. Zhao, B. Yang, X. Zheng, J. Luo, Y. Mo, B. Dunn, L. Hu, *Science* **2020**, *368*, 521.
[412] H. Xie, K. Fu, C. Yang, Y. Yao, J. Rao, Y. Zhou, B. Liu, D. Kirsch, L. Hu, *Small Methods* **2018**, *2*, 1700371.
[413] Y. Zhao, Q. Han, Z. Cheng, L. Jiang, L. Qu, *Nano Today* **2017**, *12*, 14.
[414] R. Y. Gengler, D. S. Badali, D. Zhang, K. Dimos, K. Spyrou, D. Gournis, R. J. Miller, *Nat. Commun.* **2013**, *4*, 2560.
[415] S. Moussa, G. Atkinson, M. SamyEl-Shall, A. Shehata, K. M. AbouZeid, M. B. Mohamed, *J. Mater. Chem.* **2011**, *21*.
[416] Y. Peng, J. Cao, J. Yang, W. Yang, C. Zhang, X. Li, R. A. W. Dryfe, L. Li, I. A. Kinloch, Z. Liu, *Advanced Functional Materials* **2020**, *n/a*, 2001756.
[417] L. Xiao, H. Ma, J. Liu, W. Zhao, Y. Jia, Q. Zhao, K. Liu, Y. Wu, Y. Wei, S. Fan, K. Jiang, *Nano Lett* **2015**, *15*, 8365.
[418] Y. Zhou, Q. Bao, B. Varghese, L. A. L. Tang, C. K. Tan, C.-H. Sow, K. P. Loh, *Advanced Materials* **2010**, *22*, 67.
[419] X. Chen, Y. Chen, M. Yan, M. Qiu, *ACS Nano* **2012**, *6*, 2550.
[420] B. Wicklein, A. Kocjan, G. Salazar-Alvarez, F. Carosio, G. Camino, M. Antonietti, L. Bergstrom, *Nat Nanotechnol* **2015**, *10*, 277.
[421] S. Stankovich, D. A. Dikin, R. D. Piner, K. A. Kohlhaas, A. Kleinhammes, Y. Jia, Y. Wu, S. T. Nguyen, R. S. Ruoff, *Carbon* **2007**, *45*, 1558.
[422] M. J. McAllister, J.-L. Li, D. H. Adamson, H. C. Schniepp, A. A. Abdala, J. Liu, M. Herrera-Alonso, D. L. Milius, R. Car, R. K. Prud'homme, I. A. Aksay, *Chemistry of Materials* **2007**, *19*, 4396.
[423] A. T. D. Butland, R. J. Maddison, *Journal of Nuclear Materials* **1973**, *49*, 45.
[424] X. Mu, X. Wu, T. Zhang, D. B. Go, T. Luo, *Scientific Reports* **2014**, *4*, 3909.
[425] C. J. Morath, H. J. Maris, J. J. Cuomo, D. L. Pappas, A. Grill, V. V. Patel, J. P. Doyle, K. L. Saenger, *Journal of Applied Physics* **1994**, *76*, 2636.
[426] J. D. Renteria, S. Ramirez, H. Malekpour, B. Alonso, A. Centeno, A. Zurutuza, A. I. Cocemasov, D. L. Nika, A. A. Balandin, *Advanced Functional Materials* **2015**, *25*, 4664.
[427] H. Yang, Y. Cao, J. He, Y. Zhang, B. Jin, J.-L. Sun, Y. Wang, Z. Zhao, *Carbon* **2017**, *115*, 561.
[428] H. Tian, Y. Cao, J. Sun, J. He, *RSC Advances* **2017**, *7*, 46536.
[429] M. Yang, J. Liu, S. Lee, B. Zugic, J. Huang, L. F. Allard, M. Flytzani-Stephanopoulos, *J Am Chem Soc* **2015**, *137*, 3470.
[430] L. Zhang, L. Han, H. Liu, X. Liu, J. Luo, *Angewandte Chemie International Edition* **2017**, *56*, 13694.

[431] Z. Jin, Z. Chen, Q. Li, C. Xi, X. Zheng, *Journal of Photochemistry and Photobiology A: Chemistry* **1994**, *81*, 177.
[432] N. T. Xuyen, H. K. Jeong, G. Kim, K. P. So, K. H. An, Y. H. Lee, *Journal of Materials Chemistry* **2009**, *19*, 1283.
[433] S. D. Jackson, J. Willis, G. D. McLellan, G. Webb, M. B. T. Keegan, R. B. Moyes, S. Simpson, P. B. Wells, R. Whyman, *Journal of Catalysis* **1993**, *139*, 191.
[434] C. Battistoni, A. M. Giuliani, E. Paparazzo, F. Tarli, *J. Chem. Soc., Dalton Trans.* **1984**, DOI: 10.1039/DT98400012931293.
[435] S. A. Mitchenko, T. V. Krasnyakova, R. S. Mitchenko, A. N. Korduban, *Journal of Molecular Catalysis A: Chemical* **2007**, *275*, 101.
[436] K. Hiroya, S. Matsumoto, M. Ashikawa, K. Ogiwara, T. Sakamoto, *Organic Letters* **2006**, *8*, 5349.
[437] J. A. Labinger, J. E. Bercaw, *Nature* **2002**, *417*, 507.
[438] J. Chen, P. Cui, G. Zhao, K. Rui, M. Lao, Y. Chen, X. Zheng, Y. Jiang, H. Pan, S. X. Dou, W. Sun, *Angew. Chem.-Int. Edit.* **2019**, *58*, 12540.
[439] R. Sitko, E. Turek, B. Zawisza, E. Malicka, E. Talik, J. Heimann, A. Gagor, B. Feist, R. Wrzalik, *Dalton Trans* **2013**, *42*, 5682.
[440] X. Mi, G. Huang, W. Xie, W. Wang, Y. Liu, J. Gao, *Carbon* **2012**, *50*, 4856.
[441] D. R. Lowde, J. O. Williams, P. A. Attwood, R. J. Bird, B. D. McNicol, R. T. Short, *Journal of the Chemical Society, Faraday Transactions 1: Physical Chemistry in Condensed Phases* **1979**, *75*, 2312.
[442] T. W. van Deelen, C. Hernández Mejía, K. P. de Jong, *Nature Catalysis* **2019**, *2*, 955.
[443] S. Wei, A. Li, J.-C. Liu, Z. Li, W. Chen, Y. Gong, Q. Zhang, W.-C. Cheong, Y. Wang, L. Zheng, H. Xiao, C. Chen, D. Wang, Q. Peng, L. Gu, X. Han, J. Li, Y. Li, *Nature Nanotechnology* **2018**, *13*, 856.
[444] Y. Peng, B. Lu, S. Chen, *Advanced Materials* **2018**, *30*, 1801995.
[445] H. Guo, M. Peng, Z. Zhu, L. Sun, *Nanoscale* **2013**, *5*, 9040.
[446] V. Abdelsayed, S. Moussa, H. M. Hassan, H. S. Aluri, M. M. Collinson, M. S. El-Shall, *J. Phys. Chem* **2010**, *1*, 2804.
[447] A. E. Schweizer, G. T. Kerr, *Inorganic Chemistry* **1978**, *17*, 2326.
[448] M. Acik, G. Lee, C. Mattevi, A. Pirkle, R. M. Wallace, M. Chhowalla, K. Cho, Y. Chabal, *J. Phys. Chem. C* **2011**, *115*, 19761.
[449] Z. Huang, Z. Chen, Z. Chen, C. Lv, M. G. Humphrey, C. Zhang, *Nano Energy* **2014**, *9*, 373.
[450] A. García-Miranda Ferrari, D. A. C. Brownson, C. E. Banks, *Scientific Reports* **2019**, *9*, 15961.
[451] K. Jiang, B. Liu, M. Luo, S. Ning, M. Peng, Y. Zhao, Y.-R. Lu, T.-S. Chan, F. M. F. de Groot, Y. Tan, *Nature Communications* **2019**, *10*, 1743.
[452] J. Park, S. Lee, H.-E. Kim, A. Cho, S. Kim, Y. Ye, J. W. Han, H. Lee, J. H. Jang, J. Lee, *Angewandte Chemie International Edition* **2019**, *58*, 16038.
[453] N. Cheng, S. Stambula, D. Wang, M. N. Banis, J. Liu, A. Riese, B. Xiao, R. Li, T.-K. Sham, L.-M. Liu, G. A. Botton, X. Sun, *Nature Communications* **2016**, *7*, 13638.
[454] H. Wei, H. Wu, K. Huang, B. Ge, J. Ma, J. Lang, D. Zu, M. Lei, Y. Yao, W. Guo, H. Wu, *Chem. Sci.* **2019**, *10*, 2830.
[455] L. Zhang, R. Si, H. Liu, N. Chen, Q. Wang, K. Adair, Z. Wang, J. Chen, Z. Song, J. Li, M. N. Banis, R. Li, T.-K. Sham, M. Gu, L.-M. Liu, G. A. Botton, X. Sun, *Nature Communications* **2019**, *10*, 4936.
[456] H. Zhang, P. An, W. Zhou, B. Y. Guan, P. Zhang, J. Dong, X. W. Lou, *Science Advances* **2018**, *4*, eaao6657.

[457] X. Xie, Y.-F. Jiang, C.-Z. Yuan, N. Jiang, S.-J. Zhao, L. Jia, A.-W. Xu, *The Journal of Physical Chemistry C* **2017**, *121*, 24979.
[458] X. Zeng, J. Shui, X. Liu, Q. Liu, Y. Li, J. Shang, L. Zheng, R. Yu, *Advanced Energy Materials* **2018**, *8*, 1701345.